



RIJKSUNIVERSITEIT GRONINGEN

Mid-Infrared Spectroscopy of Dusty Galactic Nuclei

PROEFSCHRIFT

ter verkrijging van het doctoraat in de
Wiskunde en Natuurwetenschappen
aan de Rijksuniversiteit Groningen
op gezag van de
Rector Magnificus, dr. F. Zwarts,
in het openbaar te verdedigen op
maandag 20 oktober 2003
om 11.00 uur

door

Henrik Willem Walter Spoon

geboren op 1 maart 1968
te Woudenberg

Promotor: Prof. dr. A. G. G. M. Tielens

Beoordelingscommissie: Dr. P.D. Barthel
Prof. dr. G. Miley
Prof. dr. D.B. Sanders

ISBN 90–367–1901–1

Voor mijn ouders

Cover:

Morning twilight on the *Salar de Uyuni* in Bolivia on April 2, 1996. An ‘embedded’ power source illuminates the ring-like salt structures, which are reminiscent of Polycyclic Aromatic Hydrocarbon molecules (PAHs). Overhead, the dusty southern starburst galaxy NGC 4945.
Cover designed by Jack Waas.

Contents

1	Introduction	1
1.1	ULIRGs: the last of the Mohicans	1
1.2	Starburst in the Nearby Universe	2
1.3	Characteristics of regions of massive star formation in our own Galaxy	5
1.3.1	Observable characteristics	5
1.4	AGNs	9
1.4.1	Observable characteristics	10
1.5	ULIRGs at mid-infrared wavelengths	10
1.6	In this thesis	12
2	Ice features in the mid-IR spectra of galactic nuclei	15
2.1	Introduction	16
2.2	Observations	17
2.2.1	ISO galaxy sample	17
2.2.2	Selected sample	17
2.3	Ice absorption and PAH emission in the 5–7 μm region	18
2.3.1	Components of the model	18
2.3.2	Effects on the model of varying the component contributions and extinction	22
2.3.3	Profile appearance as a function of redshift	23
2.4	Classification	24
2.5	Absorption and emission profile analysis	29
2.5.1	Model fits	29
2.5.2	Derived physical parameters	32
2.6	Discussion	36
2.7	Conclusions	43
3	Mid-infrared ISO spectroscopy of NGC 4945	45
3.1	Introduction	46
3.2	Observations	47
3.2.1	SWS spectroscopy	47
3.2.2	PHT-S spectrophotometry	47
3.3	Results	50

3.3.1	AGN not seen at mid-infrared wavelengths	50
3.3.2	Starburst properties	52
3.3.3	What powers the nucleus of NGC 4945?	54
3.3.4	Emission and absorption features	55
3.3.5	Molecular hydrogen: physical conditions, excitation and mass	56
3.4	Conclusions	62
4	Detection of strongly processed ice in the central starburst of NGC 4945	63
4.1	Introduction	64
4.2	Observations	66
4.3	Results	67
4.3.1	The $3\mu\text{m}$ water ice band	67
4.3.2	Processed CO and OCN ⁻ ice	68
4.3.3	The spatial distribution of the ice	71
4.4	Discussion	76
4.4.1	The nuclear geometry	76
4.4.2	On the formation of OCN ⁻ in galactic nuclei	78
4.4.3	Comparison to the lines of sight to the nuclei of M 82 and NGC 253	78
4.4.4	Comparison to the line of sight to the Galactic center	78
4.5	Conclusions	79
5	The obscured mid-infrared continuum of NGC 4418: a dust- and ice-enshrouded AGN	81
5.1	Introduction	82
5.2	Observations	82
5.3	The mid-IR spectrum of NGC 4418	83
5.3.1	Spectral features	83
5.3.2	Dust and ice column densities	86
5.4	Discussion and conclusions	86
6	Mid-infrared spectral evidence for a luminous dust enshrouded source in Arp 220	89
6.1	Introduction	90
6.2	The infrared spectrum of Arp 220	92
6.2.1	The mid-IR spectrum of Arp 220	92
6.2.2	Broad $7.7\mu\text{m}$ feature similar to Mon R2:IRS 1+2	93
6.2.3	Mid-IR continuum similar to NGC 4418	94
6.3	Mid-IR spectral decomposition	95
6.3.1	PAH and continuum templates	97
6.3.2	The extinction law at mid-infrared wavelengths	97
6.3.3	Decomposition method	99
6.3.4	Decomposition results	99
6.4	Discussion	101
6.4.1	Identification of the spectral components	101
6.4.2	The nature of the nuclear power sources	102

6.4.3	Modeling of the nuclear continuum	103
6.4.4	Mid-to-far-infrared spectral characteristics	104
6.5	Conclusions	105
7	PAHs as a tracer for star formation	107
7.1	Introduction	108
7.2	Observations	109
7.2.1	H II regions and ISM	109
7.2.2	ISO galaxy sample	112
7.3	The spectral characteristics	112
7.3.1	H II regions and ISM	112
7.3.2	Galaxy sample	114
7.4	Diagnostic tools to distinguish AGNs and starbursts	118
7.4.1	A MIR/FIR diagnostic	118
7.4.2	Laurent diagnostic diagram	130
7.4.3	The Genzel diagnostic diagram	136
7.4.4	Comparison of the three diagnostic diagrams	137
7.5	Discussion	137
7.5.1	PAH abundance	137
7.5.2	PAHs as a tracer of star formation	138
7.5.3	Conversion from PAH luminosity to IR luminosity	141
7.6	Conclusions	141
8	Conclusions and outlook	143
Nederlandse samenvatting		147
Acknowledgements		177

1

Introduction

1.1 ULIRGs: the last of the Mohicans

ONE of the most important extragalactic discoveries of IRAS was the detection of a class of galaxies with infrared (8–1000 μm) luminosities in excess of 10^{12} L_\odot and infrared-to-blue ratios (L_{IR}/L_B) ratios even higher than for lower luminosity infrared-bright galaxies. Except for Arp 220 and NGC 6240, none of these Ultra-Luminous Infrared Galaxies (ULIRGs) had been previously detected in optical surveys. Subsequent follow-up observations established that ULIRGs are advanced mergers, containing exceptionally large amounts of molecular gas in their nuclei (Sanders et al. 1988a,b; Kim et al. 2002; Veilleux et al. 2002). The origin of this strong infrared emission has been widely debated: the infrared luminosity may reflect intense star formation or the presence of a very active galactic nucleus (AGN). If powered entirely by star formation, ULIRGs are the most spectacular starburst galaxies in the universe, building up an entire stellar population in a few short bursts. If, on the other hand, ULIRGs are partly powered by AGN activity, the study of ULIRGs would catch the central engine in its most enshrouded phase.

Across all wavebands, enormous efforts have been made to determine the dominant power source. Such studies are greatly hampered by the presence of copious amounts of gas and dust. Outcomes are highly dependent on the AGN and starburst tracers used and often require quite a bit of faith in their applicability for strongly extincted lines of sight. This also applies to hard X-ray observations (e.g. Braito et al. 2003; Gallagher et al. 2002; Komossa et al. 2003; Lira et al. 2002; Xia et al. 2002), where, as Ptak et al. (2003) noted, “absence of evidence is not evidence of absence”. This being said, both the recent XMM and CHANDRA surveys seem to agree that starburst activity dominates over AGN activity in the nearby ($z < 0.045$) ULIRGs that were studied (Ptak et al. 2003; Franceschini et al. 2003). For the more distant and high-luminosity ULIRGs, no such studies have yet been made.

The general evolutionary scheme emerging from all of these studies is that ULIRGs represent an important phase in the evolution of mergers. When two dust-rich spiral galaxies merge, their gravitational interaction drives gas into the galactic nuclei. After some 500 million years, this causes a strong burst of star formation at a rate of some $100 \text{ M}_\odot/\text{yr}$. The flow of gas into the nuclei may also activate the central monster. Eventually, the remaining gas has

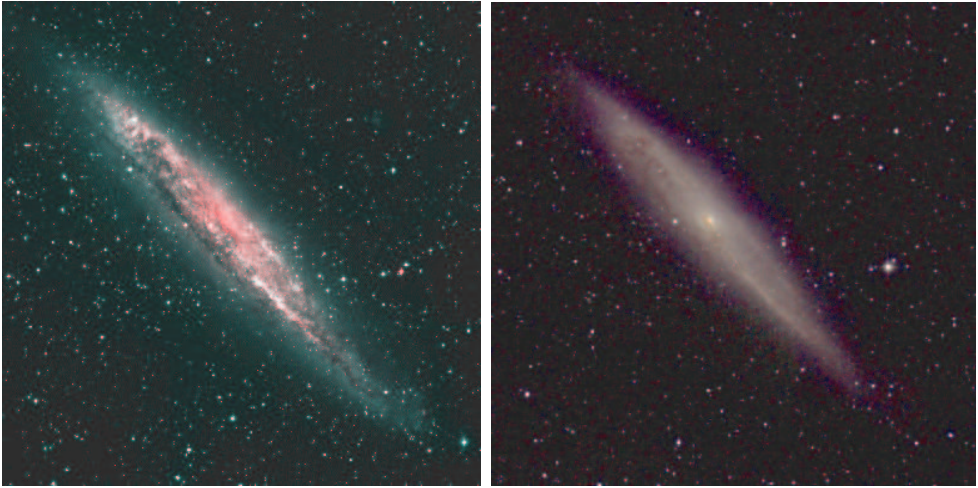


FIGURE 1.1— The nearby southern starburst galaxy NGC 4945 covers $20' \times 4'$ of the sky. 75% of its luminosity originates in the central $12'' \times 9''$ (Brock et al. 1988). **Left:** Despite the concentration of luminosity towards the center, the optical nucleus is inconspicuous due to strong extinction within the galaxy. Photo: ESO. **Right:** The effects of extinction are smaller in the near-infrared, permitting a glimpse of the strongly obscured nuclear starburst. Photo: Jarrett et al. (2003).

either been consumed by star formation or been shed by the powerful supernova explosions and all activity will cease. The only signs of the merger remaining may be the increased mass of the bulge and the increased mass of the central black hole (Kormendy & Sanders 1992; Genzel & Cesarsky 2000; Tremaine et al. 2002).

SCUBA and MAMBO studies have found that the number of galaxies with luminosities similar to ULIRGs was a factor 400 higher in the Early Universe compared to the Local Universe (Blain et al. 2002). As the Star Formation Rate (SFR) per comoving volume element is also found to be much higher in the Early Universe (the SFR increases from $z=0$ by more than a factor 10 to peak at $z=1\text{--}3$; Steidel et al. 1996; Lilly et al. 1996; Steidel et al. 1999), the fraction of star formation occurring in galaxies with ULIRG-like luminosities must have been far higher than in the Local Universe. As such, the ULIRGs may be the last of a dying race of merging galaxies, testament to an earlier epoch dominated by mergers, starbursts, and AGN activity. The study of nearby ULIRGs may hence allow us to probe the era when galaxies were hierachically assembled and their stars were formed.

While this general scenario is well accepted, the key question remains "what are the relative contributions of starburst and AGN activity to the overall energetics during the various evolutionary phases of these merging galaxies?"

1.2 Starburst in the Nearby Universe

Starburst phenomena are also known on a lesser scale in the Nearby Universe. The nearest starburst galaxy to us is M 82, at a distance of 3.3 Mpc. HST observations of the inner kpc have resolved more than a hundred compact and luminous super star clusters (de Grijs et al. 2000). The most active starburst is found in the ‘starburst core’, a region obscured by ~ 50

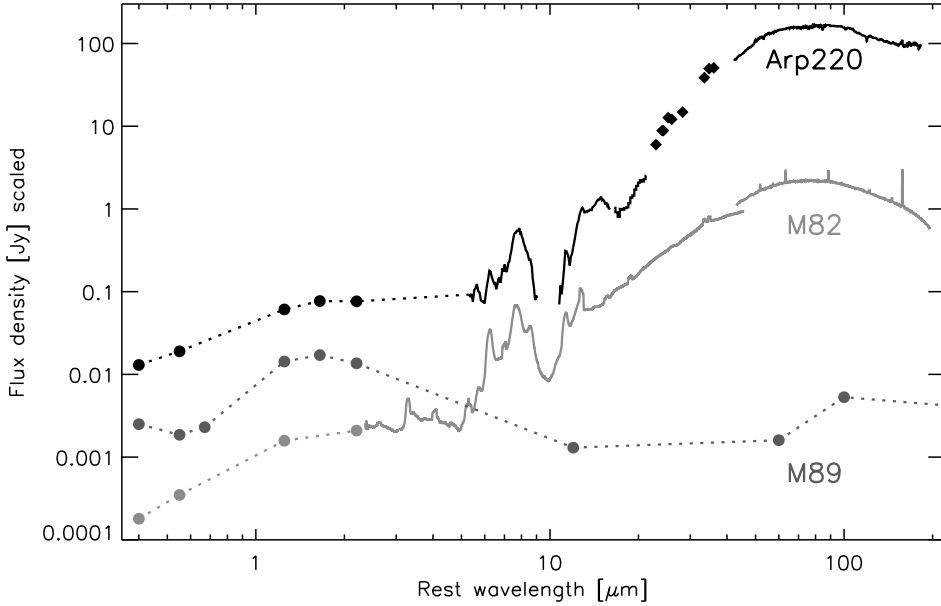


FIGURE 1.2 — Optical-infrared spectral energy distributions of M 89, M 82 and Arp 220. While the bulk of the bolometric luminosity of infrared galaxies (e.g. M 82 and Arp 220) is emitted in the mid- and far-infrared, this is not the case for most elliptical galaxies (e.g. M 89). Fluxes have been scaled and for presentation purposes, the spectrum of M 82 has been corrected for aperture effects. The ISO spectra have been taken from Fischer et al. (1997); Sturm et al. (2000); Tran et al. (2001).

magnitudes of visual extinction (Förster Schreiber et al. 2001) and responsible for most of the infrared luminosity of this galaxy. Its mid-infrared spectrum is shown in Fig. 1.9. The spectrum closely resembles the spectra of Galactic regions of massive star formation, represented in Fig. 1.9 by the spectrum of the Orion Bar (Section 1.3.1). The fierceness of the starburst is perhaps best illustrated by the presence of a nuclear bipolar outflow powered by numerous supernovae, which traces a starburst superwind out to several kpc (e.g. Lehnert et al. 1999). At the current modest star formation rate of $\sim 4 M_{\odot}/\text{yr}$, the starburst in M 82 will run out of fuel in 60 million years, hence the name ‘starburst’.

Another example of a starburst galaxy is the southern galaxy NGC 4945 (Fig. 1.1), which, like M 82, is seen nearly edge-on ($i \sim 78^\circ$). The nuclear starburst is heavily obscured at optical wavelengths, as is illustrated by the absence of an optically bright nucleus (Fig. 1.1). Unlike M 82, a powerful buried AGN lurks at the center of this galaxy, only revealing its presence in extreme hard X-rays (Iwasawa et al. 1993; Guainazzi et al. 2000).

M 82 and NGC 4945 are typical examples of ‘infrared galaxies’ — galaxies emitting more energy in the infrared than in the UV and optical bands combined (Soifer et al. 1984b). As infrared emission is generally dust emission, it follows that infrared galaxies are either rich in dust or efficient in heating the available dust. Infrared galaxies were discovered by the thousands by IRAS, which in 1983 surveyed 96% of the sky at mid- and far-infrared wavelengths. The survey established that the vast majority of the galaxies in the Local Universe ($z < 0.3$) are only modest infrared emitters at $L_{\text{IR}}/L_B \sim 0.4$, with early-type galaxies such as M 89 rank-

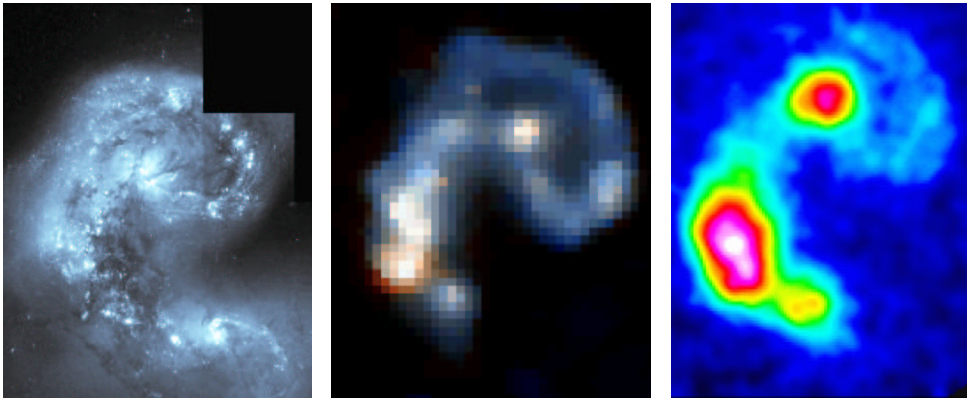


FIGURE 1.3 — “The Antennae” (NGC 4038/39) observed at three different wavelengths. **Left:** The optical image shows the distribution of stars and obscuring dust. Image: Brad Whitmore (STScI) & NASA. **Middle:** The mid-infrared image shows the interaction zone between the two nuclei to be the strongest source of warm continuum radiation. Image: ESA/ISO/ISOCAM & Laurent Vignroux. **Right:** The SCUBA image ($850 \mu\text{m}$) reveals the interaction zone to be a strong source of cold dust continuum. Image: Paul van der Werf.

ing weakest (Fig. 1.2). In contrast, classic starburst galaxies, like M 82 and NGC 253, were found to have infrared-to-blue ratios of 3 and 5 and $L_{\text{IR}}=10^{10.3}$ and $10^{10.8} L_{\odot}$, respectively. Higher infrared-to-blue ratios, in the range of 1–50, were found for a flux-limited sample of infrared selected galaxies, a quarter of which showed clear signs of interaction (Soifer et al. 1984b). IRAS further established that most infrared galaxies with $L_{\text{IR}}<10^{11} L_{\odot}$ are single, dust-rich spiral galaxies with no strong signs of AGN activity. Above $L_{\text{IR}}=10^{11} L_{\odot}$, a large fraction of the galaxies were found to be strongly interacting and extremely rich in molecular gas (Sanders & Mirabel 1996).

One of the nearest (20 Mpc) and best studied examples of a Luminous Infrared Galaxy (LIRG; $L_{\text{IR}} \geq 10^{11} L_{\odot}$) is the pair of colliding galaxies NGC 4038/39, also referred to as ‘The Antennae’. Wide-field optical and radio H I images reveal the galaxies to be accompanied by two ‘tidal tails’ extending 110 kpc in opposite directions (Hibbard et al. 2001). Structures of this kind are regarded as typical for galaxy-galaxy interactions (Toomre & Toomre 1972). In HST images (left panel of Figure 1.3), the two galaxy disks appear distorted and the two nuclei are separated by only 6.4 kpc (Whitmore & Schweizer 1995). In the overlap region between the two nuclei, strong patchy extinction coincides with a broad maximum in mid-infrared $15 \mu\text{m}$ maps (middle panel of Figure 1.3). The energy output of this region is about half of the total energy output of the system at $15 \mu\text{m}$. As its mid-infrared spectrum shows strong resemblance to spectra of sites of massive star formation in our Galaxy, it is hence likely that the interaction has triggered a massive starburst in this region. Given the absence of equally prominent starburst emission in optical or UV maps, the example of the Antennae illustrates that UV rest frame observations of galaxies at high redshift may not probe the true star formation rate in dusty mergers. In contrast, and illustrated in the right panel of Fig. 1.3, SCUBA observations at $850 \mu\text{m}$ are more effective as a tracer of star formation (Van der Werf et al., in prep.), probing the stellar energy absorbed by dust near the peak of its spectral energy distribution.

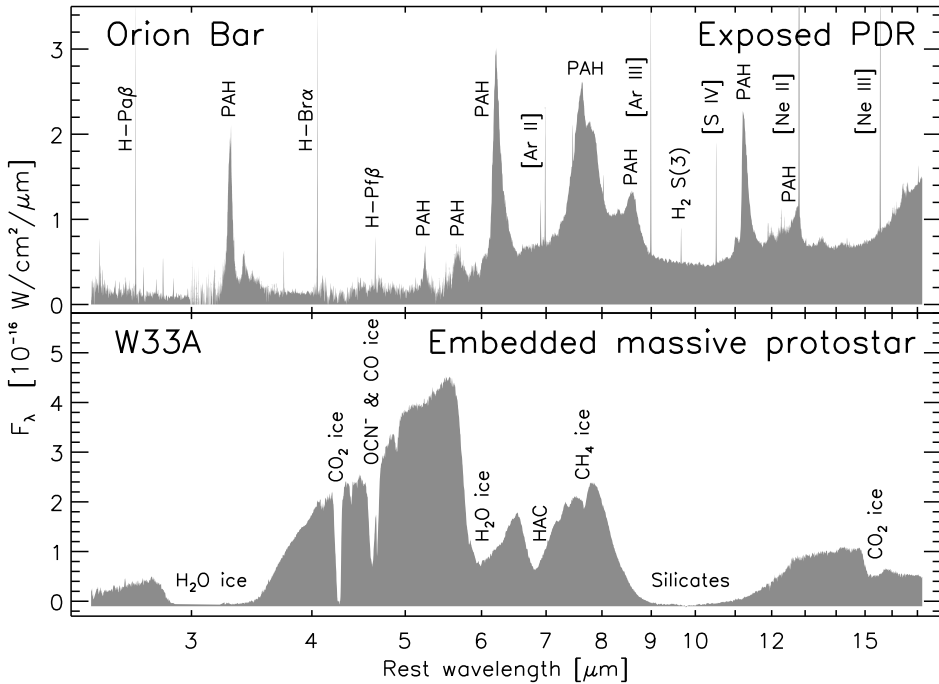


FIGURE 1.4 — Comparison of 2–17 μm spectroscopic signatures of embedded and exposed star formation. **Top panel:** Spectrum of the Orion Bar photo-dissociation region (Peeters et al. 2002a), dominated by PAH emission features at 3.3, 6.2, 7.7, 8.6, 11.2 and 12.7 μm . The emission line spectrum originates in the H II region, parts of which are included within the ISO-SWS slit. **Bottom panel:** Spectrum of the deeply embedded massive protostar W 33A (Gibb et al. 2000; Keane et al. 2001). The spectrum is dominated by deep absorption features of ices and silicates on an otherwise featureless continuum.

1.3 Characteristics of regions of massive star formation in our own Galaxy

Massive stars are formed in giant molecular clouds from small condensations which grow in mass and contract under the influence of gravity and the loss of magnetic field due to ambipolar diffusion. Eventually, after some 10^5 years, the star formation process results in the birth of a luminous embedded massive protostar. Armed with a fierce radiation field, powering a strong stellar wind, the newly born star now starts clearing a cavity around it, which turns into an H II region as a result of the irradiation with extreme-UV (EUV) stellar photons. During its expansion, the size of the H II region increases from 0.003 pc (hyper-compact) via 0.05 pc (ultra-compact) and 0.5 pc (compact) to ~ 10 pc (extended). During this phase, the H II region will be surrounded by a Photo Dissociation Region (PDR) in which the far-UV photons from the star are absorbed by dust and neutral gas.

1.3.1 Observable characteristics

The earliest stages of star formation outlined above are extremely difficult to observe (except at submm wavelengths) as they occur in the coldest and densest parts of giant molecular

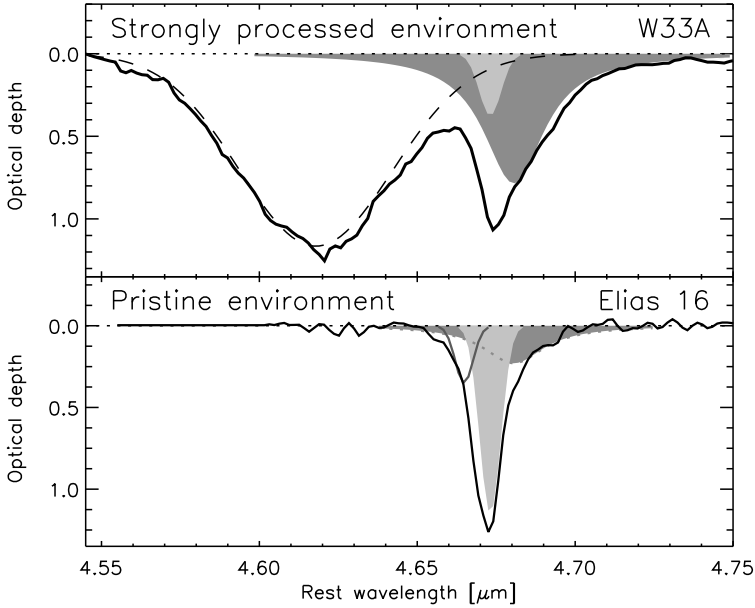


FIGURE 1.5— Optical depth spectra (black) of ices in the lines of sight towards the embedded massive protostar W 33A (top) and the field star Elias 16, located behind the Taurus molecular cloud (bottom). The CO absorption feature towards Elias 16 (Chiar et al. 1995) is dominated by volatile CO ice mixtures (light grey surface and dark grey line), with a relatively small contribution of CO trapped in water ice (dark grey surface). In contrast, the CO absorption feature towards W 33A (Gibb et al. 2000) shows far less of the volatile CO ice mixtures and is dominated instead by CO trapped in water ice. This spectrum shows in addition a broad absorption feature due to OCN[−] ice (dashed line).

clouds.

The first stage in the formation of massive stars which can be studied in the near- and mid-infrared is the phase in which the massive star has already reached the main sequence — while still accreting — and is heating the surrounding dust to temperatures which give rise to mid-infrared continuum emission. As the star at this stage is still buried deeply inside its parental cloud, the line of sight towards the star passes through the intervening molecular environment. This allows spectacular insight into the composition of the interstellar medium in the vicinity of newly formed stars. This is illustrated in the bottom panel of Fig. 1.4 for the massive embedded protostar W 33A. The spectrum is dominated by deep absorption features of ices, such as H₂O, CO, OCN[−], CO₂, CH₄ and CH₃OH, which are frozen onto the dust grains (Gibb et al. 2000; Keane et al. 2001). The dust grains themselves are represented by a deep absorption feature due to silicates. As the sublimation temperatures of the different ices range from 20 K to 90 K, the strengths of the respective absorption features are a good measure of the thermal processing of the interstellar medium by the forming star. Likewise, the presence or absence of certain molecules in the icy grain mantles may be taken as an indication of processing by UV photons emanating from the central source. Indicators of both types of processing are present in the rest frame M-band atmospheric window (4.55–5.05 μm): 4.62 μm OCN[−] ice and 4.67 μm CO ice. Fig. 1.5 compares the optical depths

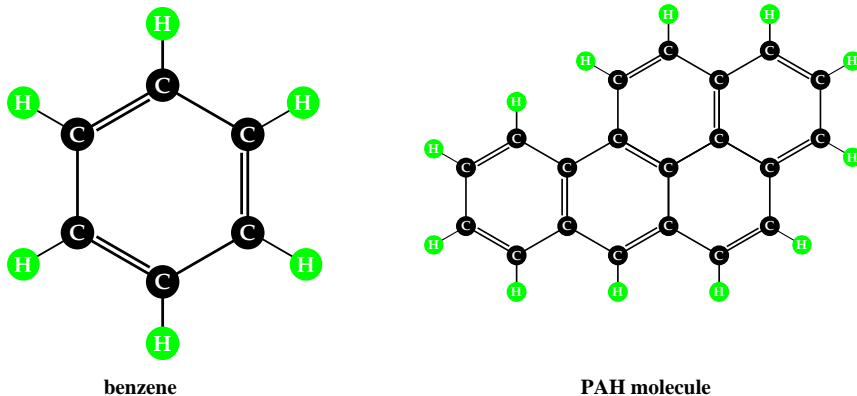


FIGURE 1.6— Emission bands from Polycyclic Aromatic Hydrocarbons (PAHs) dominate the near- and mid-infrared spectra of star forming regions. PAHs are like other aromatic molecules, such as Benzene, toxic. Graphics: E. Peeters.

of the two features in the line of sight towards the embedded massive protostar W 33A and towards the field star Elias 16, which is located behind the Taurus molecular cloud. While OCN⁻ ice is absent in the quiescent Taurus molecular cloud, it is clearly present in the vicinity of the embedded protostar. Note also the shape of the CO ice absorption feature. In a quiescent line of sight (Elias 16; Chiar et al. 1995) it is narrow and dominated by volatile apolar ice mixtures containing CO, whereas towards a highly processed environment (W 33A; Gibb et al. 2000) all that is left of the feature is the red wing originating from CO ice trapped within the far less volatile water ice.

During the initial phase of the formation of the massive star, the H II region is trapped within the accreting (or outflowing) material close to the star. Eventually, however, the star will establish an H II region around it. The presence of an H II region can be detected from afar by its characteristic recombination line spectrum and radio free-free continuum emission. Especially the latter can be observed through quite a thick layer of molecular material, allowing the detection of still deeply buried young hyper and ultra-compact H II regions (Martín-Hernández et al. 2003). H II regions are surrounded by a so-called Photo-Dissociation Region (PDR; Tielens & Hollenbach 1985), in which — by definition — EUV photons from the star do not penetrate. Here we also find in addition to all kind of neutral species, dust and robust molecular species such as H₂ and CO (Tielens & Hollenbach 1985). Far-UV (FUV) photons from the star can travel freely into a PDR (subject only to absorption by dust particles which survive in the outer parts of the H II region). Here they interact with the atoms and molecules, resulting in a lively and complex chemistry. More important, however, in the context of this thesis is the possibility that FUV photons are absorbed by complex molecules known as Polycyclic Aromatic Hydrocarbons (PAHs; Fig. 1.6). These molecules, which are formed mainly in the outflows of aging low mass stars and eventually get mixed in with the general ISM, transform their UV excitation energy into vibrational energy of the molecular bonds within the aromatic structure. This results in the cooling down of the molecule, as each vibration mode produces a number of near- or mid-infrared photons in distinct bands. The main emission bands of PAHs at wavelengths of 3.3, 6.2, 7.7, 8.6, 11.2 and 12.7 μm usually dominate



FIGURE 1.7 — Detail of the Orion nebula between the four Trapezium stars (*upper left quadrant*) and the Orion Bar (*running diagonally*). **Left:** The optical image is dominated by intricate dust structures at the interface between the H II region, ionized by Trapezium star $\theta^1\text{C}\text{ Orionis}$, and the vast molecular cloud behind it. The Orion Bar is part of this interface and is seen edge-on. Its side facing $\theta^1\text{C}\text{ Orionis}$ is ionized, while its far side is molecular. The transition zone, the PDR, is a major source of PAH emission (Hollenbach & Tielens 1999). Photo: NASA, C.R. O'Dell & S.K. Wong (Rice University); **Right:** The near-infrared image, taken with the ISAAC camera on the ESO–VLT, reveals the presence of an entire stellar cluster hidden within the molecular cloud. Photo: M. McCaughrean & ESO.

the near- and mid-infrared emission of PDRs. Depending on the abundance and temperature of the dust within the H II region and PDR, the PAH emission bands may also dominate the emission of the H II region and PDR combined.

A beautiful example of an H II region and associated PDR is the bright nebula centered on the Orion Trapezium stars, also known as the Orion nebula. The nebula is ionized by the young O6 star $\theta^1\text{C}\text{ Orionis}$, which, together with the other three Trapezium stars, cleared the optically visible cavity. The four stars are the first of an entire cluster, which for the largest part is still hidden behind the cavity (Fig. 1.7). The bright ridge running diagonally across the lefthand image of Fig. 1.7 is called the Orion Bar. This structure is part of the interface between the H II region around $\theta^1\text{C}\text{ Orionis}$ and the molecular cloud and is seen edge-on. The side facing $\theta^1\text{C}\text{ Orionis}$ is ionized, while its far side is molecular. Near-infrared L-band imaging reveal the interface, the PDR, to be a major source of PAH emission (Hollenbach & Tielens 1999). This is corroborated by the ISO–SWS spectrum (top panel of Fig. 1.4), which shows strong PAH emission features at 3.3, 6.2, 7.7, 8.6, 11.2 and 12.7 μm . A spectrum like this is fairly typical for exposed PDRs and, as such, distinctly different from spectra of embedded protostars, as exemplified by the spectrum of the line of sight towards the massive protostar W 33A (bottom panel of Fig. 1.4).

As discussed above, the FUV and EUV photons emitted by young hot stars are absorbed by the H II regions and PDRs around them. Observationally, these regions are thus characterized by hydrogen recombination lines, atomic fine structure lines, molecular lines, PAH emission bands and mid- and far-infrared dust continuum radiation. The latter constitutes the bulk of the re-emitted stellar luminosity, as is strikingly illustrated in Figure 1.8 by the spectrum of a typical compact H II region.

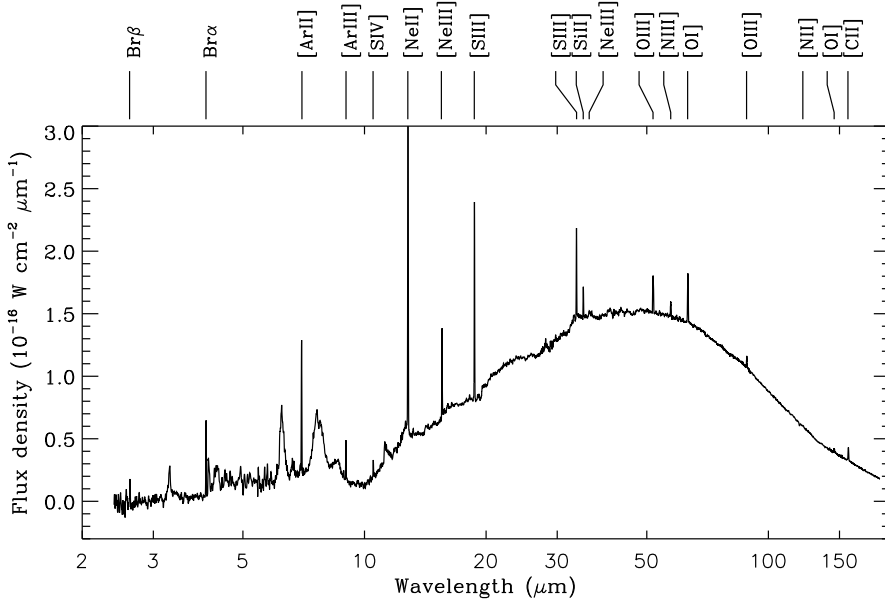


FIGURE 1.8— The spectral energy distribution of a typical compact H II region (Peeters et al. 2002b). Most of the FUV and EUV energy of the central star is re-emitted, not in the form of hydrogen recombination lines, fine structure lines or PAH emission bands, but in the form of mid- and far-infrared dust emission. Note the logarithmic scale on the wavelength axis, which compresses the far-infrared spectral range with respect to the near- and mid-infrared spectral ranges. Graphics: L. Martín-Hernández.

1.4 AGNs

AGNs can also be an important contributor to the energy budget of ULIRGs. The engine is hypothesized to be a super-massive black hole with a mass in the range of 10^6 – $10^8 M_\odot$. It is surrounded by a fiercely X-ray emitting fast-rotating accretion disk, which in turn is surrounded by the so-called Broad-Line Region (BLR). Unification schemes interrelating the various types of active galaxies (Antonucci 1993) demand an an-isotropic dust screen to hide the central engine for type-2 AGNs. Although the dimensions of this dusty torus are not well-known, its inner radius cannot be any smaller than a few parsecs, as otherwise the dust would be destroyed by the intense X-ray emission from the accretion disk. Likewise, the outer radius of the torus cannot be much larger than a few hundred parsecs, as it would otherwise have been seen in optical images. Another important component are the gas clouds which constitute the so-called Narrow-Line Region (NLR), located above the plane of the torus along its symmetry axis.

The first AGNs were discovered in spiral galaxies, the so-called Seyfert galaxies (Seyfert 1943). Later, AGNs were also found in elliptical galaxies and in point-like Quasi-Stellar Objects (QSOs; or quasar). By now, AGNs have been found in nearly all galaxy types, including several ULIRGs.

1.4.1 Observable characteristics

Thanks to the presence of an extremely hot accretion disk in combination with a surrounding molecular torus, AGNs can be studied across the entire electromagnetic spectrum.

The central region produces copious X-rays which heat and ionize the surrounding gas and dust. Their X-ray continuum can be detected by X-ray satellites. Depending on the gas column density along the line of sight, the emission may, however, be weakened or blocked completely. The latter occurs for column densities $N(H) > 10^{24.5} \text{ cm}^{-2}$, in which case the obscuring source is called ‘Compton thick’. Type-2 Seyferts generally have higher columns than type-1 AGNs. More than 50% of nearby type-2 Seyferts even have columns $N(H) > 10^{24} \text{ cm}^{-2}$ (Risaliti et al. 1999).

At radio wavelengths, the presence of an AGN can be confirmed if the brightness temperature of the central source is higher than 10^6 K (Condon 1992). An AGN may, however, remain undetected if the source is radio-quiet or strongly synchotron self-absorbed.

In the mid-infrared, the presence of an AGN may be deduced spectroscopically in several ways. First, by the presence of high excitation fine structure lines like $3.93 \mu\text{m}$ [Si IX], 14.3 & $24.3 \mu\text{m}$ [Ne V] and $7.65 \mu\text{m}$ [Ne VI], resulting from ionization of gas by X-rays from the central source (e.g. Genzel et al. 1998; Sturm et al. 2002; Lutz et al. 2002). Second, by the presence of a mid-infrared continuum, resulting from heating the torus gas by the central X-ray source. AGN unification schemes predict the strength of this continuum to be weaker for type-2 than for type-1 AGNs, because of strong extinction by the intervening torus. Such a difference has indeed been observed by Clavel et al. (2000). It is important to emphasize that the central region of the AGN shows no evidence for PAH emission features (Sturm et al. 2000; Laurent et al. 2000), likely because these molecules have been destroyed in the X-ray irradiated environment.

Given the small diameter of the ISO telescope (60 cm), direct observation of the AGN continuum without strong contamination by emission from the host galaxy, has only been possible for the nearest AGNs. Fig. 1.9 shows the 5 – $16 \mu\text{m}$ spectra of the nearby AGNs Cen A and NGC 1068 (Laurent et al. 2000). As can be clearly seen, the spectra of the central regions are continuum-dominated, in sharp contrast to the spectra of the host galaxies, which are PDR-like. Note the difference in contrast of the AGN and PDR spectra between NGC 1068 and Cen A. The effect is entirely due to the far higher AGN continuum luminosity of NGC 1068.

1.5 ULIRGs at mid-infrared wavelengths

As illustrated by Fig. 1.2, ULIRGs emit the bulk of their luminosity in the infrared. Unfortunately, studying ULIRGs at these wavelengths is extremely difficult. Telescopes need to be cooled to near-zero temperatures, development of sensitive infrared detectors is technologically challenging and the atmosphere is opaque throughout most of the infrared spectral range. As a result, mid- and far-infrared astronomy lack the spatial and spectral resolution and the sensitivity of optical and near-infrared astronomy and require a space-based observatory. Until recently, most of our understanding of the processes at work in ULIRG nuclei was therefore based on studies at optical, near-infrared, millimeter and radio wavelengths. With the advent of the *Infrared Space Observatory* (ISO), mid-infrared spectroscopy became available as another tool to study the properties of ULIRGs. Below I summarize some of the results in the context of my thesis. For a more detailed overview, I recommend the review by

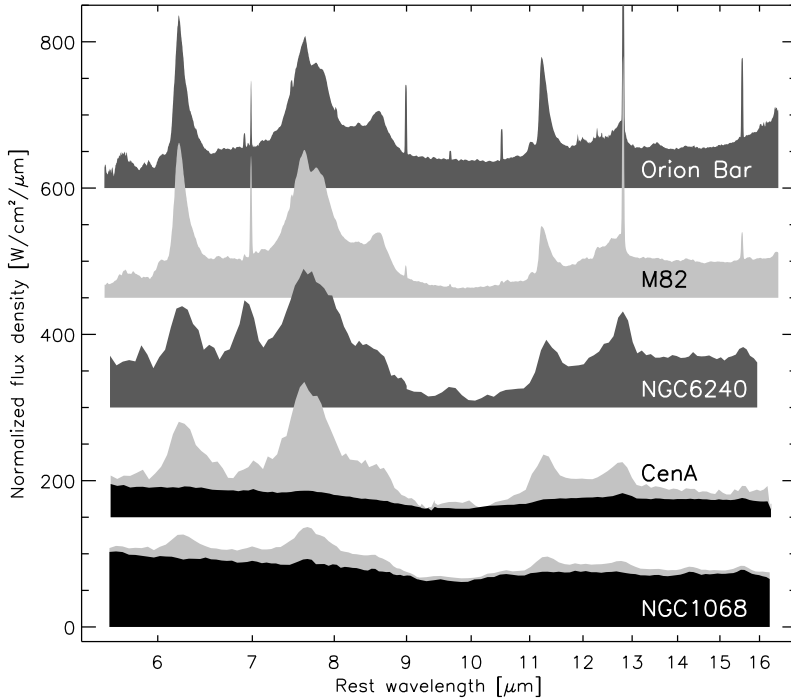


FIGURE 1.9 — 5–16 μm spectral energy distributions. The spectra have been scaled and offset. **Orion Bar:** The spectrum of the Orion Bar photo-dissociation region (Peeters et al. 2002a) is dominated by PAH emission features at 3.3, 6.2, 7.7, 8.6, 11.2 and 12.7 μm . **M 82:** The spectrum of the starburst core (Sturm et al. 2000) is like the spectrum of the Orion Bar dominated by PDRs. **NGC 6240:** The spectrum of the ULIRG NGC 6240 (Laurent et al. 2000) is dominated by PDR features. **Cen A:** The *black area* indicates the nuclear and the *grey area* the circumnuclear spectrum of Cen A (Laurent et al. 2000). **NGC 1068:** The *black area* indicates the nuclear and the *grey area* the circumnuclear spectrum of NGC 1068 (Laurent et al. 2000).

Genzel & Cesarsky (2000).

The near- and mid-infrared spectral range is extremely rich in ISM emission and absorption features. As the conditions of dust and gas depend strongly on the processing by nearby (forming) stars or the presence of an AGN, a detailed study of the spectral features will give insight in the nature of the sources responsible for the observed ISM conditions. This is maybe best illustrated by the two spectra in Fig. 1.4, which show the clearly different spectral appearance of embedded and exposed star formation.

ULIRG nuclei are known to be extremely dusty. Extinction estimates based on near- and mid-infrared hydrogen recombination lines and/or ratios of mid-infrared fine structure lines range from $A(V)=5$ to 50. The true extinction may, however, be far higher if emission and absorption components are mixed along the line of sight (Genzel et al. 1998). The nuclear power sources may remain hidden even at mid-infrared wavelengths. The nucleus of the nearby starburst/Seyfert-2 galaxy NGC 4945 (Fig. 1.1) offers an interesting testground in this respect, as hard X-ray observations have revealed the presence of a deeply enshrouded powerful AGN (e.g. Iwasawa et al. 1993), coexisting with an obscured nuclear starburst, which is

responsible for a strong starburst superwind (Moorwood et al. 1996b).

As discussed in the previous Section, the spectral signatures of AGN activity are quite different from those of exposed star formation. Genzel et al. (1998) exploited these differences in an impressive mid-infrared study of 45 ULIRG, Seyfert and starburst nuclei and found that pure AGNs and starbursts separate well in a diagnostic diagram (Fig. 1.10) with on one axis the $7.7\text{ }\mu\text{m}$ -PAH feature-to-continuum ratio and on the other axis the ratio of a high to a low excitation line (e.g. $[\text{Ne V}]/[\text{Ne II}]$ or $[\text{O IV}]/[\text{Ne II}]$). Most ULIRGs were found to be starburst-like in their $7.7\text{ }\mu\text{m}$ -PAH feature-to-continuum ratios and to have upper limits on their high-to-low excitation line ratios at the lower end of the AGN range. Genzel et al. (1998) concluded from this that ULIRGs are predominantly starburst powered. Fig. 1.9 shows the nuclear and galaxy-integrated mid-infrared spectra of two galaxies containing a type-2 AGN. In Cen A, circumnuclear star formation dominates the galaxy-integrated spectrum, while the AGN dominates the NGC 1068 spectrum. While this may be a true indication of the relative importance of AGN and starburst activity in these systems, the strength of the AGN continuum is known to vary by a factor ~ 8 , depending on the orientation of the AGN torus (Clavel et al. 2000). The importance of an AGN may hence be under- or overestimated by a factor ~ 8 if the obscuration is not corrected for. Classification of galaxies in AGN- or starburst-dominated on the basis of just their $7.7\text{ }\mu\text{m}$ -PAH feature-to-continuum ratio should therefore be avoided.

Soifer et al. (2002) took a different approach to estimate the contribution of star formation to the total luminosity of ULIRGs. Assuming the ratio $L(11.2\text{ }\mu\text{m-PAH})/L(\text{IR})$ for the nuclear starburst in M 82 to be typical for star formation elsewhere, they found that only 10% of the total luminosity of Arp 220 may be associated with exposed star formation. This fraction is far smaller than the $>50\%$ estimated from the $7.7\text{ }\mu\text{m}$ PAH line-to-continuum ratio (Genzel et al. 1998; Lutz et al. 1998; Rigopoulou et al. 1999; Tran et al. 2001).

1.6 In this thesis

A key question in astronomy is the interrelationship of mergers, starburst and AGN activity. In this thesis, I have focussed on infrared observational diagnostics of the energetic phenomena in the nuclei of (U)LIRGs and the insight they provide in the ultimate energy source of such objects.

In Chapter 2, I present the sample of mid-infrared galaxy spectra used in this thesis. The sample comprises ~ 250 spectra of normal galaxies, starburst galaxies, Seyferts, QSOs, ULIRGs and HyLIRGs. These spectra were obtained with all three mid-infrared spectrometers onboard ISO: SWS ($R \sim 1500$), PHT-S ($R \sim 90$) and CAM-CVF ($R \sim 35$). I examine the spectra for the presence of ice absorption features. This results in the detection of ice in 18 galaxies and in an ice galaxy classification, which may also represent an evolutionary sequence.

Chapters 3 and 4 present a near- and mid-infrared case study of the nearby starburst/Seyfert-2 galaxy NGC 4945. The observations reveal strong absorptions by ices and silicates towards the nuclear starburst. Solid CO_2 , CO and OCN^- are detected for the first time in an external galaxy. The profile of the solid CO band reveals the importance of thermal processing of the ice, while the prominence of the OCN^- band attests to the energetic processing of ices by FUV radiation and/or energetic particles. We find no spectral evidence for the existence of a powerful AGN, inferred from hard X-ray observations.

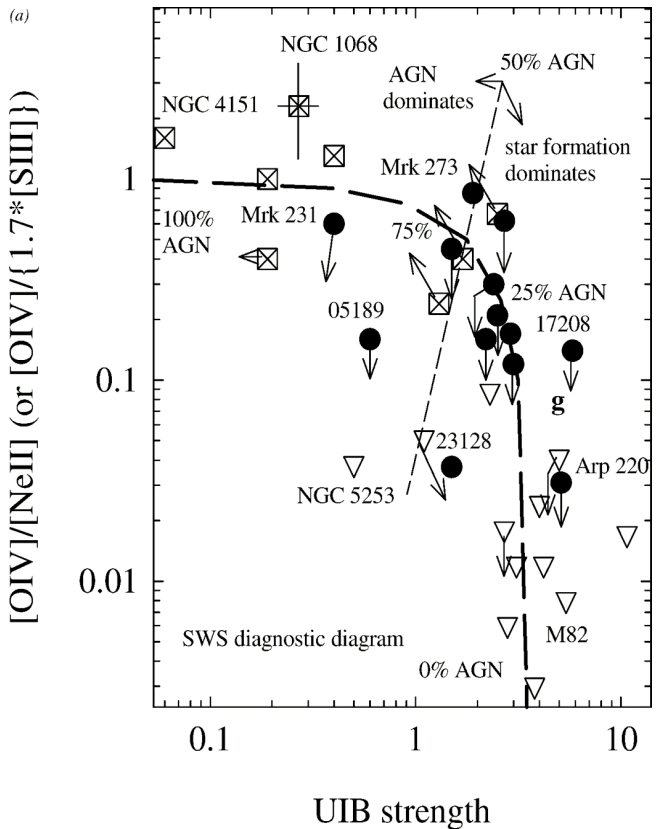


FIGURE 1.10—Genzel diagram (Genzel et al. 1998). The vertical axis measures the flux ratio of high excitation to low excitation mid-infrared emission lines, and the horizontal axis measures the strength (i.e. feature to continuum ratio) of the $7.7 \mu\text{m}$ -PAH feature. AGN templates are marked as *rectangles with crosses*, starburst templates as *open triangles*, and ULIRGs as *filled circles*. A simple mixing curve from 0% to 100% AGN is shown with *long dashes*.

In Chapter 5, the exotic mid-infrared spectrum of NGC 4418 is presented. In contrast to the spectra of most other LIRGs, the spectrum of NGC 4418 reveals no sign of PAH emission features, but is dominated instead by deep absorption features of ices and silicates. From the depth of the ice features we infer that the powerful central source responsible for the mid-infrared spectrum must be deeply enshrouded.

In Chapter 6, the $6\text{--}12 \mu\text{m}$ spectrum of Arp 220 is re-analyzed. The spectrum is not consistent with a scaled-up version of a typical starburst, but may instead be the superposition of an NGC 4418-like absorbed continuum source and a weakly absorbed starburst spectrum. Consequences for the starburst energy budget are discussed.

In Chapter 7, I investigate the role of PAHs as a tracer of star formation, based on a sample of Galactic regions of massive star formation. For this purpose, I define a MIR/FIR diagnostic diagram of far-infrared normalized $6.2 \mu\text{m}$ PAH flux versus far-infrared normalized $6.2 \mu\text{m}$ continuum flux. Within this diagram the Galactic H II regions span a sequence from embedded compact H II regions to exposed PDRs. The extragalactic sample is compared to these Galactic sources. I also investigate if PAHs are good tracers of star formation.

Finally, the results from the research presented in this thesis and its main conclusions are summarized in Chapter 8.

2

Ice features in the mid-IR spectra of galactic nuclei

Originally published as:

H.W.W. Spoon, J.V. Keane, A.G.G.M. Tielens, D. Lutz, A.F.M. Moorwood & O. Laurent
ASTRONOMY & ASTROPHYSICS, 385, 1022 (2002)

MID infrared spectra provide a powerful probe of the conditions in dusty galactic nuclei. They variously contain emission features associated with star forming regions and absorptions by circumnuclear silicate dust plus ices in cold molecular cloud material. Here we report the detection of 6–8 μm water ice absorption in 18 galaxies observed by ISO. While the mid-IR spectra of some of these galaxies show a strong resemblance to the heavily absorbed spectrum of NGC 4418, other galaxies in this sample also show weak to strong PAH emission. The 18 ice galaxies are part of a sample of 103 galaxies with good S/N mid-IR ISO spectra. Based on our sample we find that ice is present in most of the ULIRGs, whereas it is weak or absent in the large majority of Seyferts and starburst galaxies. This result is consistent with the presence of larger quantities of molecular material in ULIRGs as opposed to other galaxy types.

Like NGC 4418, several of our ice galaxy spectra show a maximum near 8 μm that is not or only partly due to PAH emission. While this affects only a small part of the galaxy population studied by ISO, it stresses the need for high S/N data and refined diagnostic methods, to properly discriminate spectra dominated by PAH emission and spectra dominated by heavy obscuration.

The spectral variation from PAH emission to absorbed continuum emission near 8 μm shows strong similarities with Galactic star forming clouds. This leads us to believe that our classification of ice galaxy spectra might reflect an evolutionary sequence from strongly obscured beginnings of star formation (and AGN activity) to a less enshrouded stage of advanced star formation (and AGN activity), as the PAHs get stronger and the broad 8 μm feature weakens.

2.1 Introduction

Prior to the ISO mission, the mid-IR spectra of galaxies could only be studied from the ground in certain windows of reduced atmospheric absorption. For the far brighter Galactic sources less limitations applied, as these could be studied with airborne telescopes, like the Kuiper Airborne Observatory (KAO: 1974–1995). Hence, before the advent of ISO, most of the prominent mid-IR ISM features had already been studied in some detail for Galactic sources, but not yet for extragalactic sources. Equipped with three mid-IR spectro(photo)meters, ISO has since enhanced considerably our knowledge of the mid-IR spectral properties of normal, starburst, Seyfert and Ultra-luminous Infrared Galaxies (ULIRGs).

The mid-IR spectra of most galaxies are dominated by ISM emission features, the most prominent of which are the well-known PAH emission bands at 6.2, 7.7, 8.6, 11.3 and 12.7 μm and atomic emission lines. The PAH features and the emission lines have been used qualitatively and quantitatively as diagnostics for the ultimate physical processes powering galactic nuclei (Genzel et al. 1998; Lutz et al. 1998; Rigopoulou et al. 1999; Clavel et al. 2000; Helou et al. 2000; Tran et al. 2001). A broad absorption band due to the Si-O stretching mode in amorphous silicates, centered at 9.7 μm , is also commonly detected in galaxies. Since the center of the silicate absorption coincides with a gap between the 6.2–8.6 μm and 11.3–12.8 μm PAH complexes, it is not readily apparent whether a 9.7 μm flux minimum should be interpreted as the “trough” between PAH emission features or as strong silicate absorption, or as a combination of the two.

In spectra observed towards heavily extinguished Galactic lines of sight, like deeply embedded massive protostars, a strong silicate feature is often accompanied by mid-IR ice absorption features due to molecules, frozen in grain mantles (Whittet et al. 1996; Keane et al. 2001). Among the simple ice molecules that have been identified in these grains are: H₂O, CO₂, CH₃OH, CO and CH₄ ice. The first detections of interstellar ices in external galaxies were reported by Spoon et al. (2000) (Chapter 3) and Sturm et al. (2000) in the nuclear spectra of NGC 4945, M 82 and NGC 253. At the low resolution of the ISO-PHT-S spectrophotometer a deep and broad 3.0 μm water ice feature, with the red wing extending far beyond the 3.3 μm PAH feature, is clearly visible in the spectrum of NGC 4945. Also identified in the spectrum of NGC 4945 are absorptions due to 4.26 μm CO₂ ice and the unresolved blend of 4.62 μm ‘XCN’ with 4.67 μm CO ice and 4.6–4.8 μm CO gas phase lines.

The first detections of 6–8 μm ices in extragalactic sources were made in the strongly absorbed mid-IR spectra of NGC 4418 (Chapter 5) and IRAS 00183–7111 (Tran et al. 2001). Especially rich is the spectrum of NGC 4418, which displays absorption features due to 6.0 μm water ice, 6.85 & 7.3 μm hydrogenated amorphous carbons (HAC) and 7.67 μm CH₄ ice, accompanied by a very deep 9.7 μm silicate feature.

Encouraged by these findings we have searched our database of \sim 250 galaxies observed spectroscopically by ISO for galaxies showing similar 6–8 μm absorptions. In this paper we present the outcome of this search, which resulted in a sample of 18 galaxies showing evidence for the presence of 6.0 μm water ice. Sect. 2.2 describes the sample. In Sect. 2.3, we discuss the complex interplay of 6.0 μm water ice and 5.25, 5.7, 6.25 μm PAH emission as well as the effect of redshift on the detectability of the blue wing of the water ice feature in ISO data. Sect. 2.4 describes the classification of the ice galaxies. In Sect. 2.5, we present the absorption and emission profile analysis. The results are discussed in Sect. 2.6. Conclusions are stated in Sect. 2.7.

2.2 Observations

2.2.1 ISO galaxy sample

In order to study the mid-infrared spectral properties of galaxies we have created a database of some 250 ISO galaxy spectra. The database has been compiled from observations performed with the PHT-S, CAM-CVF and SWS-01 instrument modes of ISO. The database comprises:

- Nearly all ISO-PHT-S galaxy observations from a variety of programs, except for galaxies at R.A. 13–24 hrs from the “Normal Galaxy” program (P.I. G. Helou).
- Four ISO-SWS-01 spectra of nearby galactic nuclei (Sturm et al. 2000).
- ISO-CAM-CVF spectra from the ZZULIRG proposal (Tran et al. 2001), as well as the active galaxy spectra discussed by (Laurent et al. 2000).

By nature, this sample is not complete in any strict statistical sense.

2.2.2 Selected sample

We have defined a subsample of galaxies with good S/N spectra and sufficient wavelength coverage blueward of $6.0\,\mu\text{m}$. The criteria we applied were $(\text{S}/\text{N})_{6.5\,\mu\text{m}} > 8$ and, for ISO-PHT-S in addition, $c\zeta > 3000\,\text{km}/\text{s}$. The resulting sample of 103 galaxies misses many of the observations of fainter ULIRGs and nearby galaxies in the ISO archive. It is dominated by Seyferts, which constitute nearly half the sample.

Within this sample we found 18 galaxies showing $6.0\,\mu\text{m}$ water ice absorption (Figs. 2.5—2.7), including NGC 4418 (Chapter 5). We also looked for galaxies showing the opposite: no sign of water ice up to $\tau_{\text{ice}} < 0.1\text{--}0.3$ along the line of sight. Within our sample of 103 good S/N galaxy spectra, 28 galaxies fulfil this criterion. Examples of ice-poor galaxies are shown in Figs. 2.2, 2.8 & 2.9. For the remaining 57 out of 103 galaxies, the quality of the spectra is either not good enough to detect the presence of a $6.0\,\mu\text{m}$ water ice feature (a higher S/N criterion would have biased the sample against PAH-dominated spectra, which are weaker at $6\text{--}7\,\mu\text{m}$ than continuum dominated AGN spectra), or to establish an upper limit better than 0.3 for the amount of water ice.

In the following Sections we show spectra for 32 galaxies. These spectra were obtained using the ISO-CAM-CVF (Cesarsky et al. 1996), ISO-PHT-S (Lemke et al. 1996) and ISO-SWS (de Graauw et al. 1996) spectro(photo)meters aboard ISO (Kessler et al. 1996).

The ISO-CAM-CVF spectra of galaxies I00183–7111, I00188–0856 and Arp 220 have been taken from Tran et al. (2001). The ISO-CAM-CVF spectra of NGC 253, NGC 613, NGC 1068, M 82, NGC 1365, NGC 1808, NGC 4945, M 83, Circinus and I23128–5919 have been taken from Laurent et al. (2000).

The ISO-PHT-S spectra of galaxies Mrk 334, NGC 23, I01173+1405, NGC 828, I04385–0828, I05189–2524, MGC 8–11–11, I06035–7102, UGC 5101, Mrk 231, Mrk 273, Mrk 279, I15250+3609, Arp 220, I17208–0014, PKS 2048–57, I20551–4250 and I23128–5919 have been reduced using standard routines of PIA¹ versions 8.1–9.0.1. The ISO-PHT-S spectra of NGC 4418 and NGC 4945 have been taken from Chapters 5 and 3, respectively.

¹PIA is a joint development by the ESA Astrophysics Division and the ISO-PHT Consortium

The ISO–SWS spectrum of the nucleus of NGC 1068 has been taken from Sturm et al. (2000), that of the Orion Bar from Peeters et al. (2002a), and, finally, that of the nucleus of Circinus from Moorwood et al. (1996a).

2.3 Ice absorption and PAH emission in the 5–7 μm region

Before discussing the presence and strength of ice features in the sources of our sample, we illustrate the interplay of emission and absorption using a simple toy model. This is necessary since the 6 μm ice feature is not always seen against a well-defined continuum. The ‘PAH’ emission features at 7.7, 6.2, 5.7, and 5.25 μm may be present as well, leading to possible confusion of minima between emissions with absorption. In addition, the wavelength coverage of the ISO data limits the accessible range, in particular for low redshift objects observed with ISO–PHOT–SL (starting at 5.84 μm). Our model produces high resolution spectra ($R = \lambda/\Delta\lambda \sim 1000$) of the 5–7 μm spectral region, comprising a water ice absorption feature and PAH emission bands superimposed on a continuum. Here, we describe the various components of the model, the consequences of rebinning to the lower ISO–PHT–S and ISO–CAM–CVF resolution ($R \sim 40$ –90) and also explore the effect that extinction may have on the resulting spectra. In addition, we produce model-spectra at different redshifts in order to investigate the effect that this has on the spectral signatures, in particular the relationship between redshift and wavelength coverage, which is particularly important for ISO–PHT–S spectra.

2.3.1 Components of the model

The components chosen for the model closely mimic absorption (ice) and emission (PAH) features seen toward a variety of Galactic objects that have been extensively studied at high resolution. The spectra are modelled as: $F_{\text{cont}} \times \exp[-\tau(\text{H}_2\text{O ice})] + \text{PAHs}$. In order to allow easy comparison of the model generated pseudo-spectra, a false flat continuum is adopted. In Sect. 2.5 the flat continuum is replaced by continuum choices fitting the individual observed spectra. Our model ignores any contribution from the PAHs to the overall continuum. This so-called PAH continuum can be seen in for instance the spectrum of the reflection nebula NGC 7023 (Moutou et al. 1998) as the continuum extending below the PAH features. Since the PAH continuum only serves to dilute the other continuum and its associated ice feature, we ignore it here.

Studies of Galactic star-forming regions, in particular high mass embedded protostars, with the short wavelength spectrometer (SWS) of ISO show strong absorption features centred around 3.0 μm and 6.0 μm attributed to amorphous water ice. The spectral characteristics of water ice (whether pure or in various mixtures) have been well studied in the laboratory (Hagen et al. 1983; Hudgins et al. 1993; Maldoni et al. 1998). The spectral changes that occur during warm-up from 10 K to 120 K are irreversible. In the case of the 6.0 μm water ice band, there is little spectral difference during warm-up from 10 K to 50 K though the band begins to broaden slightly and around 80 K this effect becomes discernible. This broadening reflects an annealing of the amorphous structure. Further thermal cycling between 120 K and 10 K produces reversible effects due to thermal shrinking and expansion of the ice lattice which causes more minor variations in the width of the bands, particularly at 6.0 μm . Beyond 120 K the ice lattice transforms to polycrystalline ice. This is particularly noticeable in the 3.0 μm water ice band as sharp structure begins to appear. Though the bulk of the interstellar 3.0 and 6.0 μm

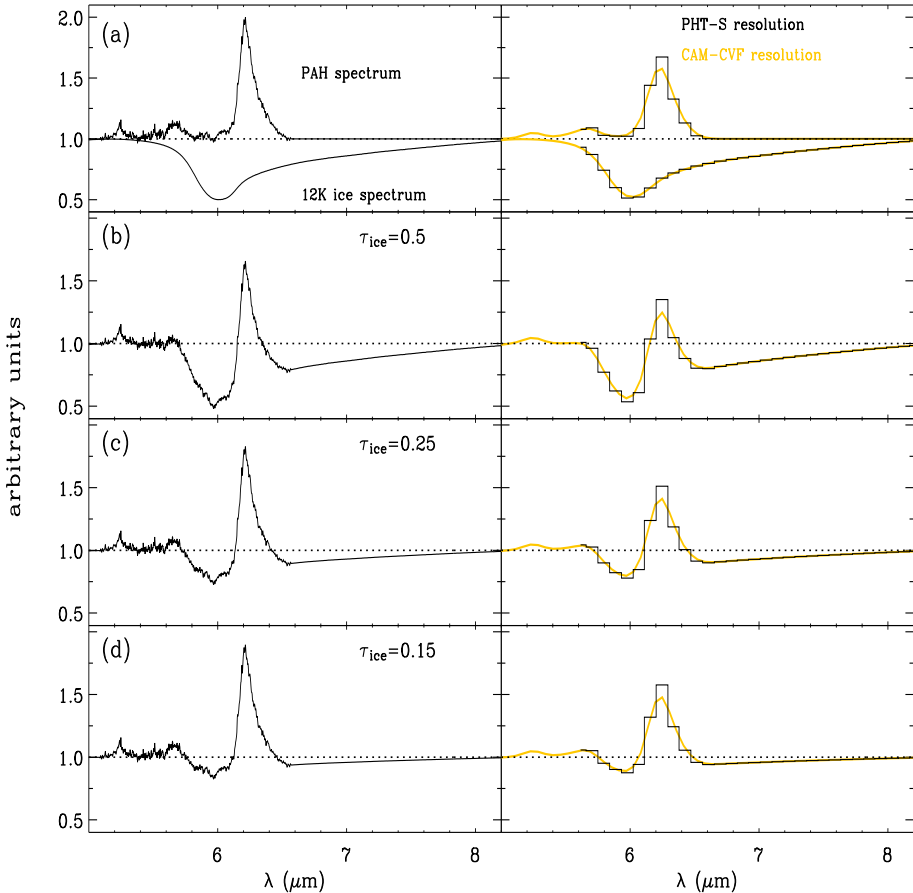


FIGURE 2.1 — A sequence of plots illustrating the effect of rebinning a pseudo high resolution spectrum (**left panels**) to the lower resolution of ISO-PHT-S and ISO-CAM-CVF (**right panels**). A redshift of $c_z=12000 \text{ km/s}$ is adopted and the grey scale represents the ISO-CAM-CVF rebinned spectra. The pseudo spectrum is composed of $6.0 \mu\text{m}$ H_2O ice absorption and PAH emission bands found in the 5–7 μm range, superimposed on a flat continuum as shown in panel (a). In the remaining panels, **(b, c, and d)**, the relative contributions of the H_2O absorption and PAH emission profiles are varied to investigate the behaviour of the spectral signatures. Note that we have discarded the $7.7 \mu\text{m}$ PAH feature in our toy model. This strong feature would start contributing to the spectrum at around $7 \mu\text{m}$.

absorption bands have been attributed to amorphous water ice, there is also evidence of additional molecules contributing to this feature in a number of sources (Dartois & d'Hendecourt 2001; Keane et al. 2001). As a consequence of this, the astronomical $6.0 \mu\text{m}$ feature varies somewhat from source to source and therefore is not well suited to our simple model. Given the lack of $3.0 \mu\text{m}$ water ice observational data for our sample, we have elected to represent the $6.0 \mu\text{m}$ ice absorption profile by a laboratory spectrum of pure amorphous water ice at 12 K. This profile has been shown to satisfactorily reproduce the $6.0 \mu\text{m}$ water ice feature ob-

served toward a number of Galactic young stellar objects (Keane et al. 2001). The left panel of Fig. 2.1a shows the profile of the 12 K water ice feature (database of the Sackler Laboratory for Astrophysics in Leiden: <http://www.strw.leidenuniv.nl/~lab/>). The most striking aspect of this profile is the broad long wavelength wing which extends at least as far as $8.0 \mu\text{m}$. There is little or no variation in the water ice profile for temperatures $\lesssim 50 \text{ K}$. For temperatures greater than this the broad wing becomes deeper and extends well beyond $8.0 \mu\text{m}$. The right panel of Fig. 2.1a shows the water ice spectrum after it has been rebinned to the lower resolution of ISO-PHT-S (histogram) and ISO-CAM-CVF (grey line), assuming a $cz=12000 \text{ km/s}$. The profile is of course very similar but for the ISO-PHT-S spectrum there is incomplete pixel coverage of the short wavelength wing when compared to the ISO-CAM-CVF spectrum. The dominant PAH emission features ($6.2, 7.7, 8.6, 11.3 \mu\text{m}$), observed toward a variety of Galactic sources, show a wide degree of variation in the detailed profile shapes and relative intensities (Peeters et al. 2002a). On the other hand, observations of PAH emission bands in external galaxies reveal very little variation in the profiles (Rigopoulou et al. 1999; Helou et al. 2000). Since one of the main aims of the model is to investigate the effect of rebinning spectral features to the lower resolutions of ISO-PHT-S and ISO-CAM-CVF, adopting extragalactic PAH emission profiles is inappropriate. Instead, high resolution Galactic PAH emission band profiles are adopted. The ISO-SWS PAH emission spectrum of the Orion bar PAH is chosen for the model as this is a good representation of a region of active star-formation (Peeters et al. 2002a). The left panel of Fig. 2.1a shows the high resolution spectrum of the Orion Bar. Apart from the typical $6.2 \mu\text{m}$ PAH C–C stretching mode, the observed spectrum also shows evidence for two weak PAH emission features near $5.25 \mu\text{m}$ and $5.7 \mu\text{m}$ (left panel of Fig. 2.1a). The nature of these weak PAH features is not very well studied but they are believed to be combinations or overtone bands involving C–H bending vibrations (Allamandola et al. 1989a). The strength of these weak bands relative to the strong $6.2 \mu\text{m}$ band is variable. Of a sample of 35 compact H II regions studied by Peeters et al. (2002b) roughly 10% of the sources show evidence for these weak PAH bands. Consequently, because of their variable strength, their presence is not always assured in spectra showing the dominant PAH bands and there is no rule of thumb defining an expected ratio for the intensity of these weak PAH bands to the $6.2 \mu\text{m}$ band. The Orion bar is among the Galactic sources with the strongest 5.25 and $5.7 \mu\text{m}$ features relative to the $6.2 \mu\text{m}$ feature. Comparison with high S/N ISO-CAM-CVF spectra of the brightest nearby starbursts suggests it to be fairly representative for those objects however (Fig. 2.2, confirmed by ISO-SWS spectroscopy of M 82 and NGC 253 (Sturm et al. 2000)). We hence adopt the Orion Bar as a template for the $5.25, 5.7$, and $6.2 \mu\text{m}$ PAH features. The PAH spectrum in Fig. 2.1 was obtained by subtracting a spline continuum from its spectrum. Fig. 2.1 then suggests that in the presence of strong PAH emission, a shallow $6.0 \mu\text{m}$ ice absorption of less than about 10% of the peak height of the $6.2 \mu\text{m}$ PAH feature is very difficult to discriminate from the minimum between the 5.7 and $6.2 \mu\text{m}$ PAH features, especially for the limited wavelength coverage of ISO-PHT-S. Finally, the 7.7 and $8.6 \mu\text{m}$ PAH bands have been clipped from the spectrum as they are not relevant for this study.

The right panel of Fig. 2.1a shows the Orion-Bar PAH features rebinned to the lower resolution of ISO-PHT-S (histogram) and ISO-CAM-CVF (grey line). In rebinning, the peak height of the $6.2 \mu\text{m}$ feature is reduced, more for ISO-CAM-CVF than for ISO-PHT-S. In the ISO-CAM-CVF spectrum, the weak PAH bands are still present, though they are flattened and broadened as compared to the high resolution spectrum. Only the peak of the

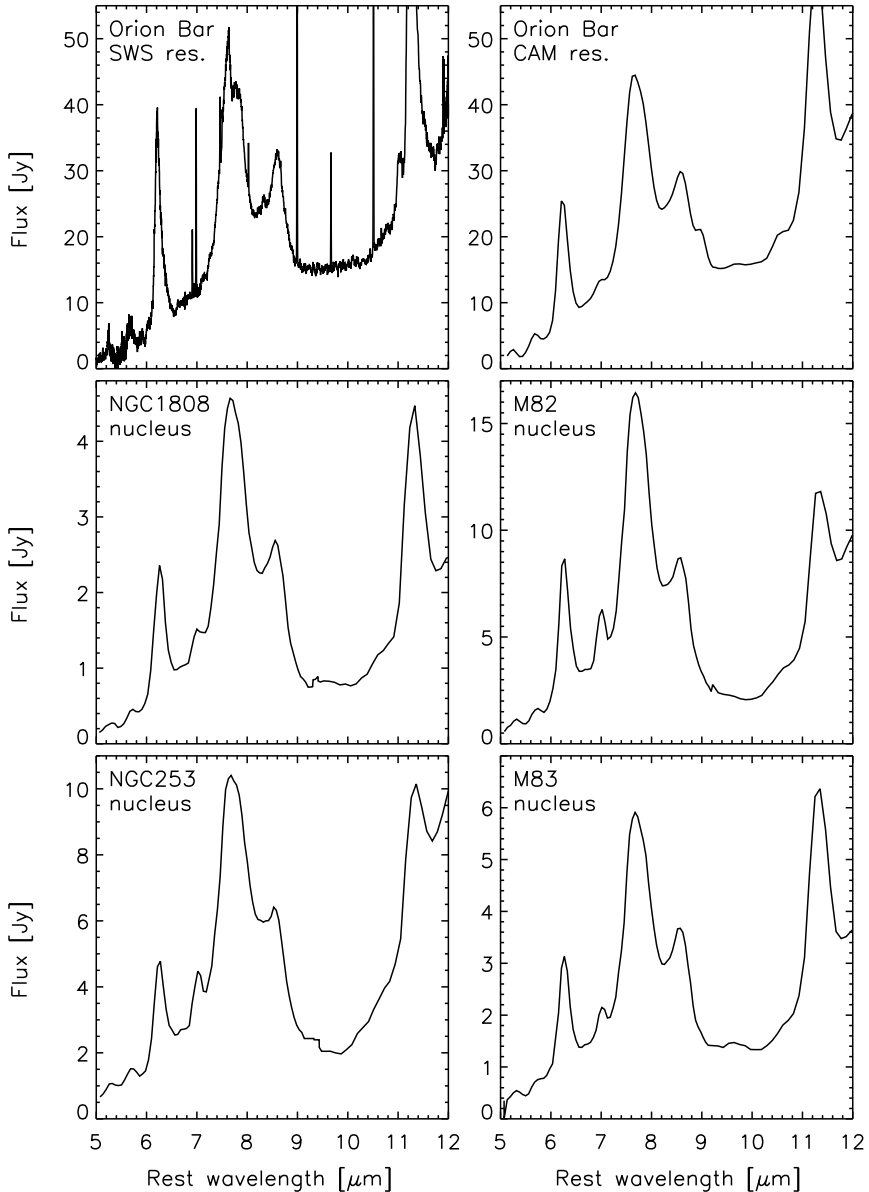


FIGURE 2.2— A collection of spectra showing strong 5.25 and 5.7 μm PAH features (Class 6 galaxies; see Sect. 2.4). The four galaxies shown in the **middle and lower panels** were observed using ISO-CAM-CVF, at low spectral resolution. The **top panels** show the spectrum of the Orion Bar, as observed at high spectral resolution by ISO-SWS (**upper left**) and degraded to ISO-CAM-CVF resolution (**upper right**). Note that the four galaxies shown represent the strongest cases of 5.25 μm and 5.7 μm PAH emission. The average galaxy may have far lower 5.25 μm /6.2 μm and 5.7 μm /6.2 μm PAH ratios.

$5.7\text{ }\mu\text{m}$ weak PAH feature is present in the ISO-PHT-S spectrum since at a cz of 12000 km/s the first pixel is at $5.6\text{ }\mu\text{m}$. This is discussed further in Sect. 2.3.3. Finally, the location of the water (i.e., in front, behind or mixed with the PAHs) had little effect on the resulting shape of the spectral features, in particular on the profile of the $6.2\text{ }\mu\text{m}$ feature. We hence ignored extinction on the PAHs in our toy model. Detailed fits to the extragalactic spectra are presented in Sect. 2.5, in which the flat continuum is replaced by continua determined individually for each galaxy.

2.3.2 Effects on the model of varying the component contributions and extinction

To investigate the interplay of the water ice absorption feature and the $6.2\text{ }\mu\text{m}$ PAH emission bands, the relative contribution of each component is varied. This is shown in Fig. 2.1b–d, where the left panel is the high resolution input spectrum and the right panel represents the rebinned low resolution pseudo spectra of the model. The dotted line indicates the flat continuum. Panel (b) illustrates the effect of a strong water ice band on the PAH emission bands. Regardless of the fact that the $6.2\text{ }\mu\text{m}$ features lies within the long wavelength wing of the water ice feature, its profile is preserved (Fig. 2.1 left panel). The $5.7\text{ }\mu\text{m}$ weak PAH band, on the other hand, is lost within the short wavelength wing, though there is a slight hint of a peak at $5.7\text{ }\mu\text{m}$. The $5.25\text{ }\mu\text{m}$ PAH feature is still present as the water ice profile does not reach as far as this short wavelength position. Rebinning to the low resolution of ISO-PHT-S and ISO-CAM-CVF (Fig. 2.1 right panel) shows that the water ice feature, in combination with the $6.2\text{ }\mu\text{m}$ PAH emission band, dominate the model spectrum and there is little if no evidence for the weak PAH bands in the ISO-PHT-S spectrum. Only the ISO-CAM-CVF spectrum reveals the presence of the $5.25\text{ }\mu\text{m}$ weak PAH band, due to the wider wavelength coverage. As the strength of the water ice absorption band is reduced (Fig. 2.1 panels (c) and (d)), the $6.2\text{ }\mu\text{m}$ feature starts to dominate the model spectra and now only weakly sits within the long wavelength wing of the water ice feature. Also, the spectral signature of the $5.7\text{ }\mu\text{m}$ weak PAH band starts to become pronounced and in Panel (d) the structure is clearly distinguished lying above the flat continuum. The crucial result of this study is that the profile of the $6.2\text{ }\mu\text{m}$ PAH band is little affected by the presence of an water ice ice absorption feature. In addition, it is evident from this analysis that the weak PAH bands do not influence the overall characteristics of the structure seen in the model spectra. However, the weak PAH emission features may enhance/mimick the effects of weak ice absorption.

The possible effect that extinction may have on the spectral features of the pseudo spectra were also investigated. In light of the fact that the Galactic center has been well studied and also because of the homogeneous nature of the foreground extinction, the extinction law derived by (Lutz 1999) for the Galactic center is adopted (Fig. 2.3a). We have also investigated the effect of other extinction laws (Tran et al. 2001; Draine 1989) but they are substantially the same and only the effects of the Lutz Law are discussed in detail here. The extinction is applied as if the continuum+PAH+ice combination were behind a column of material. Though the situation is less clear for external galaxies, this approach allows for a qualitative assessment of the effect of extinction on the model spectra. In order to clearly demonstrate the effect of extinction, the 7.7 and $8.6\text{ }\mu\text{m}$ PAH bands of the Orion Bar have been included. The top plot in Fig. 2.3b shows the unextincted ($A_v=0$) model spectrum. As the degree of extinction increases from $A_v=0$ to $A_v=25$ the $8.6\text{ }\mu\text{m}$ PAH band is "eaten away" by the short wavelength wing of the $9.7\text{ }\mu\text{m}$ silicate feature. Eventually, the depth of the silicate band is so great that the $8.6\text{ }\mu\text{m}$ feature is completely lost within this band. The same effect, but with

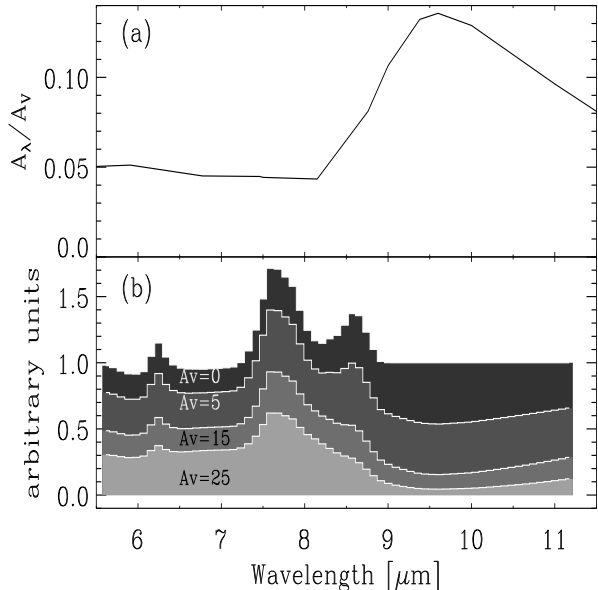


FIGURE 2.3 — Panel (a) shows a mid-IR extinction law of the Galactic center derived from hydrogen recombination lines (Lutz 1999). Illustrated in **panel (b)** is the effect of extinction on the model spectra for different amounts of A_v , assuming the above extinction curve. The effect is most severe for the $8.6 \mu\text{m}$ band as all profile information becomes lost within the $9.7 \mu\text{m}$ silicate feature.

less severity, is noticeable for the $7.7 \mu\text{m}$ emission feature. In the case of the $6.2 \mu\text{m}$ band, the peak intensity decreases as the degree of extinction increases, but information on the profile shape remains intact and distinguishable. Thus, the spectral characteristics of features shortward of $7 \mu\text{m}$ are unaffected by the effects of extinction. Furthermore, due to the sensitivity of the features beyond $7 \mu\text{m}$ to the degree of extinction they have been neglected in the model.

2.3.3 Profile appearance as a function of redshift

We have also investigated the effects of redshift combined with the limited spectral coverage on the appearance of the spectrum. A redshift (cz) range of 0 km/s to 20 000 km/s was chosen as this is representative of the cz range of the observed galaxies (Table 2.1). Fig. 2.4 illustrates the spectral variation as a function of redshift. The high resolution spectrum shown in panel (b) of Fig. 2.1 was adopted as the input to the rebinning routines and as before the histogram and the grey line represent the ISO-PHT-S and ISO-CAM-CVF rebinned data, respectively. Since the spectral coverage of ISO-CAM-CVF extends down as far as $5 \mu\text{m}$ there is not much variation in the position of the first pixels as a function of redshift. Hence in Fig. 2.4 only one ISO-CAM-CVF spectrum is shown. For redshifts of 6000 km s^{-1} or greater, the $6.0 \mu\text{m}$ water ice absorption profile is readily seen in the model ISO-PHT-S spectra. On the other-hand, the presence of water ice is not so obvious in ISO-PHT-S spectra for redshifts less than 6000 km s^{-1} . As the redshift decreases the pixel coverage of the short wavelength wing of the water ice absorption feature diminishes and only one or two pixels begin to rise at the shortest wavelengths. Consequently, there is not much real evidence for the blue wing of the water ice band even though the original high resolution model spectrum clearly shows strong water ice absorption (panel (b) in Fig. 2.1). In the case of the $6.2 \mu\text{m}$ PAH emission band, the only notable change is that the rebinned structure of the profile peak varies with redshift.

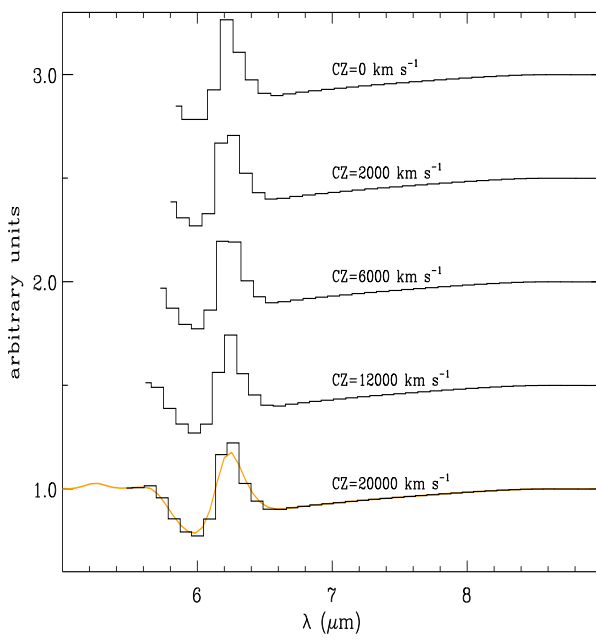


FIGURE 2.4 — A comparison of the spectral appearance of panel (b) from Fig. 2.1 rebinned to ISO-PHT-S resolution as a function of redshift. At low redshifts the presence of $6.0\ \mu\text{m}$ H_2O ice absorption is not very convincing. However, as the redshift is increased the starting position of the first pixel shifts to lower wavelengths resulting in more of the $6.0\ \mu\text{m}$ H_2O profile being clearly discernible. Since the wavelength coverage of ISO-CAM-CVF (grey line) is significantly larger than that of ISO-PHT-S, there is not much variation in wavelength of the first pixel with redshift.

2.4 Classification

Although likely the spectra of galaxies represent a continuous distribution with variable absorption and emission components, we have classified the galaxies in our sample into six categories, based on their mid-IR spectral properties. The first three categories comprise the galaxies with evidence for the presence of $6.0\ \mu\text{m}$ water ice absorption in their spectra:

- **Class 1:** These galaxies (Fig. 2.5) exhibit a $6.0\ \mu\text{m}$ water ice absorption feature, without contamination by $6.2\ \mu\text{m}$ PAH emission. Galaxies of this type also show other $6\text{--}8\ \mu\text{m}$ absorption features – most commonly the $6.85\ \mu\text{m}$ feature, attributed to HAC. Note that all galaxies in this class have a broad flux peak at $\sim 8\ \mu\text{m}$. Judging from their complete $2\text{--}200\ \mu\text{m}$ SEDs, all Class 1 galaxies have a deep $9.7\ \mu\text{m}$ silicate feature. For the two galaxies for which $2\text{--}5\ \mu\text{m}$ ISO-PHT-S data is available, NGC 4418 and IRAS 15250+3609, there is a sharp increase in flux between 5 and $6\ \mu\text{m}$.
- **Class 2:** These galaxies (Fig. 2.6) show $6.0\ \mu\text{m}$ water ice absorption features, partially filled-in by weak $6.2\ \mu\text{m}$ PAH emission. Other $6\text{--}8\ \mu\text{m}$ absorption features are not always as apparent. Note that like in Class 1, all galaxies in this class have a broad $8\ \mu\text{m}$ feature.
- **Class 3:** These galaxies (Fig. 2.7) exhibit a $6.0\ \mu\text{m}$ water ice absorption feature, largely filled in by strong $6.2\ \mu\text{m}$ PAH emission. No other $6\text{--}8\ \mu\text{m}$ absorption features have been found. All galaxies in this class show a $7.7\ \mu\text{m}$ PAH emission peak, clearly narrower than the broad $8.0\ \mu\text{m}$ feature seen in Class 1 & 2 galaxies.

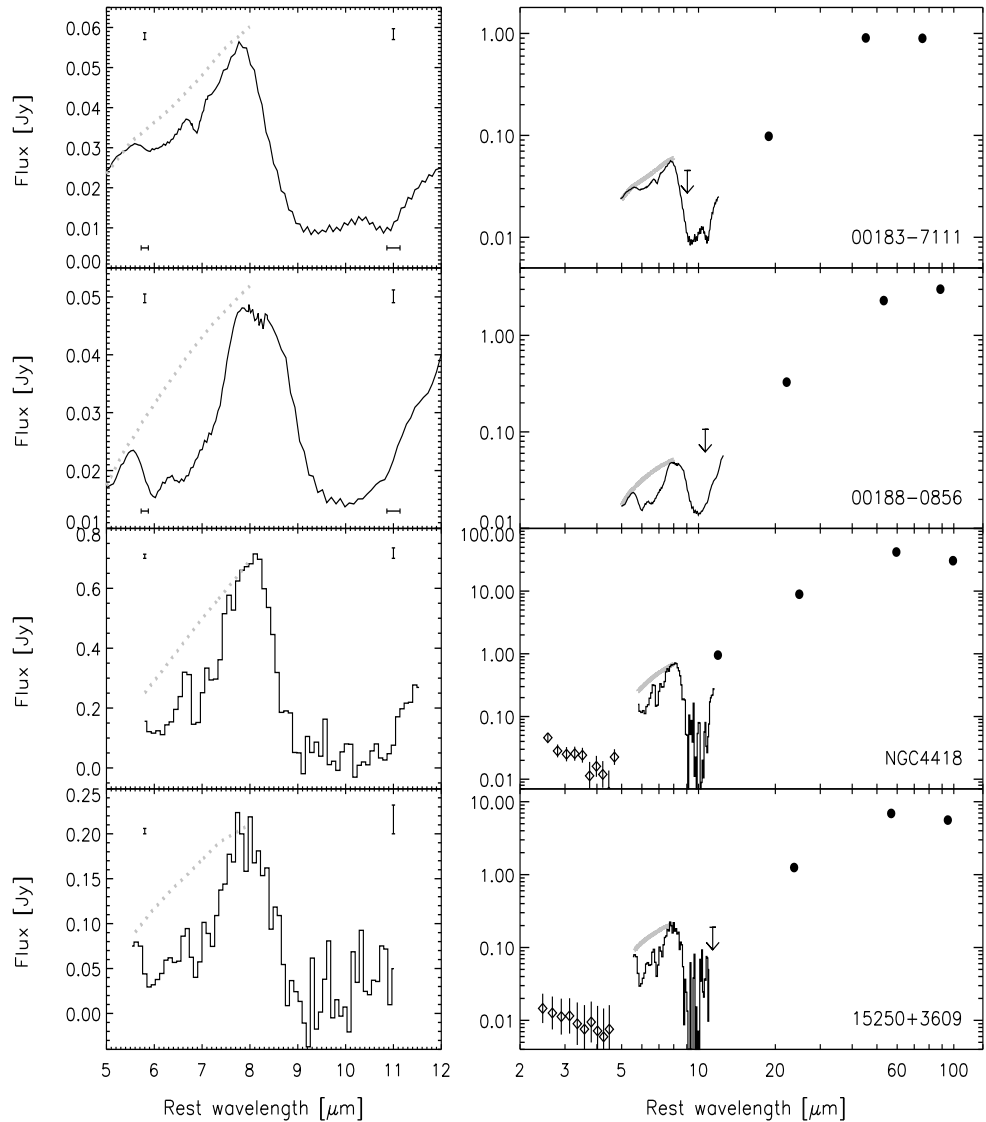


FIGURE 2.5 — Class-1 mid-IR galaxy spectra. Galaxies in Class 1 exhibit a clear $6.0\,\mu\text{m}$ ice absorption feature, without clear evidence for the presence of a $6.25\,\mu\text{m}$ PAH feature. All sources in this class have in common that they have a broad continuum flux peak near $7.7\,\mu\text{m}$, clearly broader than a $7.7\,\mu\text{m}$ PAH feature. The **panels on the left** show the $5\text{--}12\,\mu\text{m}$ spectra on a linear scale, while the **panels on the right** show the same spectra on logarithmic scale, with smoothed and rebinned $2\text{--}5\,\mu\text{m}$ ISO-PHT-S spectra and $12\text{--}100\,\mu\text{m}$ IRAS fluxes added. All fluxes have been k-corrected. The *thick grey lines* show what the $5.5\text{--}8.0\,\mu\text{m}$ continuum would be like if no ice absorption were present. The vertical error bars at 5.8 and $11\,\mu\text{m}$ denote the pixel to pixel flux error (1σ , so not $\pm 1\sigma$), while the horizontal error bars denote the gradually changing ISO-CAM-CVF spectral resolution ($R \sim 40$).

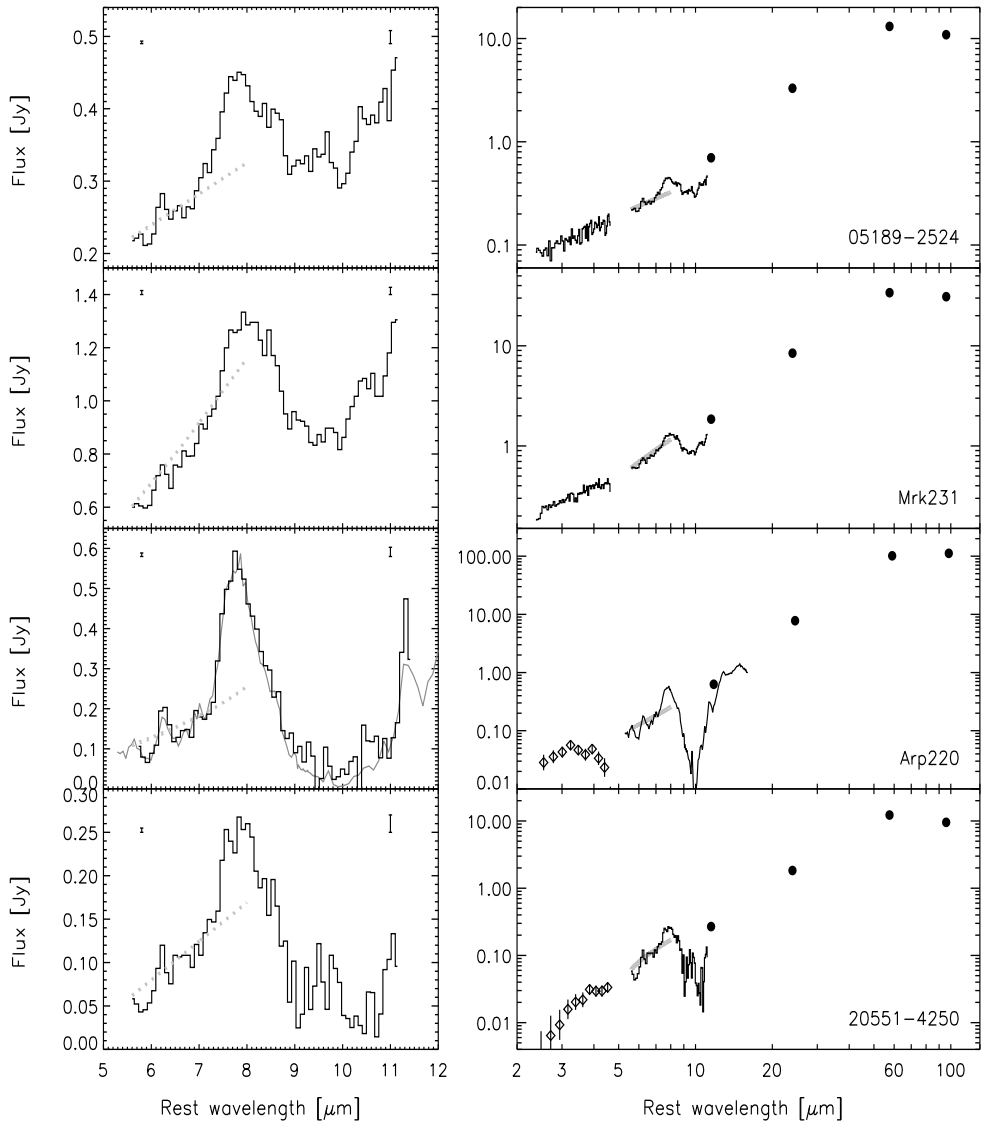


FIGURE 2.6— Class-2 mid-IR galaxy spectra. Galaxies in Class 2 exhibit a clear $6.0\,\mu\text{m}$ ice absorption feature, with clear evidence for the presence of a $6.25\,\mu\text{m}$ PAH feature. All sources in this class have in common that they have a broad continuum flux peak near $7.7\,\mu\text{m}$, clearly broader than a $7.7\,\mu\text{m}$ PAH feature. The **panels on the left** show the $5\text{--}12\,\mu\text{m}$ spectra on a linear scale, while the **panels on the right** show the same spectra on logarithmic scale, with smoothed and rebinned $2\text{--}5\,\mu\text{m}$ ISO-PHT-S spectra and $12\text{--}100\,\mu\text{m}$ IRAS fluxes added. All fluxes have been k-corrected. The *thick grey lines* show what the $5.5\text{--}8.0\,\mu\text{m}$ continuum would be like if no ice absorption were present. For Arp 220 both the ISO-PHT-S (*black*) and ISO-CAM-CVF (*grey*) spectrum are shown in the left panel. The vertical error bars at 5.8 and $11\,\mu\text{m}$ denote the pixel to pixel flux error (1σ , so not $\pm 1\sigma$).

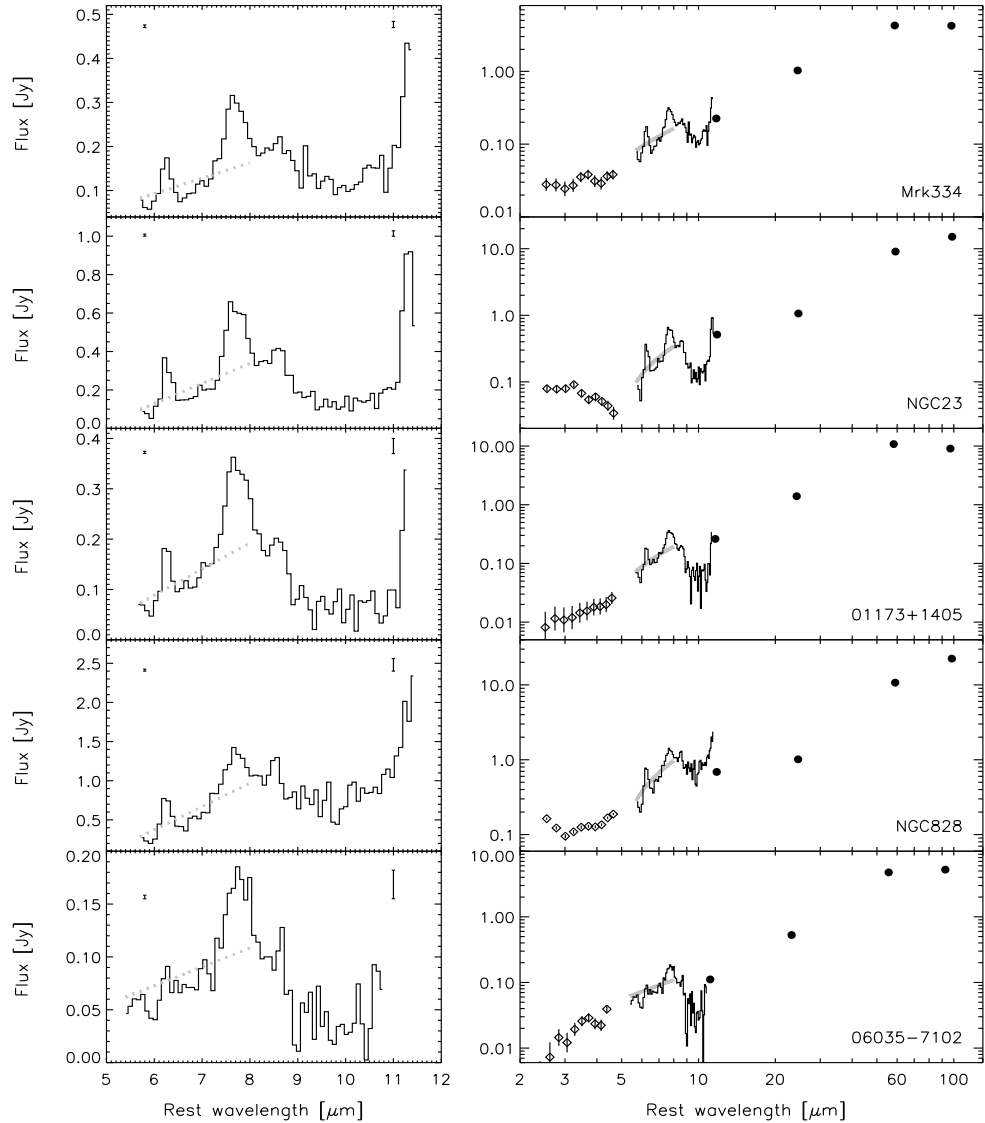


FIGURE 2.7 — Class-3 mid-IR galaxy spectra. Galaxies in Class 3 exhibit a narrow $6.0\ \mu\text{m}$ ice absorption feature, partially filled in by the wings of the $6.25\ \mu\text{m}$ PAH feature. All sources in this class have in common that the flux peak near $7.7\ \mu\text{m}$ has the typical PAH width. The **panels on the left** show the $5\text{--}12\ \mu\text{m}$ spectra on a linear scale, while the **panels on the right** show the same spectra on logarithmic scale, with smoothed and rebinned $2\text{--}5\ \mu\text{m}$ ISO-PHT-S spectra and $12\text{--}100\ \mu\text{m}$ IRAS fluxes added. All fluxes have been k-corrected. The *thick grey lines* show what the $5.5\text{--}8.0\ \mu\text{m}$ continuum would be like if no ice absorption were present. For NGC 4945 both the ISO-PHT-S (*black*) and ISO-CAM-CVF (*grey*) spectrum are shown in the left panel. The vertical error bars at 5.8 and $11\ \mu\text{m}$ denote the pixel to pixel flux error (1σ , so not $\pm 1\sigma$).

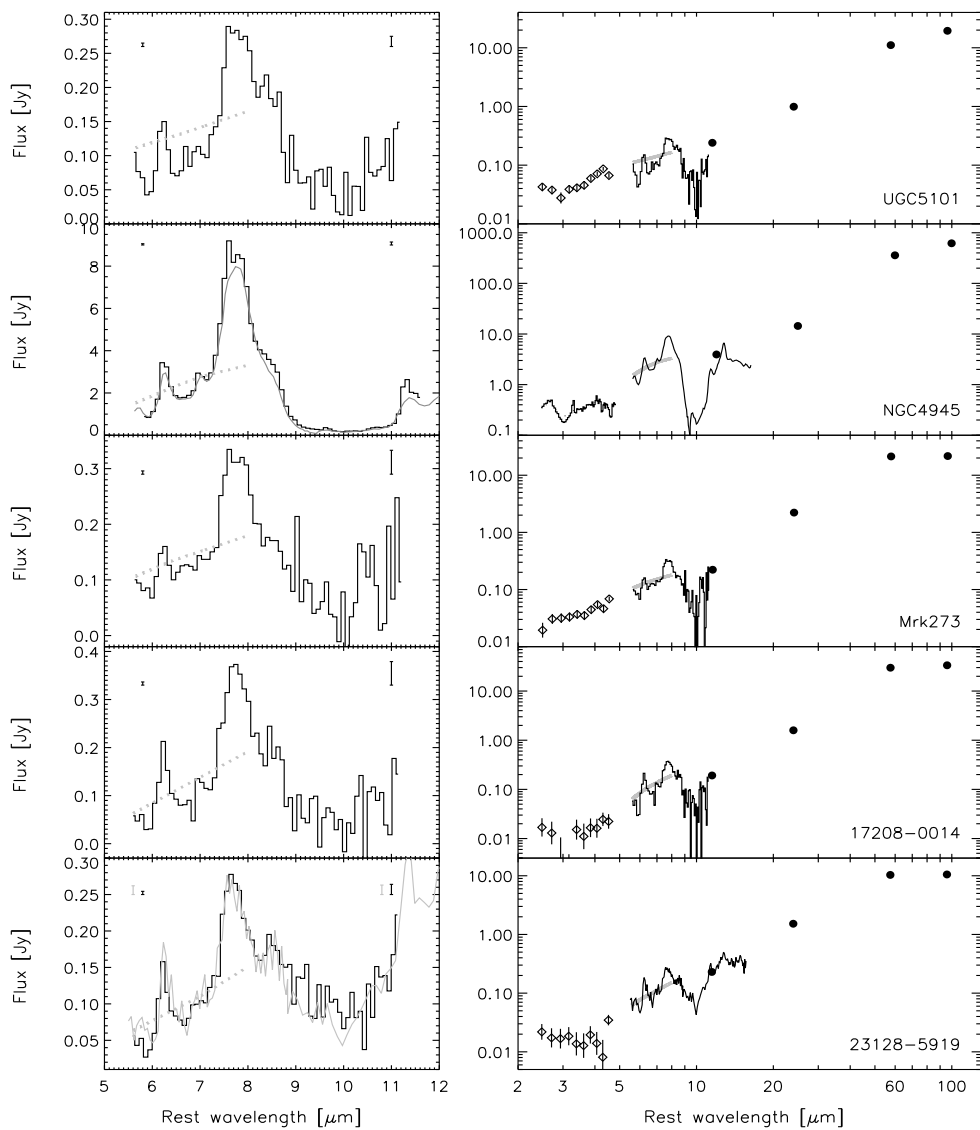


FIGURE 2.7 — Class 3 (continued)

Table 2.1 lists the classification for all 18 ice galaxies. For completeness we also list galaxies with $3.0\,\mu\text{m}$ ice absorption in their nuclear spectra: NGC 253, M 82 and NGC 4945 (Sturm et al. 2000, Chapter 3). Only for NGC 4945 has the usually far weaker $6.0\,\mu\text{m}$ feature also been detected – at similar strength as the $3.0\,\mu\text{m}$ one. This apparent inconsistency may be due to aperture size effects (the $3.0\,\mu\text{m}$ feature was measured by ISO–PHT–S; the $6.0\,\mu\text{m}$ feature by ISO–CAM–CVF) or due to dilution by less obscured emission, filling in the water ice features.

Within our sample of 103 galaxies with good S/N spectra and sufficient wavelength coverage we also recognize three other classes of spectra:

- **Class 4:** These galaxies (Fig. 2.8) show a smooth featureless continuum in the $5\text{--}6\,\mu\text{m}$ range as well as definite signs of $9.7\,\mu\text{m}$ silicate absorption. The presence of silicate absorption is most easily determined by interpolating the $6\,\mu\text{m}$ ISO and the $12\,\mu\text{m}$ IRAS flux points (or in case of ISO–CAM–CVF, using the $13\text{--}15\,\mu\text{m}$ continuum instead).
- **Class 5:** These galaxies (Fig. 2.9) show a smooth featureless continuum in the $5\text{--}6\,\mu\text{m}$ range without clear signs of $9.7\,\mu\text{m}$ silicate absorption. The absence of a clear silicate absorption feature is most easily determined by interpolating the $6\,\mu\text{m}$ ISO and the $12\,\mu\text{m}$ IRAS flux points (or in case of ISO–CAM–CVF, using the $13\text{--}15\,\mu\text{m}$ continuum instead).
- **Class 6:** These galaxies (Fig. 2.2) clearly show 5.25 and $5.7\,\mu\text{m}$ PAH features, without clear signs of $9.7\,\mu\text{m}$ silicate absorption. The absence of a clear silicate absorption feature is most easily determined by interpolating the $6\,\mu\text{m}$ ISO and the $12\,\mu\text{m}$ IRAS flux points (or in case of ISO–CAM–CVF, using the $13\text{--}15\,\mu\text{m}$ continuum instead).

Table 2.3 lists the observed mid-IR features for the 13 out of 28 Class 4–6 galaxies displayed in this paper. It is hard to quantify consistently the limits on ice absorption in these three classes because of the presence of PAH features. For Class 4 and 5 we estimate $\tau_{\text{ice}} < 0.1\text{--}0.3$. For Class 6, in all spectra the presence of weak $5.7\,\mu\text{m}$ and strong $6.2\,\mu\text{m}$ features may easily mask ice features as strong as $\tau_{\text{ice}}=0.3$. We note that among the Class 6 galaxies, both NGC 253 and M 82 do have a weak $3.0\,\mu\text{m}$ water ice feature (Sturm et al. 2000), but the $6.0\,\mu\text{m}$ ice limit is $\tau_{\text{ice}}=0.3$ for both galaxies.

The total number of ISO galaxies classified into Classes 1–6 is small: just 46 out of ~ 250 galaxies in our sample. The combination of both a good coverage of the $5.5\text{--}6.0\,\mu\text{m}$ range and a good S/N over $5.5\text{--}6.5\,\mu\text{m}$ proves to be a hard requirement to meet. With its superior sensitivity and better coverage of the $6\,\mu\text{m}$ region, SIRTF can be expected to refine our classification, find new members and provide a larger sample for statistical analyses.

2.5 Absorption and emission profile analysis

2.5.1 Model fits

The model described in Sect. 2.3 is now applied to the Class 1–3 sources presented in Sect. 2.4. The flat continuum of Sect. 2.3 is replaced by the $5\text{--}8\,\mu\text{m}$ continua derived individually for each source (thick grey lines in Figs. 2.5–2.7). For Class 2 and 3 sources, the continua were determined by interpolating the ISO–PHT–S short wavelength spectrum ($2\text{--}5\,\mu\text{m}$) linearly or logarithmically (depending on the SED shape) to the long wavelength

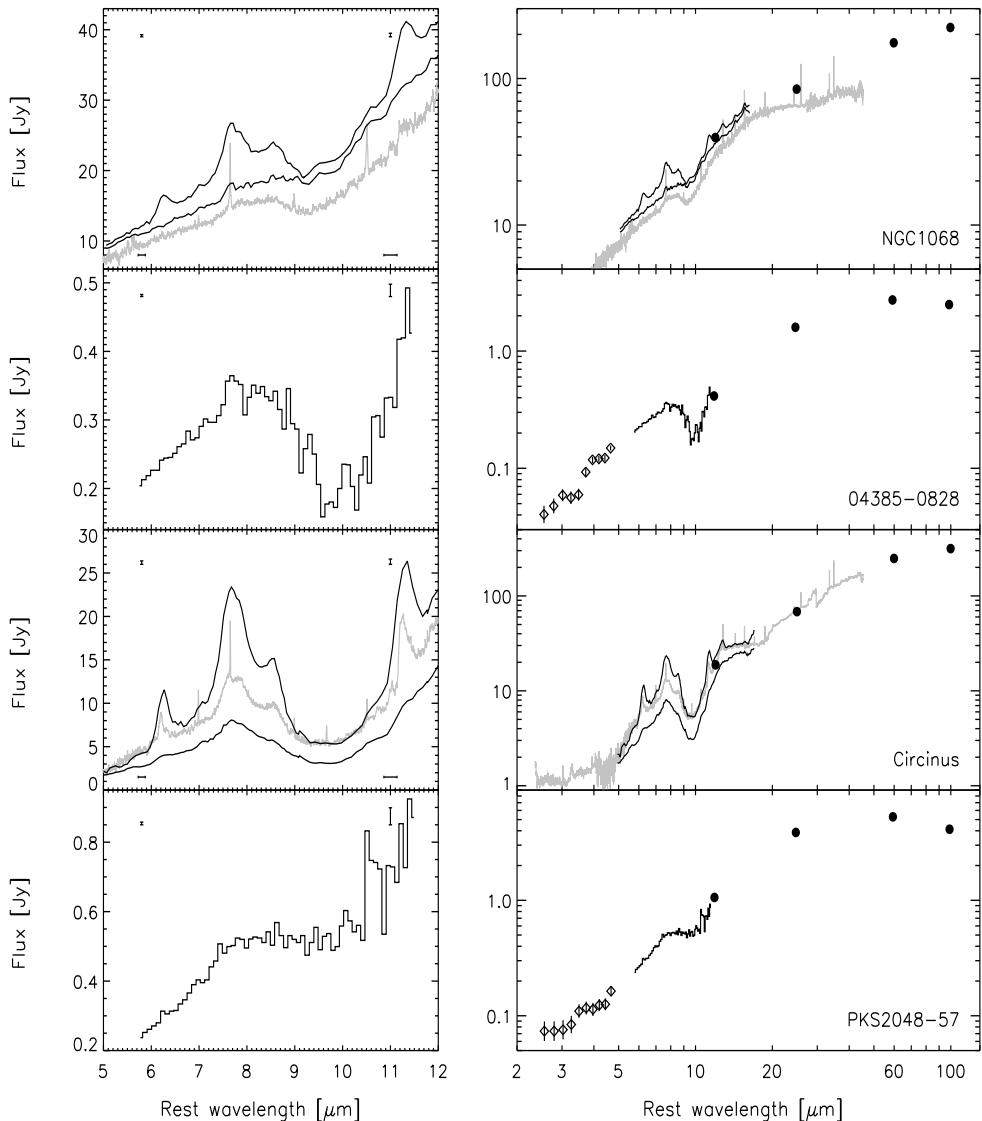


FIGURE 2.8 — Class 4 mid-IR galaxy spectra. Galaxies of this kind are ice-poor and show the presence of silicates along the line of sight. The presence of silicates is inferred from the absorption feature at $9.7\ \mu\text{m}$, characteristic for silicates. The upper limit on water ice is inferred from the absence of a $6.0\ \mu\text{m}$ absorption feature. For NGC 1068 and for Circinus three spectra are shown: the ISO-SWS nuclear spectrum in grey and the ISO-CAM-CVF nuclear and total spectra in black. The offset between the three spectra is most likely an aperture effect. The **panels on the left** show the $5\text{--}12\ \mu\text{m}$ spectra on a linear scale, while the **panels on the right** show the same spectra on logarithmic scale, with smoothed and rebinned $2\text{--}5\ \mu\text{m}$ ISO-PHT-S spectra and $12\text{--}100\ \mu\text{m}$ IRAS fluxes added. All fluxes have been k-corrected. The vertical error bars at 5.8 and $11\ \mu\text{m}$ denote the pixel to pixel flux error (1σ , so not $\pm 1\sigma$), while the horizontal error bars denote the gradually changing ISO-CAM-CVF spectral resolution ($R\sim 40$).

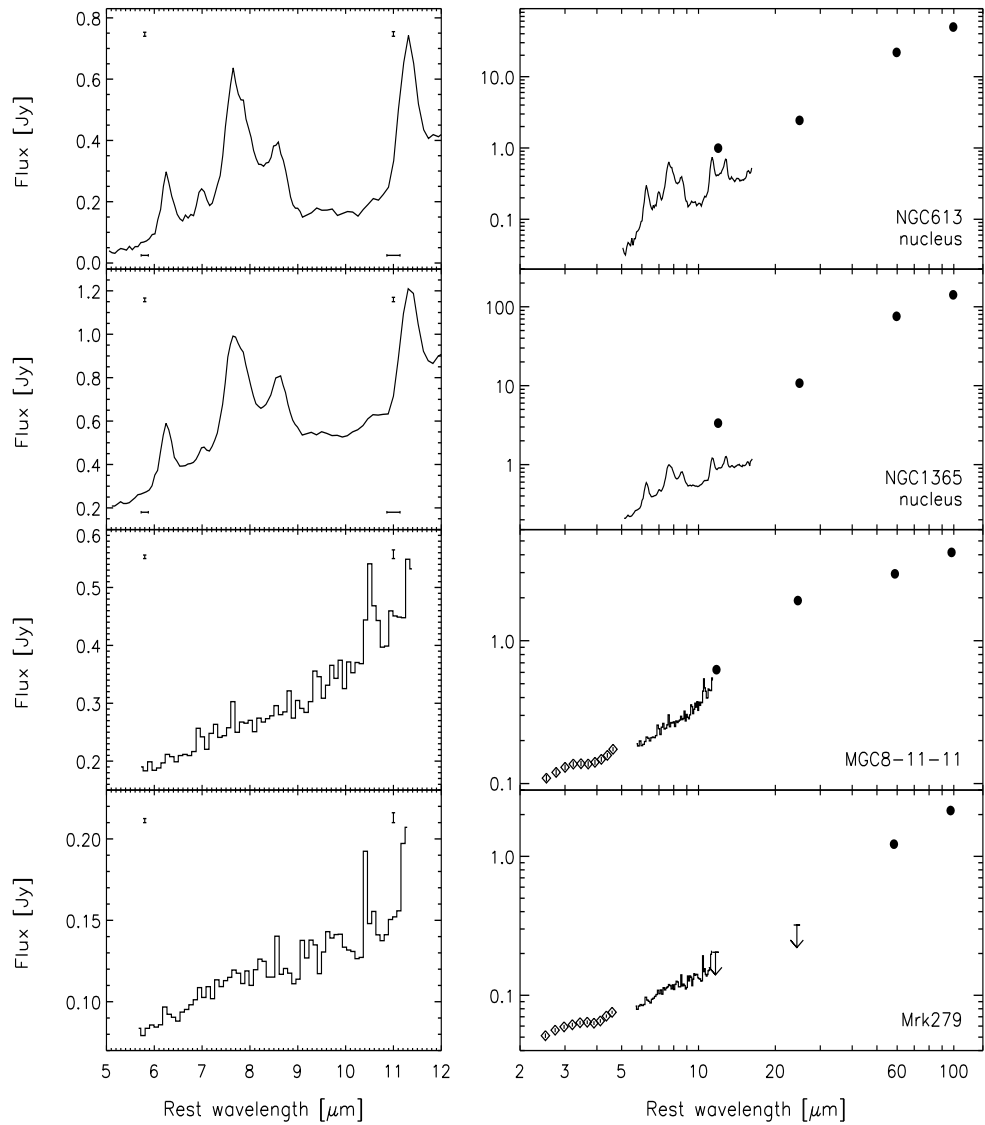


FIGURE 2.9 — Class 5 mid-IR galaxy spectra. Galaxies of this kind are ice-poor and show no clear evidence for the presence of silicates along the line of sight. Note the clear mismatch of the IRAS FSC fluxes with the ISO-CAM-CVF nuclear spectra for both NGC 613 and NGC 1365. This most probably is an aperture-size effect. The presence of strong PAH emission both short- and longward of $9.7\ \mu\text{m}$ makes it difficult to completely rule out silicate absorption in the nuclei of NGC 613 and NGC 1365. Compared to Circinus and NGC 520 however (Fig. 2.8), the silicate depth must at least be small. The **panels on the left** show the $5\text{--}12\ \mu\text{m}$ spectra on a linear scale, while the **panels on the right** show the same spectra on logarithmic scale, with smoothed and rebinned $2\text{--}5\ \mu\text{m}$ ISO-PHT-S spectra and $12\text{--}100\ \mu\text{m}$ IRAS fluxes added. All fluxes have been k-corrected. The vertical error bars at 5.8 and $11\ \mu\text{m}$ denote the pixel to pixel flux error (1σ , so not $\pm 1\sigma$), while the horizontal error bars denote the gradually changing ISO-CAM-CVF spectral resolution ($R\sim 40$).

IRAS data, ignoring the presence of PAH emission features. For Class 1 sources we followed another recipe. In the absence of contamination by PAH emission bands, we assumed the $8\text{ }\mu\text{m}$ flux peak to represent the local $8\text{ }\mu\text{m}$ continuum (see Sect. 2.6 for a discussion on the nature of the $8\text{ }\mu\text{m}$ flux peak). For the three sources observed with ISO-CAM-CVF we then derived the $5\text{--}8\text{ }\mu\text{m}$ continuum by interpolating to the observed $5\text{ }\mu\text{m}$ flux. For NGC 4418 and I 15250+3609 we interpolated to the reddest $2\text{--}5\text{ }\mu\text{m}$ ISO-PHT-S data point, assuming a continuum shape similar to that of I 00188–0856. Note that for all Class 1 sources we included a $6.85\text{ }\mu\text{m}$ absorption feature due to hydrogenated amorphous carbon (HAC; Furton et al. 1999). A (strong) $6.85\text{ }\mu\text{m}$ absorption feature is commonly observed towards Galactic lines of sight (Chiar et al. 2000; Keane et al. 2001).

Fig. 2.10 displays the model fits to all the sources, except for the three sources discussed below (Fig. 2.11). The grey histogram represents the model and in all cases the model spectra match very well the observed data. For two sources, Arp 220 and NGC 4945, the ISO-CAM-CVF spectra have also been included (thin line). Reading from left to right, of the first 5 panels in Fig. 2.10 a HAC absorption feature has been included for four of the sources. This profile matches very well the strong absorption feature seen near $6.85\text{ }\mu\text{m}$ in these sources. In the case of I 00188–0856, absorption between 6.4 and $7.4\text{ }\mu\text{m}$ is not consistent with the $6.85\text{ }\mu\text{m}$ absorption profile and therefore only the $6.0\text{ }\mu\text{m}$ water ice profile is modeled. We are not aware of any other valid or likely candidate that can give rise to the absorption observed in I 00188–0856. For the remainder of the sources this feature has been omitted from the model. A qualitative comparison of the panels of Fig. 2.10 reveals that the observed features at $6.0\text{ }\mu\text{m}$ and $6.2\text{ }\mu\text{m}$ are successfully reproduced for all sources.

For three of our ice galaxies (Mrk 231, NGC 828, Mrk 334) proving the presence of $6.0\text{ }\mu\text{m}$ ice absorption – the very key to membership of Classes 1–3 – turned out to be non-trivial. For each of these galaxies (see Fig. 2.11) the number of pixels in the blue wing is small, as is the depth of the ice feature. In all cases continua exist which do not require the presence of $6.0\text{ }\mu\text{m}$ ice absorption. However, such continua, which are defined here as the superposition of hot dust plus PAH continua, must give a good fit in the $6\text{--}8\text{ }\mu\text{m}$ range (i.e., any emission above or below the continuum level should be accounted for by known emission and absorption features) and the continuum should join smoothly to the long wavelength ($\geq 12\text{ }\mu\text{m}$) data. In the case of Mrk 231, there is a preference for the fit requiring the presence of water ice (Fig. 2.11, left panel). This fit adopts a much more realistic continuum (cf. Fig. 2.6) and it provides a more realistic value for the $6.2\text{ }\mu\text{m}/7.7\text{ }\mu\text{m}$ PAH ratio than the fit not requiring the presence of water ice (Fig. 2.11, right panel). Moreover, the fit without water ice would result in a very broad $7.7\text{ }\mu\text{m}$ PAH feature which does not resemble PAH features in Galactic sources. However, the total amount of ice absorption is difficult to quantify. A slightly lower but still permissible continuum can reduce the ice optical depth by a factor 2. For the other two galaxies (NGC 828, Mrk 334) the fits with and without water ice are equally viable.

2.5.2 Derived physical parameters

Table 2.1 summarizes the physical parameters of the detected features. The range in optical depths of the water ice absorption band is large, extending from small depths of $\tau_{\text{ice}}=0.13$ (I 05189–2524) to very deep features with $\tau_{\text{ice}}=1.3$ (UGC 5101). The optical depths of the water ice band were converted to column densities by dividing the peak optical depth by the intrinsic peak strength ($4.2 \times 10^{-20}\text{ cm}^2\text{ molecules}^{-1}$; Hagen et al. 1983). The derived col-

TABLE 2.1 — Observed physical parameters for the features residing in the 3–8 μm spectral region.

Target	Galaxy type	cz [km/s]	Class	H ₂ O ice	H ₂ O ice	PAH	HAC	HAC	Silicates	N(H ₂ O)
				3.0 μm τ	6.0 μm τ	6.25 μm $10^{-19} \text{ Wcm}^{-2}$	6.85 μm τ	7.3 μm τ	9.7 μm τ	10^{18} cm^{-2}
Mrk 334	Sy2	6582	3		0.55	2.0			0.8	12.8
NGC 23	SB	4566	3		0.94	5.6			1.0	22.0
I00183–7111	Ulrig	98032	1		0.20	—	0.3		>1.9	4.6
I00188–0856	Ulrig	38550	1		0.55	—			>1.5	12.8
NGC 253	SB	245	—	0.25 ^a						
I01173+1405	SB	9362	3		0.70	2.5			1.3	16.3
NGC 828	SB	5374	3		0.78	11			0.8	18.1
I05189–2524	Sy2	12760	2		0.13	1.1			0.15	3.0
I06035–7102	Ulrig	23823	3		0.70	0.9			1.5	16.3
UGC 5101	Ulrig	12000	3		1.30	2.0			>1.5	30.2
M 82	SB	203	—	0.2 ^a						
NGC 4418 ^b	Sy?	2179	1		0.90	—	1.1	✓	>2.9	21.0
Mrk 231	Ulrig	12660	2		0.14	1.5			0.65	3.3
NGC 4945	SB/Sy2	560	3	0.90 ^c	0.90	47			>3.7	21.0
Mrk 273	Ulrig	11132	3		0.60	1.5			1.2	14.3
I 15250+3609	Ulrig	16000	1		1.20	—	1.3	✓	>3.3	28.0
Arp 220	Ulrig	5450	2		0.74	2.3			>2.4	17.2
I 17208–0014	Ulrig	12900	3		1.14	3.3			2.0	26.5
I 20551–4250	Ulrig	12788	2		0.70	1.4			1.8	16.3
I 23128–5919	Ulrig	13371	3		1.30	2.5			0.7	30.2

^(a) Sturm et al. (2000); ^(b) Chapter 5; ^(c) Chapter 3.

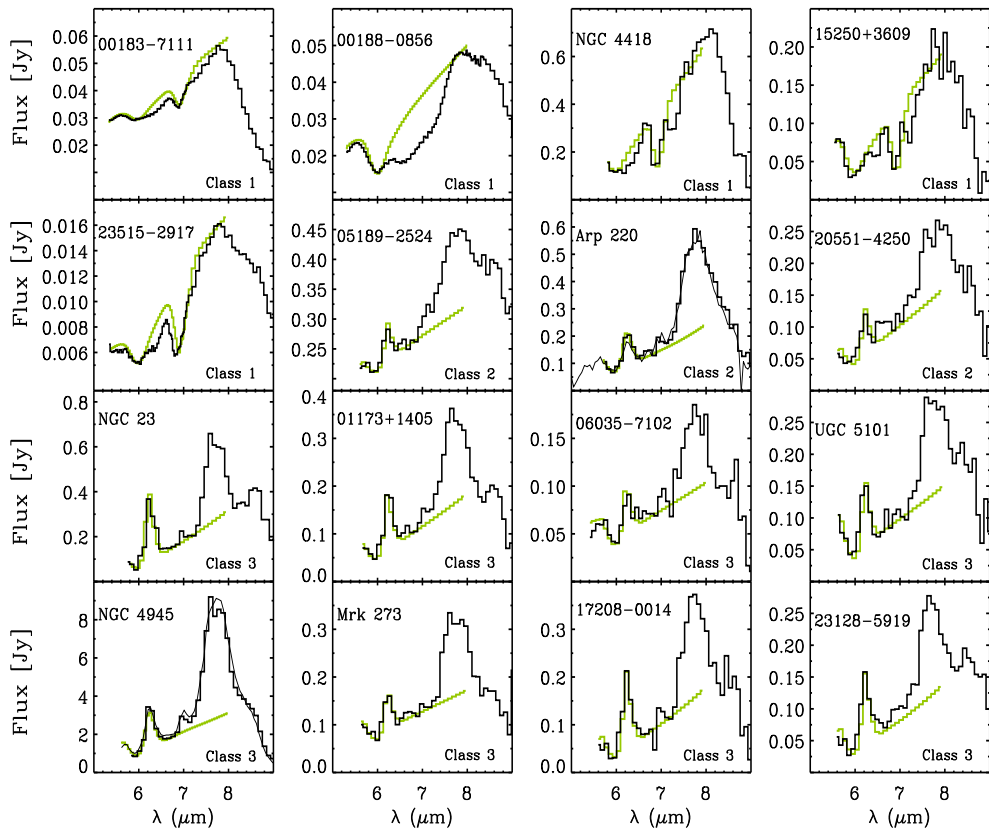


FIGURE 2.10 — A comparison of all the sources with the best fitting models which contain both water ice absorption and PAH emission bands. The *grey histogram* data represent the model fits. The three sources plotted in Fig. 2.11 are not shown here.

umn densities are comparable to water ice column densities determined for Galactic molecular clouds (Keane et al. 2001). All sources in Class 1, except for I 00188-0856, also show evidence for additional absorption features centered at 6.85 μm , 7.3 μm , 7.67 μm . The 6.85 μm feature resides in the long wavelength wing of the water ice band, and hence the depth of this feature is more accurately determined by dividing out the continuum plus water ice feature rather than just the continuum. For Class 1 galaxies, except for I 00183-7111, the depth of this feature is very strong and is greater than the corresponding water ice optical depths. In Galactic dense molecular clouds, on the other hand, the water ice absorption is always the stronger of the two (Keane et al. 2001). The origin of the 6.85 μm feature is unknown. The presence of a 7.3 μm feature in some spectra suggests it is carried by HAC residing in

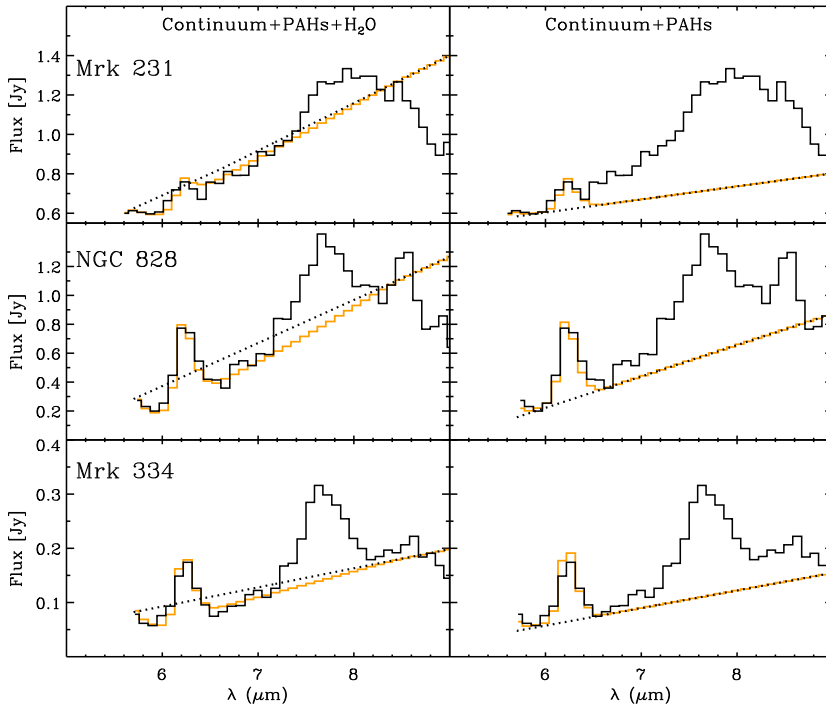


FIGURE 2.11 — Examples of 3 sources which show only a few pixels in the $6.0\ \mu\text{m}$ range and which might hinder the interpretation of water ice being present. The **left panel** shows the best fits by a model containing both water ice absorption and $5\text{--}6\ \mu\text{m}$ PAH emission. The **right panel** shows the best possible fits by a model which only contains $5\text{--}6\ \mu\text{m}$ PAH emission features. The adopted continua are denoted by the *dashed lines* and the resulting fits are represented by the *line shown in grey*. Note that since our model does not take into account the 7.7 and $8.6\ \mu\text{m}$ PAH features (see Sect. 2.3.1), the quality of the fit can only be tested shortward of $7\ \mu\text{m}$.

the diffuse ISM, very much like the Galactic center (Chiar et al. 2000). An absorption feature at $7.3\ \mu\text{m}$ is present in the spectra of I 15250+3609 and NGC 4418 (Chapter 5). On the other hand, many Galactic young stellar objects show a strong $6.85\ \mu\text{m}$ feature due in part to an unidentified ice component (Keane et al. 2001). Observations of the $3\ \mu\text{m}$ region could distinguish between these two possibilities because HAC material presents a strong $3.4\ \mu\text{m}$ absorption feature which is absent in Galactic YSOs (Pendleton et al. 1994; Pendleton & Chiar 1997). A $3.4\ \mu\text{m}$ absorption feature observed towards a few extragalactic sources has been tentatively attributed to HAC (Wright et al. 1996b). Finally, one source, NGC 4418, has an absorption feature at $7.67\ \mu\text{m}$ which has been attributed to methane ice (CH_4 ; Chapter 5).

Since the $6.2\ \mu\text{m}$ PAH feature lies, in general, within the wing of the water ice absorption band and hence slightly beneath the continuum, it is necessary to subtract a combination

TABLE 2.2 — Break-down of ice galaxies over the three main galaxy types in our sample of 103 ISO galaxies having good S/N spectra and sufficient wavelength coverage blueward of $6\mu\text{m}$.

Gal. type	PHT-S	CAM-CVF	total
Seyfert	2/55	0/7	2/62
ULIRG	9/12	3/7	12/19
Starburst	3/12	1/9	4/21
Other	0/1	0/0	0/1

of the continuum plus water ice from the observational data. After subtraction, the intensity (W cm^{-2}) of the $6.2\mu\text{m}$ band is determined between $6.0\mu\text{m}$ and $6.55\mu\text{m}$. The derived $6.2\mu\text{m}$ PAH intensities are listed in Table 2.1. Note that for models in which the water ice is mixed with or in front of the PAH emitting region, the intrinsic $6.2\mu\text{m}$ PAH intensities would be greater.

An estimate of the $9.7\mu\text{m}$ silicate optical depth (τ_{sil}) for each of the sources is also given in Table 2.1. In order to be able to compute this quantity, the $9.7\mu\text{m}$ continuum was interpolated from the $5\text{--}8\mu\text{m}$ continuum and the long wavelength data ($>12\mu\text{m}$). For some sources the peak absorption of the silicate feature is saturated and the true depth of the band is thus uncertain. In these cases fitting the wings of the feature can be attempted. Given the possibility of additional sources of emission along the line of sight, however, we prefer here to just state lower limits for τ_{sil} . The column density of hydrogen is computed from the $9.7\mu\text{m}$ silicate depth by assuming a Galactic conversion factor: $N_H = \frac{N_H}{A_V} \times \frac{A_V}{\tau_{\text{sil}}} \times \tau_{\text{sil}} = \tau_{\text{sil}} \times 3.5 \times 10^{22}\text{ cm}^{-2}$ (Roche & Aitken 1984; Bohlin et al. 1978).

2.6 Discussion

Within our sample of 103 galaxies with good S/N and sufficient wavelength coverage shortward of $6.0\mu\text{m}$, we have found water ice in up to 18 galaxies and upper limits of better than $\tau_{\text{ice}}=0.1\text{--}0.3$ for the absence of water ice absorption in another 28 galaxies. Although a small sample, it is of interest to correlate galaxy types with the mid-IR absorption/emission characteristics. The results of our analysis are presented in Table 2.2.

Table 2.2 suggests that water ice might be a common species in ULIRGs, since 12 out of 19 do show ice. Seyferts, on the other hand, seem to be ice-poor, with ice detected in only 2 out of 62 galaxies. For starburst galaxies the numbers are less obvious, with 4 detections on a total of 21 galaxies.

In order to investigate this issue further we have composed average spectra for the three main galaxy types listed in Table 2.2. Since the presence of $5\text{--}6\mu\text{m}$ PAHs in spectra complicates the detection of the $6.0\mu\text{m}$ water ice feature, we have decided to generate separate average spectra for continuum-dominated Seyferts and ULIRGs and for PAH-dominated Seyferts and ULIRGs. We classify a spectrum as continuum-dominated when the $6.2\mu\text{m}$ PAH line-to-continuum ratio is less than 0.15 and PAH-dominated when the ratio exceeds this value. The resulting five average spectra are shown in Fig. 2.12 and are based on 138 out of 250 galaxy spectra in our database. The galaxies included in the averaging process were selected on the basis of their noise after scaling by their individual $6.5\mu\text{m}$ flux.

The top panel of Fig. 2.12 shows the average PAH-dominated Seyfert galaxy, composed of 34 galaxy spectra. In addition to the well-known PAH emission features, the spectrum shows the $6.99\text{ }\mu\text{m}$ [Ar II] and $10.54\text{ }\mu\text{m}$ [S IV] forbidden lines, the latter of which usually is strong in active galaxies. The spectrum bears no trace of $6.0\text{ }\mu\text{m}$ water ice absorption. The second panel of Fig. 2.12 depicts the average continuum-dominated Seyfert, composed of 45 galaxy spectra. The spectrum is dominated by the [S IV] line, with traces of [Ar II], maybe of $7.65\text{ }\mu\text{m}$ [Ne VI] and of weak PAH emission — the latter in accordance with our selection criterion of $6.2\text{ }\mu\text{m-PAH L/C}<0.15$. The $9.7\text{ }\mu\text{m}$ silicate absorption feature is strikingly absent, as is the $6.0\text{ }\mu\text{m}$ water ice absorption feature. The third panel of Fig. 2.12 shows the average continuum-dominated ULIRG, composed of 11 galaxy spectra, among which are all Class 1 sources except for NGC 4418, as well as the Class 2 source Mrk 231. The spectrum is dominated by a broad flux peak centered at $\sim 8\text{ }\mu\text{m}$. A $6.0\text{ }\mu\text{m}$ water ice feature can be easily recognized, starting at $\sim 5.6\text{ }\mu\text{m}$ and reaching maximum depth at $5.9\text{--}6.0\text{ }\mu\text{m}$. The spectrum is noticeably different from the other continuum-dominated spectrum, the Seyfert spectrum, in the panel above. The fourth panel shows the average PAH-dominated ULIRG, composed of 19 galaxy spectra. Among the selected sources are several Class 2 and Class 3 sources. The spectrum shows strong resemblance to the average starburst galaxy (panel below; 29 spectra), with two exceptions: (1) the average PAH-dominated ULIRG shows a clear $6.0\text{ }\mu\text{m}$ water ice feature, partially filled in by $6.2\text{ }\mu\text{m}$ PAH emission, the average starburst galaxy does not; and (2) the average starburst spectrum shows a hint of $5\text{--}6\text{ }\mu\text{m}$ PAH features (Fig. 2.2), where the average PAH-dominated ULIRG as well as the other three average spectra do not. The presence of the $5\text{--}6\text{ }\mu\text{m}$ spectral structure near $6.0\text{ }\mu\text{m}$ forces a higher upper limit to the amount of ice in the average starburst spectrum than in the two average Seyfert spectra.

The average spectra largely confirm our initial findings: ULIRGs have on average more ice than Seyfert and starburst galaxies. The absence of contaminating PAH emission in the continuum-dominated Seyfert spectrum implies a tighter upper limit for the presence of water ice absorption than in the PAH-dominated Seyfert and starburst spectra.

Also of interest is the presence of a broad flux peak centered at $\sim 8\text{ }\mu\text{m}$ in the continuum-dominated ULIRG (Fig. 2.12, middle panel). In the absence of strong $6.2\text{ }\mu\text{m}$ PAH emission ($L/C<0.15$), the $8\text{ }\mu\text{m}$ flux peak cannot be attributed to strong and exceptionally broad PAH emission. We will come back to this issue later this Section.

The galaxies in our sample have turbulent and hostile environments (i.e., the diffuse interstellar medium or the immediate surroundings of the central starburst or AGN) which significantly process and often destroy the molecular material that reside in or close to these regions. However, within our ice-galaxy sample, volatile material (which is easily destroyed) is clearly present. This suggests that some shielding from harsh environments must occur. In the diffuse medium supernova shock waves are the predominant destruction mechanism for interstellar dust (Jones et al. 1994). Refractory grains and most likely PAHs are typically destroyed within 10^8 yr, whereas ice grains of 1000 \AA can only survive for $\sim 10^6$ yr. These lifetimes increase significantly in dense clouds where the molecules are protected from processes such as sputtering by shocks. On the other hand, molecular material in an AGN torus (or in nearby dusty clouds) is exposed to the intense hard X-rays originating from the central engine. Due to their extreme energies, hard X-ray photons are able to penetrate column densities of $\sim 10^{25}\text{ cm}^{-2}$ (e.g. NGC 4945: Iwasawa et al. 1993). Hence, under such conditions, ice mantles on the dust grains would be unable to survive. PAHs, on the other hand, might be able to survive for lifetimes of $> 10^4$ yr if the column density is greater than $\sim 10^{23}\text{ cm}^{-2}$.

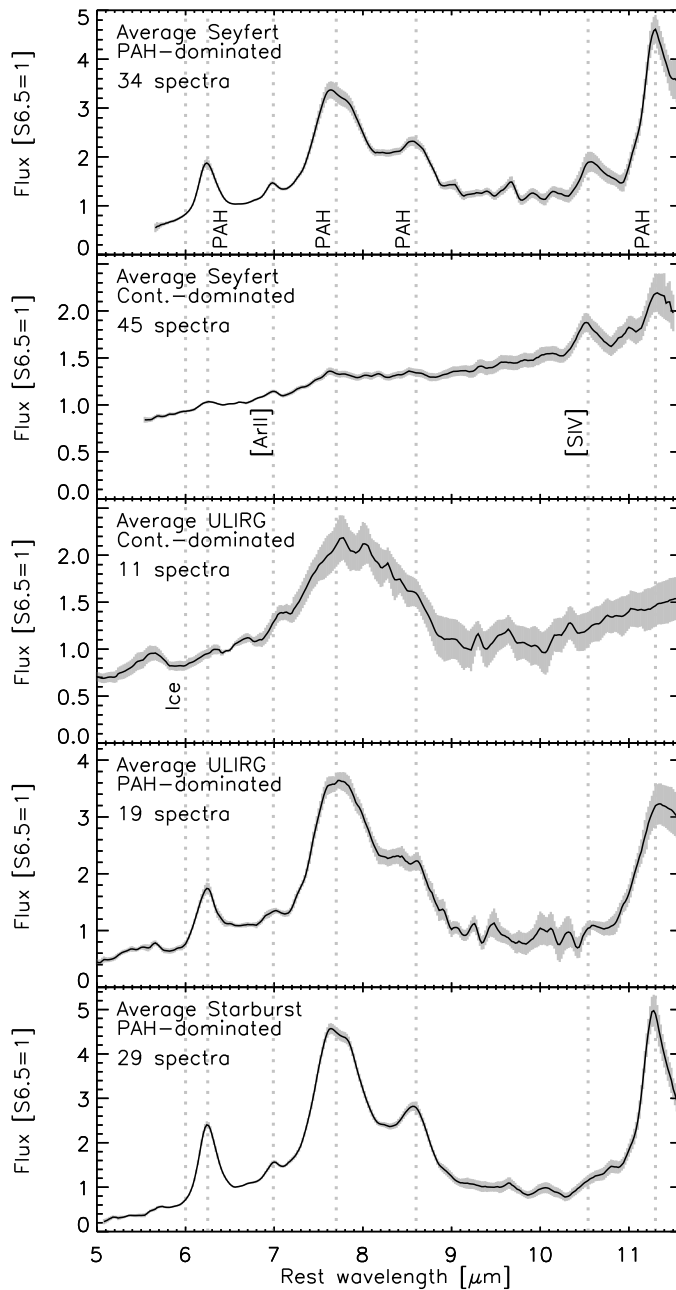


FIGURE 2.12 — Panels showing the average spectra of PAH-dominated ($6.2 \mu\text{m}$ -PAH L/C>0.15) and continuum dominated ($6.2 \mu\text{m}$ -PAH L/C<0.15) Seyferts, ULIRGs and starburst galaxies. Grey shaded areas indicate the standard deviations in the average spectra. Vertical dotted lines denote the central wavelengths of well-known spectral features (see text).

(Voit 1992) and hence it is more likely to see PAHs as opposed to ices in such environments. Nevertheless, the harsh conditions in AGN toroids may well influence the composition of the emitting PAH family. Further modelling and laboratory experiments are required to determine to what extent PAHs and ices are processed by the hard radiation present in AGNs.

ULIRGs are merger systems in which the tidal forces have allowed molecular material from the galaxy disks to accumulate in the nuclei of the system (e.g. Solomon et al. 1997; Downes & Solomon 1998; Sakamoto et al. 1999; Tacconi et al. 1999). The presence of water ice in ULIRGs thus comes as no surprise. In the many dense shielded cloud cores, that are likely to be present, water ice can survive until these clouds are dispersed by starformation. Clearly, the “icy” ULIRGs still have ample cold dense molecular material to continue star formation for some time. In Galactic dense molecular clouds the $6.0\text{ }\mu\text{m}$ water ice absorption feature is seen against the mid-IR continuum of deeply embedded protostars, like W 33A and NGC 7538 IRS9. In external galaxies, the background continuum source might also be provided by hot dust associated with the AGN torus or with starburst activity. The similarity of the average ULIRG spectrum (Fig. 1 of Lutz et al. 1998) to Class 3 spectra with strong PAHs, suggest that ice absorption in ULIRGs is preferentially linked to a scaled up star formation process. The lower luminosity example of NGC 4418 cautions, however, that this link cannot be generalized to all individual objects: ice absorption may also be seen against AGN.

Little can be derived from our data on the ice absorption properties of lower luminosity starbursts. The very strong PAH emission features prevent the detection of moderately strong $6.0\text{ }\mu\text{m}$ features. In fact, given the lower obscuration of starbursts compared to ULIRGs or to Galactic protostars, weaker ice features in starbursts are expected for similar properties of the obscuring matter. The examples of M 82 and NGC 253 (Sturm et al. 2000) suggest that the $3\text{ }\mu\text{m}$ region may be better suited to quantify such weaker ice absorptions, with the caveat for ground-based observations of the $3\text{ }\mu\text{m}$ region being a difficult atmospheric window. Ice is seen in these starbusts at $3\text{ }\mu\text{m}$ but not detectable in the heavily structured $6\text{ }\mu\text{m}$ spectrum.

The conditions for the existence of water ice near Seyfert nuclei seem to be generally poor. If most of the obscuration occurs in a dense torus that is surrounding the nuclear region and heated by the X-rays from the central engine, ices are unlikely to survive. Indeed, $3\text{ }\mu\text{m}$ spectra of AGN (Bridger et al. 1994; Wright et al. 1996b; Imanishi 2000; Sturm et al. 2000) tend to show $3.4\text{ }\mu\text{m}$ hydrocarbon absorptions but no ices.

The low number of Seyfert and starburst ice-galaxies, as inferred from the mid-IR spectra, might indicate that dense shielded molecular cloud cores are far less abundant in these systems than in ULIRGs. Likely, most of the absorption in Seyferts originates in the dense toroid surrounding the nuclear region, which is thoroughly energetically or thermally processed by the X-rays of the internal monster and therefore contains no ices.

As a corollary and as illustrated by Fig. 2.8 the presence of silicates does not automatically imply the presence of water ice. If the environment is not sufficiently shielded or is too warm, water ice cannot exist. For the five galaxies displayed (one starburst galaxy and four Seyferts) this might be the case.

Conversely, does water ice correlate with the presence of shielding dust (e.g., silicates)? Except for I05189–2524, all our ice-galaxies show a strong $9.7\text{ }\mu\text{m}$ silicate absorption feature (see Table 2.1), with $\tau_{\text{sil}} > 1.5$ for most sources. The ratio $\tau_{\text{ice}}/\tau_{\text{sil}}$ spans a range of < 0.10 for I00183–7111 to 1.8 for I23128–5919, with a mean value of 0.67 for the galaxies with a non-saturated silicate feature. In contrast, all five Class 1 galaxies have $\tau_{\text{ice}}/\tau_{\text{sil}} < 0.37$. This

TABLE 2.3 — Overview of features observed in Class 4–6 galaxies shown in Figs. 2.2, 2.8 & 2.9, all displaying no sign for $6\mu\text{m}$ water ice absorption at the $\tau(6\mu\text{m}\text{ice})=0.1\text{--}0.3$ level.

Target	Galaxy type	cz [km/s]	$5\mu\text{m}$ PAH emission	$9.7\mu\text{m}$ silicate absorption
NGC 253	SB	245	++	?
NGC 520	SB	2281	++	+
NGC 613	SB	1475	-	?
NGC 1068	Sy2	1148	-	+
NGC 1365	Sy1.8	1636	?	?
I 04385–0828	Sy2	4527		++
NGC 1808	Sy2	1000	++	?
MGC 8–11–11	Sy1.5	6141		-
M 82	SB	203	++	?
M 83	SB	516	++	?
Mrk 279	Sy1.5	8814		-
Circinus	Sy2	439	?	++
PKS 2048–57	Sy2	3402		+

++ = strongly present

? = maybe present

+ = present

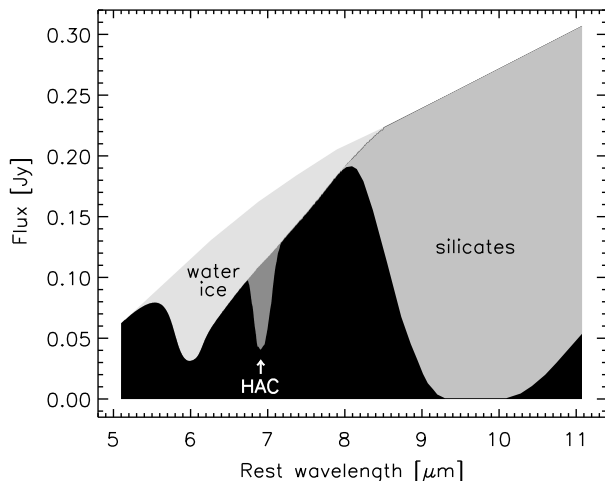
- = absent

suggests that silicate and water ice optical depths are not correlated on the galaxy-wide scale that we probe with our ISO observations. We note that low mass protostars in individual clouds (e.g. Taurus) do show a good correlation between ice optical depth and the strength of the silicate feature (Whittet et al. 1983, 1988). However, for massive luminous protostars in different clouds, no such correlation exists, largely due to the extensive thermal processing of the environment by the newly formed star (cf. Tielens & Whittet 1997). Obviously, the abundance of water ice is controlled by special conditions, which in our sample are apparently only met in some of the regions within our Class 1 ice galaxies.

Though originally published as a unique source, it is apparent from our study that some characteristics of NGC 4418 are seen in a larger number of galaxies. Mid-IR absorptions of water ice are detected in about one sixth of the galaxies for which ISO spectra of adequate S/N are available, and perhaps the majority of ULIRGs. These detections range from spectra dominated by an absorbed continuum (Class 1) over spectra mainly showing absorption signatures but also clear PAH emission (Class 2) to spectra that resemble normal PAH emission spectra subjected to additional dust and ice obscuration (Class 3).

Short of full spectral modelling, empirical criteria help to assess the relative importance of emission and absorption in shaping these spectra. First and most important is the distinction between a $6.2\mu\text{m}$ PAH emission and the $6.5\text{--}6.7\mu\text{m}$ pseudo maximum in an absorption dominated spectrum (Chapter 5). Second, there are differences in the shape of the maximum in the $8\mu\text{m}$ region. PAH dominated spectra exhibit relatively narrow 7.7 and $8.6\mu\text{m}$ emissions (e.g. Helou et al. 2000; Rigopoulou et al. 1999). Also, they show a very steep rise between 7.2 and $7.7\mu\text{m}$. Obscuration of such a spectrum (assumed to be intrinsically

FIGURE 2.13— Schematic view of the impact of dust and ice absorption on a mid-IR continuum spectrum. All shaded areas combined constitute the adopted local mid-IR continuum. The *black area* is all that is left of the local continuum after ices and silicates absorb substantial portions of the 5–12 μm local continuum. Note the presence of an emission-like broad feature near 8 μm in the resulting observed spectrum, which at first glance or at poor S/N may be mistaken for 7.7 μm PAH emission.



unchanged) affects mainly the relative strengths of such features but keeps the 7.7 μm peak narrow ($\text{FWHM} \approx 0.6 \mu\text{m}$, e.g. Fig. 2.3; Fig. 6 of Rigopoulou et al. 1999) and its ascent steep. In contrast, absorption dominated spectra tend to show a wider, less well defined peak around 8 μm (e.g. Fig. 2.13), with significant variation depending on continuum shape and optical depth of the various features.

The change from an absorbed continuum to an absorbed PAH spectrum is illustrated further in spectra of three adjacent positions in the Galactic star forming complex W 3 (Fig. 2.14, D. Cesarsky, priv. comm.). The top panel towards the infrared source is dominated by a continuum absorbed by ice, HAC, and silicates with a broadish 8 μm bump. The middle panel is an intermediate case and the bottom shows an obscured PAH spectrum. These spectra illustrate that the qualitative features discussed above and outlined in the schematic views of Fig. 2.3 and Fig. 2.13 can indeed originate from radiative transfer through a dense and dusty medium, and that star formation in our own galaxy can reproduce the full range of phenomena.

Differences in the shape of the 8 μm maximum may help in understanding the vast majority of sources that are not pure absorbed continua. Is the frequently observed weakness of the 6.2 μm feature (compared to the 7.7/8 μm maximum) due to obscuration of a PAH-dominated spectrum or due to superposition of a little obscured PAH spectrum and a strongly obscured continuum? The intrinsic 6.2/7.7 PAH ratio is quite stable for many Galactic sources (Peeters et al. 2002a) as well as the ISM in normal and starburst galaxies (Helou et al. 2000; Rigopoulou et al. 1999, our Fig. 2.2). Lutz et al. (1998) and Rigopoulou et al. (1999) argued in favour of obscuration as cause of the 6.2 weakness, using an observed correlation between 6.2/7.7 feature ratio and extinction to the starburst region, as measured from independent mid-IR emission line data (Genzel et al. 1998). On the other hand, suggestions have been made of an effectively unobscured 'surface layer' producing most of the PAH emission, CII line emission, and submm continuum of ULIRGs (e.g. Fischer 2001; Haas et al. 2001). Such an approach tackles problems like the observed [C II] deficit of ULIRGs at the expense of breaking the link between PAHs and the star formation observed in the mid-infrared fine

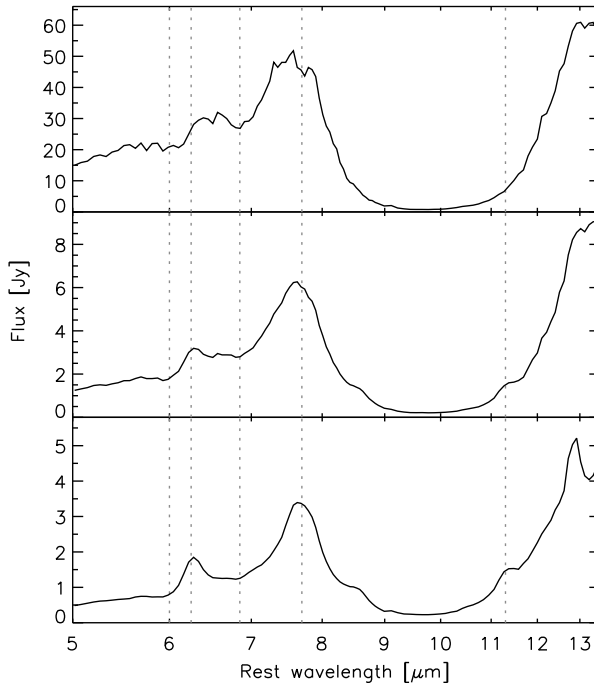


FIGURE 2.14 — ISO-CAM-CVF spectra of three adjacent positions in the W3 molecular cloud (D. Cesarsky, priv. comm.), showing a gradual transition between an obscured PAH-dominated mid-IR spectrum (**bottom**) and a strongly absorbed hot dust continuum (**top**). The vertical dotted lines show the positions of $6.0\,\mu\text{m}$ water ice, $6.25\,\mu\text{m}$ PAH, $6.85\,\mu\text{m}$ HAC and $7.7\,\mu\text{m}$ & $11.3\,\mu\text{m}$ PAH.

structure lines, and of introducing an unknown fully obscured component.

Water feature optical depths of $\tau_{\text{ice}} \sim 1$ (Table 2.1) are sufficient to modify the ratio of the 6.2 and $7.7\,\mu\text{m}$ PAH features by a factor ~ 2 . While this is enough to explain the weakness of the $6.2\,\mu\text{m}$ feature in many objects by obscuration, both the uncertainty in the optical depth values and the lack of knowledge to which extent the ice features apply to the PAHs and/or an underlying continuum make conclusions for individual objects very difficult. Here, use of the shape of the feature near $7.7/8\,\mu\text{m}$ can help with breaking the degeneracy. As long as the intrinsic shapes of the PAH features are assumed to remain constant, a wider than usual peak near $8\,\mu\text{m}$ argues for a considerable contribution of a heavily absorbed continuum. Our Class 1 and 2 spectra (Fig. 2.5 and 2.6) suggest that this is the case for a number of galaxies. In Chapter 6 we will derive quantitative fits to the high quality Class 2 spectrum of Arp 220, arguing for a best fit with a considerable contribution by an absorbed continuum. The existence of Class 1 and Class 2 sources implies that estimates of the PAH contribution on the basis of a line-to-continuum ratio (Genzel et al. 1998) or of fits with extinction laws that do not include ices (e.g. Tran et al. 2001) will overestimate the importance of PAHs, more noticeably for the simple line-to-continuum ratio. This effect is highly relevant for some of the Class 1 and 2 spectra, but less so for Class 3 or the ULIRGs in general. High S/N spectra, extended wavelength coverage, and fits of the entire wavelength range with PAHs and continua obscured by dust and ices are needed for quantitative progress.

The issue of broad $8\,\mu\text{m}$ features is complicated further by the presence of yet another category of "8\,\mu\text{m maxima}" in addition to PAHs and absorbed spectra: Several luminous AGN-like ULIRGs (Tran et al. 2001; Taniguchi et al. 1997) show broad $8\,\mu\text{m}$ maxima on top of a smooth mid-infrared continuum, with PAH absent or very weak. Clear examples for this

include I09104+4109, I00275–2859, I22192–3211, and I23529–2119. The key difference to our Class 1 and Class 2 spectra with broad $8\text{ }\mu\text{m}$ maxima is that these objects do not show the very deep silicate feature of the absorbed Class 1 and 2 spectra. Tran et al. (2001) discussed these features in terms of self-absorbed silicate emission or a modified PAH origin, without definite conclusion. Recent surveys of galactic PAHs (Peeters et al. 2002a; Verstraete et al. 2001) fail to observe similar profiles even under unusual conditions. The nature of these features remains uncertain.

It is interesting to speculate in analogy to Galactic sources that our classification might reflect an evolutionary sequence. If an evolved starburst is represented by a PAH spectrum, while strong mid-infrared continua are typical for the H II-region continuum of intense compact starbursts (Laurent et al. 2000) or AGN, then Class 1 may trace the deeply embedded beginnings of star formation (or AGN activity), while the latter classes reflect more advanced and less enshrouded stages.

Finally, a point of caution. Since the $3.0\text{ }\mu\text{m}$ water ice absorption extends over a difficult part of the L band, its definition is not easy in ground based spectra like those of Imanishi et al. (2001). Its short end is outside the L band and its long end coincides with the $3.3\text{ }\mu\text{m}$ PAH emission and $3.4\text{ }\mu\text{m}$ hydrocarbon absorption. A gradually increasing continuum from 3.15 to $4.0\text{ }\mu\text{m}$ is however visible in their spectrum of UGC 5101. Depending on the location along the line of sight, the water ice absorption will strongly affect measured quantities like the $3.3\text{ }\mu\text{m}$ continuum, the $3.3\text{ }\mu\text{m}$ PAH flux, its equivalent width and the $3.3\text{ }\mu\text{m}$ -PAH-to-far-IR flux ratio. Hence, in galaxies with water ice absorption (like UGC 5101, $\tau_{6.0\text{ }\mu\text{m}\text{ ice}}=1.3$), both uncorrected $3.3\text{ }\mu\text{m}$ and $6.2\text{ }\mu\text{m}$ PAH fluxes will provide underestimates when used as star formation indicators. For the $3.3\text{ }\mu\text{m}$ PAH, aperture losses of present instruments are an additional reason for underestimates as in the case of UGC 5101 where the north-south oriented $1.2''$ slit of Imanishi et al. (2001) is perpendicular to the orientation of the $>2''$ star forming region (Genzel et al. 1998).

2.7 Conclusions

Following the discovery of water ice in NGC 4418 (Chapter 5), we have searched our sample of ISO galaxy spectra for galaxies showing similar signs of $6.0\text{ }\mu\text{m}$ water ice absorption. We have found in total 18 galaxies, which we grouped into three classes. The classification is based on the presence of ice absorption, $6.2\text{ }\mu\text{m}$ PAH emission, and the nature of the 7.7 – $8\text{ }\mu\text{m}$ feature: PAH emission or absorbed mid-IR continuum, or a combination of the two. We also looked for galaxies showing no signs of water ice absorption. This sample contains 28 galaxies with water ice upper limits ranging from $\tau_{\text{ice}}=0.1$ – 0.3 , depending on the S/N and the complexity of the 5 – $7\text{ }\mu\text{m}$ spectrum. We classified these galaxies in another three classes (Class 4–6), depending on the presence of $9.7\text{ }\mu\text{m}$ silicate absorption and 5 – $6\text{ }\mu\text{m}$ PAH emission.

We have modeled the complicated interplay of $6.0\text{ }\mu\text{m}$ water ice absorption and $6.2\text{ }\mu\text{m}$ PAH emission, which in ISO-PHT-S spectra takes place at the blue end of the PHT-SL range and, hence, only can be recognized in galaxies with a redshift in excess of 3000 km/s . For spectra obtained with the ISO-CAM-CVF instrument no such limitations apply. Our modeling supports the presence of ice in the Class 1–3 sources, except in a few cases where ice is not strictly required to obtain an acceptable fit to the observed spectrum.

Based on a subsample of 103 good S/N ISO galaxy spectra with sufficient wavelength

coverage blueward of $6\text{ }\mu\text{m}$, a substantial fraction of ULIRGs (12 out of 19) contain detectable amounts of water ice. On the other hand, the majority of Seyfert (2 out of 62) and starbursts galaxies (4 out of 21) probably do not. These results are confirmed by the spectral structure seen in our average spectra of Seyfert, ULIRG and starburst galaxies: water ice absorption is only obvious in the average ULIRG.

Class 1 & 2 ice galaxies are dominated by a broad feature near $8\text{ }\mu\text{m}$ which indicates a strong contribution by a dust and ice-absorbed continuum, similar to that seen in NGC 4418. These observations stress the need for high S/N data and refined diagnostic methods, to properly discriminate spectra dominated by PAH emission and spectra dominated by heavy obscuration.

The interplay of the broad $8\text{ }\mu\text{m}$ feature and PAH emission, as seen in our ice galaxies, shows strong similarities with features seen in Galactic star forming clouds. This leads us to believe that our classification of ice galaxy spectra in three classes might reflect an evolutionary sequence from strongly obscured beginnings of star formation (and AGN activity) to a less enshrouded stage of advanced star formation (and AGN activity), as the PAHs get stronger and the broad $8\text{ }\mu\text{m}$ feature weakens.

Acknowledgements

The authors wish to thank Diego Cesarsky, Els Peeters and Eckhard Sturm for discussions. This research has made use of the NASA/IPAC Extragalactic Database (NED) which is operated by the Jet Propulsion Laboratory, California Institute of Technology, under contract with the National Aeronautics and Space Administration.

3

Mid-infrared ISO spectroscopy of NGC 4945

Adapted from:

H.W.W. Spoon, J. Koornneef, A.F.M. Moorwood, D. Lutz & A.G.G.M. Tielens
ASTRONOMY & ASTROPHYSICS, 357, 898 (2000)

We have observed the central region of the nearby starburst galaxy NGC 4945 with the mid-infrared spectrometers SWS and PHT-S aboard ISO. We do not find any evidence for the existence of the powerful AGN, inferred from hard X-ray observations. The upper limits on our AGN tracers [Ne V]14.32 μm & 24.3 μm and [Ne VI] 7.65 μm imply an $A_V > 160$ towards the NLR, assuming the NLR to be of equal strength as in the Circinus galaxy. Other possibilities are discussed. The starburst excitation indicators [Ne III]15.56 μm /[Ne II]12.81 μm and $L_{\text{bol}}/L_{\text{LyC}}$ suggest that the starburst in the central region is at least 5×10^6 yrs old, and that it accounts for at least half of the nuclear bolometric luminosity. The starburst might well power the entire bolometric luminosity, but the available constraints are also consistent with an up to 50% contribution of the embedded AGN. With ISO-PHT-S, at a resolution of ≈ 90 , we detect strong absorption features of water ice, and, for the first time in an external galaxy, of CO₂ and CO. The same ISO-PHT-S spectrum also reveals strong emission from the family of PAH features. Finally, we have observed and detected several pure rotational and ro-vibrational H₂ lines, two of which, the (0–0) S(0) & S(1) lines, allow us to determine the excitation temperature (160 K) and warm H₂ mass ($2.4 \times 10^7 M_\odot$). The low excitation temperature shows Orion-like shocks not to be representative for the entire emission of the central region of the galaxy and fairly normal PDRs to be perhaps more typical.

3.1 Introduction

NGC 4945 is a nearby, large ($20' \times 4'$) spiral galaxy seen nearly edge on ($i \sim 78^\circ$; Ott 1995). At a recession velocity of 560 km/s it is at the mean radial velocity of the Centaurus group (Hesser et al. 1984), of which it is believed to be a member. Distance estimates vary between 3.5 and 4.0 Mpc (see Bergman et al. (1992) and Mauersberger et al. (1996) for discussions). In this paper we will adopt a distance of 3.9 Mpc (Bergman et al. 1992), which implies that 1'' is equivalent to 18 pc.

NGC 4945 is one of the brightest infrared galaxies in the sky: $S[12]=24$ Jy, $S[25]=43$ Jy, $S[60]=588$ Jy, $S[100]=1416$ Jy (Rice et al. 1988). The total infrared luminosity amounts to $L(8\text{--}1000\,\mu\text{m})=2.95 \times 10^{10} L_\odot$, $\sim 75\%$ of which originates in the central $12'' \times 9''$ (Brock et al. 1988).

Near infrared observations reveal the nuclear region to be the site of a powerful, yet visually obscured, starburst. Br γ (Moorwood et al. 1996b) and Pa α (Marconi et al. 2000) recombination line maps show the starburst to be concentrated in a circumnuclear disk or ring ~ 200 pc across (11''). Further evidence for (a period of) strong star formation comes from the discovery of a conical structure, roughly perpendicular to the galaxy major axis. It is believed to be a cavity, vacated by a starburst-driven superwind (Heckman et al. 1990; Moorwood et al. 1996b). The non-detection of [O III] within the cone and the absence of coronal lines excludes an AGN as the driver of the outflow.

Clear evidence for the presence of an AGN comes from hard X-ray observations (Iwasawa et al. 1993; Guainazzi et al. 2000). The AGN X-ray emission is however heavily absorbed by a column density of $10^{24.7}\,\text{cm}^{-2}$, which obscures the AGN at all optical and infrared wavelengths. Previous authors have attributed most of the IR luminosity to the starburst (e.g. Moorwood & Oliva 1994; Koornneef & Israel 1996). Hard X-ray observations with *BeppoSAX* indicate that the bolometric luminosity may as well be accounted for by the AGN alone (Guainazzi et al. 2000).

3 cm & 6 cm ATCA radio maps of the central region of NGC 4945 (Forbes & Norris 1998) are dominated by strong nuclear emission, and emission extended along the disc of the galaxy. There is also evidence for some filamentary structure associated with the cavity cleared by the starburst superwind. VLBI observations by Sadler et al. (1995) reveal the existence of a compact radio core. This, as well as the presence of H₂O megamasers in a Keplerian disc about a $\sim 10^6 M_\odot$ black hole (Greenhill et al. 1997), are taken as further evidence for the presence of an AGN.

Near infrared observations of molecular hydrogen emission in NGC 4945 have been reported by several authors over the last 15 years (e.g. Moorwood & Glass 1984; Moorwood & Oliva 1988; Koornneef 1993; Moorwood & Oliva 1994; Koornneef & Israel 1996; Moorwood et al. 1996b; Quillen et al. 1999; Marconi et al. 2000). While fluxes are known for eight ro-vibrational transitions accessible from the ground (Koornneef & Israel 1996), spatial information is available only for the (1–0) S(1) $2.1218\,\mu\text{m}$ line. These observations show the H₂ emission to be associated with the hollow cone, *not* with the starburst traced in hydrogen recombination emission. The absence of a correlation argues against photons as the source of excitation. Instead, the emission is attributed to shock heating of the molecular material at the face of the cavity (Moorwood et al. 1996b; Marconi et al. 2000).

Mid-infrared spectroscopy is much less affected by intervening extinction than the UV and optical equivalents, with $A(\lambda)/A_V$ less than 0.1. Observations of the central region of the

galaxy, using the mid-infrared spectrometer SWS (de Graauw et al. 1996) and the spectrophotometer PHT-S (Lemke et al. 1996), both aboard ISO (Kessler et al. 1996), are therefore very useful to study the nuclear components otherwise hidden by heavy extinction. In Sect. 3.3.1 we present the results of the search for high excitation emission from the AGN. In Sect. 3.3.2 we study the properties of the nuclear starburst. In Sect. 3.3.3 we discuss the dominant nuclear power source. Sect. 3.3.4 discusses the broad emission and absorption features, tracing the properties of the interstellar medium in and in front of the nucleus. Finally, in Sect. 3.3.5 we discuss the physical conditions and excitation of the warm molecular hydrogen.

3.2 Observations

As part of the Central Program “MPEXGAL”, we have observed the central region of NGC 4945 with the Short Wavelength Spectrometer (SWS) and the spectrophotometer PHT-S on board ISO.

3.2.1 SWS spectroscopy

ISO-SWS grating line profile scans (SWS02 mode) were obtained on 1996 February 6 for 28 spectral lines in the range of 2.42 to 40.34 μm . The spectral resolution in this range varies between $R=900$ and 2000, corresponding to a velocity resolution of 330–150 km/s. Aperture sizes used range between $14'' \times 20''$ and $20'' \times 33''$. ISO-SWS was centered on the 1.4GHz continuum peak from Ables et al. (1987), which coincides with the the position of the L-band peak of Moorwood et al. (1996b). At the time of observation the position angle of the major axis of the SWS apertures was 35.4° , 8° off from that of the galaxy major axis (43°).

The data reduction was performed using the SWS Interactive Analysis system (SIA; Lahuis et al. 1998; Weprecht et al. 1998), putting special emphasis on tools to improve cosmic ray spike removal, dark current subtraction and flat fielding. The wavelength calibration of ISO-SWS is discussed by Valentijn et al. (1996a). We used calibration files as of March 1999. The accuracy of the flux calibration is estimated to be 30% (Schaeidt et al. 1996). The resulting spectra are shown in Fig. 3.1.

In total 17 spectral lines were detected. For another 11 lines we derived upper limits, using gaussian profiles of width equal to other lines of the same (or comparable) species, scaled to a peak height corresponding to approximately 3σ of the noise. Both detections and upper limits are presented in Table 3.1.

3.2.2 PHT-S spectrophotometry

We have obtained two low resolution ($\lambda/\Delta\lambda \sim 90$) ISO-PHT-S spectra, on 1996 October 12 and 1997 August 3, respectively. ISO-PHT-S comprises two low-resolution grating spectrometers covering simultaneously the wavelength range 2.47 to 4.87 μm and 5.84 to 11.62 μm . The spectrum is registered by two linear arrays of 64 Si:Ga detectors with a common entrance aperture of $24'' \times 24''$. The measurements were carried out in rectangular chopped mode, using a chopper throw of $180''$. The resulting spectra thus are free of contributions from zodiacal light, that would otherwise affect the spectrum. The pure on-source integration times were 512 and 1024 s.

The ISO-PHT-S data were reduced using PIA¹ (Gabriel et al. 1997) version 8.1. Steps

¹PIA is a joint development by the ESA Astrophysics Division and the ISO-PHT Consortium

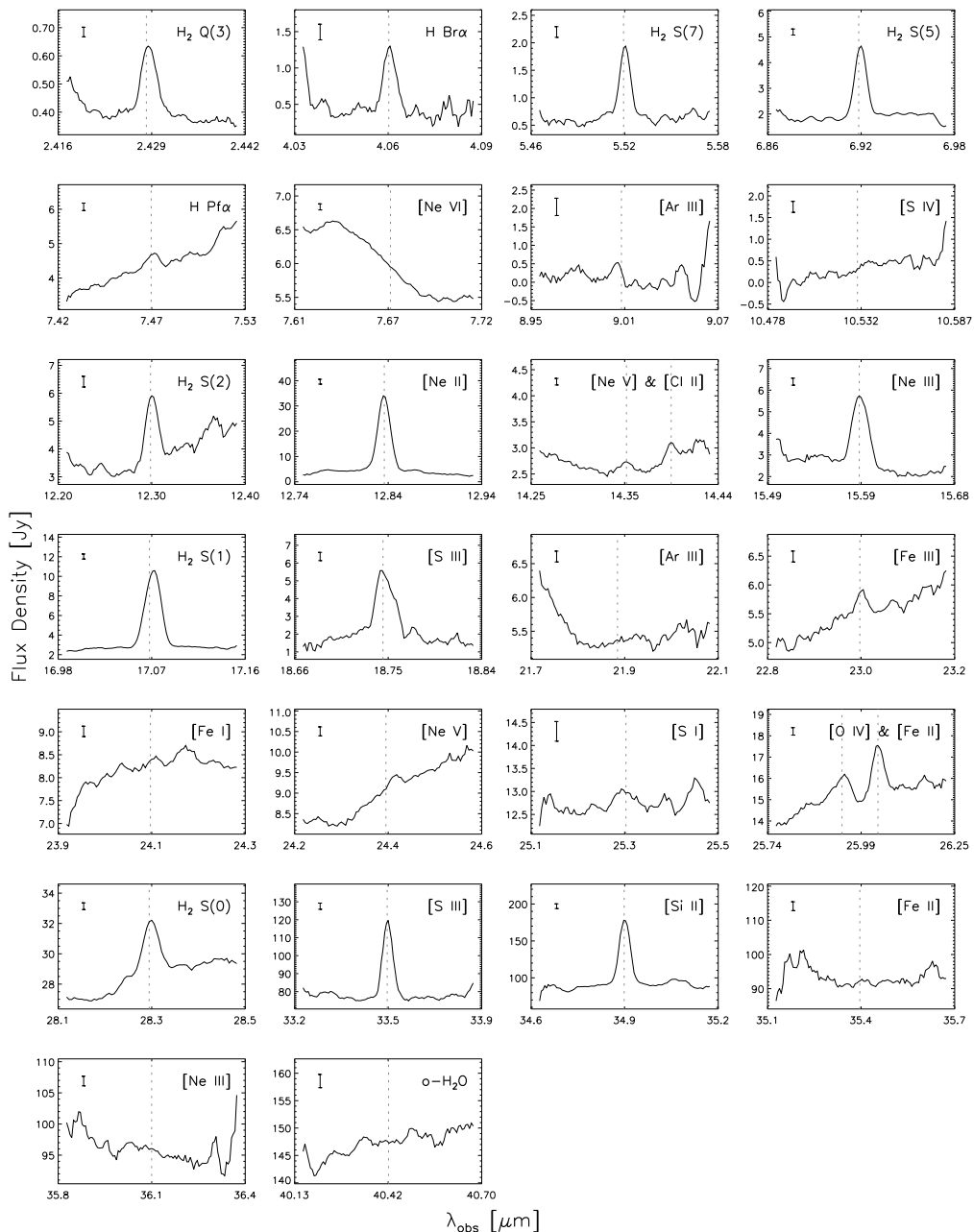


FIGURE 3.1 — SWS line spectra of NGC 4945. Typical $\pm 1\sigma$ error bars are marked. Note that noise increases towards the edges of scans

TABLE 3.1 — NGC 4945 results from SWS observations

Identification	λ_{rest} [μm]	F_{obs} [W/cm 2]	Aperture ["' \times "']
H ₂ (1–0) Q(3)	2.424	$3.20 \cdot 10^{-20}$	14×20
H I Br α	4.052	$7.79 \cdot 10^{-20}$	14×20
H ₂ (0–0) S(7)	5.510	$1.11 \cdot 10^{-19}$	14×20
H ₂ (0–0) S(5)	6.909	$1.54 \cdot 10^{-19}$	14×20
H I Pf α	7.460	$1.95 \cdot 10^{-20}$	14×20
[Ne VI]	7.652	<7.3 10 $^{-21}$	14×20
[Ar III]	8.991	<2.3 10 $^{-20}$	14×20
[S IV]	10.511	<8.8 10 $^{-21}$	14×20
H ₂ (0–0) S(2)	12.279	$7.45 \cdot 10^{-20}$	14×27
[Ne II]	12.814	$8.68 \cdot 10^{-19}$	14×27
[Ne V]	14.322	<7.0 10 $^{-21}$	14×27
[Cl II]	14.368	$5.19 \cdot 10^{-21}$	14×27
[Ne III]	15.555	$7.51 \cdot 10^{-20}$	14×27
H ₂ (0–0) S(1)	17.035	$1.51 \cdot 10^{-19}$	14×27
[S III]	18.713	$6.88 \cdot 10^{-20}$	14×27
[Ar III]	21.829	<5.1 10 $^{-21}$	14×27
[Fe III]	22.925	$6.46 \cdot 10^{-21}$	14×27
[Fe I]	24.042	<5.4 10 $^{-21}$	14×27
[Ne V]	24.318	<5.5 10 $^{-21}$	14×27
[S I]	25.257	<1.4 10 $^{-20}$	14×27
[O IV]	25.890	$3.00 \cdot 10^{-20}$	14×27
[Fe II]	25.988	$4.11 \cdot 10^{-20}$	14×27
H ₂ (0–0) S(0)	28.221	$4.82 \cdot 10^{-20}$	20×27
[S III]	33.481	$4.87 \cdot 10^{-19}$	20×33
[Si II]	34.815	$9.66 \cdot 10^{-19}$	20×33
[Fe II]	35.349	<2.8 10 $^{-20}$	20×33
[Ne III]	36.014	<1.6 10 $^{-20}$	20×33
o-H ₂ O	40.341	<2.8 10 $^{-20}$	20×33

in the data reduction included: 1) deglitching on ramp level. 2) subdivision of ramps in two sections of 32 non destructive read-outs. 3) ramp fitting to derive signals. 4) masking of bad signals by eye-inspection. 5) kappa sigma and min/max clipping on remaining signal distribution. 6) determination of average signal per chopper plateau. 7) masking or correction of bad plateaux by eye-inspection. 8) background subtraction using all but the first four plateaux. 9) finally, flux calibration, using the signal dependent spectral response function of Acosta-Pulido (1999). This spectral response function avoids some deficiencies of the previous PIA response function, in particular in the 3 μm region near the “ice” feature. The absolute calibration is accurate to within 20%.

The two resulting spectra were obtained at slightly different position angles about the

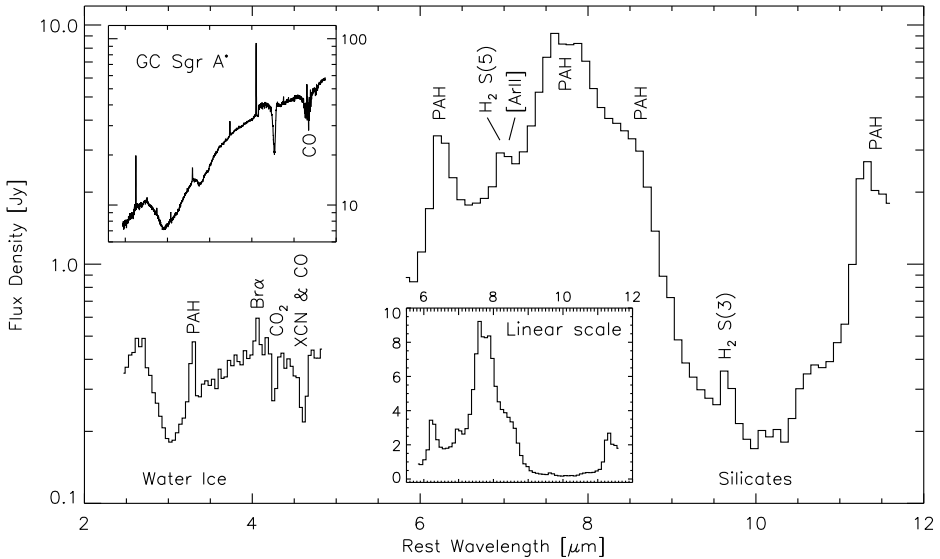


FIGURE 3.2 — The average ISO–PHT–S spectrum of NGC 4945. **Upper inset:** comparison with the ISO–SWS spectrum of the line of sight towards the Galactic center. **Lower inset:** the ISO–PHT–SL spectrum in linear flux scale

nucleus. For the first, the square aperture was aligned with the galaxy major axis (45°). For the second, the position angle was 31.1° . Fig. 3.2 shows the averaged ISO–PHT–S spectrum. The on-source integration times were used as weight factors in the computation of the average spectrum.

A number of emission lines can be identified in the ISO–PHT–S spectrum. These include $9.66\text{ }\mu\text{m}$ H_2 (0–0) S(3), the unresolved blend of $6.99\text{ }\mu\text{m}$ [Ar II] and $6.91\text{ }\mu\text{m}$ H_2 (0–0) S(5), and $4.05\text{ }\mu\text{m}$ $\text{H}\alpha$ Br α . For the $9.66\text{ }\mu\text{m}$ H_2 (0–0) S(3) line, not included in the SWS02 line scans, we measure a flux of $5.4 \times 10^{-20} \text{ W/cm}^2$, with an uncertainty of 30%.

3.3 Results

3.3.1 AGN not seen at mid-infrared wavelengths

NGC 4945 is a peculiar and interesting target for studying the relation of AGN and star formation in galaxies. Clear evidence for hidden AGN activity comes from hard X-ray observations. NGC 4945 is amongst the brightest hard X-ray emitting galaxies and exhibits variability of its 13–200keV flux on timescales of ~ 10 hrs, which clearly establishes its AGN origin (Iwasawa et al. 1993; Guainazzi et al. 2000; Marconi et al. 2000). The AGN X-ray emission is heavily absorbed by a column density of $10^{24.7} \text{ cm}^{-2}$ (corresponding to $A_V \sim 2600$), a high value, but within the range observed for Seyfert 2 galaxies (e.g. Risaliti et al. 1999). In unified schemes, the X-ray obscuration measures a line of sight towards the very center. Obscuration

towards the NLR probes a different line of sight and is usually significantly lower, making the NLR visible in Seyfert 2 galaxies.

Mid-infrared high excitation lines are able to penetrate a far larger dust obscuration than their optical and UV counterparts. They are therefore ideally suited as tracers of embedded AGN activity. Mid-infrared emission lines like [Ne V] $14.32\text{ }\mu\text{m}$ & $24.32\text{ }\mu\text{m}$, [Ne VI] $7.65\text{ }\mu\text{m}$ and [O IV] $25.9\text{ }\mu\text{m}$ are prominently present in the spectra of all Seyferts observed with ISO (Moorwood et al. 1996a; Genzel et al. 1998). On the other hand, the same emission lines are also weakly visible towards, for instance, supernova remnant RCW 103 (Oliva et al. 1999). [O IV] emission (at the few percent level compared to [Ne II]) has also been detected in a sample of starburst galaxies (Lutz et al. 1998), again at a level much weaker than seen in typical AGNs. The origin of the weak level emission in these sources is believed to be shocks. A detection of any of the high excitation lines discussed above does therefore not automatically imply the detection of an AGN in NGC 4945.

We do not detect the lines of [Ne V] and [Ne VI]. No trace of [Ne VI] is seen in the wing of the nearby PAH emission feature (Fig. 3.1). From Fig. 3.1 it might appear that the two [Ne V] lines were indeed detected. However, at the level at which the features appear, instrumental effects play a significant role. In the $14.35\text{ }\mu\text{m}$ line scan a strong fringe in the relative spectral response function coincides *exactly* with the expected position for the [Ne V] line. Depending on the size of the emitting area, the feature may be entirely attributed to this instrumental effect. We therefore chose to state an upper limit for the $14.32\text{ }\mu\text{m}$ [Ne V] line. The feature seen in the other [Ne V] scan, centered at $24.4\text{ }\mu\text{m}$, was registered by only two detectors, although 12 detectors scanned over the central wavelength. As visible in Fig. 3.1, the feature is redshifted with respect to the NGC 4945 systemic velocity. This shift is not observed for any other line we observed. We therefore derive an upper limit for this [Ne V] line too.

The only detected high ionization line in NGC 4945 is the $25.9\text{ }\mu\text{m}$ [O IV] line. An AGN contribution to this line is possible — to match the limits on higher excitation lines, only part of the [O IV] emission would be related to an AGN. The detection of possibly shock-related [O IV] in many starbursts (Lutz et al. 1998) cautions, however, that this may be a more plausible origin of [O IV] in NGC 4945. The ratio of 0.033 with respect to $[\text{Ne II}]+0.44\times[\text{Ne III}]$ is above average, but well within the range observed for the Lutz et al. (1998) starbursts, also considering that the high extinction (Sect. 3.3.2) will increase the observed ratio relative to the intrinsic one. A population of Wolf-Rayet stars as origin of the [O IV] emission seems unlikely. Lutz et al. (1998) have shown that the [O IV] emission would have to originate in widely dispersed small H II regions and would have to be relatively strong. [O IV] emission at this level has not been observed in local star forming regions. A conservative analysis will hence not attribute the [O IV] emission in NGC 4945 to the AGN nor to a population of Wolf-Rayet stars.

The limits on high excitation AGN tracers are consistent with several scenarios, or perhaps more likely a combination of them:

- **The Narrow Line Region is extremely obscured even in the mid-IR.** We derive an $A_V \geq 160$ ($A(7.65\text{ }\mu\text{m})=A(14.3\text{ }\mu\text{m})=A(24.3\text{ }\mu\text{m}) \geq 4.3$) to the NLR from a comparison of Circinus and NGC 4945 [Ne V] and [Ne VI] line strengths, under the assumption that the galaxies' NLRs are similar. The choice for Circinus is motivated in Table 3.2.
- **UV photons from the AGN are absorbed close to the nucleus along all lines of sight**

TABLE 3.2 — In X-ray properties NGC 4945 is very similar to Circinus. However, infrared indicators for a narrow line region are missing in NGC 4945

	NGC 4945	Circinus
Distance [Mpc]	3.9	4 ^a
H col. dens. to AGN [cm ⁻²]	5×10^{24}	4×10^{24} ^b
A _V to AGN	2600	2100
L(2–10keV) [L _⊙]	78×10^7 ^c	$8.8\text{--}44 \times 10^7$ ^b
$\nu L_{\nu}(100\text{keV})/L_{\text{FIR}}$	0.003 ^d	0.002 ^d
L(8–1000 μm) [L _⊙]	2.2×10^{10}	1.2×10^{10} ^a
[Ne V]14.3 μm [W/cm ²]	$<7.0 \times 10^{-21}$	440×10^{-21} ^e
[Ne V]24.3 μm [W/cm ²]	$<5.5 \times 10^{-21}$	244×10^{-21} ^e
[Ne VI]7.65 μm [W/cm ²]	$<7.3 \times 10^{-21}$	413×10^{-21} ^e

(^a) Siebenmorgen et al. (1997); (^b) Matt et al. (1999); (^c) Guainazzi et al. (2000)

(^d) Marconi et al. (2000); (^e) Moorwood et al. (1996a)

- **The extreme ultraviolet luminosity of the AGN is lower than in Circinus.** In comparison to the Circinus SED, this would imply a large deficiency in UV relative to X-ray flux (Table 3.2).

3.3.2 Starburst properties

Near-infrared broad-band and emission-line imaging has revealed the nucleus of NGC 4945 to be the site of a sizeable starburst, the presence of which is illustrated by the conically shaped starburst superwind-blown cavity traced at many near-infrared wavelengths (Moorwood et al. 1996b; Marconi et al. 2000). Hampered by the large extinction even in the near-infrared, age estimates for the nuclear starburst are sparse and intrinsically uncertain. ISO-SWS offers the possibility for the first time to observe the mid-infrared line ratio [Ne III] 15.56 μm / [Ne II] 12.81 μm. This ratio, which is much less affected by extinction than visible and UV lines, is sensitive to the hardness of the stellar radiation field and hence is a good indicator for the age of the nuclear starburst. We observed the two lines in the same ISO-SWS aperture, which was centered on the nucleus (see Table 3.1).

To estimate the extinction to the NGC 4945 nuclear starburst we use the ratio of the 18.71 μm to the 33.48 μm [S III] line. This ratio is commonly used as a density diagnostic for the density range $10^{2.5}\text{--}10^{4.5}$ cm⁻³ and is only mildly dependent on the temperature of the emitting gas. Assuming a typical starburst gas density of 300 cm⁻³ (Kunze et al. 1996; Rigopoulou et al. 1996), the intrinsic ratio should be ~ 0.43 (i.e. the value in the low density limit, computed using the collision strengths of Tayal & Gupta (1999)). The observed ratio is far lower: 0.14 ± 0.06 . We hence deduce a screen extinction of A(18.7 μm)= $1.7^{+0.8}_{-0.5}$, which, using the Galactic center extinction law of Draine (1989), amounts to A_V= 36^{+18}_{-11} . As the 18.71 μm [S III] line was measured in a 14''×27'' aperture and the 33.48 μm [S III] line in a 20''×33'' aperture, the observed [S III] ratio may be a lower limit and the derived extinction an upperlimit in case the [S III] emitting area is larger than 14''×27''.

Another independent estimate of the extinction is usually obtained from hydrogen recom-

bination line strengths, assuming ‘case-B’ conditions and standard extinction properties. The NGC 4945 data set contains two H I lines: $4.05\text{ }\mu\text{m Br}\alpha$ and $7.46\text{ }\mu\text{m Pf}\alpha$, both measured in the same aperture. The ratio of these two lines is $\text{Pf}\alpha/\text{Br}\alpha=0.25\pm0.10$. ‘Case-B’ recombination theory predicts a ratio of 0.32. The extinction at $7.46\text{ }\mu\text{m}$ must therefore be similar or slightly *larger* than at $4.05\text{ }\mu\text{m}$. This indicates that the grain composition is unusual and probably more similar to the composition found in the line of sight towards the Galactic center (Lutz et al. 1996; Lutz 1999) than found towards other parts of our Galaxy (Bertoldi et al. 1999; Martín-Hernández et al. 2003). An extinction towards the NGC 4945 nuclear starburst can therefore at present not be derived from lines in the $4\text{--}8\text{ }\mu\text{m}$ range.

The extinction derived for the nuclear starburst ($A_V=36$) is somewhat larger than the value we derive for the warm molecular hydrogen ($A_V=20$; see Sect. 3.3.5). This indicates that the warm molecular hydrogen and nuclear starburst emission are coming from different nuclear components, the latter possibly more enshrouded than the former. With the unusual grain composition in mind, it is striking how well the Galactic center extinction law fits our molecular hydrogen data, resulting in a smooth excitation diagram, even for the H₂ (0–0) S(3) line in the center of the $9.7\text{ }\mu\text{m}$ silicate feature (see Sect. 3.3.5). We are therefore confident that the extinction correction for the starburst, derived using the [S III] ratio, is also useful.

In order to determine the excitation of the nuclear starburst we apply the extinction correction derived from the [S III] ratio to the observed [Ne III]/[Ne II] ratio. The extinction corrections amount to $A(12.8\text{ }\mu\text{m})=1.51$ and $A(15.6\text{ }\mu\text{m})=1.19$. The extinction corrected [Ne III]/[Ne II] ratio is $0.064^{+0.037}_{-0.032}$. Thornley et al. (2000) list observed [Ne III]/[Ne II] ratios for 26 starburst galaxies, all measured in the same ISO–SWS configuration. Clearly, NGC 4945 is among the lowest excitation targets in their sample. Note that the ISO–SWS aperture used is large compared to the typical size scales in starbursts. The ratios listed by Thornley et al. (2000) should therefore be regarded as aperture averaged.

For starburst galaxies $L_{\text{bol}}/L_{\text{LyC}}$ is another measure of the excitation of star clusters. Depending on the upper mass cut-off, the star formation decay time scale and the age of the clusters, Thornley et al. (2000) modeled $L_{\text{bol}}/L_{\text{LyC}}$ to lie between 3 and 200. The measured values for starburst galaxies range between 3 and 50. Below we will determine $L_{\text{bol}}/L_{\text{LyC}}$ for the NGC 4945 nuclear starburst. We assume $L_{\text{bol}}=L_{\text{IR}}$ (i.e. *no* AGN contribution to L_{IR}) and estimate L_{LyC} from the dereddened $4.05\text{ }\mu\text{m Br}\alpha$ flux. For $A(4.05\text{ }\mu\text{m})=1.2$ (applying the Galactic center law of Draine (1989) for $A_V=36^{+18}_{-11}$) and $L_{\text{LyC}}=670\text{ L}_{\text{Br}\alpha}$ we find $L_{\text{LyC}}=8^{+9}_{-4}\times10^8\text{ L}_\odot$ and $L_{\text{bol}}/L_{\text{LyC}}=28^{+26}_{-15}$. Using the $12.81\text{ }\mu\text{m}$ [Ne II] line and the empirical scaling $L_{\text{LyC}}=64\text{ L}_{\text{Ne II}}$ (Genzel et al. 1998) a similar result is obtained.

Given the variety of possible star forming histories, it is hard to constrain the age of the nuclear starburst (assuming *no* AGN contribution to L_{IR}). However, both excitation diagnostics agree on a low excitation which suggests an evolved burst with an age in excess of 5×10^6 years, but would also be consistent with a low IMF upper mass cut-off.

Marconi et al. (2000) show that it is possible to construct starburst models which are consistent with their near-infrared observations of NGC 4945, but differ by the total luminosity generated (their Fig. 4). An instantaneous burst would not leave space in the energy budget for a sizable contribution from the hidden AGN, whereas a combination of instantaneous burst and constant star formation would. We would like to point out here that the latter model would be inconsistent with the low [Ne III]/[Ne II] ratio observed by us. Only their instantaneous burst is in agreement with both the near-infrared and mid-infrared observations.

3.3.3 What powers the nucleus of NGC 4945?

The large extinction towards the nuclear starburst and the AGN buried within, makes it very difficult to assess the contributions of either component to the nuclear bolometric luminosity. The optical, near-infrared, mid-infrared and far-infrared spectra of NGC 4945 are entirely consistent with a starburst-like nature: BLR or NLR high-excitation lines are absent; the starburst excitation indicator $[\text{Ne III}]/[\text{Ne II}]$ has a starburst-like value; the ratios of $6\ \mu\text{m}$ (ISO-PHT-S), S12 or S25 to S60 or S100 fluxes are all very low and consistent with emission from cold dust only. Furthermore, the ratio $L_{\text{bol}}/L_{\text{lyc}}=28^{+26}_{-15}$, is perfectly consistent with the low excitation of the starburst as deduced from $[\text{Ne III}]/[\text{Ne II}]$. And last, NGC 4945 lies on the radio-far-infrared correlation for starburst galaxies (Forbes & Norris 1998). Hence, the starburst might well account for the the entire observed bolometric luminosity.

On the other hand, Guainazzi et al. (2000), who have observed the AGN in NGC 4945 in hard X-rays, compute the AGN to be able to account for all the bolometric luminosity observed, *if* it has a typical quasar $L_{\text{X}}/L_{\text{bol}}$ ratio. Since there is no such thing as a template AGN spectrum, the conversion factor applied, $L_{1-10\text{keV}}/L_{\text{bol}} \sim 0.05$ (Elvis et al. 1994), may have an uncertainty which could easily allow for the NGC 4945 starburst to dominate the bolometric luminosity instead.

The same uncertainties surround the accretion rate of the $\sim 1.6 \times 10^6 M_{\odot}$ black hole inferred from H₂O maser observations (Greenhill et al. 1997). A high but not implausible rate of 50% of the Eddington rate ($L_{\text{Edd}} \sim 4.1 \times 10^{10} L_{\odot}$) would suffice to power the observed bolometric luminosity. Given the wide range of efficiencies inferred for Seyferts, this information does not add anything to identify the dominant power source.

In this complex situation with two potentially dominant power sources, the most significant constraint on their relative weight is the total $L_{\text{bol}}/L_{\text{lyc}}$ ratio and its implications on the $L_{\text{bol}}/L_{\text{lyc}}$ of the *starburst* component. $L_{\text{lyc}}^{\text{sb}}$ is directly constrained by observations, but $L_{\text{bol}}^{\text{sb}}$ changes for different assumptions on the starburst and AGN contributions to the total bolometric luminosity. If there is a significant AGN contribution, $(L_{\text{bol}}/L_{\text{lyc}})_{\text{sb}}$ will be less than the global value of 28. Values as low as ~ 3 which are possible for a zero age massive star population with Salpeter IMF (e.g. Leitherer & Heckman 1995) are strongly inconsistent with the low excitation observed in NGC 4945. Thornley et al. (2000) model $[\text{Ne III}]/[\text{Ne II}]$ and $L_{\text{bol}}/L_{\text{lyc}}$ ratios of starbursts, taking into account clusters of different ages within the ISO-SWS aperture. An evolving starburst with $[\text{Ne III}]/[\text{Ne II}] = 0.064$ as in NGC 4945 must have a $L_{\text{bol}}/L_{\text{lyc}} \geq 15$ (their Fig. 8). This limit simply reflects the higher $L_{\text{bol}}/L_{\text{lyc}}$ of later type O stars and persists if the low excitation is due to an upper mass cut-off rather than evolution. With a lower limit of ~ 15 on $(L_{\text{bol}}/L_{\text{lyc}})_{\text{sb}}$, the starburst contribution to the bolometric luminosity must be at least $\sim 50\%$.

We hence conclude that the AGN in NGC 4945 plays a secondary although most likely not insignificant role in the energetics of this nearby galaxy. Extremely small values for the AGN contribution to the bolometric luminosity would imply an unrealistically high ratio of $L_{\text{X}}/L_{\text{bol}}$ for the AGN. The very low inferred black hole mass, the very cold mid-infrared to far-infrared colors, and the absence of any clear line of sight towards the AGN, support our view that starburst activity dominates AGN activity in NGC 4945.

TABLE 3.3 — Column densities of solid state features towards the nucleus of NGC 4945 and towards the Galactic center (SgrA^{*}). In order to derive the column densities we integrated $\int \tau_{\nu} d\nu$ over the width of the band and divided the result by the bandstrength A. N_H was determined from N_H= 1.9×10^{21} A_V, where A_V=30 for SgrA^{*} and A_V=36 for NGC 4945

Species	λ_{rest} [μm]	A [cm/mol.]	τ_{center}		N		N/N _H	
			NGC 4945	Sgr A [*]	NGC 4945 [mol./cm ²]	Sgr A [*]	NGC 4945	Sgr A [*]
H ₂ O	3.09	2×10^{-16} ^a	0.9	0.50 ^b	2.4×10^{18}	1.3×10^{18} ^b	3.5×10^{-5}	2.3×10^{-5}
CO ₂	4.27	7.4×10^{-17} ^c	0.8 ^d	0.72 ^e	2.0×10^{17}	1.7×10^{17} ^e	2.9×10^{-6}	3.0×10^{-6}
XCN	4.60	—	—	—	—	—	—	—

(^a) Hagen & Tielens (1981); (^b) Chiar et al. (2000); (^c) Gerakines et al. (1995)

(^d) Determined by fitting a Gaussian profile followed by rebinning to the ISO-PHT-S instrument resolution

(^e) Gerakines et al. (1999)

3.3.4 Emission and absorption features

The infrared spectrum of the central region of NGC 4945 obtained with ISO-PHT-S (see Fig. 3.2) presents a new view of the ISM in starburst galaxies. Even at the low spectral resolving power of R≈90 the spectrum is dominated by a wealth of emission and absorption features.

Especially prominent is the family of PAH emission features at 3.3, 6.2, 7.7, 8.6 and 11.3 μm , which ISO confirmed to be common-place in most galactic and extragalactic ISM spectra (e.g. Acosta-Pulido et al. 1996; Rigopoulou et al. 1999; Mattila et al. 1999; Clavel et al. 2000). Nevertheless, the weakness of the 8.6 and 11.3 μm PAH bands in NGC 4945 is unusual. Consistent with A_V≈36 and with the strength of the absorption features discussed below, we explain this weakness by heavy extinction, which will suppress these two features placed in the wings of the silicate absorption feature.

Perhaps the most important result, however, is the rich absorption spectrum, indicating that we are observing the infrared sources in the central region of NGC 4945 through a medium containing molecular ices. Interstellar absorptions of 4.27 μm (2343cm⁻¹) solid CO₂ and 4.68–4.67 μm ‘XCN’+CO are detected, the first time in an extragalactic source to our knowledge. At our resolving power and signal-to-noise we cannot determine the contribution of 4.62 μm (2165cm⁻¹) XCN, 4.67 μm (2140cm⁻¹) CO ice and of gaseous CO absorptions to the 4.58–4.67 μm absorption complex. The strength of the XCN absorption appears to be remarkable, suggestive of ice grain processing in an energetic environment (Lacy et al. 1984). We defer a more detailed analysis of the XCN/CO feature to a future paper, which will also include the results of follow-up observations with ISAAC at the VLT (Chapter 4). A strong silicate feature is observed around 9.7 μm (see also Moorwood & Glass 1984). A deep minimum is also detected around 3.0 μm , which is suggestive of water ice (or more precise, the O-H stretch) absorption. Table 3.3 gives column densities for some of the absorption features discussed above. The presence and strength of these absorption features is consistent with the high starburst obscuration derived from the emission lines (but see also Chiar et al. (2000) for variations in the strength of features along lines of sight of similar A_V).

At the resolution of ISO-PHT-S the molecular absorption features in NGC 4945 show striking similarities with the features seen in the ISO-SWS spectrum of the line of sight towards the Galactic center (see Fig. 3.2; Lutz et al. 1996). Observations at our spectral res-

olution do, however, not permit a detailed comparison. Regarding the $4.26\text{ }\mu\text{m}$ CO₂ feature it is likely that the feature can be attributed to solid state CO₂, since high spectral resolution ISO-SWS observations of other sources indicate that the contribution of gaseous CO₂ to the observed feature is very small (see in particular van Dishoeck et al. 1996). In the $4.6\text{--}4.8\text{ }\mu\text{m}$ region, the spectra of NGC 4945 and the Galactic center differ more strongly, and a more careful inspection is required to assess the contributions of gaseous and solid CO and XCN. ISO-SWS spectroscopy of the Galactic center (Lutz et al. 1996) clearly shows that what we see at low resolution as a relatively shallow and broad feature is in fact dominated by individual lines of gaseous CO. Contributions of a potential underlying solid CO/XCN component are possible but difficult to separate until our high resolution follow-up observations have been executed.

3.3.5 Molecular hydrogen: physical conditions, excitation and mass

Near infrared observations of molecular hydrogen emission in NGC 4945 have been reported by several authors over the last 15 years. The most complete set of observations is published by Koornneef & Israel (1996), who observed 8 ro-vibrational transitions with IRSPEC at the ESO NTT. With ISO-SWS and ISO-PHT-S we have extended the number of observed lines from 8 to 14 by observing the pure rotational transitions S(0), S(1), S(2), S(3), S(5) and S(7) as well as the (1–0) Q(3) line. The latter was also observed with IRSPEC and can therefore be used to determine the proper aperture correction factor for the IRSPEC data set. An overview of the observed lines is presented in Table 3.4.

Information on the spatial extent of the H₂ emitting region is only available for the $2.12\text{ }\mu\text{m}$ (1–0) S(1) line (Koornneef & Israel 1996; Moorwood et al. 1996b; Quillen et al. 1999; Marconi et al. 2000). Based on Fig. 3a of Moorwood et al. (1996b) we estimate that more than 90% of the (1–0) S(1) emission fits within the smallest ISO-SWS aperture ($14''\times20''$). It is not unreasonable to expect the H₂ emitting area to increase with decreasing H₂ temperature. The aperture sizes used to observe the respective H₂ transitions increase with increasing sensitivity to lower temperature H₂. Based on this, we will assume in what follows that ISO-SWS and ISO-PHT-S have observed all available warm H₂. Further to this, all three instruments were centered on the same nuclear position and viewed the nuclear region under more or less similar position angles (see Sect. 3.2). We will use the ratio of the 1–0 Q(3) line fluxes measured by ISO-SWS and IRSPEC to scale the other IRSPEC lines to the ISO-SWS aperture size. This ratio is 2.33.

From the 14 transitions observed it is possible to compute the upper level populations for 12 levels. We assumed the H₂ levels to be optically thin. The excitation diagram in Fig. 3.3 shows a plot of the natural logarithm of the total number of H₂ molecules (N_u), divided by the statistical weight (g_u), in the upper level of each transition detected, versus the energy of that level (E_u/k). The plot shows the situation after extinction correction (see below).

The excitation temperature (T_{ex}) of the gas is the reciprocal of the slope of the excitation diagram. If the warm H₂ is in LTE, the excitation temperature directly corresponds to the kinetic temperature. As is clearly visible from Fig. 3.3, (extinction corrected; see below) the excitation temperature increases monotonically with upper level energy, from 160 K for the combination of (0–0) S(0) & S(1) to 2200 K for the ro-vibrational lines.

In a highly obscured galaxy like NGC 4945, extinction corrections to the H₂ emission will be important. The extinction can be estimated from the H₂ data themselves taking into account that any known excitation mechanism should produce a “smooth” excitation diagram

TABLE 3.4— NGC 4945 molecular hydrogen data. $A(\lambda)$ is the extinction correction in magnitudes; A_{ul} is the Einstein coefficient for the transition from level u to level l . T_u is the upper level energy of level u ; g_u is the statistical weight of level u ; $N_u(\nu, J)$ is the number of H₂ molecules in upper level u

Identification	λ_{rest} [μm]	$F_{\text{obs}}^{\text{a}}$ [W/cm ²]	Instrument	Aperture ["' × "']	$A(\lambda)^{\text{b}}$	A_{ul} [1/s]	T_u [K]	g_u	$N_u(\nu, J)/g_u^{\text{c}}$
0-0 S(0)	28.2207	4.82×10^{-20}	SWS	20×27	0.44	2.94×10^{-11}	510	5	1.27×10^{62}
0-0 S(1)	17.0346	1.51×10^{-19}	SWS	14×27	0.84	4.76×10^{-10}	1015	21	5.13×10^{60}
0-0 S(2)	12.2785	7.45×10^{-20}	SWS	14×27	1.04	2.76×10^{-9}	1682	9	8.79×10^{59}
0-0 S(3)	9.6649	5.43×10^{-20}	PHT-S	24×24	2.34	9.84×10^{-9}	2504	33	1.28×10^{59}
0-0 S(5)	6.9091	1.54×10^{-19}	SWS	14×20	0.27	5.88×10^{-8}	4587	45	4.74×10^{57}
1-0 Q(1)	2.4066	1.48×10^{-20}	IRSPEC	6×6	1.72	4.29×10^{-7}	6150	9	9.69×10^{56}
1-0 Q(2)	2.4134	5.1×10^{-21}	IRSPEC	6×6	1.71	3.03×10^{-7}	6471	5	8.47×10^{56}
1-0 S(0)	2.2235	4.4×10^{-21}	IRSPEC	6×6	1.98	2.53×10^{-7}	6471	5	1.03×10^{57}
1-0 Q(3)	2.4237	3.20×10^{-20}	SWS	14×20	1.70	2.78×10^{-7}	6951	21	5.82×10^{56}
1-0 Q(3)	2.4237	1.36×10^{-20}	IRSPEC	6×6	1.70	2.78×10^{-7}	6951	21	5.82×10^{56}
1-0 S(1)	2.1218	1.29×10^{-20}	IRSPEC	6×6	2.15	3.47×10^{-7}	6951	21	5.84×10^{56}
0-0 S(7)	5.5103	1.11×10^{-19}	SWS	14×20	0.40	2.00×10^{-7}	7197	57	7.13×10^{56}
1-0 Q(4)	2.4375	2.2×10^{-21}	IRSPEC	6×6	1.68	2.65×10^{-7}	7584	9	2.28×10^{56}
2-1 S(1)	2.2477	2.3×10^{-21}	IRSPEC	6×6	1.94	4.98×10^{-7}	12550	21	6.36×10^{55}
2-1 S(2)	2.1542	0.6×10^{-21}	IRSPEC	6×6	2.09	5.60×10^{-7}	13150	9	3.79×10^{55}

(^a) Before aperture correction. (^b)Extinction law 'A' & $A_V=20$ (see text).

(^c)After aperture correction (IRSPEC data only) and extinction correction. Adopted distance D=3.9Mpc.

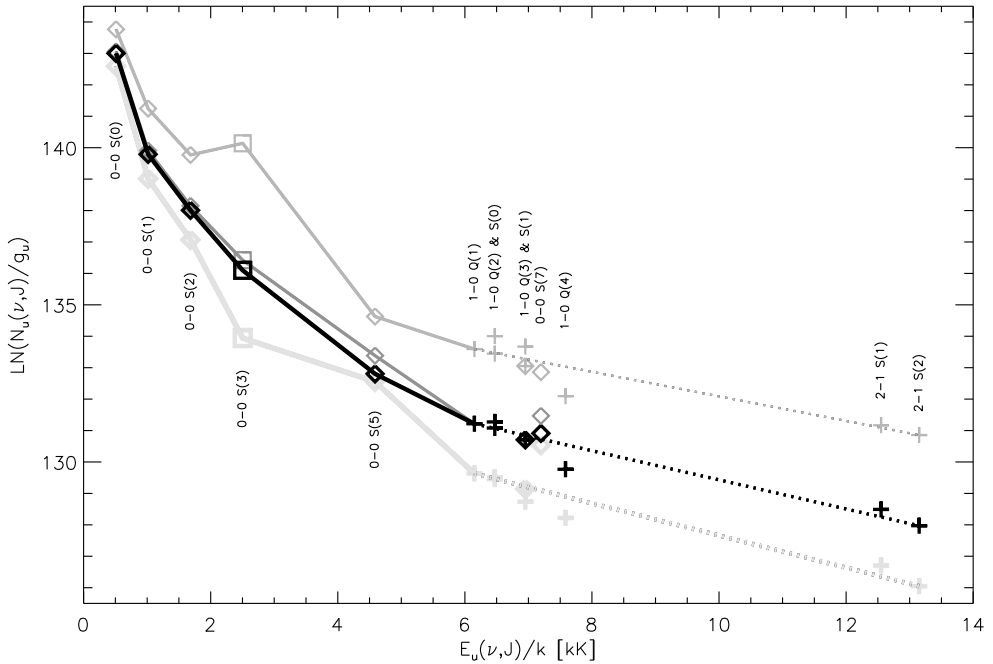


FIGURE 3.3 — Excitation diagram for molecular hydrogen in NGC 4945. Different symbols are used to distinguish different instrumental origin: *diamond*: ISO-SWS; *square*: ISO-PHT-S; and *cross*: IRSPEC. Results are shown for four different dereddening schemes, marked by different shades of grey. *Light-grey* denotes no extinction correction, *middle-grey* denotes the combination extinction law ‘B’ & $A_V=50$, *dark-grey* denotes extinction law ‘B’ & $A_V=20$ and *black* extinction law ‘A’ & $A_V=20$

for the pure rotational lines, and that transitions originating in a common upper level should give consistent results. More specifically, we use three criteria:

- The excitation temperature should increase monotonically from the lowest to the highest energy levels. This sets limits on the extinction correction for the (0–0) S(3) line in the center of the 9.7 μm silicate absorption feature.
- The ratio of the (1–0) Q(3) & (1–0) S(1) lines at 2.42 & 2.12 μm should be its intrinsic ratio determined by molecular constants only. The same applies to the (1–0) Q(2) & (1–0) S(0) lines at 2.41 & 2.22 μm , that originate from identical upper levels too.
- In LTE, the upper level populations normalized by the statistical weights should be similar for the 0–0 S(7) & 1–0 Q(3) lines at 5.51 & 2.42 μm , which differ by only 4% in upper level energy.

We have varied the extinction and tried several extinction laws. We present the most applicable extinction laws here:

- Law A: $A(\lambda) \propto \lambda^{-1.75}$ for $\lambda < 8 \mu\text{m}$. For $\lambda > 8 \mu\text{m}$ we took the Galactic center law of Draine (1989), with $A(9.7 \mu\text{m})/A_V=0.12$ (Roche & Aitken 1985).

TABLE 3.5 — Warm molecular hydrogen mass estimates for the nucleus of NGC 4945 using the best fit power law $dM/dT=4.43\times10^{15} T^{-4.793} M_{\odot}/K$. The total H₂ gas mass estimated from CO amounts to $2.7\times10^8 M_{\odot}$

Temp. range [K]	M(warm H ₂) [M _⊕]	% of total M(H ₂)
200–10000	2.19×10^6	0.8%
150–10000	6.51×10^6	2.4%
120–10000	1.52×10^7	5.6%
100–10000	3.03×10^7	11%
90–10000	4.52×10^7	17%
80–10000	7.06×10^7	26%
70–10000	1.17×10^8	43%
60–10000	2.10×10^8	78%
50–10000	4.20×10^8	156%

- Law B: The same as law ‘A’, except for the range $\lambda=[2.6,8.8]\mu m$, where we took the extinction law as found towards the Galactic center by Lutz (1999). In the 3–8 μm range this reddening law constitutes a significantly higher extinction than usually assumed. For the silicate optical depth we assumed $A(9.7 \mu m)/A_V=0.14$ (Lutz 1999).

From Fig. 3.3 and the criteria defined above, moderate extinctions of $A_V=17$ –23 are clearly preferred. Extinction law A provides a somewhat better fit than extinction law B. None of the 3 solutions gives a good fit to the (1–0) Q(4) data point. In the following analysis, we use the preferred extinction correction of $A_V=20^{+3}_{-3}$ and extinction law A. We note that the extinction to the H₂ emitting region is slightly less than that to the starburst H II regions (Sect. 3.3.2). This plausibly matches the morphological results of Moorwood et al. (1996b), who find the starburst in an obscured disk, but the H₂ emission extending into a less obscured wind blown cavity.

A rough estimate of the amount of warm molecular hydrogen in the nucleus of NGC 4945 can be derived from the level populations of the pure rotational S(0) and S(1) transitions. The excitation temperature for the upper levels of these transitions (J=2 and J=3) is 160 K. Assuming the same excitation conditions for the J=0 and J=1 levels, we compute a warm molecular hydrogen mass of $2.4\times10^7 M_{\odot}$. This is 9% of the total H₂ gas mass estimated from CO and 0.7% of the dynamical mass interior to the molecular ring (Bergman et al. 1992, see below).

As already noted, the excitation temperature changes significantly with level energy. This is the consequence of the natural fact that the emitting gas will consist of a mixture of temperatures. The rich NGC 4945 dataset allows us to address this in a more quantitative way. Experiments with fits assuming a number of discrete temperature components lead us to suggest that a power law might give a good representation of the mass distribution as a function of temperature. We obtain a good fit for the following power law: $dM/dT=4.43\times10^{15} T^{-4.793} M_{\odot}/K$. The quality of the fit is shown in Fig. 3.4.

Table 3.5 gives warm molecular masses for several low temperature cut-offs. Since H₂

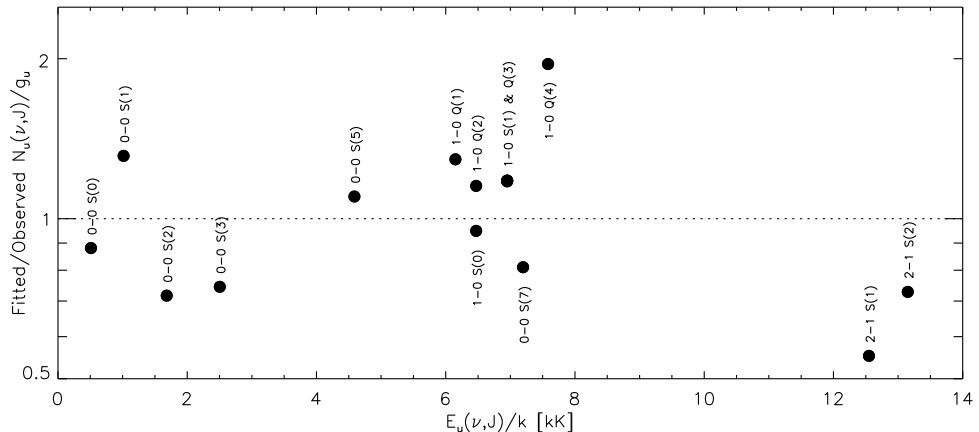


FIGURE 3.4 — Ratio of the fitted and observed H₂ excitation diagram for the best fitting power law $dM/dT = 4.43 \times 10^{15} T^{-4.793} M_{\odot}/K$

gas at temperatures below 70 K does not contribute to the (0–0) S(0) flux, nor to any of the other pure rotational lines, we cannot verify whether our power law mass distribution continues down to the lowest temperatures. Nevertheless, we have included mass estimates down to a low temperature cut-off of 50 K. This number is reasonable, since we don't expect the giant molecular clouds (GMCs) to be as cold as in the Galactic disk (10–20 K). Rather we expect conditions as found near the Galactic center, where the GMCs are believed to have temperatures exceeding 50 K (Armstrong & Barrett 1985).

It is interesting to compare our warm molecular hydrogen gas mass estimate with values found in the literature (see Moorwood & Oliva (1994) for a review). Bergman et al. (1992), using the inner molecular rotation curve of Whiteoak et al. (1990), compute a dynamical mass interior to the molecular ring ($R \leq 280$ pc = 15.6'') of $3.3 \times 10^9 M_{\odot}$. The same authors use CO to derive a total H₂ gas mass of $2.7 \times 10^8 M_{\odot}$ for the ring, assuming the rather high kinetic gas temperature of 100 K. Note that a low temperature cut-off of the order 50–60 K in our H₂ temperature distribution would bring our estimate of the total H₂ gas mass in agreement with that derived from the low level CO observations. The total H₂ gas mass of $2.7 \times 10^8 M_{\odot}$ agrees well with a starburst-like position of NGC 4945 in the L_{IR}–M(H₂) diagram Young & Scoville (1991).

In Table 3.6 we list for a number of external galaxies and Galactic template sources temperatures and masses of the warm molecular hydrogen gas. With a value of 9%, NGC 4945 has a warm H₂ gas fraction similar to that found for most of the other galaxies listed. Note however that the results for NGC 3256, NGC 4038/39 and Arp 220 are less well constrained than for NGC 6946 and NGC 4945: only for the latter two can the temperature of the warm H₂ gas be determined from the (0–0) S(0) and S(1) transitions directly.

For the same reason a comparison of the H₂ gas temperatures is of limited value unless they are derived from identical line combinations. Fairly low temperatures can be derived from the (0–0) S(0) and S(1) lines, 160 K and 179 K for NGC 4945 and NGC 6946, respectively. Limits for other galaxies listed in Table 3.6 are consistent with a similarly low temperature. This temperature is well below that observed for an Orion type shock (>500 K). It is closer

TABLE 3.6 — Warm molecular hydrogen in external galaxies and Galactic template sources. In column 4 detected lines are printed bold, upper limits normal. T_{01} refers to the excitation temperature computed from the (0–0) S(0) & S(1) fluxes. Likewise, T_{12} refers to the excitation temperature computed from the (0–0) S(1) & S(2) fluxes. T_{rot} is the best fit excitation temperature to several of the lowest rotational transitions. The warm H₂ gas mass (M_{warm}) is computed using the gas temperature listed in any of the preceding three columns. The last column gives the fraction of H₂ gas in the warm component

Object	Type	Ref	Rot. lines observed	T_{01} [K]	T_{12} [K]	T_{rot} [K]	M_{warm} [M _⊙]	% of total H ₂
NGC3256	galaxy	a	S0, S1, S2, S5	150 ^α			10^9	3
NGC4038/39	galaxy	b	S1, S2	200 ^α		405	5.6×10^7	8
							8×10^6	1
NGC4945	galaxy		S0—S3,S5,S7	160			2.4×10^7	9
						380	1.2×10^6	0.4
NGC6946	galaxy	c	S0,S1,S2	179 ^β			5×10^6	5–10
Arp220	galaxy	d	S0, S1, S2, S5	150 ^α			3.5×10^9	10
Orion Bar	PDR	e	S0—S5,S7,S12,S13,S15,S19,S21	155			—	—
S140	PDR	f	S0—S5,S7,S9,S13	159			—	—
Orion Peak 1	shock	e	S0, S1—S21, S25		578		—	—
Cepheus A West	shock	g	S1—S5,S7,S9			700	—	—
Cepheus A East	shock	h	S0, S1—S8,S9,S10,S11			740	—	—

(^α) assumed; limits are measured for NGC 3256 (> 140K) and Arp 220 (> 114K); (^β) T_{01} recomputed from the original (0–0) S(0) & S(1) fluxes.

References: (^a) Rigopoulou et al. (1996); (^b) Kunze et al. (1996); (^c) Valentijn et al. (1996b); (^d) Sturm et al. (1996); (^e) D. Rosenthal (priv. comm.); (^f) Draine & Bertoldi (1999);

(^g) Wright et al. (1996a); (^h) van den Ancker et al. (2000)

to what is observed for the same line combination in PDRs (e.g. Orion Bar: 155 K, D. Rosenthal priv. comm.; S140: 159 K, Draine & Bertoldi (1999)). While a variety of regions may contribute to the galaxy-integrated temperature distribution, this comparison clearly shows Orion-like shocks to be not representative for the entire emission, and fairly normal PDRs (or less energetic shocks) to be perhaps more typical. If excited by shocks (as suggested by the morphology, Moorwood et al. (1996b)), then the near-infrared H₂ emission in NGC 4945 must trace a small subcomponent of faster shocks.

3.4 Conclusions

The main results of this paper can be summarized as follows:

The nuclear starburst is heavily obscured by 36^{+18}_{-11} mag. of visual extinction, as inferred from the [S III] 18.71 μm / 33.48 μm ratio.

The excitation of the nuclear starburst is very low, as deduced from excitation indicators [Ne III] 15.56 μm / [Ne II] 12.81 μm and L_{bol}/L_{lyc}, consistent with an age of at least 5×10^6 yrs. Comparison with starburst models implies that at least 50% of the bolometric luminosity is powered by the starburst.

The very low inferred black hole mass, the very cold mid-infrared to far-infrared colors, and the absence of any free line of sight to the NLR supports the conclusion that the starburst dominates the bolometric luminosity.

Our mid-infrared ISO spectroscopy does not provide any evidence for the existence of an AGN in the nucleus of NGC 4945. The only high excitation line detected, the 25.9 μm [O IV] line, is most likely produced in shocks associated with the nuclear starburst.

The AGN, detected in hard X-rays, is unusual in not revealing itself at optical, near-infrared and mid-infrared wavelengths. Hence, either the NLR is extremely obscured ($A_V > 160$), or UV photons from the AGN are absorbed close to the nucleus along all lines of sight, or the AGN is deficient in UV relative to its X-ray flux.

Many ISM solid state and molecular features have been observed with ISO-PHT-S in the 2.4–11.7 μm range. Most prominent in emission are the PAH features at 3.3, 6.2, 7.7 and 11.2 μm. The strongest absorption features are those of water ice, CO₂ and CO, seen against the nuclear spectrum. These features show striking similarities to the absorption features seen towards the Galactic center.

We have studied the physical conditions, excitation and mass of warm H₂, combining IRSPEC and ISO observations of 14 transitions. We derive a visual extinction of 20^{+3}_{-3} mag. to the H₂ emitting region. From the (0–0) S(0) & S(1) lines, we compute a warm (160 K) H₂ gas mass of $2.4 \times 10^7 M_{\odot}$, 9% of the total gas mass inferred from CO. The excitation diagram is best fitted by a power law of the form $dM/dT = 4.43 \times 10^{15} T^{-4.793} M_{\odot}/K$. The low excitation temperature of 160 K shows Orion-like shocks not to be representative for the entire emission, and fairly normal PDRs to be perhaps more typical.

Acknowledgements

The authors wish to thank Dietmar Kunze and Fred Lahuis for help in the SWS data reduction and Matt Lehnert, Steve Lord and Eckhard Sturm for stimulating discussions.

4

Detection of strongly processed ice in the central starburst of NGC 4945

Adapted from:

H.W.W. Spoon, A.F.M. Moorwood, K.M. Pontoppidan, J. Cami, M. Kregel,
D. Lutz & A.G.G.M. Tielens
ASTRONOMY & ASTROPHYSICS, 402, 499 (2003)

THE composition of ice grains provides an important tool for the study of the molecular environment of star forming regions. Using ISAAC at the VLT to obtain spectra around $4.65\text{ }\mu\text{m}$ we have detected for the first time ‘XCN’ and CO ice in an extragalactic environment: the nuclear region of the nearby dusty starburst/AGN galaxy NGC 4945. The profile of the solid CO band reveals the importance of thermal processing of the ice while the prominence of the XCN band attests to the importance of energetic processing of the ice by FUV radiation and/or energetic particles. In analogy to the processing of ices by embedded protostars in our Galaxy, we attribute the processing of the ices in the center of NGC 4945 to ongoing massive star formation. Our M-band spectrum also shows strong H I Pf β and H₂ 0–0 S(9) line emission and gas phase CO absorption lines. The H I, H₂, PAH, gas phase CO and the ices seem to be embedded in a rotating molecular disk which is undergoing vigorous star formation. Recently, strong OCN[−] absorption has been detected in the spectrum of the Galactic center star GC:IRS 19. The most likely environment for the OCN[−] absorption is the strongly UV-exposed GC molecular ring. The presence of processed ice in the center of NGC 4945 and our Galactic center leads us to believe that processed ice may be a common characteristic of dense molecular material in star forming galactic nuclei.

4.1 Introduction

It has long been recognized that dust is an important component of the ISM in star forming regions in our galaxy and nearby galaxies. Optical studies of high redshift galaxies as well as deep mid-infrared and submm surveys have recently stressed the importance of dust in galaxies up to high redshifts. Understanding the composition, origin and evolution of dust – particularly in star forming regions – is therefore a key question of astrophysics. Of special importance are interstellar ices, which are only present in molecular cloud environments. Mid-infrared spectra taken with the spectrometers aboard the Infrared Space Observatory (ISO) have shown ices to exist in a variety of extragalactic sources, from nearby starburst nuclei up to distant dust-enshrouded ultra-luminous infrared galaxies (ULIRGs). Weak H₂O ice absorptions were first detected in the nuclear spectra of the nearby galaxies M 82 and NGC 253 (Sturm et al. 2000). Strong ice absorptions of H₂O, CO₂ and the XCN/CO blend were first seen in the nucleus of NGC 4945 (Chapter 3). This was followed by the discovery of H₂O, ‘HAC’ and CH₄ ice in the nuclear spectrum of NGC 4418 (Chapter 5). So far ices have been found in some twenty galaxies (Chapter 2), the most distant of which is IRAS 00183–7111, a ULIRG at z=0.33 (Tran et al. 2001).

Interstellar ices are ideal probes for the conditions in the coldest and best shielded galaxy components – their molecular clouds. Embedded protostars can process interstellar ice in their environment thermally as well as through FUV photolysis. Solid CO and ‘XCN’ provide prime probes for this processing. The fundamental vibrational modes of these species correspond to wavelengths around 4.65 μm in the M-band atmospheric window. CO ice is highly sensitive to thermal processing of its environment. In quiescent molecular clouds, as probed by e.g. the field star Elias 16, the CO ice feature is dominated by the feature characteristic for an apolar ice mixture. When heated to temperatures above 20 K, this ice mixture sublimates and the only CO ice mixture surviving is a mixture dominated by H₂O ice. This mixture has a distinctly different profile and sublimates at temperatures of \sim 90 K. The spectrum of the deeply embedded massive protostar W 33A is dominated by this type of CO profile (Chiar et al. 1998). The presence of ‘XCN’, or OCN[−] ice, after its most popular identification (Demyk et al. 1998), is indicative of strong processing of icy grains by UV light, energetic particles or heating (Lacy et al. 1984; Grim et al. 1989; Palumbo et al. 2000, F. van Broekhuizen, priv. comm.). In our Galaxy, OCN[−] ice is strongest in the embedded massive protostar W 33A (e.g. Pendleton et al. 1999). The feature is generally weak (compared to CO ice) in other protostars (e.g. Pendleton et al. 1999) and absent in quiescent molecular clouds, such as probed by the line of sight towards the field star Elias 16 (Chiar et al. 1995).

Here we report on our VLT/ISAAC L and M-band follow-up spectroscopy of the rich ice absorption spectrum of the nucleus of NGC 4945 (Chapter 3), a nearby (3.9 Mpc; 1''=18 pc; Bergman et al. 1992) luminous ($L_{\text{IR}}=3\times 10^{10} L_{\odot}$) infrared galaxy, seen nearly edge-on ($i\sim 78^\circ$; Ables et al. 1987). The central region of this galaxy is dominated by a visually obscured starburst (Moorwood et al. 1996b; Marconi et al. 2000) and a heavily enshrouded AGN, only seen in hard X-rays (Iwasawa et al. 1993; Guainazzi et al. 2000). Pa α (1.88 μm) and K-band (2.2 μm) images obtained with HST/NICMOS (Marconi et al. 2000) reveal a complicated nuclear morphology, resulting from a nuclear starburst partially obscured by a strongly absorbing circumnuclear star forming ring, seen nearly edge-on. Fig. 4.1 shows the HST/NICMOS K-band image (Marconi et al. 2000), rotated such that the galaxy major axis lies horizontally. A possible geometry for the circumnuclear starburst ring, seen under an

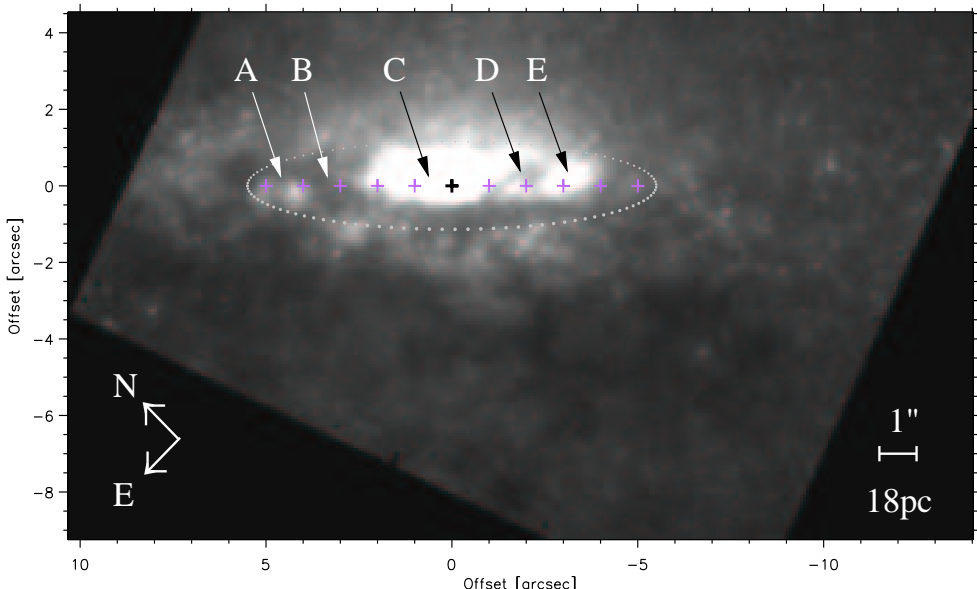


FIGURE 4.1 — HST/NICMOS K-band image of the nucleus of NGC 4945 (reproduced from Marconi et al. (2000)). The image has been rotated so that the galaxy major axis ($PA=43^\circ$) is oriented horizontally. The position of the VLT/ISAAC slit is marked by crosses, spaced $1''$ apart. Arrows indicate several positions of interest, which are discussed in the text. The dotted ring gives an impression of how a circumnuclear ring with radius $5.5''$ (100 pc) would be seen under an inclination of 78° .

inclination of $\sim 78^\circ$, is indicated by a dotted circle with radius $5.5''$ (100 pc). The apparent asymmetric distribution of the nuclear emission interior to this ring (strong emission at position E, no emission at position B) has been attributed to patchy absorption within the ring (Marconi et al. 2000). Note that the emission at position A on the galaxy major axis appears to arise in the circumnuclear ring, not in the nuclear starburst. The dark structures seen at position D in Fig. 4.1 are likely gas filaments rising above the star forming ring and appearing in absorption against the bright nuclear continuum. The Pa α image (Fig. 4.2; Marconi et al. 2000) shows more of these dark filamentary structures, one of which passes in front of the K-band nucleus. The AGN, the second brightest Seyfert 2 nucleus in the sky at hard X-rays (Done et al. 1996), does not appear in any of the HST/NICMOS images. Ground-based $10\ \mu m$ ESO/TIMMI images ($1''$ seeing) reveal no sign of the central monster either (Marconi et al. 2000). Also mid-infrared spectroscopic AGN tracers, like $7.65\ \mu m$ [Ne VI] and 14.3 & $24.3\ \mu m$ [Ne V], resulted in strong upper limits only (Chapter 3). It is hence likely that the AGN is strongly obscured in all directions by material which is most probably close to the black hole for the obscuration to be this effective. The conical cavity, protruding from the nucleus along the minor axis and seen in the near-infrared (Moorwood et al. 1996b) and in soft X-rays (Schurch et al. 2002), is therefore not a Seyfert ionization cone, but a cavity cleared by a supernova-driven starburst 'superwind' (Moorwood et al. 1996b).

Here we present infrared L and M-band spectra of all nuclear components discussed above obtained using VLT/ISAAC with its slit aligned with the galaxy major axis (Fig. 4.1).

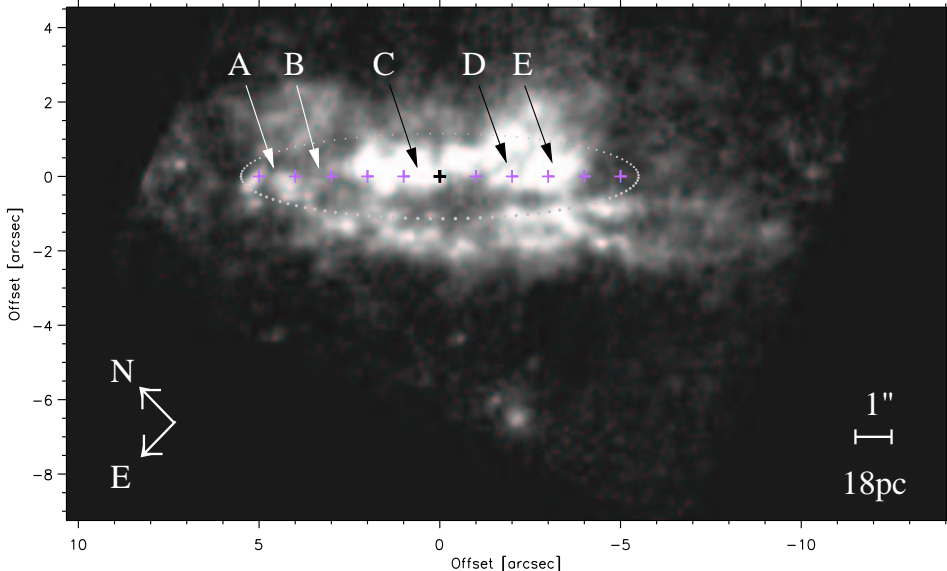


FIGURE 4.2 — HST/NICMOS H I Pa α image of the nucleus of NGC 4945 (reproduced from Marconi et al. (2000)). The image has been rotated so that the galaxy major axis ($PA=43^\circ$) is oriented horizontally. The position of the VLT/ISAAC slit is marked by crosses, spaced $1''$ apart. Arrows indicate several positions of interest, which are discussed in the text. The dotted ring gives an impression of how a circumnuclear ring with radius $5.5''$ (100 pc) would be seen under an inclination of 78° .

4.2 Observations

The 3–5 μm spectra of the NGC 4945 nucleus were obtained using the Infrared Spectrometer And Array Camera (ISAAC) mounted on the VLT (UT1-Antu) at the ESO Paranal Observatory. The observations were performed on the night of June 15, 2000 for the L-band spectrum and on the nights of June 15–16, 2000 and July 1–3, 2001 for the M-band spectrum. The low resolution grating and the $1''$ slit were used for the L-band spectrum with a corresponding resolving power of $R=360$. The M-band spectrum was obtained using the medium resolution grating and the $1''$ slit, resulting in a spectral resolving power of $R=3000$ ($\Delta v=100 \text{ km/s FWHM}$). In both cases, a single setting was done covering the entire L-band and the region from 4.56 to 4.80 μm in the M-band. The spectra have a total integration time of 240 s and 5123 s for the L and the M-band, respectively. The telescope was operated in the standard chop-nod mode with a chop throw of $20''$. The telluric standard BS 5571 (B2III) was observed just before or after each observation of NGC 4945 with a maximal airmass difference of 0.15.

The data were reduced using our own IDL routines. The individual frames were corrected for the non-linearity of the Aladdin detector, distortion corrected using a star trace map and bad pixels and cosmic ray hits were removed before co-adding. For the M-band this procedure resulted in six co-added source frames and six co-added standard star frames. Standard star spectra were obtained by extracting the positive spectral trace from each of the

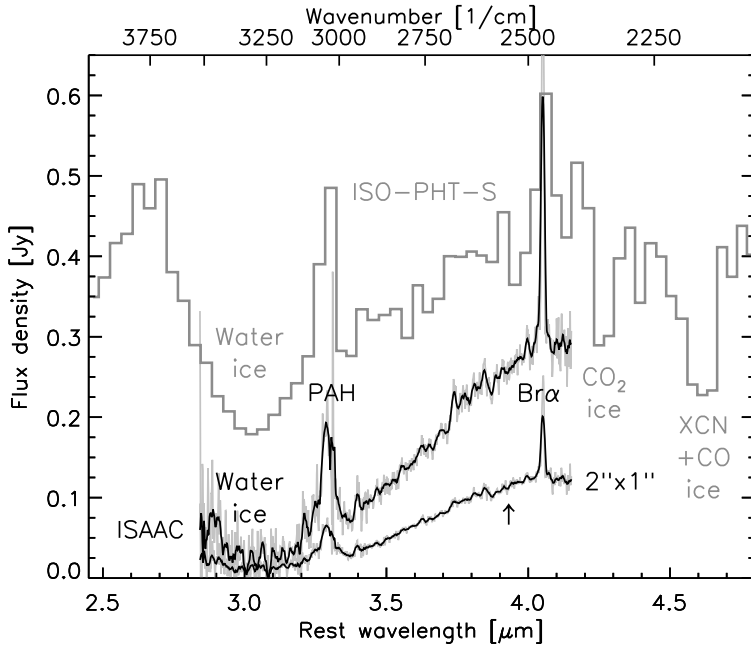


FIGURE 4.3— The VLT/ISAAC rest frame L-band spectrum of the central $2'' \times 1''$ ($36 \times 18 \text{ pc}^2$) and $11.5'' \times 1''$ ($210 \times 18 \text{ pc}^2$) of NGC 4945 (black) compared with the ISO-PHT-S spectrum obtained in a $24'' \times 24''$ aperture (grey histogram). The arrow indicates the expected wavelength of the $3.93 \mu\text{m}$ [Si IX] line.

six standard star frames. The six source frames were then divided by their associated standard star spectra, taking into account an optimal small shift between the source frame and standard spectrum by requiring that the pixel-to-pixel noise on the continuum of the final source frame be minimized. No correction for airmass differences was attempted due to insufficient signal-to-noise ratio of the source frames. No hydrogen recombination lines were detected in the standard spectrum and thus no attempts were made to correct the standard for photospheric lines. Next, each source frame was flux calibrated relative to the standard and wavelength calibrated using the telluric absorption lines in the standard star spectrum. The final source frame was then produced by stacking the six source frames, taking into account small dispersion shifts among the frames.

The flux calibration is estimated to be better than 15% and the wavelength calibration is accurate to 150 km/s and 15 km/s for the L and M-band spectra, respectively.

4.3 Results

4.3.1 The $3 \mu\text{m}$ water ice band

The ISAAC L-band spectrum of the central region of NGC 4945 (Fig. 4.3) is dominated by a broad (2.7 – $4.0 \mu\text{m}$) absorption band attributed mainly to water ice (e.g. Smith et al. 1989b; Chiar et al. 2000). The width of the feature is best appreciated in the low resolution $24'' \times 24''$

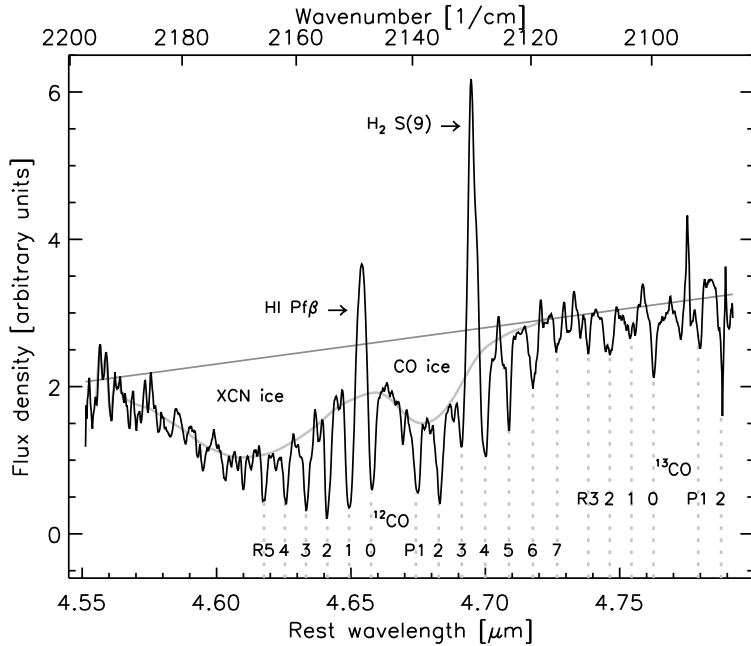


FIGURE 4.4 — The VLT/ISAAC rest frame M-band spectrum of the central $2'' \times 1''$ ($36 \times 18 \text{ pc}^2$) of NGC 4945. The spectrum shows emission lines of H I $\text{Pf}\beta$ and H_2 0–0 S(9), broad absorption features of ices containing XCN and CO, and absorption lines of gas phase ^{12}CO and ^{13}CO . The adopted continuum and the shape of the ice feature, corrected for the presence of gas phase ^{12}CO and ^{13}CO lines, are drawn in grey.

ISO-PHT-S spectrum, which is shown for comparison. Superimposed on the absorbed L-band continuum are the PAH emission bands at 3.3 & $3.4 \mu\text{m}$ as well as the H I $\text{Br}\alpha$ line at $4.05 \mu\text{m}$. The ISAAC spectra of the central $2'' \times 1''$ and $11.5'' \times 1''$ agree well with the larger beam ISO-PHT-S spectrum, assuming the water ice feature in the latter spectrum to be diluted by a non-absorbed stellar and dust continuum. Adopting a flat continuum (fixed at 4.0 – $4.1 \mu\text{m}$) and depending on whether we fit the bottom or the blue wing of the feature, we find a water ice column of 41 – $47 \times 10^{17} \text{ cm}^{-2}$ (assuming a band strength of $2.0 \times 10^{16} \text{ cm/molecule}$; Gerakines et al. 1995). Note the absence of $3.94 \mu\text{m}$ [Si IX] line emission from the ISAAC L-band spectrum. This line arises in soft X-ray photoionized gas and is comparable to or brighter than the H I $\text{Br}\alpha$ line in many Seyfert galaxies (Oliva et al. 1994; Lutz et al. 2002). The absence ($[\text{Si IX}]/\text{H I Br}\alpha < 0.10$) may be taken as evidence for the extremely high obscuration of the AGN in NGC 4945 in the L-band.

4.3.2 Processed CO and OCN[−] ice

The M-band spectrum of the central $2'' \times 1''$ of the nuclear region of NGC 4945 (Fig. 4.4) contains strong and relatively broad absorption features at 4.62 and $4.67 \mu\text{m}$ as well as gas lines due to H I, H ₂ and CO. The line centers of the gas phase lines shift as a function of

position along the slit.

In order to investigate the various M-band absorption features, we fitted a linear continuum to the two pivot ranges 4.54–4.55 μm and 4.78–4.79 μm . The resulting optical depth spectrum is shown in Fig. 4.5a. In Fig. 4.5b, 4.5c and 4.5d we show spectra of three comparison objects: the embedded massive protostar W 33A with the strongest known XCN feature; the Galactic center (Moneti et al. 2001) showing XCN absorption towards its massive star forming region which is obscured in what is effectively an ‘edge-on’ view towards the center of our own galaxy; and, finally, the unprocessed line of sight to the field star Elias 16 located behind the Taurus molecular cloud (Chiar et al. 1995). The similarity of NGC 4945 to W 33A is particularly striking and will be discussed later.

Following Galactic ice studies (Tielens et al. 1991; Schutte & Greenberg 1997; Chiar et al. 1998; Demyk et al. 1998; Pendleton et al. 1999) we identify the prominent absorption feature centered at 2168.0 cm^{-1} (FWHM=24.0 cm^{-1}) with solid state ‘XCN’, or OCN[−] after its most likely identification (Demyk et al. 1998). In order to measure the shape and depth of the feature, we adopt the ice feature shown in Fig. 4.4. This continuum has been corrected for the presence of gas phase ^{12}CO and ^{13}CO absorption lines, discussed later in this Section. The OCN[−] feature appears slightly blueshifted and narrower than in W 33A ($\nu_0=2165.5 \text{ cm}^{-1}$; FWHM=26.7 cm^{-1}). The differences are similar to those found between the embedded protostars AFGL 961 and W 33A (Pendleton et al. 1999) and may be attributed to differences in ice composition (Grim & Greenberg 1987). The column density of OCN[−] is listed in Table 4.1 and was computed assuming an OCN[−] bandstrength of 1.3×10^{-16} (F. van Broekhuizen, priv. comm.).

Detailed studies of the observed profiles of the solid CO ice band in Galactic sources have shown that they can all be fitted by varying contributions of the same three components (Boogert et al. 2002a,b; Pontoppidan et al. 2003). These three components are thought to represent “pure” solid CO (Gaussian centered at $\nu_0=2139.9 \text{ cm}^{-1}$ with FWHM=3.5 cm^{-1}), traces of CO trapped in H₂O ice (“polar CO”; Lorentzian centered at $\nu_0=2136.5 \text{ cm}^{-1}$ with FWHM=10.6 cm^{-1}) and CO in solid CO₂ ice (“apolar CO”; Gaussian centered at $\nu_0=2143.7 \text{ cm}^{-1}$ with FWHM=3.0 cm^{-1}) (Boogert et al. 2002b; Pontoppidan et al. 2003). Here we note that the spectrum of NGC 4945 is dominated by traces of CO trapped in H₂O ice with little or no evidence for the other two components (Fig. 4.5a). In contrast, the spectrum of W 33A (Fig. 4.5b) has a noticeable contribution of the “pure” solid CO component (Tielens et al. 1991). Table 4.1 lists the column densities of the various CO ice components, which were computed assuming a CO bandstrength of $1.1 \times 10^{17} \text{ cm/molecule}$ (Gerakines et al. 1995).

The nuclear spectrum of NGC 4945 also reveals CO in the gas phase. In Fig. 4.4 we identify a total of 13 fundamental ro-vibrational absorption lines of ^{12}CO and several of ^{13}CO . This is a sufficient number of lines to attempt a single component model fit to determine the temperature, intrinsic line width and ^{12}CO and ^{13}CO gas column densities. For this purpose we use the isothermal plane-parallel LTE CO gas models of Cami (2002), folded with the appropriate VLT/ISAAC spectral resolution ($R=3000$; $\Delta\nu=100 \text{ km/s}$ FWHM). In the fitting procedure both the observed spectrum and the model spectra are normalized through division by a strongly smoothed version of the respective spectra. A four-parameter least-squares minimization procedure then picks the best fitting model. Fig. 4.6 shows the result for the nuclear spectrum of NGC 4945. The CO gas appears moderately warm at $35_{-2.5}^{+7.5} \text{ K}$, with an intrinsic line width (FWHM) of $50 \pm 5 \text{ km/s}$ and column densities $\log N(^{12}\text{CO})=18.3 \pm 0.1 \text{ cm}^{-2}$

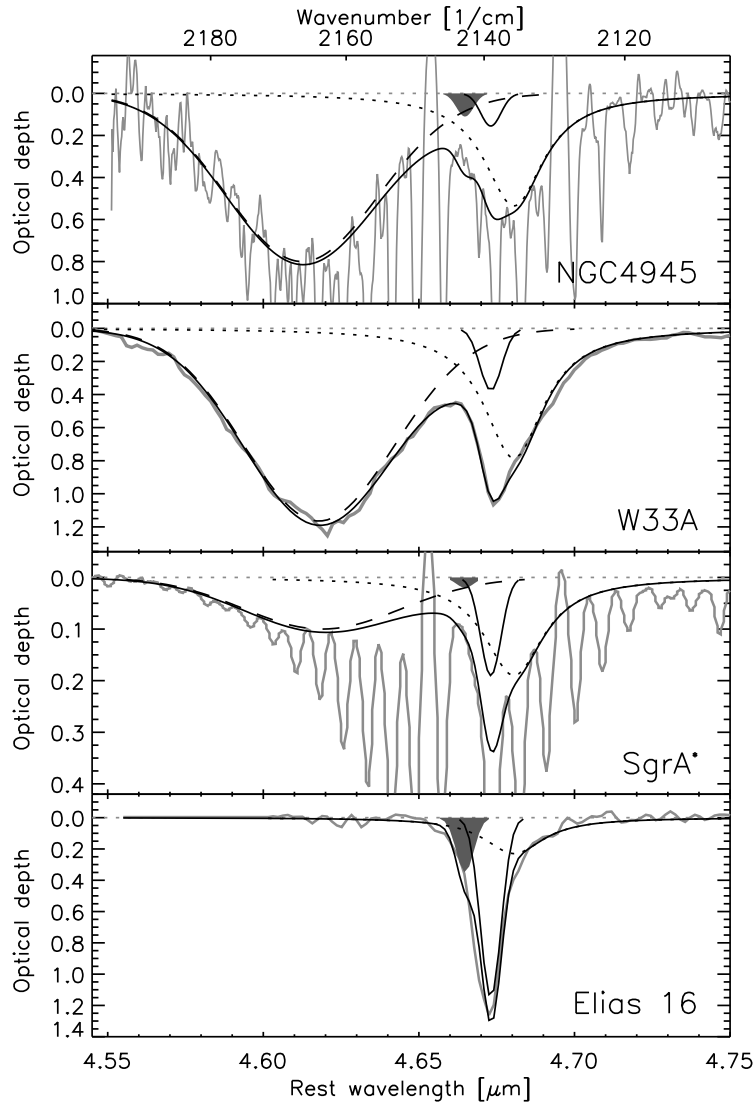


FIGURE 4.5 — The optical depth spectrum of ices in NGC 4945 compared to ices seen in Galactic lines of sight. The **Top panel** shows the optical depth spectrum of the central $2'' \times 1''$ ($36 \times 18 \text{ pc}^2$) of NGC 4945 (grey), determined adopting the continuum shown in Fig. 4.4. Also indicated are the results of the fit to the ice profile. The OCN⁻ fit component is denoted by a *dashed line*, the polar CO component by a *dotted line*, the pure CO component by a *continuous line* and the apolar component by a *grey surface*. The overall fit is shown as a *black line*. The spectrum was obtained at a resolving power of R=3000. **Second panel:** Optical depth spectrum for the massive embedded protostar W 33A. The spectrum has been degraded to a resolving power of R=750 (Gibb et al. 2000). **Third panel:** Idem for the ISO-SWS line of sight to the Galactic Center (Sgr A^{*}). The spectrum was obtained at a resolving power of R=2000 (Moneti et al. 2001). **Bottom panel:** Idem for the unprocessed line of sight to field star Elias 16, located behind the Taurus molecular cloud. The spectrum was obtained at a resolving power of R=1200 (Chiar et al. 1995).

TABLE 4.1— Measured column densities (10^{17} molecules/cm 2) and column density ratios for NGC 4945, the massive embedded protostar W 33A, the line of sight towards the Galactic center (Sgr A*) and towards a field star, Elias 16, located behind the Taurus molecular cloud.

	N4945	W33A	Sgr A*	Elias16
N(polar CO ice)	9.4	11.4	2.8 ^e	2.9
N(pure CO ice)	0.19	1.4		4.3
N(apolar CO ice)	0.16	0.0		1.0
N(total CO ice)	9.7	12.7	3.5 ^e	8.2
N(XCN ice)	1.6	2.6	0.2 ^e	<0.13 ^b
N(cold CO gas) ^a	—	130 ^c	66 ^d	18 ^h
N(warm CO gas) ^a	130	140 ^c	1 ^d	—
N(CO gas)	130	270 ^c	67 ^d	18 ^h
N(H ₂ O ice)	41–47	110 ^b	12 ^f	25 ^g
N(CO ₂ ice)	≥2.0 ⁱ	14 ^j	1.7 ^j	5 ^j
N(polar CO)/N(CO)	0.97	0.89	0.8	0.35
N(XCN)/N(CO)	0.17	0.20	0.07	<0.02
N(CO)/N(H ₂ O)	0.21–0.24	0.12	0.3	0.33
N(XCN)/N(H ₂ O)	0.034–0.039	0.024	0.02	<0.005
N(CO ice)/N(CO gas)	0.08	0.047	0.05	0.5

(^a) We define CO gas as cold if $T_{\text{gas}} < 30$ K and as warm if $T_{\text{gas}} \geq 30$ K

(^b)Gibb et al. (2000); (^c)Mitchell et al. (1988); (^d)Moneti et al. (2001)

(^e)Based on the Sgr A* spectrum of Moneti et al. (2001); (^f)Chiar et al. (2000); (^g)Chiar et al. (1995)

(^h)Whittet et al. (1989); (ⁱ)Chapter 3; obtained in a $24'' \times 24''$ aperture; (^j)Gerakines et al. (1999)

and $\log N(^{13}\text{CO})=17.2_{-0.05}^{+0.15} \text{ cm}^{-2}$, assuming a covering factor 1 for the absorber. The uncertainties listed above do not take into account the systematic errors resulting from the data reduction, which may be appreciable. The very low $^{12}\text{CO}/^{13}\text{CO}$ ratio of ~ 13 indicates that some ^{12}CO lines are likely optically thick. In addition, the absorbing material may not be in a uniform screen 'covering factor 1' configuration (Fig. 4.1). This will particularly affect the derived column for ^{12}CO . A more realistic, yet more uncertain, value for the ^{12}CO gas column may be derived from the ^{13}CO column. Assuming a $^{12}\text{CO}/^{13}\text{CO}$ ratio of 80, we find $\log N(^{12}\text{CO})=19.1_{-0.05}^{+0.15} \text{ cm}^{-2}$. Note that the (high resolution) spectrum of the physically closest resembling object, the protostar W 33A, also contains CO gas phase lines (Mitchell et al. 1988). At the resolution of the ISO-SWS spectrum ($R \sim 750$; Gibb et al. 2000) these are however not detectable.

4.3.3 The spatial distribution of the ice

The analysis presented above focusses on the nuclear spectrum of NGC 4945, which comprises the central $2'' \times 1''$. The nuclear continuum emission extends however from $\sim 4.5''$ SW to $\sim 2''$ NE of the nucleus, measured in a $1''$ wide slit along the SW-NE oriented ($\text{PA}=43^\circ$) galaxy major axis (see Fig. 4.1). Line emission (Fig. 4.7) can be traced as far out as $\sim 4.5''$ SW (position E) and $\sim 5.5''$ NE (position A) of the nucleus. Both the continuum and line emission appear clearly weakened in a $\sim 1''$ long strip located $1.7''$ SW (position D) of the

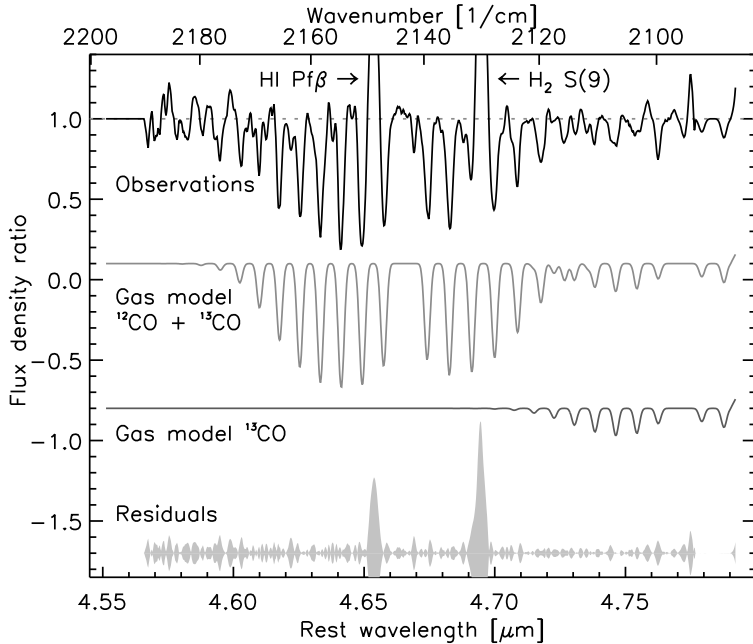


FIGURE 4.6—CO gas absorption lines in the spectrum of the central $2'' \times 1''$ ($36 \times 18 \text{ pc}^2$) of NGC 4945. The observed spectrum, after dividing out the ice feature, is shown in *black*. The best fitting CO gas model is drawn in *dark grey*. Fit residuals are shown in *light grey*.

nucleus. This strip coincides with a dark filamentary structure in the HST/NICMOS K-band image (Fig. 4.1) of Marconi et al. (2000). The same image further shows strong extinction from what might be a circumnuclear ring to be responsible for limiting the observable part of the major axis continuum to the range found (see Sect. 4.1). Our analysis further shows that the ice and gas absorption features are detected wherever there is background continuum to absorb. The depth of the ice features appears to be quite constant (Fig. 4.8), except for position D, where the solid state absorptions may be significantly stronger. Again interestingly, this position coincides with the dark filamentary structure seen in the HST/NICMOS K-band and H I Pa α images (Figs. 4.1 & 4.2).

The lower panels of Fig. 4.7 show position-velocity diagrams for the H I Pf β and H₂ 0–0 S(9) emission lines. The distributions are remarkably similar over the central $\pm 2''$, both indicating rotation about the nucleus. The only significant deviation occurs at a position $0.7''$ NE of the nucleus (position C), where the H₂ 0–0 S(9) emission extends $\sim 40 \text{ km/s}$ beyond the highest velocity traced by H I Pf β . We speculate that this position may coincide with the start of the N–S oriented molecular ridge, traced in H₂ 1–0 S(1) (see Fig. 4.9) by Moorwood et al. (1996b) and Marconi et al. (2000), bordering the conical cavity cleared by a starburst superwind (Moorwood et al. 1996b). Another deviation occurs $3''$ – $4''$ NE of the nucleus (position B), where a dark cloud in the circumnuclear ring weakens the line emission from the nuclear starburst it eclipses. Given the high inclination of the circumnuclear ring, the dark

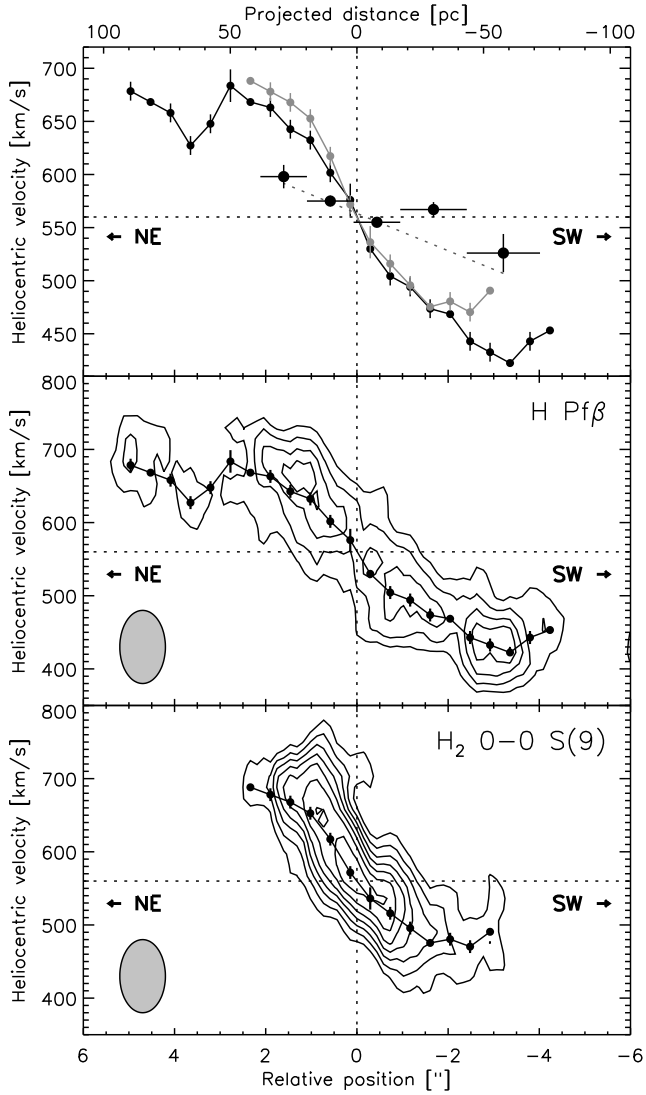


FIGURE 4.7 — Position-velocity information for several species detected in the M-band spectrum of NGC 4945. **Top panel:** Velocity curves for $\text{H}_1 \text{ Pf}\beta$ (black) and $\text{H}_2 0-0 \text{ S}(9)$ (grey) as determined from the position-velocity diagrams in the panels below. The data have been rebinned to half the size of a seeing element ($0.5''$). The five large dots denote the CO gas line velocities in five positional intervals along the galaxy major axis. A linear fit to the CO gas line points (excluding the point at $1.7''$ SW, which seems to trace a separate filament) is shown as a dashed line. The position of the nucleus is indicated by the vertical dotted line, the systemic velocity (561 km/s) by the horizontal line. **Middle panel:** Position-velocity diagram along the major axis for the $\text{H}_1 \text{ Pf}\beta$ emission line. Contours run from 4 to 10σ in steps of 2σ . The black points indicate the center of the gauss fit to the line profile at indicated positions along the galaxy major axis. The spatial and spectral resolution is indicated in the lower left corner. **Bottom panel:** Idem for the $\text{H}_2 0-0 \text{ S}(9)$ emission line. Contours run from 4 to 14σ in steps of 2σ .

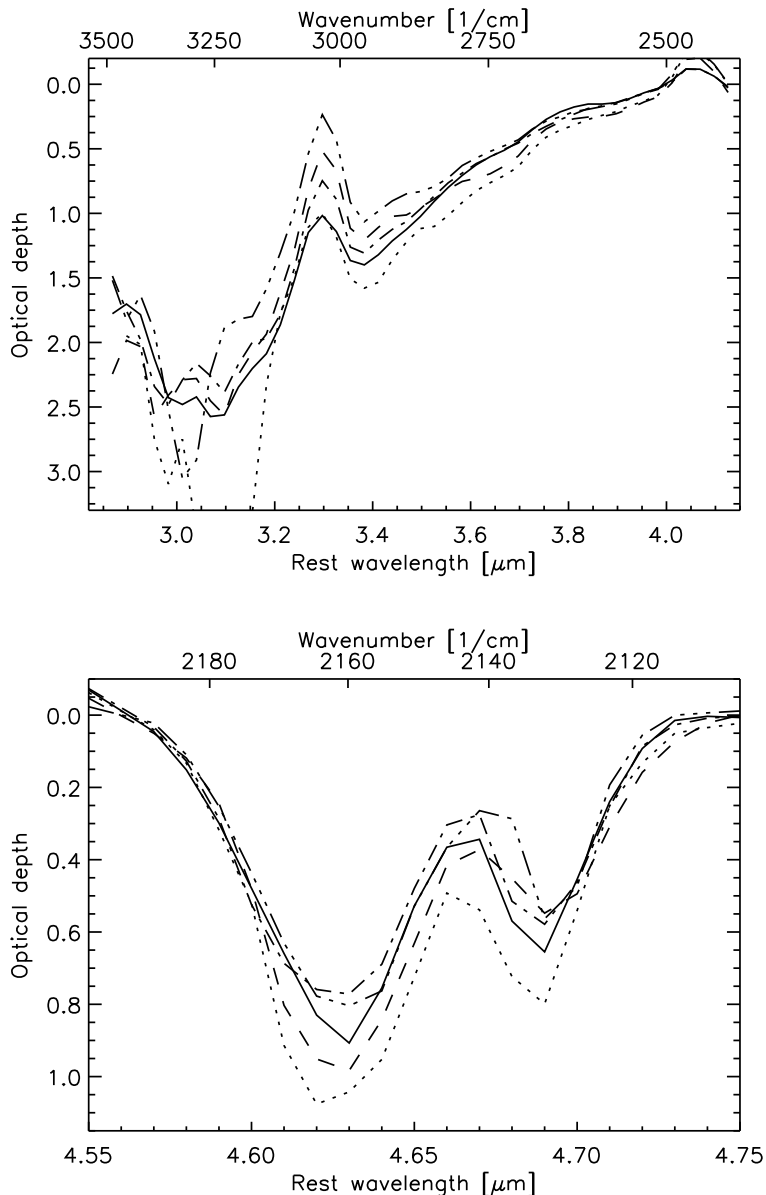


FIGURE 4.8 — Optical depth spectra of ice features in NGC 4945 for 5 adjacent positions (3.2'' SW: triple dot-dashed, 1.7'' SW: dotted, 0.45'' SW: solid, 0.60'' NE: dot-dashed, 1.6'' NE: dashed) along the galaxy major axis. The spectra have been smoothed and rebinned to lower spectral resolution. The optical depth spectra reveal no significant differences, except for the generally larger optical depth at position D, 1.7'' SW of the nucleus (dotted line). **Top:** Optical depth spectra of water ice. The feature centered at $3.3\text{ }\mu\text{m}$ is due to the presence of PAH emission in the water ice absorption feature. **Bottom:** Optical depth spectra of XCN and CO ice.

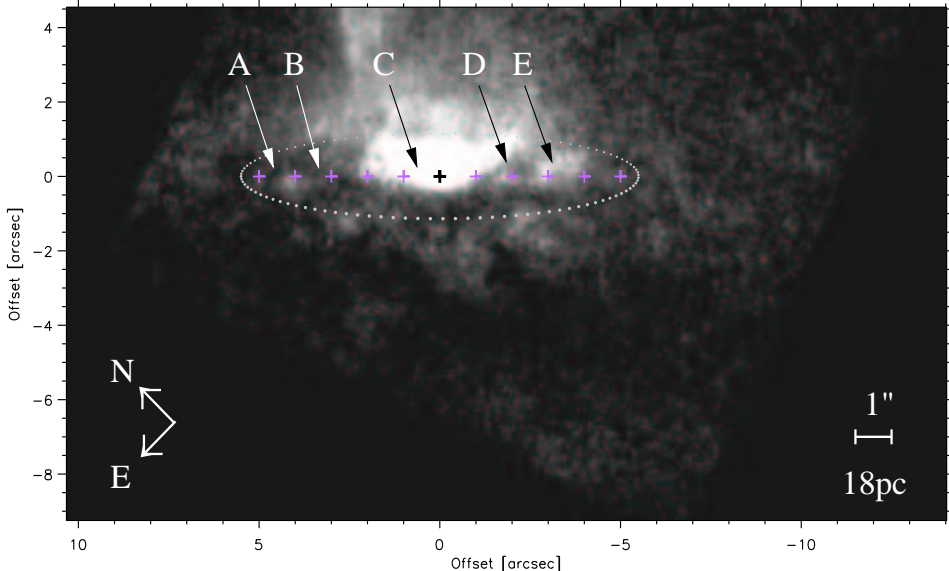


FIGURE 4.9 — HST/NICMOS H₂ 1–0 S(1) image of the nucleus of NGC 4945 (reproduced from Marconi et al. (2000)). The image has been rotated so that the galaxy major axis (PA=43°) is oriented horizontally. The position of the VLT/ISAAC slit is marked by crosses, spaced 1'' apart. Arrows indicate several positions of interest, which are discussed in the text. The dotted ring gives an impression of how a circumnuclear ring with radius 5.5'' (100 pc) would be seen under an inclination of 78°.

cloud may actually be in an orbit in the outer part of the circumnuclear ring, with an appreciable tangential orbital velocity component. This would explain why the H I Pfβ emission from that cloud is ∼50 km/s lower than that of the bright patch 1'' NE of it (position A). The top panel of Fig. 4.7 shows the velocity curves derived from fitting single Gaussians to the line emission in each of the observed H I Pfβ and H₂ 0–0 S(9) position-velocity distributions. The velocity curves obtained for both emission lines are consistent and yield the same velocity gradient of ∼60 km/s/arcsec across the nuclear region. The heliocentric systemic velocity of 561 ± 4 km/s (Dahlem et al. 1993) occurs at the brightest M-band cross dispersion pixel. Away from the nucleus the velocity curves flatten off to rotational velocities 120 ± 10 km/s above and below systemic. This value agrees well with the results for H I Brγ and H₂ 1–0 S(1) obtained by Moorwood & Oliva (1994). Note that Ott et al. (2001) find rotational velocities up to 160 km/s for H I (21 cm). Assuming that the measured velocities trace the potential, the mass within the nuclear region amounts to $1 \times 10^8 M_{\odot}$ at 50 pc and $3 \times 10^8 M_{\odot}$ at 100 pc. Also shown in the upper panel of Fig. 4.7 is the velocity curve for gas phase CO. The CO absorption line velocities were derived by cross-correlating the CO absorption line spectra with the best fitting CO gas model. In order to acquire sufficient signal-to-noise in the lines, the spatial information has been combined into 5 bins of 1.0''–1.5'' along the major axis. The resulting velocity curve for the CO absorption lines (excluding the point at 1.7'' SW; position D; see below) clearly samples a different velocity field than the emission lines do. Based on

the four CO points, we measure a velocity gradient for the CO gas of 17 km/s/arcsec across the nucleus. The velocity measured for the 1.7'' SW point (position D) clearly does not fit in with the velocity gradient seen for the other four CO points. Interestingly, the HST/NICMOS K-band image (Fig. 4.1) shows at this position a dark filamentary structure against the bright K-band continuum. Possibly, the CO gas radial velocity measured at 1.7'' SW is related to this foreground (circumnuclear ring?) structure instead of to the rotating inner ring/disk.

4.4 Discussion

The wealth of ISM features detected in the VLT/ISAAC L & M-band spectra of NGC 4945 allows us for the first time to study simultaneously the conditions of ionized hydrogen, molecular hydrogen, PAHs, icy grains and cold CO gas in the central region of another galaxy. Combined with the spatial information obtained in a 1'' wide slit oriented along the galaxy major axis, our observations give insight in the kinematics and spatial location of the different ISM components probed.

4.4.1 The nuclear geometry

The picture that emerges is of an extended, fragmented and vigorously star forming, rotating molecular ring/disk, surrounding the deeply buried, and hence passified, AGN. The H I, H₂ and PAHs trace the interaction of the massive stars – interspersed within the ring, as indicated by the velocity behavior of the H I and H₂ lines – creating H II regions and PDRs. The extended continuum emission source created this way, forms the background against which we see the various absorption features. The contribution of the AGN to this continuum is insignificant, as may be concluded from the absence of a pointlike source in both the HST K-band image (Marconi et al. 2000) and our ISAAC spectra. Hard X-ray observations have shown that the direct view of the AGN is blocked by a hydrogen column density of $10^{24.7} \text{ cm}^{-2}$ (Iwasawa et al. 1993, $A_V \sim 2500$). The absence of the $3.94 \mu\text{m}$ [Si IX] coronal line and other NLR fine structure lines (Fig. 4.3; Chapter 3) from this region indicates that the ionizing radiation does not escape in other directions either. The shallow velocity curve of the cold CO gas is consistent with the CO being distributed in the outskirts of the nearly edge-on, rotating molecular ring/disk, of which the CO gas velocities are sampled only in front of the bright nuclear continuum, where the line of sight velocity component increases only slowly with projected distance (see Fig. 4.10). An indication of its scale can be obtained in the simplified assumption of absorption in a single ring rotating at 120 km/s. To reproduce the observed velocity gradient of CO absorption, the radius of this ring would be $\sim 7''$ (~ 120 pc). Other distributions of absorbing material on similar scales, and in particular similar to the dust ring seen in the data of Marconi et al. (2000), will reproduce the data as well. The material seen in H I absorption by Ott et al. (2001) and the rotating central ($< 20''$) mm-wave-CO emission likely belong to the same structure. Although there is no velocity information, we are tempted to co-locate the H₂O, CO and OCN⁻ ice with the CO gas. First, the solid H₂O, CO and OCN⁻ can be traced as far out as the gas phase CO (Fig. 4.8). Second, the optical depth of the solid state features is constant over the spatial range probed (except for the 1.7'' SW point in Fig. 4.8), implying co-location of the ices in a foreground position. Third, the filamentary structure seen at 1.7'' SW (position D) shows both deeper solid state features (Fig. 4.8) and a deviant CO gas velocity, suggesting co-location of the ices with the CO gas. Fourth, the absence of the pure CO ice component indicates grains which have been thermally processed

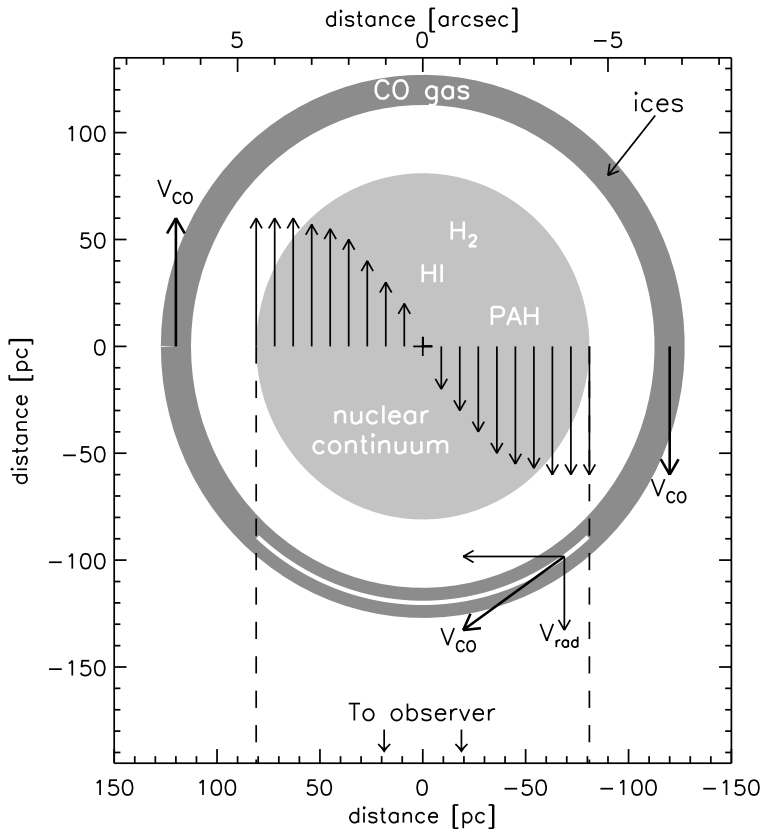


FIGURE 4.10 — Schematic face-on view of the central region of NGC 4945. In our model the H I Pfβ and H₂ 0–0 S(9) emission lines trace the rotation of the inner disk. Their velocity curves (Fig. 4.7a) indicate that the rotational velocity increases outward to become constant (~ 120 km/s) at $r \sim 60$ pc. Assuming the CO gas phase absorption lines to arise in the outskirts of the rotating disk ($V_{rot} = 120$ km/s), the CO velocity gradient (17 km/s/arcsec ≈ 1 km/s/pc; Fig. 4.7a) sampled in front of the nuclear continuum indicates that the “CO ring” must have a radius of ~ 120 pc. The white strip in the CO ring indicates the section of the CO ring where CO gas absorption lines can be detected against the nuclear continuum. The line of sight sight velocity component (V_{rad}) in this strip changes only slowly with projected distance, in agreement with the observed shallow CO velocity curve (Fig. 4.7 top panel).

to above 20 K. Hence, unlike for dark cloud lines of sight in our galaxy (such as Elias 16 in the Taurus molecular cloud), these ice grains are not located in some random, foreground, dark cloud along the line of sight, but instead close to a source of thermal heating. Fifth, the deep OCN⁻ ice band shows that the ice is heavily processed. That again locates the ices within regions of massive star formation or close to the AGN rather than some foreground material. From the spatial extent and uniformity of the OCN⁻ ice absorption (Fig. 4.8), a location close to the AGN can, however, be excluded. The only likely location therefore remain within or close to regions of massive star formation in the circumnuclear starburst. Indeed, within our

own galaxy, the massive protostar W 33A is an extreme example of processed ices (Chiar et al. 1998; Gibb et al. 2000). Dark cloud material in general does not show any evidence for the OCN⁻ absorption band (Fig. 4.5d; Whittet et al. 2001). In fact, no other Galactic, luminous protostar shows such a strong OCN⁻ band.

4.4.2 On the formation of OCN⁻ in galactic nuclei

The presence of OCN⁻ in ice grain mantles is often taken as a sign of energetic processing by particles or UV photons. Recent experiments suggest however that also thermal processing may result in the formation of OCN⁻ (F. van Broekhuizen, priv. comm.). A fourth possibility presents itself in the vicinity of an AGN: processing by AGN X-ray photons. The AGN in NGC 4945 is, however, strongly obscured and only hard X-ray photons manage to escape. Assuming similar obscuration towards the r~100 pc ice region in NGC 4945 as towards our line of sight, we estimate a hard X-ray (20–100 keV) flux of $\sim 0.5 \text{ erg/cm}^2/\text{s}$ from the observations of Guainazzi et al. (2000). This is two orders of magnitude less than the UV flux in a photon-dominated region next to massive stars (e.g. Tielens & Hollenbach 1985). The available very hard (unabsorbed) AGN X-rays are hence energetically insignificant compared to the starburst UV photons. In addition, such hard X-rays may not couple efficiently into individual ice grains. Further laboratory studies are required to settle these issues.

4.4.3 Comparison to the lines of sight to the nuclei of M 82 and NGC 253

The starburst in NGC 4945 is similar in luminosity to the prototypical starbursts M 82 and NGC 253 which are also located in the nuclear regions of almost edge-on galaxies. Comparing ISO spectra of NGC 4945 (Chapter 3) to ISO data for M 82 and NGC 253 (Sturm et al. 2000; Förster Schreiber et al. 2003), the obscuration of NGC 4945 is clearly higher towards the ionized medium (as derived from the 18.71/33.48 μm [S III] ratio in the low density limit), towards the PAH emitting medium (8.6 μm and 11.3 μm PAH emission features strongly suppressed by 9.7 μm silicate absorption), and in 3 μm water ice absorption ($\tau_{\text{ice}} \sim 2.5$). It remains unclear, however, whether this is just an on average higher absolute absorbing column towards the nuclear region of NGC 4945, as perhaps not implausible given also the slightly smaller physical size of its starburst, or whether there are differences in the properties of the absorbing medium. Higher quality M band spectra of M 82 and NGC 253 are needed to test whether those starbursts also host processed ices as NGC 4945, but with columns corresponding to their lower obscuration.

4.4.4 Comparison to the line of sight to the Galactic center

The spectrum of the nearest edge-on galactic nucleus, our Galactic center, also shows absorption features due to CO and OCN⁻ ice. The spectrum of GC:IRS 19 (Chiar et al. 2002) shows the features at similar relative strengths as in W 33A and NGC 4945. The star itself (M star) is most likely not the source of the energetic processing. A chance projection with the processed surroundings of a young foreground star is possible, but also unlikely. The projected distance of GC:IRS 19 to the GC molecular ring is, however, small. The material in this ring is exposed to high UV fluxes from the central cluster, crudely comparable to the radiation field within the molecular ring in NGC 4945. It is hence plausible that energetic processing has created similar ice properties in both NGC 4945 and in the GC molecular ring.

The ‘pencil beam’ line of sight to GC:IRS 19 may pass through this processed ring material, explaining the presence of strong OCN[−] absorption in the spectrum of GC:IRS 19. The larger beam 14''×20'' ISO–SWS spectrum of Sgr A* also shows CO and OCN[−] ice (Fig. 4.5; Moneti et al. 2001). The OCN[−] column is, however, nearly an order of magnitude smaller than in the pencil beam towards GC:IRS 19. This difference is likely due to the large number of background stars within the ISO–SWS beam, whose combined line of sight results in the observed low OCN[−] optical depth. While some of these pencil beams pass through the processed GC molecular ring, other pencil beams only sample unprocessed foreground material. If the latter line of sight dominates within the 14''×20'' ISO–SWS beam, this would be a natural explanation for the low OCN[−] optical depth in the Sgr A* spectrum of Moneti et al. (2001).

The presence of processed ice in the centers of NGC 4945 and the Galaxy leads us to believe that processed ices are one characteristic of dense molecular material in star forming nuclear regions of galaxies, and can be detected in favorable orientations. The amount of processing may then be a measure of the nuclear star formation activity and/or geometry.

4.5 Conclusions

Using ISAAC at the VLT to obtain spectra at 2.85–4.10 μm and 4.55–4.80 μm , we have detected for the first time ‘XCN’ and CO ice in an extragalactic environment: the central region of the nearby dusty starburst/AGN galaxy NGC 4945.

The profile of the solid CO band reveals the importance of thermal processing of the ice while the prominence of the XCN band attests to the importance of energetic processing of the ice by FUV radiation, energetic particles and/or heating. In analogy to the processing of ices by embedded protostars in our Galaxy, we attribute the processing of the ices in the center of NGC 4945 to ongoing massive star formation.

Our M-band spectrum also shows strong H I Pfβ and H₂ 0–0 S(9) line emission and gas phase CO absorption lines. The H I, H₂, gas phase CO and the ices seem to be embedded in a rotating molecular disk which is undergoing vigorous star formation.

The non-detection of the 3.94 μm [Si IX] coronal line in our VLT/ISAAC L-band spectrum is in full agreement with the very high obscuration towards the AGN derived from mid-infrared coronal line observations and from the absence of a point-like source in K-band and N-band images. With the source of the obscuration probably close to the AGN for the obscuration to be effective, the radiation from the AGN cannot be responsible for processing the ices.

The obscuration towards the starburst in NGC 4945 is far higher than towards similar starbursts in M 82 and NGC 253, also seen nearly edge-on. It is unclear whether this is just an on average higher absolute absorbing column towards the nuclear region of NGC 4945, or whether there are differences in the properties of the absorbing medium. Higher quality M-band observations of M 82 and NGC 253 are required.

Recently, strong OCN[−] absorption has been detected in the spectrum of the Galactic center star GC:IRS 19. The most likely environment for the OCN[−] absorption is the strongly UV-exposed GC molecular ring. The presence of processed ice in the center of NGC 4945 and our Galactic center leads us to believe that processed ice may be a common characteristic of dense molecular material in star forming galactic nuclei.

Acknowledgements

The authors wish to thank Jean Chiar, Andrea Moneti and Alessandro Marconi for sharing data with us, Fernando Comeron for help in optimising our observing proposal and Adwin Boogert, Jean Chiar and Jacqueline Keane for discussions. The VLT-ISAAC data were obtained as part of an ESO Service Mode run.

5

The obscured mid-infrared continuum of NGC 4418: a dust- and ice-enshrouded AGN

Originally published as a Letter to the Editor:
H.W.W. Spoon, J.V. Keane, A.G.G.M. Tielens, D. Lutz & A.F.M. Moorwood
ASTRONOMY & ASTROPHYSICS, 365, L353 (2001)

WE report the detection of absorption features in the 6–8 μm region superimposed on a featureless mid-infrared continuum in NGC 4418. For several of these features this is the first detection in an external galaxy. We compare the absorption spectrum of NGC 4418 to that of embedded massive protostars and the Galactic center, and attribute the absorption features to ice grains and to hydrogenated amorphous carbon grains. From the depth of the ice features, we infer that the powerful central source responsible for the mid-infrared emission must be deeply enshrouded. Since this emission is warm and originates in a compact region, an AGN must be hiding in the nucleus of NGC 4418.

5.1 Introduction

The ISO mission has considerably enhanced our knowledge of the mid-IR properties of normal, starburst, Seyfert and Ultra-luminous Infrared Galaxies (ULIRGs). The spectra of most sources are dominated by ISM emission features, the most prominent of which are the well-known PAH emission bands at 6.2, 7.7, 8.6, 11.3 and 12.7 μm . The PAH features and the emission lines have been used qualitatively and quantitatively as diagnostics for the ultimate physical processes powering galactic nuclei (Genzel et al. 1998; Lutz et al. 1998; Rigopoulou et al. 1999; Tran et al. 2001). A broad absorption band due to the Si–O stretching mode in amorphous silicates, centered at 9.7 μm , is also commonly detected in galaxies. Since the center of the silicate absorption coincides with a gap between the 6.2–8.6 μm and 11.3–12.8 μm PAH complexes, it is not readily apparent whether a 9.7 μm flux minimum should be interpreted as the “trough” between PAH emission features or as strong silicate absorption, or as a combination of the two. In spectra of heavily absorbed Galactic lines of sight, a strong silicate feature is often accompanied by ice absorption features in the 6–8 μm region (e.g. Whittet et al. 1996). Until recently this combination had not been reported in equally extinguished extragalactic sources, despite detections of ice features at shorter wavelengths (Chapter 3; Sturm et al. 2000). In this Chapter we report on the detection of ices in the strongly absorbed, ISO–PHT–S spectrum of NGC 4418, a nearby ($D=29$ Mpc; $1''=140$ pc) luminous ($L_{\text{IR}}=10^{11} L_{\odot}$) bright IRAS galaxy. NGC 4418 and the distant ULIRG IRAS 00183–7111 (Tran et al. 2001) are the first detections of these ice features in external galaxies.

NGC 4418 is well-known for its deep 9.7 μm silicate feature (Roche et al. 1986). Additional evidence for strong extinction is the weakness ($\text{H}\alpha$) and absence ($\text{H}\beta$, $\text{Br}\alpha$, $\text{Br}\gamma$) of hydrogen recombination line emission (Kawara et al. 1989; Ridgway et al. 1994; Lehnert & Heckman 1995, L.Kewley, priv. comm.), commonly detected in galaxies. HST–NICMOS images (Scoville et al. 2000) show hardly any structure in the inner 400 pc \times 400 pc, except for large scale extinction ($\Delta A_V \sim 2$). The IRAS colors of NGC 4418 indicate that — unlike most other galaxies — the 12–100 μm emission is dominated by a warm dust component, peaking shortward of 60 μm (see Fig. 5.1). VLA radio maps at 6 and 20 cm (Condon et al. 1990; Eales et al. 1990) show NGC 4418 to be compact (70 pc \times 50 pc at most). This, as well as the presence of large quantities of warm dust, has been taken as evidence for the presence of an otherwise hidden AGN in NGC 4418. In this Chapter we present mid-IR spectral evidence lending further support for the presence of an AGN in NGC 4418.

5.2 Observations

A low resolution ($\lambda/\Delta\lambda \sim 90$) ISO–PHT–S spectrum of the central $24'' \times 24''$ of NGC 4418 was obtained on 1996 July 14 as part of a project on the interstellar medium of normal galaxies (Helou et al. 2000). The measurement was carried out in triangular chopped mode, using a chopper throw of 150''. The resulting spectrum is thus free of contributions from zodiacal light. The ISO–PHT–S data were reduced using PIA 8.2. The absolute calibration is accurate to within 20%. The resulting spectrum is shown in Fig. 5.3.1.

In Fig. 5.1 we compile the 1–3000 μm (spectro)photometric observations of NGC 4418, including the new, standard reduced, ISO–PHT–S, ISO–CAM and ISO–LWS observations. Stellar emission probably dominates the near-IR regime up to 4 μm , beyond which a strong mid-infrared continuum sets in. The SED reveals that a substantial part of the emission emanates from optically thick warm dust (Roche & Chandler 1993; Lisenfeld et al. 2000),

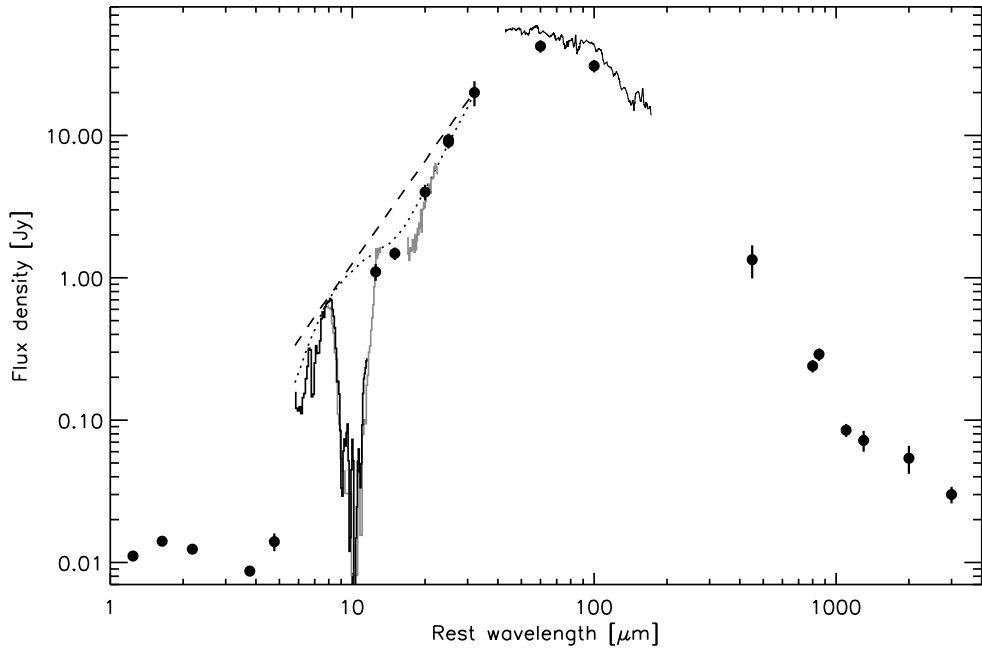


FIGURE 5.1 — The 1–3000 μm spectral energy distribution of NGC 4418, including the new ISO-PHT-S, ISO-CAM and smoothed ISO-LWS data. The data shown in grey is the spectrophotometry of Roche et al. (1986). Other data shown has been taken from Dudley (1997), Lisenfeld et al. (2000), Roche & Chandler (1993), Soifer et al. (1989) and Wynn-Williams & Becklin (1993). The *dotted and dashed curves* show two choices for the local mid-IR continuum. The *dotted line* interpolates the peaks of the observed data, whereas the *dashed line* assumes a stronger 18 μm silicate absorption.

peaking at 40–60 μm . Also shown in Fig. 5.1 are two equally possible choices of local continuum which we have adopted to analyse the ice, hydrogenated amorphous carbon (HAC) and silicate absorption. This will be discussed in detail in Sect. 5.3.2.

5.3 The mid-IR spectrum of NGC 4418

5.3.1 Spectral features

The mid-IR spectrum of NGC 4418 (Fig. 5.3.1) bears little resemblance to the spectrum of (almost) any other galaxy obtained by ISO. The spectra of normal and starburst galaxies (Rigopoulou et al. 1999; Helou et al. 2000) are dominated by strong PAH emission features. Seyfert galaxies with a clear line of sight to AGN-heated hot dust, on the other hand, are dominated by a strong mid-IR continuum with PAHs barely recognizable (Clavel et al. 2000). The mid-IR spectrum of NGC 4418 is rich in features but does not resemble PAH spectra. Rather it is similar to spectra observed towards heavily extinguished Galactic lines of sight, such as deeply embedded massive protostars or the Galactic center (Fig. 5.3.1). These show no evidence for PAH emission features but do show strong absorption features. A simple criterion for the role of PAH emission and absorption features is based on the location of maxima in

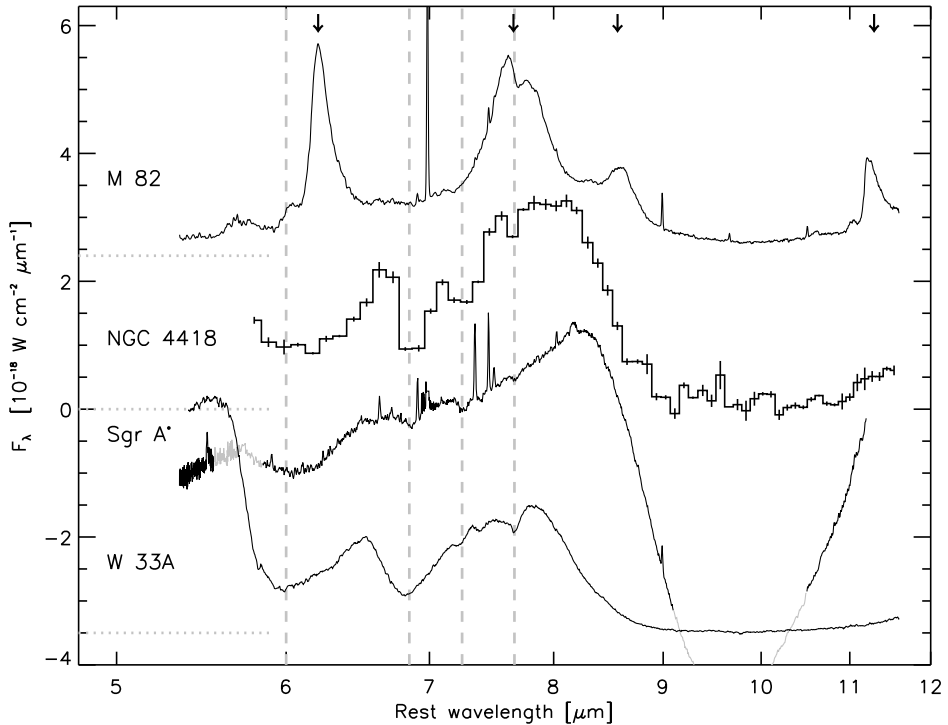


FIGURE 5.2 — A comparison of the ISO spectra of NGC 4418, M 82, the embedded massive protostar W 33A and the Galactic center (Sgr A*). Except for NGC 4418, the spectra have been scaled and offset. We removed the strong $7\mu\text{m}$ [Ar II] line from the Sgr A* spectrum. The *vertical dashed lines* facilitate comparision between the four spectra with well known Galactic absorption features. The *arrows* mark the rest wavelengths of the 6.2 , 7.7 , 8.6 and $11.3\mu\text{m}$ PAH features. The zero flux levels for M 82, NGC 4418 and W 33A are indicated with *horizontal dotted lines*.

the $6\text{--}7\mu\text{m}$ region: PAH spectra show the $6.2\mu\text{m}$ emission feature, whereas absorption spectra show a peak at $6.5\text{--}6.7\mu\text{m}$, which is not an emission feature but a window of reduced absorption between two features.

A detailed comparison of the absorption features with Galactic templates may be able to shed further light on the origin of the extinction in NGC 4418. The absorption features were determined by fitting a local polynomial to the peaks of the $5.8\text{--}8\mu\text{m}$ spectrum of NGC 4418. The absence of the $6.2\mu\text{m}$ PAH feature indicates that emission features are very weak in the spectrum, and justifies this simple procedure to derive the shape and depth of the absorption features. Fig. 5.3.1 shows the resulting NGC 4418 optical depth spectrum along with the optical depth spectrum of ices towards the massive protostar W 33A (Gibb et al. 2000) and the spectrum of the Galactic center (Sgr A*), which displays absorptions due to ices as well as features due to dust in the diffuse ISM (Chiar et al. 2000). The spectrum of NGC 4418 shows absorption features at 6.0 , 6.8 , 7.3 , 7.6 , 10 and $18\mu\text{m}$ (Table 5.1). The $6.0\mu\text{m}$ feature in NGC 4418 is similar to that in the Galactic sources but with a perhaps more pronounced long

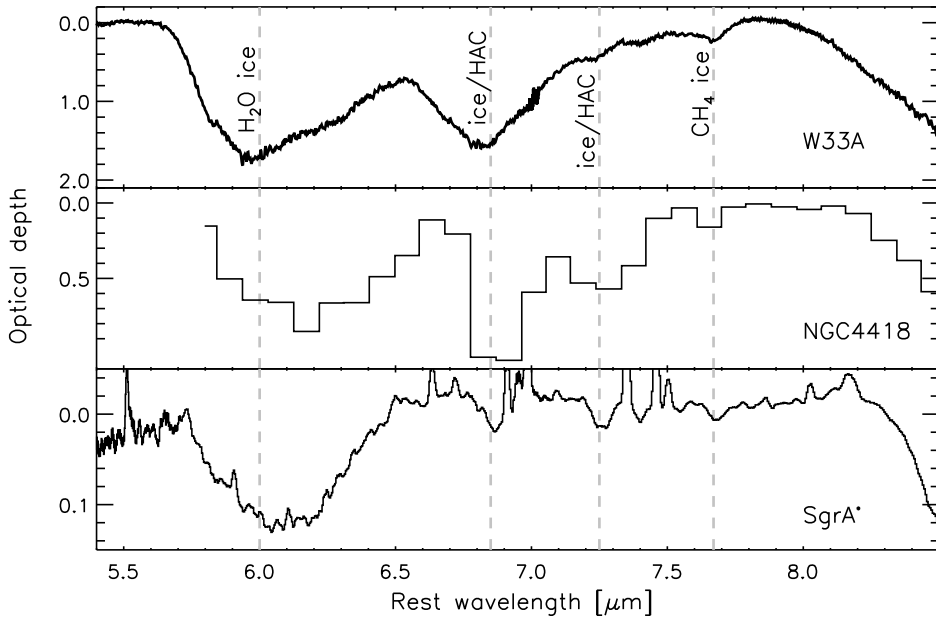


FIGURE 5.3 — The optical depth spectra for W 33A, NGC 4418, and Sgr A*. The *vertical lines* indicate the positions of the 6.0 , 6.85 , 7.3 , and $7.6\mu\text{m}$ ice and HAC absorption bands seen toward Galactic lines of sight.

wavelength wing. The $6.85\mu\text{m}$ feature is considerably narrower than the molecular cloud feature but is similar in width to the diffuse ISM feature. The band at $7.3\mu\text{m}$ is substantially broader than the molecular cloud and diffuse ISM features. The absorption band near $7.6\mu\text{m}$ is similar to that observed locally.

The presence of ice along the line of sight toward NGC 4418 is suggested by the identification of the $7.6\mu\text{m}$ band with CH_4 (Boogert et al. 1996, 1997) and by the presence of the $6.0\mu\text{m}$ band due to H_2O ice (Keane et al. 2001; Chiar et al. 2000). The origins of the $6.85\mu\text{m}$ and $7.3\mu\text{m}$ bands in NGC 4418 are unclear. Interstellar ices also show features at these wavelengths, however, their relative strengths as well as widths are markedly different in NGC 4418. The $6.85\mu\text{m}$ and $7.3\mu\text{m}$ band ratios are consistent with the features observed towards Sgr A*, which have been attributed to CH deformation modes in HAC-like dust grains (Chiar et al. 2000). Thus, as for the Galactic center, both ice characteristics for shielded dense molecular cloud environments and HAC-like grain characteristics for diffuse ISM dust seem to be present along the line of sight. This conclusion could be tested through observations in the $3\mu\text{m}$ window, which contains the strong $3\mu\text{m}$ H_2O ice band and the $3.4\mu\text{m}$ CH stretching modes of HAC materials. Guided by variations seen for the Galactic center region (Chiar et al. 2000), and between M 82 and NGC 1068 (Sturm et al. 2000), we speculate that the relative weight of ice and HAC components may vary considerably among galaxies.

TABLE 5.1 — Observed parameters for the NGC 4418 features.

λ [μm]	τ	τ_{int} [cm^{-1}]	carrier	N [10^{17} cm^{-2}]
6.0	0.8	87	H_2O	73
6.85	1.1	27	HAC?	~ 200
7.3	0.6	12	HAC?	~ 200
7.67	0.12	1.2	CH_4	1.6
9.7	7	—	silicates	—
18	~ 1.5	—	silicates	—
			atomic H	$\sim 2 \times 10^6 *$

(*) Column to the mid-IR dust source calculated assuming Galactic gas to dust ratios.

Note that the X-ray absorbing column to the central engine may be even higher.

5.3.2 Dust and ice column densities

The column densities of the ice species can be derived by dividing the integrated optical depth (τ_{int}) by the molecular band strength (Gerakines et al. 1995; Boogert et al. 1997). Table 5.1 summarizes the computed column densities of CH_4 and H_2O ice. The column densities are consistent with those derived for embedded massive protostellar objects in molecular clouds (Boogert et al. 1996; Keane et al. 2001). Also shown in Table 5.1 are the calculated HAC column densities for the 6.85 and 7.3 μm bands, assuming the intrinsic integrated band intensities for saturated aliphatic hydrocarbons from values by Wexler (1967). These integrated intensities are stronger than other current literature values (Sandford et al. 1991; Furton et al. 1999). For NGC 4418 a substantial fraction of the carbon is locked up in HAC ($\sim 20\%$) as compared to the Galactic center (a few % in Sgr A*, Pendleton et al. 1994).

As mentioned previously (Sect. 5.2), two continua, differing only longward of 8 μm were considered for NGC 4418 (Fig. 5.1). The effect of the different continua on the silicate feature is noticeable when fitting the silicate profile by the Galactic Center Source GCS 3, a pure absorption feature, i.e. no intrinsic emission (Figer et al. 1999). However, the exact optical depth is still difficult to determine due to saturation of the silicate feature in NGC 4418. Adopting the dotted line in Figure 5.1 results in a NGC 4418 silicate profile in which the blue wing is well matched but the red wavelength wing is poorly fitted by the GCS 3 profile. If, however, the dashed line is adopted, then the fit to the red wing improves while still maintaining a reasonable match to the blue wing of the 9.7 μm silicate band. The 9.7 μm and 18 μm optical depths for the second case are $\tau_{9.7} \sim 7$ (corresponding to $A_V \sim 130$) and $\tau_{18} \sim 1.5$. These numbers, along with the derived hydrogen column density, are shown in Table 5.1. The apparent optical depth ratio of the 9.7/18 μm silicate bands, regardless of adopted continuum, is significantly larger than the ratio determined by Demyk et al. (1999) for two Galactic protostars. This might suggest that complex radiative transfer effects are important, which are however beyond the scope of this publication.

5.4 Discussion and conclusions

We have compared the ISO-PHT-S spectrum of NGC 4418 with spectra of our template sources and found no sign of PAH emission, neither from the nucleus, nor from that part

of the disk contained within the $24'' \times 24''$ ISO-PHT-S aperture. Instead we found deep absorption features imposed upon a featureless mid-IR continuum. We identify the $6\text{--}8\mu\text{m}$ absorption features with foreground ices and HAC-like grains.

The nature of the central source in NGC 4418 cannot be inferred from the observed mid-to far-IR spectrum alone, given the absence of any “signposts”, like the $6.2\mu\text{m}$ PAH emission feature ($F_{\text{PAH}} < 6 \times 10^{-20}\text{ W/cm}^2$), and of fine structure lines ([O I], [C II] and [O III], Malhotra et al. (1999); $F_{[\text{Ne II}]} < 2.3 \times 10^{-20}\text{ W/cm}^2$, from archival ISO-SWS data). Both a heavily enshrouded AGN or a similarly obscured nuclear starburst could be responsible for the observed continuum. Even if a starburst could be accommodated within the compact central source (<70 pc in the mid-IR (Scoville et al. 2000) and 25–70 pc at 6 and 20 cm (Eales et al. 1990; Kawara et al. 1990)), it would be highly unlikely to block the escape of any mid-IR starburst indicator from a region of that size. The most likely origin is therefore a heavily enshrouded AGN as suggested previously by Roche et al. (1986), Kawara et al. (1990) and Dudley & Wynn-Williams (1997). The $0.1''$ point source (5 mJy) detected with the Parkes Tidbinbilla Interferometer (PTI) at 13 cm (Kewley et al. 2000, L.Kewley, priv. comm.) may actually pinpoint the AGN itself. Far-IR to millimetre sizes are less well constrained but the warm IRAS colours suggest that the emission in this range also arises in the nuclear region.

Our finding of strong absorptions due to cold silicates and ices in NGC 4418 leads us to believe that the same absorptions may be present in the mid-IR spectra of other galaxies. Indeed, we have found similar absorptions in 17 out of ~ 250 galaxies observed spectroscopically by ISO (Chapter 2). Spectral identifications have to be done with great care since simultaneous presence of PAH emission makes other spectra more complex than the one of NGC 4418.

Since the overall shape of the NGC 4418 $6\text{--}11\mu\text{m}$ spectrum with its maximum near $8\mu\text{m}$ mimicks at first glance a PAH spectrum, we point out the need for high S/N spectra to clearly identify the indicators for bona fide PAH spectra or absorption dominated spectra. The most obvious discriminator is the $6.2\mu\text{m}$ PAH peak to be contrasted with the $6.5\text{--}6.7\mu\text{m}$ pseudo-maximum in absorption spectra, which is due to a window between two absorption features. In Chapter 2 this issue is addressed for our large ISO galaxy sample.

Acknowledgements

The authors wish to thank Olivier Laurent and Leticia Martín-Hernández for performing the ISO-CAM and ISO-LWS data reduction, respectively, as well as Ilse van Bemmel, Peter Barthel, Matthew Lehnert, Dave Sanders, Nick Scoville, Ralf Siebenmorgen, Eckhard Sturm and Dan Tran for discussions.

6

Mid-infrared spectral evidence for a luminous dust enshrouded source in Arp 220

Submitted for publication:

H.W.W. Spoon, A.F.M. Moorwood, D. Lutz, A.G.G.M. Tielens,
R. Siebenmorgen & J.V. Keane
ASTRONOMY & ASTROPHYSICS

WE have re-analyzed the 6–12 μm ISO spectrum of the ultra-luminous infrared galaxy Arp 220 with the conclusion that it is not consistent with that of a scaled up version of a typical starburst. Instead, both template fitting with spectra of the galaxies NGC 4418 and M 83 and with dust models suggest that it is best represented by combinations of a typical starburst component, exhibiting PAH emission features, and a heavily absorbed dust continuum which contributes \sim 40% of the 6–12 μm flux and likely dominates the luminosity. Of particular significance relative to previous studies of Arp 220 is the fact that the emission feature at 7.7 μm comprises both PAH emission and a broader component resulting from ice and silicate absorption against a heavily absorbed continuum. Extinction to the PAH emitting source, however, appears to be relatively low. We tentatively associate the PAH emitting and heavily dust/ice absorbed components with the diffuse emission region and the two compact nuclei respectively identified by Soifer et al. (2002) in their higher spatial resolution 10 μm study. Both the similarity of the absorbed continuum with that of the embedded Galactic protostars and results of the dust models imply that the embedded source(s) in Arp 220 could be powered by, albeit extremely dense, starburst activity. Due to the high extinction, it is not possible with the available data to exclude that AGN(s) also contribute some or all of the observed luminosity. In this case, however, the upper limit measured for its hard X-ray emission would require Arp 220 to be the most highly obscured AGN known.

6.1 Introduction

The galaxy Arp 220 (IC 4553; $cz=5450$ km/s; $D=73$ Mpc) was originally classified by Arp (1966) as a “galaxy with adjacent loops”. Its optical image ($1'' = 352$ pc) shows faint structures, reminiscent of tails or loops, suggesting it to be the remnant of a recent galaxy merger (Toomre & Toomre 1972). IRAS (1983) increased interest in Arp 220 through the discovery of its far-IR luminosity and IR-to-blue ratio which characterized it as an extreme member of the “unidentified infrared sources” discovered during the mission (Houck et al. 1984; Soifer et al. 1984a). When later the spectroscopic redshifts of these “unidentified infrared sources” became available, Arp 220 turned out to have a similarly large IR luminosity ($1.35 \times 10^{12} L_\odot$), making it the nearest member (by a factor of ~ 2) of the new class of Ultra-Luminous InfraRed Galaxies (ULIRGs; Sanders et al. 1988a), with $L_{\text{IR}} \geq 10^{12} L_\odot$. Numerous studies across all wavebands have since examined Arp 220 in close detail, also showing this nearest ULIRG to be unusual in some aspects rather than being typical for the class.

Like most other ULIRGs, Arp 220 is the product of the interaction of two gas-rich disk galaxies (Sanders & Mirabel 1996). Groundbased observations at $10\text{--}30\,\mu\text{m}$ suggest that its luminosity arises in the innermost 250 pc (Wynn-Williams & Becklin 1993). Radio and mm observations reveal its two nuclei to be surrounded by molecular disks of $r \sim 100$ pc, which counterrotate with respect to each other (Sakamoto et al. 1999). The eastern nucleus seems to be embedded within an outer gas disk of $r \sim 1$ kpc, which rotates in the same sense. The western nucleus is connected to the eastern nucleus by a thin gas bridge, traced in H I absorption, and appears to lie above the outer gas disk (Mundell et al. 2001). The projected separation of the two nuclei amounts to 345 pc (0.98''); Baan & Haschick 1995).

At shorter wavelengths (in the UV, optical and near-IR) the view towards the nuclear components is greatly impaired by strong dust extinction of at least $A_V=30\text{--}50$ (Sturm et al. 1996). In the mid-IR, the dust opacity (A_λ) is a factor of 10–100 less than at optical wavelengths and Smith et al. (1989a) used this property to study the nature of the central power source in Arp 220 in the $8\text{--}13\,\mu\text{m}$ (N-band) and $17\text{--}22\,\mu\text{m}$ (Q-band) atmospheric windows. Based on the weakness of the $11.2\,\mu\text{m}$ PAH emission band within the deep $9.7\,\mu\text{m}$ silicate absorption feature, they concluded that only 2–10% of the total infrared luminosity is powered by starburst activity, with an obscured AGN responsible for the rest. Further analysis of the $9.7\,\mu\text{m}$ silicate absorption feature led Dudley (1997) to conclude, however, that the obscured power source resembles a scaled-up embedded protostar.

Not limited to the mid-IR atmospheric windows, ISO spectroscopy revealed two pronounced spectral features in the previously unstudied $5\text{--}8\,\mu\text{m}$ range. In line with ISO observations of Galactic star forming regions, the two features were identified as the $6.2\,\mu\text{m}$ and $7.7\,\mu\text{m}$ PAH emission bands (Genzel et al. 1998). Using the ratio of $7.7\,\mu\text{m}$ PAH emission to the underlying $7.7\,\mu\text{m}$ continuum as a criterium to discern starburst- and AGN-dominated galaxies, Genzel et al. (1998), Lutz et al. (1998), Spoon et al. (1998), Rigopoulou et al. (1999) and Tran et al. (2001) classified Arp 220 as starburst-dominated. High angular resolution groundbased N-band spectroscopy has since shown the $11.2\,\mu\text{m}$ PAH emission in the nuclear region to be diffusely distributed over the central $\sim 2''$ and the starburst associated with the PAH emission not to be able to account for more than 10–50% of the bolometric luminosity (Soifer et al. 2002). In summary, the mid-IR low-resolution spectral diagnostics appear mostly starburst-like but star formation appears quantitatively insufficient to account for the bolometric luminosity, unless strongly obscured or otherwise modified. The same is,

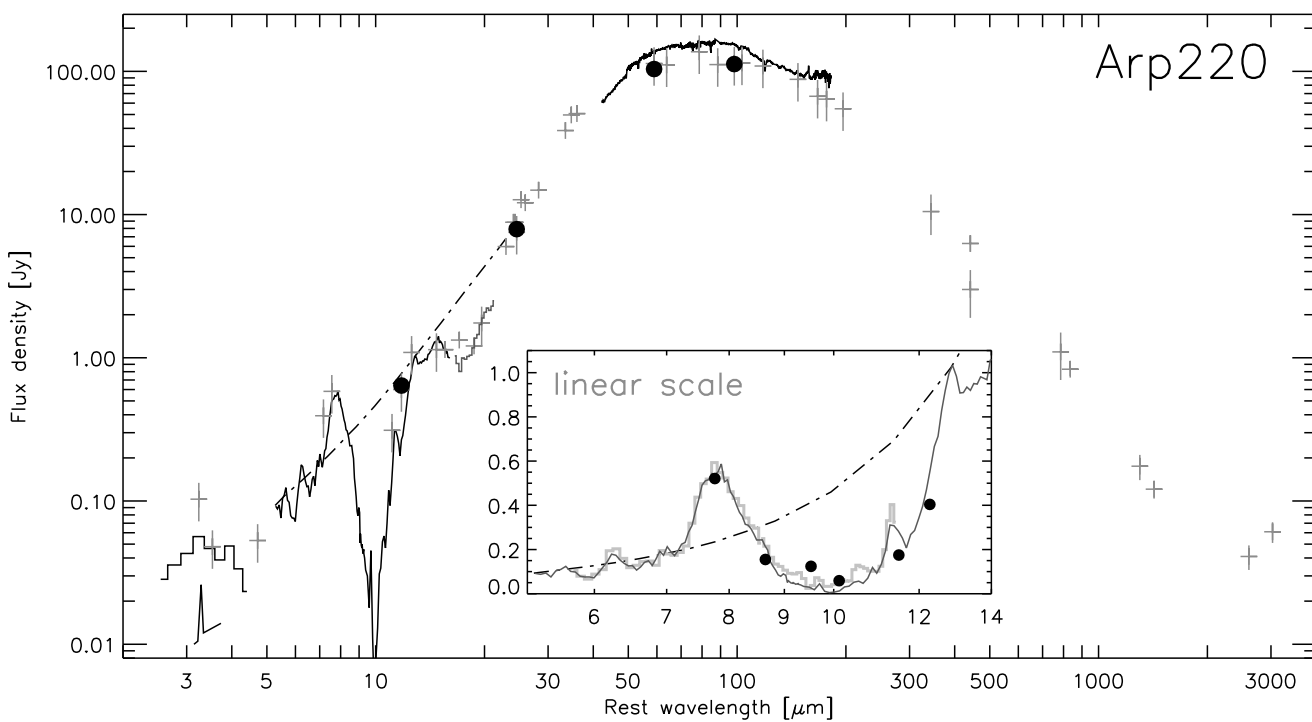


FIGURE 6.1 — The 2–3000 μm spectrum of Arp 220. Filled circles represent the IRAS fluxes. Spectra shown are: the smoothed 2.4–4.9 μm ISO-PHT-S spectrum (Chapter 2); the 3.2–3.8 μm CGS4 spectrum obtained in a 1.2'' slit (Imanishi & Dudley 2000); the 5.0–16 μm ISO-CAM-CVF spectrum (Tran et al. 2001); the 17–22 μm UCL spectrum (Smith et al. 1989a); the smoothed 45–200 μm ISO-LWS spectrum (Fischer et al. 1997). Other spectral data included in the plot are ISO-PHT photometry (Klaas et al. 1997, M.Haas, priv. comm.); ISO-SWS background subtracted continuum measurements (E.Sturm, priv. comm.); UKIRT and SCUBA far-IR photometry (Eales et al. 1989; Dunne et al. 2000; Dunne & Eales 2001) and mm-observations (Anantharamaiah et al. 2000). The dash-dotted line is one choice for the local continuum in the 5–25 μm region (see also Fig. 6.5). The inset shows a comparison of the 5.8–11.7 μm ISO-PHT-S (Chapter 2) and the 5.0–16 μm ISO-CAM-CVF spectra (shown as grey and black lines respectively) with the Keck-MIRLIN photometry (filled circles) of Soifer et al. (1999).

to a lesser degree, true for the more direct tracing of starburst activity by mid-IR fine-structure lines. The ratio of $\sim 1/37$ of starburst ionizing luminosity and bolometric luminosity, derived by Genzel et al. (1998) for this source, is about a factor 2 less than in comparison starbursts.

Since Arp 220 is often regarded as a nearby template for dusty galaxies at high redshift undergoing vigorous star formation (e.g. faint SCUBA sources), it is imperative to clearly identify its power source(s). Despite the quantitative problems with the starburst origin for the luminosity, alluded to above, the general consensus since ISO has been massive young stars (Genzel & Cesarsky 2000). However, the infrared luminous galaxy NGC 4945, which shows no outward evidence for an active galactic nucleus even in ISO observations (Chapter 3; Genzel et al. 1998), has turned out to contain a heavily obscured AGN visible only in hard X-rays (Iwasawa et al. 1993; Done et al. 1996; Guainazzi et al. 2000). For Arp 220, *BeppoSAX* and Chandra observations do not detect a similar hard X-ray source (Iwasawa et al. 2001; Clements et al. 2002). The only possibility for an energetically significant AGN to exist in Arp 220 would therefore be in the form of a deeply embedded source, hidden behind a ‘Compton-thick’ shell of $N_{\mathrm{H}} \geq 10^{25} \text{ cm}^{-2}$ with a covering factor close to unity (Iwasawa et al. 2001). The presence of huge amounts of molecular gas in the central parts ($\sim 10^{10} M_{\odot}$; Scoville et al. 1997; Sakamoto et al. 1999) indicates that sufficient obscuring material is indeed at hand. And the very large $850 \mu\text{m}$ dust-continuum flux to $7.7 \mu\text{m}$ PAH flux (Haas et al. 2001) could mean that the luminosity of this embedded source is redistributed into the far-IR.

6.2 The infrared spectrum of Arp 220

The $2\text{--}3000 \mu\text{m}$ spectral energy distribution of Arp 220 (Fig. 6.1) is characterised by a steeply rising dust continuum, setting in around $4\text{--}5 \mu\text{m}$, and leading up to a remarkably strong far-IR flux peak at $60\text{--}100 \mu\text{m}$. The most prominent features in the infrared spectrum are the silicate absorption features at $9.7 \mu\text{m}$ and $18 \mu\text{m}$ and a broad flux peak at $7.8 \mu\text{m}$.

6.2.1 The mid-IR spectrum of Arp 220

In Fig. 6.2 we compare the mid-IR spectra of Arp 220, NGC 4418 and the central region of the starburst galaxy M 83. At first sight the three spectra look quite similar. The spectral structure in the spectrum of NGC 4418 is, however, the product of strong ice and silicate absorptions (Chapter 5), whereas the spectrum of M 83 is dominated by the commonly observed emission bands of Polycyclic Aromatic Hydrocarbons (PAHs). The spectrum of Arp 220 shows characteristics of both: PAH emission is readily detected at $6.2 \mu\text{m}$ and $11.2 \mu\text{m}$ (and in the groundbased $3 \mu\text{m}$ spectrum; Imanishi & Dudley 2000), while absorptions from water ice and silicates are found at $6.0 \mu\text{m}$ and $9.7 \mu\text{m}$, respectively (Chapter 2). The strongest feature in the spectrum, peaking at $7.7 \mu\text{m}$, has been previously attributed exclusively to PAH emission. On closer inspection, however, the feature seems to be a blend of a $7.7 \mu\text{m}$ PAH emission feature and a continuum peak resulting from absorption by ice on the short wavelength side and silicates on the long wavelength side.

Close comparison of the $7.7 \mu\text{m}$ feature in the spectrum of Arp 220 with the $7.7 \mu\text{m}$ PAH feature in the spectrum of the starburst galaxy M 83 (Fig. 6.3) shows that the $7.7 \mu\text{m}$ feature in Arp 220 is quite broad. Moreover, the ratio of the $7.7 \mu\text{m}$ peak to the $6.2 \mu\text{m}$ and $11.2 \mu\text{m}$ PAH bands is very large in Arp 220 compared to other sources (cf. Fig. 6.3). The profile of $7.7 \mu\text{m}$ PAH emission bands is, however, known to be very stable over a wide range of

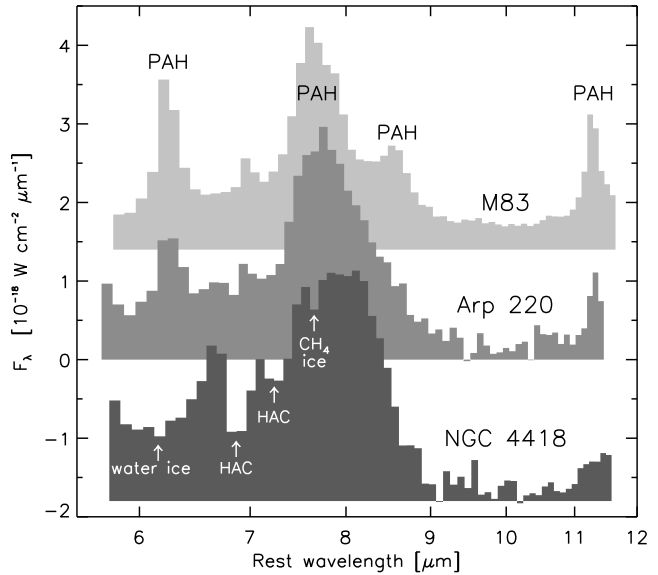


FIGURE 6.2— A comparison of the ISO-PHT-S spectra of M 83, Arp 220 and NGC 4418. While the spectrum of M 83 is dominated by PAH emission bands, the spectrum of NGC 4418 is dominated by absorption bands of ices and silicates. The spectrum of Arp 220 shows characteristics of both. The spectra of M 83 and NGC 4418 have been scaled and offset.

integrated galaxy spectra (Helou et al. 2000). Peeters et al. (2002a) found that Galactic ISM spectra show a similarly stable $7.7\text{ }\mu\text{m}$ PAH feature. Only for evolved stars and isolated Herbig AeBe stars are the width and central wavelength of the $7.7\text{ }\mu\text{m}$ PAH feature known to vary (Peeters et al. 2002a). These stars are however very unlikely to dominate the spectrum of Arp 220. Therefore, there is no reason to assume that PAH features in Arp 220, if present, should have an intrinsically different shape than in any other galaxy spectrum. Likewise, while the relative strengths of the PAH features are known to vary from source to source, no Galactic or extragalactic sources show such extreme ratios as Arp 220 (Peeters et al. 2002a). Strong extinction as a cause for the unusual strength and width of the $7.7\text{ }\mu\text{m}$ peak can also be ruled out. This is best illustrated by fitting a starburst spectrum (here: M 83) to the peak of the $7.7\text{ }\mu\text{m}$ feature and applying foreground extinction (Fig. 6.3). The weakness of the $6.2\text{ }\mu\text{m}$ PAH feature is reproduced well for a foreground extinction $A(V)=105$, but the spectrum beyond $8.5\text{ }\mu\text{m}$ and the $8.6\text{ }\mu\text{m}$ and $11.3\text{ }\mu\text{m}$ PAH features are not. While the relative feature strengths depend on the adopted extinction curve (Sect. 6.3.2), no plausible extinction will be able to widen the $7.7\text{ }\mu\text{m}$ feature. We here propose instead the weakness of the $6.2\text{ }\mu\text{m}$ PAH feature to be indicative of an unusually small contribution of the family of PAH emission features to the mid-IR spectrum of Arp 220 and the unusual strength and width of the $7.7\text{ }\mu\text{m}$ feature to be the result of an underlying mid-IR continuum, peaking strongly near $7.7\text{ }\mu\text{m}$. Evidence in support for this model is presented below.

6.2.2 Broad $7.7\text{ }\mu\text{m}$ feature similar to Mon R2:IRS 1+2

The shape of the $7.7\text{ }\mu\text{m}$ feature in Arp 220 appears to be unique among a sample of more than 250 galaxies observed spectroscopically in the $6\text{--}12\text{ }\mu\text{m}$ range (Spoon et al. in prep.). The feature has, however, a Galactic counterpart: the ISO-SWS spectrum of the combined line of sight to the sources Mon R2:IRS 1+2 (Fig. 6.4). Mon R2 is a massive Galactic star formation region. Infrared observations show several compact sources and extended emission in the

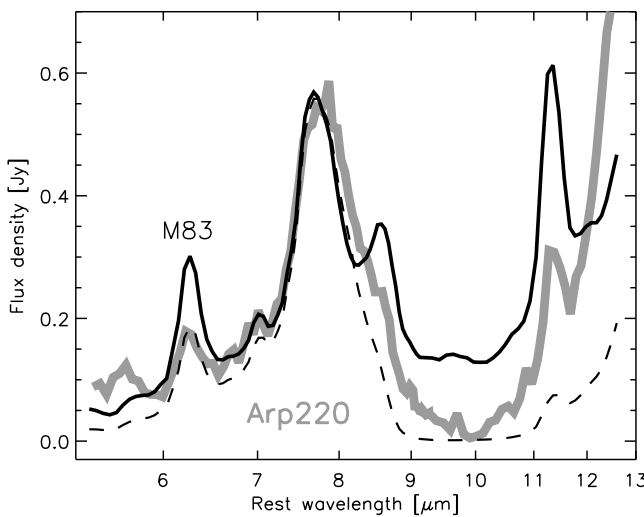


FIGURE 6.3 — Comparison of the spectra of Arp 220 (thick grey line) and the central region of starburst galaxy M83 (black line). The M83 spectrum shows strong PAH emission features at 6.2, 7.7, 8.6 and 11.2 μm . In contrast, in Arp 220 the 6.2, 8.6 and 11.2 μm features are weak. The black dashed line illustrates the effect of strong extinction ($A(V)=105$; $A(7.7 \mu\text{m})=1.2$) on the M83 spectrum. Both versions of the M83 spectrum have been scaled to match the 7.7 μm peak in the spectrum of Arp 220.

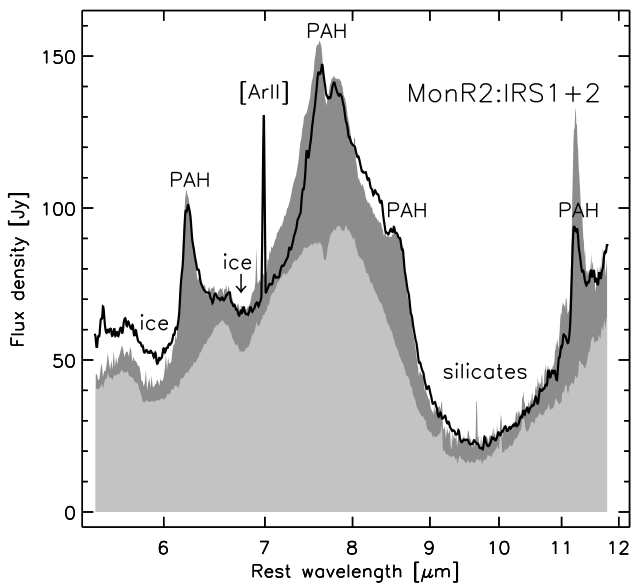
central region of the giant molecular cloud (Beckwith et al. 1976). An elliptical ring encloses two IR sources, IRS 1 and IRS 2. IRS 1, with a presumed spectral type of B0 (Downes et al. 1975; Howard et al. 1994), is the exciting source of the compact H II region enclosed by the IR ring (Massi et al. 1985). IRS 2 is still deeply embedded in the molecular cloud and most probably at an earlier stage of formation. Given this confused line of sight, the broad 7.7 μm feature in the spectrum of Mon R2:IRS 1+2 may well be the result of the superposition of a strongly absorbed continuum, peaking at $\sim 8 \mu\text{m}$, and a ‘normal’ 7.7 μm PAH emission feature. Fig. 6.4 shows the result of a crude decomposition of the Mon R2:IRS 1+2 spectrum into the ISO-SWS spectra of the embedded protostar NGC 7538:IRS 9 and the reflection nebula NGC 7023. The fit is quite good given the fact that the columns of ices and silicates vary a lot from one embedded protostar to the other. Note that the 8.6 μm PAH feature is not suppressed by extinction, but instead stands out as a shoulder on the flank of the 7.7 μm feature, filling in the blue wing of the 9.7 μm silicate absorption feature.

6.2.3 Mid-IR continuum similar to NGC 4418

In Fig. 6.5 we compare the mid-IR spectra of Arp 220 and NGC 4418. The spectrum of NGC 4418 is dominated by strong silicate absorption bands at 9.7 μm and 18 μm (Roche et al. 1986) and ice absorption bands at 6.0 μm (H_2O), 6.85 μm & 7.25 μm (Hydrogenated Amorphous Carbons; HAC) and 7.67 μm (CH_4) (Chapter 5). No mid-IR emission features, including the commonly detected 12.81 μm [Ne II] fine structure line, have been detected so far (Chapter 5; R. Siebenmorgen, unpublished TIMMI2 spectra). A first order estimate for the mid-IR local continuum of NGC 4418 is obtained by fitting a power law through two feature-free “pure continuum” pivots at 8.0 μm and 25 μm (the dashed continuum in Fig. 6.5). Another, more conservative choice of continuum, assuming “pure continuum” at 6.7 μm and 13 μm too, is shown as a dotted line in Fig. 6.5.

The mid-IR spectrum of Arp 220 (Fig. 6.5) looks very similar to the pure absorption spectrum of NGC 4418, except for the presence of weak emission features due to PAHs (6.2 μm ,

FIGURE 6.4— The line of sight to the embedded protostar MonR2:IRS 1 passes through the ultra compact H II region Mon R2:IRS 2. The ISO-SWS spectrum of Mon R2:IRS 1+2 (black) hence shows features of both type of environments: PAH emission from the ultra compact H II region and a dust and ice absorbed continuum from the embedded protostar. Here we show a simple 2-component fit to the Mon R2:IRS 1+2 spectrum, using the ISO-SWS spectra of the protostar NGC 7538:IRS 9 (light grey area) and the reflection nebula NGC 7023 (dark grey area) as fitting templates.



$7.7\text{ }\mu\text{m}$ and $11.2\text{ }\mu\text{m}$), $6.91\text{ }\mu\text{m}$ H_2 0–0 S(5) and $12.81\text{ }\mu\text{m}$ [Ne II] (Sturm et al. 1996; Genzel et al. 1998). Using the same method as for NGC 4418, we estimate the local continuum in Arp 220 by fitting a power law through two feature-free “pure continuum” pivots at $5.5\text{ }\mu\text{m}$ and $25\text{ }\mu\text{m}$ (the dashed continuum in Fig. 6.5). A more conservative estimate for the local continuum is obtained by including “pure continuum” pivots at $6.7\text{ }\mu\text{m}$ and 14 – $15\text{ }\mu\text{m}$ as well. This results in the dotted continuum for Arp 220. The dash-dotted continuum in Fig. 6.5 is a compromise between the two. Note that besides the obvious silicate absorption features at $9.7\text{ }\mu\text{m}$ and $18\text{ }\mu\text{m}$ all three continua imply the presence of an absorption feature due to water ice, which runs from $5.7\text{ }\mu\text{m}$ to $8.0\text{ }\mu\text{m}$ (Chapter 2). The emission features within this range, $6.2\text{ }\mu\text{m}$ PAH, $6.91\text{ }\mu\text{m}$ H_2 0–0 S(5), $7.7\text{ }\mu\text{m}$ PAH and likely (though not targeted by ISO-SWS) $7.0\text{ }\mu\text{m}$ [Ar II], fill up the absorption partially or even turn it into emission.

Given the close similarity of the mid-IR continua of Arp 220 and NGC 4418 and the presence of strong silicate and ice absorption features in both spectra, the mid-IR spectrum of Arp 220 seems to be the superposition of a strongly absorbed continuum and a typical PAH-dominated spectrum. In the next Section we will test this hypothesis by decomposing the mid-IR spectrum of Arp 220 into a PAH-dominated spectrum and an absorbed continuum.

6.3 Mid-IR spectral decomposition

In order to test the superposition hypothesis, we have fit several combinations of a mid-IR absorbed continuum source and a PAH template to the observed Arp 220 mid-IR spectrum. Our method differs from existing methods (e.g. Tran et al. 2001) by using observed templates instead of model mid-IR continua. The latter usually do not take into account the complex radiative transfer effects due to ices and silicates that give rise to the exotic observed spectral shapes of the continuum sources and hence may fail to reproduce their spectra properly.

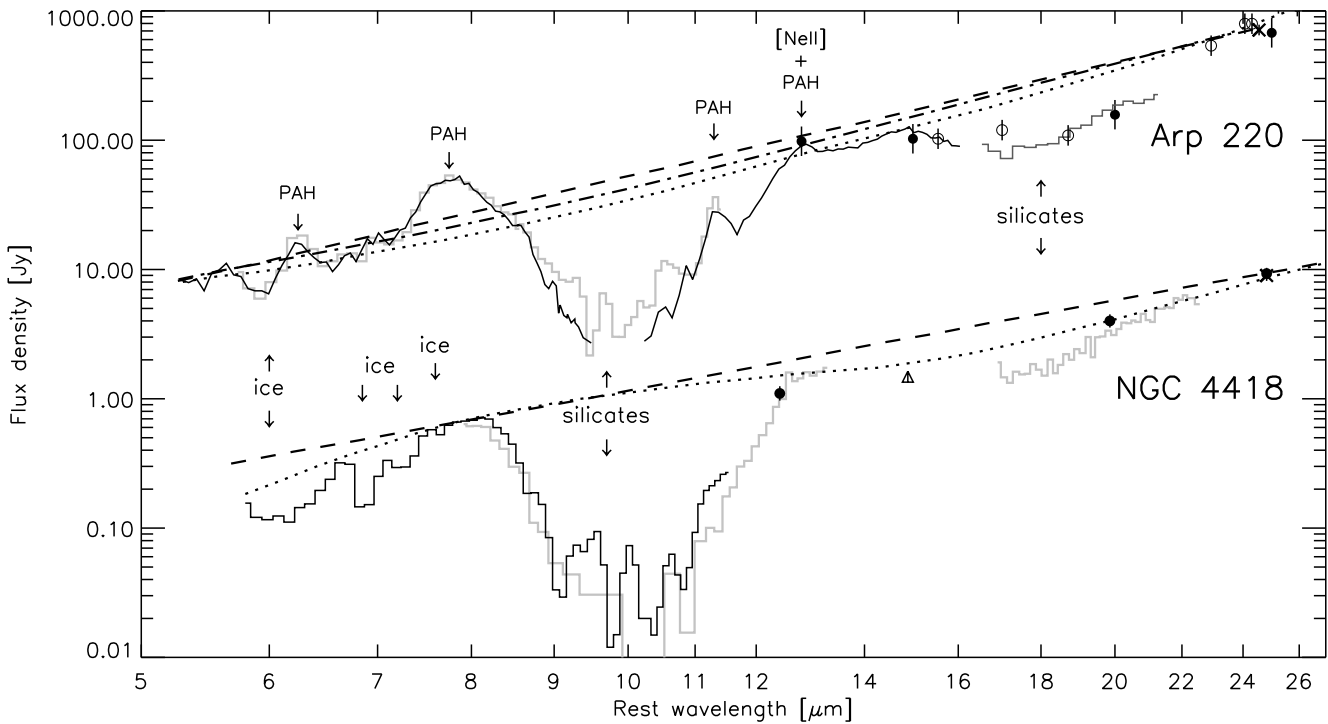


FIGURE 6.5 — Comparison of the mid-IR spectra of Arp 220 (multiplied by 90) and NGC 4418. For **Arp 220** the following spectra are plotted: in *black* the 5–16 μm ISO-CAM-CVF spectrum, in *light grey* the 5.6–11.4 μm ISO-PHT-S spectrum and in *dark grey* the 17–22 μm UCL spectrum (Smith et al. 1989a). ISO-SWS continuum points are marked by *open circles*, ISO-PHT photometry by *filled circles* and the IRAS 25 μm flux by a *cross*. For **NGC 4418** the spectra plotted are: in *black* the 5.6–11.4 μm ISO-PHT-S spectrum and in *light grey* the 8–13 μm and 17–23 μm UCL spectra of Roche et al. (1986). IRTF photometry (Wynn-Williams & Becklin 1993) is marked by *filled circles*, ISO-CAM (LW3) photometry by a *triangle* and the IRAS 25 μm flux by a *cross*. The positions of absorption and emission bands are indicated, as are several choices for the local continuum for each object.

6.3.1 PAH and continuum templates

The absorbed continuum sources span a range of spectral shapes (Fig. 6.6), with $6\text{--}12\,\mu\text{m}$ peak flux wavelengths ranging between $7.7\,\mu\text{m}$ for I03344–2103 and $8.3\,\mu\text{m}$ for the Galactic center (Sgr A *). All four sources exhibit a strong $9.7\,\mu\text{m}$ silicate feature and three of them also show clear signs of ice absorption features. The silicate optical depths range from $\tau_{\text{sil}} \sim 1.9^1$ for Sgr A * and $\tau_{\text{sil}} > 1.9$ for IRAS 00183-7111 (Chapter 2) to $\tau_{\text{sil}} > 3.5$ for IRAS 03344–2103 and $\tau_{\text{sil}} > 3.7$ for NGC 4418. For the latter, Roche et al. (1986) claim an even higher value, $\tau_{\text{sil}} \sim 7$. Judging from the steepness of the blue wing of its silicate feature (Fig. 6.6), NGC 4418 may well have the largest dust column of all four absorbed continuum templates.

As PAH templates we selected the reflection nebula NGC 7023, the Orion Bar star forming region and the central region of the starburst galaxy M 83. The latter has been preferred over other nearby starburst templates, like M 82 or NGC 253, because its $5\text{--}16\,\mu\text{m}$ spectrum appears less affected by extinction than the other two galaxy spectra. Together, the three selected PAH templates (Fig. 6.6) are meant to cover the full range of spectral shapes from quiescent PDRs to intense star forming regions. Note the large difference in strength of the $9\text{--}12\,\mu\text{m}$ continuum between the spectra of NGC 7023 and the Orion Bar. The difference is attributed to the presence of hot dust in the Orion H II region, which is absent in the cold environment of a reflection nebula. In contrast, the PAH spectra are quite similar, except for a somewhat weaker $6.2\,\mu\text{m}$ PAH feature relative to the $7.7\,\mu\text{m}$ PAH feature in M 83 and a somewhat stronger $11.2\,\mu\text{m}$ PAH feature relative to the $7.7\,\mu\text{m}$ PAH feature in the Orion Bar spectrum.

6.3.2 The extinction law at mid-infrared wavelengths

Unlike the extinction law at optical or near-IR wavelengths, surprisingly little is known about the shape and the general applicability of the extinction law at mid-IR wavelengths. Results obtained for different lines of sight vary considerably. A good definition of the shape of the mid-IR extinction law is, however, important for a good decomposition of the Arp 220 spectrum.

The differences among extinction laws appear largest at $3\text{--}8\,\mu\text{m}$. Assuming a standard graphite-silicate mixture, a $\lambda^{-1.75}$ power law fall-off is expected for this wavelength range (Fig. 6.7; Draine 1989; Martin & Whittet 1990). ISO measurements of molecular hydrogen towards the Orion Peak-1 as well as H I recombination lines of compact H II regions support this model (Bertoldi et al. 1999; Martín-Hernández et al. 2003). H I recombination line observations, probing the dusty, complex line of sight to the Galactic center (Sgr A *), indicate, however, a nearly flat extinction curve between 3 and $8\,\mu\text{m}$ (Fig. 6.7; Lutz 1999), with A_λ/A_V a factor ~ 4 higher at $7\,\mu\text{m}$ compared to the extinction law of Draine (1989). This would point to the presence of larger, fluffier grains in the line of sight to the Galactic center than towards other Galactic sources (e.g. Kruegel & Siebenmorgen 1994).

Beyond $8\,\mu\text{m}$, the 9.7 and $18\,\mu\text{m}$ bands of amorphous silicates dominate the extinction curve. Both the shape (FWHM) and the strength of the bands (both $A_{9.7}/A_V$ and $A_{9.7}/A_{18}$) are reported to vary between different lines of sight (e.g. Fig. 6.6) and from observer to observer (Draine 1989). Here we will adopt the astronomical silicate profile of Weingartner

¹this is the apparent optical depth, measured from the ISO-SWS spectrum (Fig. 6.6). Corrected for silicate emission along the line of sight the true value is 3.6 ± 0.3 Roche & Aitken (1985).

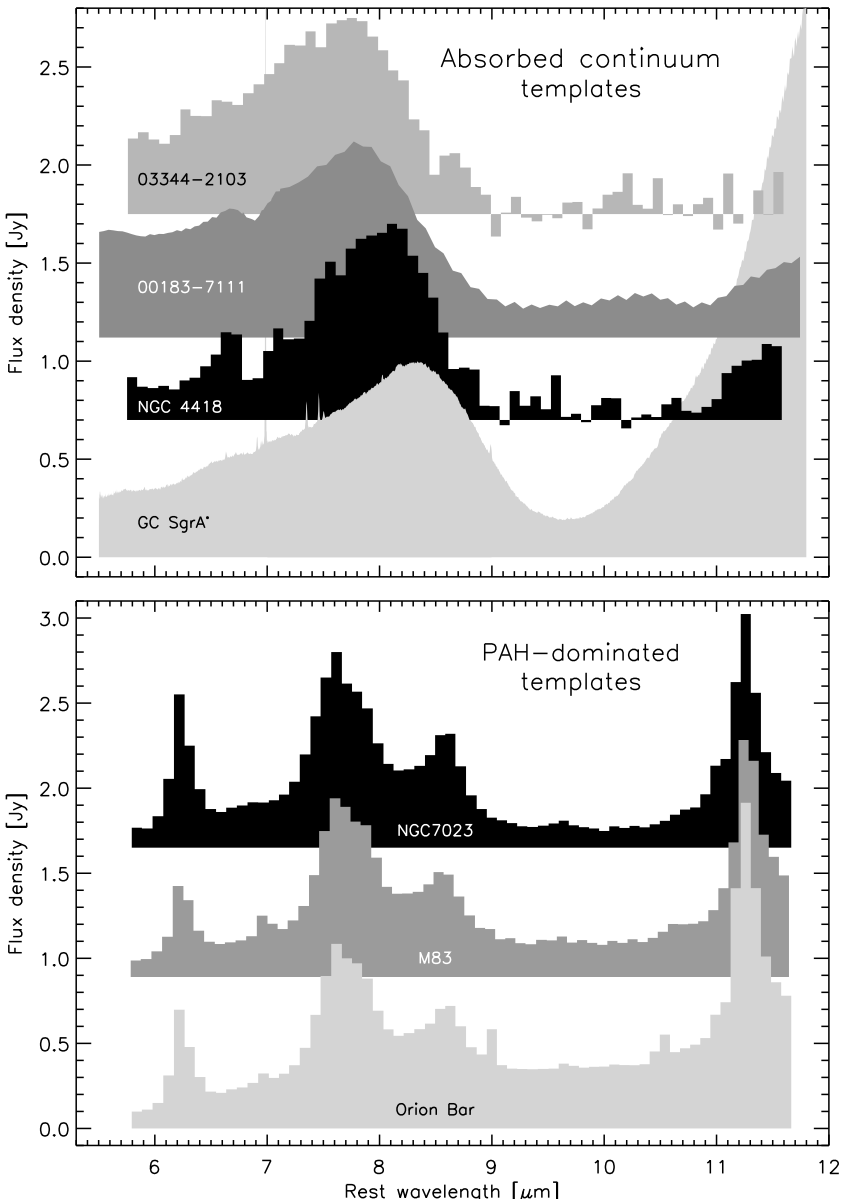


FIGURE 6.6— PAH and continuum templates used in the decomposition of the observed mid-IR spectrum of Arp 220. **Upper panel:** Four mid-IR absorbed continuum spectra. The spectra are shown at their instrumental resolution: $R \sim 90$ for IRAS 03344–02103 and NGC 4418; $R \sim 40$ for IRAS 00183–7111; $R \sim 1000$ for Sgr A*. The spectra have been normalized to their 7.5–8.5 μm peak fluxes and are sorted according to the central wavelength of their 7.5–8.5 μm peak flux. **Lower panel:** Three mid-IR PAH-dominated spectra, shown at a spectral resolution $R \sim 90$. The spectra have been normalized to their 7.7 μm peak fluxes and are sorted in order of increasing 9–12 μm continuum.

& Draine (2001).

In order to explore the effect of differences between mid-IR extinction curves on the spectral decomposition, we here define two extinction curves which should be representative for the range of extinction properties between different lines of sight. The extinction law, which we will refer to as `Draine_local`, combines the $\lambda^{-1.75}$ power law fall-off for $\lambda < 8.14 \mu\text{m}$ with a silicate feature of strength $A_{9.7}/A_V=0.06$ typical for the local solar neighbourhood (Roche & Aitken 1984). In contrast, the `Lutz_gc` extinction law is ‘flat’ from 3–8 μm and has a silicate feature strength of $A_{9.7}/A_V=0.14$ (Lutz 1999). Both extinction laws are shown in Fig. 6.7

6.3.3 Decomposition method

For each continuum and PAH template combination we have explored a four parameter space for the best fit to the observed Arp 220 ISO spectrum. The four parameters explored are:

- the contribution of the absorbed-continuum spectrum to the total spectrum
- the contribution of the PAH spectrum to the total spectrum
- the adopted extinction law: either `draine_local` or `Lutz_gc`
- the amount of reddening (A_V) on the PAH spectrum

For a 2-component model spectrum to give a good fit to the Arp 220 spectrum, the model spectrum has to reproduce several key spectral features which make the Arp 220 spectrum stand apart from other mid-IR galaxy spectra. These key features are, in order of decreasing importance:

- the width of the 7.7 μm feature
- the absence of the 8.6 μm PAH feature in the red flank of the 7.7 μm feature
- the strength of the 11.2 μm PAH feature relative to the 7.7 μm feature
- the strength of the 6.2 μm PAH feature relative to the 7.7 μm feature
- the depth of the 9.7 μm silicate feature
- the profile of the 6.0 μm water ice feature

6.3.4 Decomposition results

In Fig. 6.8 we present the best fits to the 6–12 μm Arp 220 spectrum. The fits clearly show that an appreciable contribution from a strongly absorbed continuum source (e.g. NGC 4418, or a stronger absorbed version of this spectrum) is required for a good fit to the observed spectral features. Compared to the extinction on the continuum source ($\tau_{\text{sil}}>3.7$), the extinction on the PAH component is minor, ranging from $\tau_{\text{sil}}=0.2$ to 1.4). At these small obscurations, the choice of extinction law does not play an important role. The best fits further reveal that a direct measurement of the silicate optical depth from the ISO spectrum will be severely hampered by the presence of filled-in emission from the PAH component (see Fig. 6.8), resulting in a serious underestimation of the true silicate optical depth.

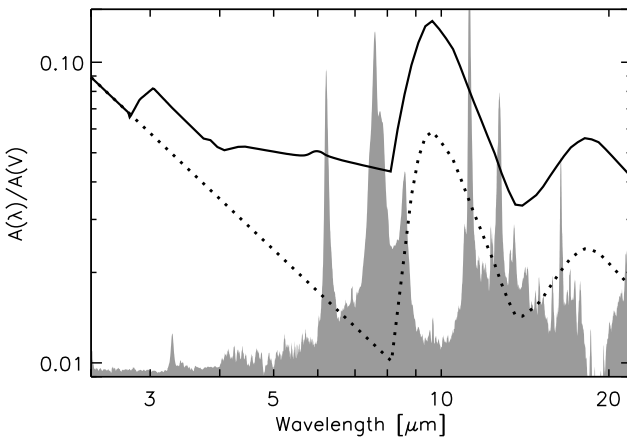


FIGURE 6.7 — Comparison of two mid-IR extinction laws, overlayed on the PAH emission spectrum of reflection nebula NGC 7023 (grey area). The Galactic center extinction law of Lutz (1999) is shown as a *black line*, the extinction law of Draine (1989) for the local solar neighbourhood as a *dotted line*. The extinction laws are referred to as `Lutz_gc` and `draine_local`, respectively.

Other combinations of our continuum and PAH templates fail to reproduce key features of the Arp 220 spectrum. Fits involving the continuum templates IRAS 03344–2103 and IRAS 00183–7111, for example, fail to fit the width of the $7.7\text{ }\mu\text{m}$ feature, because their continua peak at too short a wavelength (Fig. 6.6). The continuum of Sgr A*, on the other hand, does peak at the right wavelength, but its silicate feature is too shallow and too narrow to leave much room for any contribution from the PAH component to the 8.5 – $11.5\text{ }\mu\text{m}$ fit. Strong extinction will have to be imposed on the PAH component to minimize its contribution to the 8.5 – $11.5\text{ }\mu\text{m}$ fit. This, however, also minimizes the flux in the $11.2\text{ }\mu\text{m}$ PAH feature to beyond what is still consistent with the observations. A similar problem exists for the Orion Bar PAH template. Its $10\text{ }\mu\text{m}$ continuum is the strongest among the three PAH templates (Fig. 6.6) and hence requires an appreciable extinction on its contribution to any Arp 220 fit; too much for a good fit to the $11.2\text{ }\mu\text{m}$ PAH feature. PAH template NGC 7023 suffers from the opposite problem. Its continuum is too weak to produce good fits to the Arp 220 spectrum.

Absorptions by ices play an important role in distorting the spectral shape of strongly dust enshrouded sources like NGC 4418 (Chapter 5; Fig. 6.6). Their impact is, however, small for moderately absorbed spectra like the line of sight to Sgr A* (Fig. 6.6). On the other hand, as the abundance of ices is variable and changes from one Galactic molecular cloud to another, it is useful to assess the impact of an increased water ice abundance on our fits. We therefore ran tests with a `Lutz_gc` extinction law with five times higher water ice abundance and compared the best fitting parameters to those for the unmodified `Lutz_gc` extinction law. Only for those template combinations requiring high foreground extinction on the PAH template were the individual parameters found to change noticeably (but $<10\%$). For all other combinations, including our best fits (Fig. 6.8), the effects turn out to be negligible. Further experiments with an extinction curve supplemented with both the $6.0\text{ }\mu\text{m}$ water ice and $6.8\text{ }\mu\text{m}$ HAC absorption features show that under these conditions successful fits can be obtained also with an (additionally obscured) Sgr A* continuum. This stresses the presence of ice absorptions in the continuum as a key requirement for a successful fit, and one of the reasons why NGC 4418 produces the best results in our original fits.

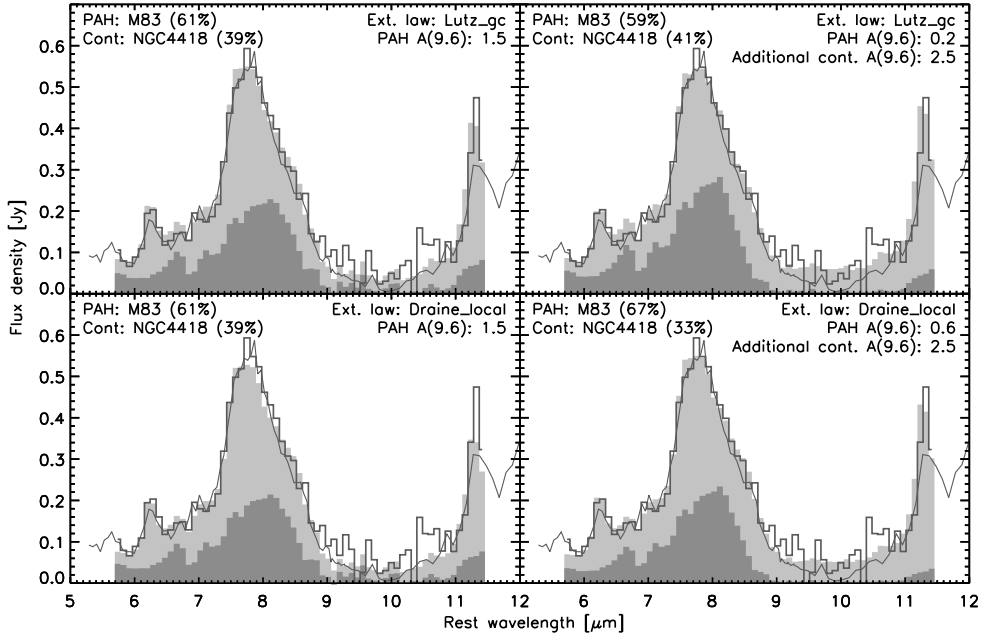


FIGURE 6.8.— Four 2-component fits to the Arp 220 mid-IR ISO spectra (ISO-PHT-S: *dark grey histogram*; ISO-CAM-CVF: *dark grey line*). In each panel the *dark grey area* represents the contribution of the continuum component and the *light grey area* the contribution of the PAH component. The PAH component is the same in all panels: the spectrum of the starburst galaxy M 83. The absorbed continuum component differs between left and right panels. In the **left panels** it is NGC 4418 as observed; in the **right panels** it is NGC 4418 as seen through an additional screen of $A(9.6 \mu\text{m})=2.5$, equivalent to a factor ten more attenuation at $9.6 \mu\text{m}$. The fractional contribution of each fit component to the total $6-12 \mu\text{m}$ fit is stated in brackets behind the name of the template. Also indicated is the amount of $9.6 \mu\text{m}$ screen extinction on the PAH component.

6.4 Discussion

Our successful decomposition of the $6-12 \mu\text{m}$ ISO-PHT-S spectrum into a strongly absorbed continuum and a weakly absorbed PAH component confirms our initial suspicion that a) its exotic mid-IR spectrum resembles a blend of the spectra of NGC 4418 and M 83 (Fig. 6.2) and b) that the only difference between the mid-IR spectra of Arp 220 and a strongly ice- and dust-absorbed source like NGC 4418 is the additional presence of PAH emission features in the spectrum of Arp 220 (Fig. 6.5).

6.4.1 Identification of the spectral components

The large difference in obscuration of the two spectral components of our fit indicates that these most likely represent two *spatially* separate components. Recent high angular resolution N-band spectroscopy of the nuclear region (Soifer et al. 2002) show the $11.2 \mu\text{m}$ PAH emission and the $11-12 \mu\text{m}$ continuum emission to have clearly different distributions. While

the absorbed-continuum emission clearly peaks on the two nuclei, the PAH emission extends over a far wider area and does not peak on either nucleus. We therefore associate our absorbed continuum component with the two nuclei and our PAH component with the region in between and around the two nuclei.

We estimate the infrared luminosity associated with the diffusely distributed PAH component from the observed $6.2\text{ }\mu\text{m}$ PAH emission feature by assuming a generic conversion ratio between $L(6.2\text{ }\mu\text{m PAH})$ and $L(\text{IR})$ and taking into account the weak obscuration on the $6.2\text{ }\mu\text{m}$ PAH feature as indicated by our best 2-component model fits. We derive the $L(6.2\text{ }\mu\text{m PAH})/L(\text{IR})$ ratio from our sample of ~ 70 mid-IR ISO spectra of normal and starburst galaxies and obtain a value of 0.003 ± 0.001 . Assuming this conversion factor applies also to the conditions in the ULIRG Arp 220 and applying it to our four best fitting template combinations (Fig. 6.8) we find the infrared luminosity associated with the diffuse PAH component to amount to $1.2\text{--}2.1 \times 10^{11}\text{ }L_{\odot}$; 9–15% of the total infrared luminosity of the system. A comparable result is obtained from the peak flux density of the $7.7\text{ }\mu\text{m}$ PAH feature, using the empirical conversion factor $S(7.7\text{ }\mu\text{m PAH})/F(\text{IR})=10^{-11.84}\text{ Jy W}^{-1}\text{ m}^2$ for starburst galaxies, determined by Lutz et al. (2003). Taking into account the weak obscuration on the $7.7\text{ }\mu\text{m}$ PAH feature (ranging from $A(7.7\text{ }\mu\text{m})=0.07$ to 0.49 for our best 2-component fits), the implied infrared luminosity is $0.7\text{--}1.8 \times 10^{11}\text{ }L_{\odot}$; 5–13% of the total infrared luminosity of the system. The results from both methods are in complete agreement with the value derived by Soifer et al. (2002), who inferred a PAH-associated infrared luminosity of $1.2 \times 10^{11}\text{ }L_{\odot}$ (9% of the total infrared luminosity) from their N-band spectrum. Based on the small scatter between the three different methods, we conclude that the infrared luminosity associated with the diffusely distributed PAH component in Arp 220 amounts to 5–15% of the bolometric luminosity of the system, with some uncertainty due to the trend towards a larger FIR/PAH emission ratio with increasing interstellar radiation field intensity in galaxies (e.g. Dale et al. 2001).

The literature reports the detection in the nuclear region of several near- and mid-IR recombination and fine structure lines from star formation. While no spatial information is available as to the origin of the mid-IR lines (Sturm et al. 1996), both the near-IR recombination lines (Armus et al. 1995; Larkin et al. 1995) and the radio recombination lines (Anantharamaiah et al. 2000) are mostly concentrated towards the two nuclei, rather than following the diffuse PAH component. Extinction estimates range from $A(V)\sim 10$ in the near-IR (Armus et al. 1995; Larkin et al. 1995) up to $A(V)\sim 40\text{--}60$ in the mid-IR and radio (Sturm et al. 1996; Anantharamaiah et al. 2000), with noticeable uncertainties e.g. due to the measured line fluxes. This suggests that the starburst activity traced by the emission lines includes an intermediate obscuration component that is more concentrated on the nuclei than the PAH emission. Two factors suggest this component includes intermediate obscuration parts of the regions around the two nuclei rather than the deepest embedded parts: $A(V)\lesssim 50$ appears still moderate compared to the extremely obscured NGC 4418-like continuum, and the energy budget of this component stays a factor ~ 2 below the bolometric luminosity of Arp 220 (Genzel et al. 1998). The infrared emission lines may thus give a partial view of the circumnuclear absorbed region, but very likely not a complete one.

6.4.2 The nature of the nuclear power sources

Given the relatively small fraction of the bolometric luminosity associated with the diffuse PAH emission (5–15%), the bulk of the luminosity of the Arp 220 system must be associated

with the absorbed-continuum component from the two nuclei. To be responsible for only $\sim 40\%$ of the $6\text{--}12\,\mu\text{m}$ luminosity but for $85\text{--}95\%$ of the total Arp 220 infrared luminosity, these nuclei must, hence, be deeply enshrouded indeed. Given the large amounts of molecular material detected in the nuclear environment ($\sim 10^{10}\,\text{M}_\odot$ half of which is in the disk enclosing the two nuclei; Scoville et al. 1997; Sakamoto et al. 1999), this comes as no surprise. Unfortunately, strong obscuration erases source-specific spectral signatures, not only at X-ray, UV, optical, near- and mid-IR wavelengths, but, depending on the absorbing column, also out to far-IR and, possibly, sub-mm wavelengths.

Based on the few identified spectral signatures at hand, we consider two possibilities for the nature of the nuclear power sources. First, each of the nuclei may contain a deeply embedded, extremely dense and luminous stellar cluster – a super-star cluster containing some 10^6 massive O stars within a region less than 100 pc in size. Less extreme deeply embedded clusters have been discovered in the starburst galaxies NGC 5253 and He 2–10 (Gorjian et al. 2001; Vacca et al. 2002). A stellar nature for the nuclear power sources in Arp 220 is further supported by the 18 cm VLBI observations of Smith et al. (1998, 1999), which show a dozen or so sources scattered over the two nuclei. These “knots” are consistent with free-free emission from luminous radio supernovae expanding in the dense (circum)nuclear environment (Smith et al. 1998, 1999). Second, we consider two deeply embedded AGNs. Despite the lack of AGN features in any waveband, a deeply embedded powerful AGN at the center of each nucleus cannot be ruled out. The column density required to block the AGNs from detection by *BeppoSAX* in hard X-rays is $N_{\text{H}_2}=10^{25.1}\text{--}10^{25.3}\,\text{cm}^{-2}$ with a large covering factor (Iwasawa et al. 2001). The non-detection of a high- T_b radio core in the 18 cm VLBI maps of Smith et al. (1998, 1999) would then imply the AGNs to be radio-quiet or strongly free-free absorbed.

6.4.3 Modeling of the nuclear continuum

In order to test whether the low mid-to-far-IR continuum ratio in Arp 220 may be attributed to strong dust obscuration on the emission of two identical, deeply buried, energetically dominant, nuclear sources, we used the dust radiative transfer code of Siebenmorgen et al. (1999, 2001) to model the 2–3000 μm nuclear spectrum.

In the model we assume a cluster of OB stars, with stellar densities similar to those inferred for ultra-dense H II regions (UD H II regions; Vacca et al. 2002), to reside at the center of each nucleus. For a given luminosity of $6\times 10^{11}\,\text{L}_\odot$, the stars will occupy a sphere with radius $r=25\,\text{pc}$. Adopting a nuclear gas mass of $10^9\,\text{M}_\odot$, spherical symmetry, constant gas density and a silicate optical depth of $\tau_{\text{sil}}=4.6$ (consistent with the silicate optical depth for our best fitting absorbed continuum source NGC 4418), we are forced to place the outer radius of the dust shell as far out as $\sim 325\,\text{pc}$ in order to lower the dust temperature to values consistent with the observed 12–50 μm SED. The FWHM of the $11\,\mu\text{m}$ light profile is $\sim 20\,\text{pc}$, consistent with the observations of Soifer et al. (2002). As the temperature in the dust shell does not drop below 40 K at the outer edge, we consider an additional cold dust component to account for the coldest dust in the system. This component likely accounts for the far-IR/submm emission associated with the diffuse PAH component and for far-IR/submm emission from the nuclear region not covered by our ‘simple’ model. Here, we characterize the cold dust component by a grey body spectrum of 30 K with a dust emissivity index of 1.8 and a dust optical depth of 1 at $100\,\mu\text{m}$. Both the model spectrum of the nuclei and the grey body spectrum are shown in Fig. 6.9. The Figure also shows the assumed contribution of the diffuse

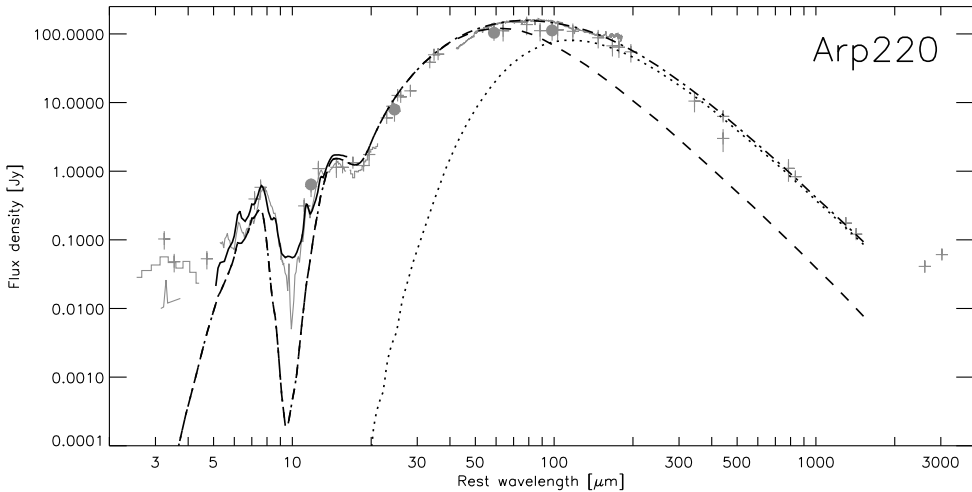


FIGURE 6.9 — The 2–3000 μm spectrum of Arp 220 (grey) overplotted with a three component fit. The *black dashed* curve represents the model SED for the two identical nuclei. The *black dotted* curve represents grey body emission from 30 K cold dust. The *black dash-dotted* curve is the sum of these two components. The *black continuous* curve is the sum of the model SED and the weakly absorbed diffuse PAH component (M 83) from our 2-component decomposition (Sect. 6.3).

PAH component (M 83; see Sect. 6.3.4) to the Arp 220 mid-IR spectrum.

We conclude from our modeling that the low ratios $S(6\,\mu\text{m})/S(60\,\mu\text{m})$ and $S(6\,\mu\text{m})/S(100\,\mu\text{m})$ can, *in principle*, be explained by the effects of strong dust obscuration on two deeply buried, energetically dominant, nuclear sources. However, this model predicts a hydrogen column of only $\sim 10^{23.2}\,\text{cm}^{-2}$ and hence favours stellar heating, as this column is a factor ~ 100 too small to account for the upper limits on the hard X-ray flux if the total luminosity were dominated by AGN activity (Iwasawa et al. 2001).

Note that if any deeply hidden AGN ($N_{\text{H}} \geq 10^{25}\,\text{cm}^{-2}$) were present, the covering factor of the obscuration would have to be large in order to be consistent with the lack of reflected X-ray light measured by *BeppoSAX* (Iwasawa et al. 2001). The AGN would hence strongly contribute to the far-IR continuum, but could not be responsible for the mid-IR continuum.

6.4.4 Mid-to-far-infrared spectral characteristics

Arp 220 is an outlier in many spectroscopic diagnostic diagrams linking mid-IR to far-IR quantities. In all cases Arp 220 stands out by having a low ratio of the mid-IR characteristic with respect to the far-IR characteristic:

- Already in the Bright Galaxy Sample of Sanders et al. (1988a), Arp 220 stands out by the smallest S12/S60 ratio.
- Similarly, Arp 220 has the lowest S5.9/S60 ratio among the larger sample studied spectroscopically in the mid-IR by Lutz et al. (1998).

- The ratio of $F(6.2 \mu\text{m PAH})/F(\text{FIR})$ is lower than for any other galaxy in our database of more than 250 ISO mid-IR galaxy spectra.
- The ratio $F([\text{Ne II}])/F(\text{FIR})$ is a factor three lower than for the average starburst galaxy (Genzel et al. 1998).
- The ratio $F(7.7 \mu\text{m PAH})/F(850 \mu\text{m})$ is the lowest among a sample of normal and ultra-luminous galaxies (Haas et al. 2001).

Our spectral decomposition offers a simple explanation for the above observations. A typical starburst spectrum associated with the extended PAH component will contribute strongly to the mid-IR but weakly to the far-IR, while the dominant deeply enshrouded nuclei contribute weakly to the mid-IR and strongly to the far-IR. The resulting combined 3–1000 μm SED is hence mostly starburst-like in the mid-IR and dominated by cold dust emission from the enshrouded nuclei in the far-IR. Ratios of mid-IR to far-IR quantities, like $F([\text{Ne II}])/F(\text{FIR})$, $F(6.2 \mu\text{m PAH})/F(\text{FIR})$ or $F(7.7 \mu\text{m PAH})/F(850 \mu\text{m})$, will hence all be systematically lower than the values typically found for starburst galaxies. Interestingly, Luhman et al. (2003) advocate a similar scenario as a contributor to the low $F([\text{C II}])/F(\text{FIR})$ ratio of Arp 220.

Other galaxies may exist with even more strongly obscured nuclei, emitting an even smaller fraction of the nuclear luminosity in the mid-IR than Arp 220 does. These galaxies would hence look starburst-like in the mid-IR (contributed by a [weakly obscured] circumnuclear starburst) but would be characterized by a very strong cold dust continuum in the far-IR. Galaxies of this type, may be recognized spectroscopically by their low $S5.9/S60$, $S5.9/S100$, $S5.9/S850$ or $F([\text{C II}])/F(\text{FIR})$ ratios and their starburst-like 6.2 μm -PAH line-to-continuum ratios. Perusal of our ISO spectral database has led to the identification of several candidate galaxies. Arp 220 may thus be a local and less extreme template of the class of SCUBA sources seen in the Hubble Deep Field.

Arp 220 is not the only galaxy with spectral structure in the 6–12 μm range reminiscent of strongly modified PAH bands. Other examples are Mrk 231 and most of the galaxies in the sample of Tran et al. (2001). Some of these spectra show, in addition to strong silicate absorption longward of 7.7 μm , clear signs of water ice absorption shortward of 7.7 μm . Depending on the strength of the PAH emission features these galaxies have been classified as class I, II or III ice galaxies (Chapter 2). Like Arp 220, their spectra may well be the result of strong extinction on one or more spectral components.

6.5 Conclusions

We have shown that the 6–12 μm spectrum of Arp220 is not that of a scaled-up typical starburst galaxy but contains a ‘normal’ starburst component characterized by PAH emission features plus a highly obscured dust continuum with ice and silicate absorption. Attempts to decompose the spectrum using a variety of extragalactic and Galactic template spectra yields a best fit in which a typical starburst, represented by M 83, contributes $\sim 60\%$ and an ice absorbed continuum galaxy, represented by NGC 4418, $\sim 40\%$ of the 6–12 μm luminosity. An important result in relation to previous studies is our conclusion that the pronounced emission feature peaking around 7.7 μm is a blend of PAH emission and a broader feature in the continuum caused by ice absorption at shorter and silicate absorption at longer wavelengths. We tentatively conclude that the PAH emitting component is only weakly absorbed

and arises in the extended region imaged at higher resolution around $10\,\mu\text{m}$ by Soifer et al. (2002) whereas the absorbed continuum is associated with one or both of the compact nuclei. This extended starburst component contributes only 5–15% of the total luminosity with the bulk emitted by the heavily obscured nuclear component(s). One possibility is that this luminosity is generated by starburst activity occurring in a higher density environment than found in lower luminosity starburst galaxies due to the larger quantity of molecular gas and dust funnelled to the center by merging of the two nuclei. Due to the high extinction, it is not possible with the available data to exclude that AGN(s) also contribute some or all of this luminosity. Based on the upper limits for hard X-ray emission (Iwasawa et al. 2001), however, Arp 220 would need to be the most highly obscured AGN known.

Acknowledgements

The authors wish to thank Tom Soifer and Eiichi Egami for sharing data with us and George Helou, Olivier Laurent, Matt Lehnert, Neil Nagar, Dave Sanders, Eckhard Sturm and Jacqueline van Gorkum for discussions. This research has made use of the NASA/IPAC Extragalactic Database, which is operated by the Jet Propulsion Laboratory, Caltech under contract with NASA.

7

PAHs as a tracer for star formation

To be submitted :

E. Peeters, H.W.W. Spoon & A.G.G.M. Tielens
ASTROPHYSICAL JOURNAL, 2003

INFRARED emission features at 3.3, 6.2, 7.7, 8.6 and 11.3 μm are generally attributed to infrared fluorescense from FUV pumped large Polycyclic Aromatic Hydrocarbon (PAH) molecules. As such, these features trace the FUV stellar flux and are thus a measure of star formation. We have examined the infrared spectral characteristics of a sample of Galactic regions of massive star formation and of a sample of normal and starburst galaxies, as well as AGNs and ULIRGs. The goal of this study is to analyze various tracers of star formation with the aim of identifying the dominant processes contributing to the infrared emission from ULIRGs. We have developed a MIR/FIR diagnostic diagram based upon a Galactic sample of star forming regions. This diagnostic is derived from the far-infrared normalized 6.2 μm PAH flux and the far-infrared normalized 6.2 μm continuum flux. Within this diagram, the Galactic sources form a sequence spanning a range of 3 orders of magnitude in these ratios, ranging from embedded compact H II regions to exposed Photo Dissociation Regions (PDRs). However, the 6.2 μm PAH line-to-continuum ratio is remarkably constant over this range. We have compared our extragalactic sample to these Galactic sources. This revealed an excellent resemblance of normal and starburst galaxies with exposed PDRs. While Seyfert-2's coincide with the starburst trend, Seyfert-1's are displaced by a factor 10 in 6.2 μm continuum flux, in accordance with general unification schemes for AGNs. ULIRGs show a diverse spectral appearance. Some show a typical AGN hot dust continuum. More, however, are either starburst-like or show signs of strong dust obscuration in the nucleus. One characteristic of the ULIRGs also seems to be the presence of more prominent far-infrared emission than either starburst galaxies or AGNs. We discuss the observed variation in the Galactic sample in view of the evolutionary state and the PAH/dust abundance. Finally, we have examined the use of PAHs as quantitative tracers of star formation activity. Based on these investigations we find that PAHs may be better suited as a tracer of B stars, which dominate the Galactic stellar energy budget, than as a tracer of massive star formation.

7.1 Introduction

The mid-infrared (MIR) spectra of many objects with associated dust and gas are dominated by the well-known emission features at 3.3, 6.2, 7.7, 8.6 and 11.2 μm commonly called the unidentified infrared (UIR) bands (cf. Gillett et al. 1973; Geballe et al. 1985; Cohen et al. 1986; Roche et al. 1989). These bands are now generally attributed to vibrational emission of Polycyclic Aromatic Hydrocarbons (PAHs) containing $\simeq 50$ carbon atoms (Léger & Puget 1984; Allamandola et al. 1985, 1989b; Puget & Léger 1989; Tielens et al. 2000). One key aspect of these IR emission features is that they are particularly bright in regions illuminated by UV bright, early type stars (<B1) responsible for H II regions and reflection nebulae.

With the launch of the Infrared Space Observatory (ISO), a huge amount of infrared spectral data became available, showing the omnipresent nature of these PAH features. By now, the features have been detected in a wide range of objects and environments, from post-AGB stars and planetary nebulae, to H II regions, reflection nebulae, the diffuse interstellar medium and extragalactic sources, the most distant of which is the Ultra-Luminous Infrared Galaxy (ULIRG) IRAS 03538–6432 at a redshift of $z=0.3$. Various studies of Galactic sources with bright PAH emission features have been performed (see e.g. the ISO special issue, A&A, 315 1996). Of particular importance here are the studies of the PAHs in a sample of H II regions, which characterized the IR emission features (and the variations among these features) in massive star forming regions (Verstraete et al. 1996; Hony et al. 2001; Peeters et al. 2002a; Vermeij et al. 2002; Verstraete et al. 2001; van Diedenhoven et al. 2003).

The MIR extragalactic ISO studies were dominated by four major programs, which focussed on the spectral properties of active galaxies (e.g. Mirabel et al. 1998; Charmandaris et al. 1999), Seyfert galaxies (e.g. Clavel et al. 2000), normal galaxies (e.g. Helou et al. 2000) and ULIRGs (e.g. Genzel et al. 1998; Lutz et al. 1998; Rigopoulou et al. 1999; Tran et al. 2001). These studies established that PAH emission features in extragalactic environments are very similar to those in Galactic star forming regions. This property has since been used qualitatively and quantitatively as diagnostics for the ultimate physical processes powering Galactic nuclei.

In an impressive study involving ISO–PHT–S and ISO–SWS observations of some 45 Active Galactic Nuclei (AGNs), starburst galaxies and ULIRGs, Genzel et al. (1998) found that the 7.7 μm PAH feature-to-continuum ratio is on average an order of magnitude smaller for AGNs than for starburst galaxies. Conversely, the ratio of the high- to low-excitation emission lines [O IV]/[Ne II] was found to be two orders of magnitude higher for AGNs than for starburst galaxies. The 7.7 μm PAH feature-to-continuum ratio was then used together with the gas excitation line ratio to separate AGNs and starburst galaxies in a 2-dimensional diagnostic plot. ULIRGs were found to reside in between the two groups, although closer to the starburst galaxies. This led Genzel et al. (1998) to conclude that 80% of the ULIRGs are predominantly powered by star formation.

A second MIR diagnostic plot was devised by Laurent et al. (2000) for the interpretation of ISO–CAM–CVF spectra of the nuclei and disks of nearby active and inactive galaxies. The diagnostic diagram separates H II regions, PDRs and AGNs on the basis of their distinctly different ratio of warm (15 μm) to hot (6 μm) continuum and the value of their 6.2 μm PAH feature-to-continuum ratio. It thereby allows to estimate the contribution of the AGN, PDRs and H II regions to a given MIR spectrum.

Clavel et al. (2000) compared the MIR spectral properties of a sample of 28 type-1 and 29

type-2 Seyfert galaxies to test AGN unification schemes. The study established that the 7.7 μm PAH luminosity distributions of both samples are the same, indicating that the properties of the Seyfert host galaxies are unrelated to the type-1/2 classification of the nuclear activity. The study also found that the average 7.7 μm PAH equivalent width of the Seyfert-1 sample is a factor ~ 8 smaller than of the Seyfert-2 sample, implying that, on average, the 7.7 μm continuum of type-2 Seyferts is a factor ~ 8 weaker than of type-1 Seyferts. Clavel et al. (2000) attribute this difference to dust obscuration in the nuclear environment, which, in line with the unified models for AGNs (Antonucci 1993), is attributed to the orientation of the AGN torus. An important result from this work is that except for the emission line spectrum, the 3–12 μm spectra of type-2 Seyferts appear very similar to those of normal and starburst galaxies.

The goal of this Chapter is to establish the characteristics of PAH emission bands in regions of massive star formation in the Milky Way, in order to use them as a tool for studying star formation on a galaxy-wide scale and to apply these tools to a study of extragalactic starbursts in Seyferts, (ultra-luminous) infrared galaxies and QSOs.

This Chapter is organized as follows. In Sect. 7.2, we present the observations of the MIR emission features in a sample of H II regions and ISM positions in our Galaxy, as well as in a large sample of normal, starburst, Seyfert and (ultra-luminous) infrared galaxies and QSOs. Spectral characteristics of these samples are discussed in Sect. 7.3. In Sect. 7.4, we investigate three infrared diagnostic tools designed to distinguish AGN- from starburst-dominated spectra. Sect. 7.5 highlights the PAH abundance as fraction of the total amount of dust and the application of the PAH emission bands as tracers of star formation. The conclusions are stated in Sect. 7.6.

7.2 Observations

7.2.1 H II regions and ISM

The sample of H II regions was taken from the Galactic “Ultra Compact H II region” ISO program (Peeters et al. 2002b) complemented with spectra of the Orion Bar, M17 and 30 Dor. Only those spectra with sufficient S/N are included in this sample. As a reference, we included reflection nebulae (NGC 2023, NGC 7023), heavily embedded protostars exhibiting PAH emission (MonR2 IRS2, NGC7538 IRS1), molecular clouds and the (diffuse) ISM in various regions. For details on the sources and references, see Table 7.1.

Most spectra were obtained with the Short Wavelength Spectrometer (SWS, de Graauw et al. 1996) on board the Infrared Space Observatory (ISO, Kessler et al. 1996). These spectra were taken using the AOT 01 scanning mode at various speeds with resolving power ($\lambda/\Delta\lambda$) ranging from 400 to 1500 (see Table 7.1). These data were processed with the SWS Interactive Analysis package IA³ (de Graauw et al. 1996) using calibration files and procedures equivalent with pipeline version 10.0 or later. A detailed account of the reduction of ISO-SWS spectra can be found in Peeters et al. (2002b). Few sources were obtained with ISO-PHT-S, ISO-CAM-CVF, IRTS-MIRS and MSX with resolving power ($\lambda/\Delta\lambda$) of respectively $\sim 90, 35, 30$ and 800. We refer to the original papers (see Table 7.1) for an account of the reduction process.

TABLE 7.1 — Journal of observations together with the derived fluxes. The coordinates of the ISO pointings are given.

Source	α (J2000) ^a	δ (J2000) ^a	Instrument ^b	TDT ^c	Ref.	6.2 PAH ^d W/m ²	cont. [5.3,5.8] ^d W/m ²	cont. [6.0,,6.5] ^d W/m ²	cont. [14-15] ^d W/m ²	FIR ^d W/m ²	Ref. FIR
W 3A 02219+6125 [#]	02 25 44.59	+62 06 11.20	ISO-SWS 01(2)	64600609	1	2.158(-13)	3.769(-13)	4.990(-13)	4.040(-12)	1.555(-09)	1
			ISO-SWS 01(2)	78800709	1	2.363(-13)	3.375(-13)	4.874(-13)	4.384(-12)	1.555(-09)	1
30 Dor	05 38 46.00	-69 05 07.91	ISO-SWS 01(4)	17100512	2	2.606(-14)	7.179(-14)	4.839(-14)	3.084(-13)	5.915(-11)	16
OrionBar D8	05 35 18.22	-05 24 39.89	ISO-SWS 01(2)	69501409	3	3.156(-13)	2.046(-13)	3.303(-13)	1.719(-12)	-	
OrionBar BRGA	05 35 19.31	-05 24 59.90	ISO-SWS 01(2)	69502108	-	3.760(-13)	2.103(-13)	3.311(-13)	1.071(-12)	-	
OrionBar D5	05 35 19.81	-05 25 09.98	ISO-SWS 01(2)	83101507	-	5.437(-13)	2.343(-13)	3.821(-13)	1.006(-12)	3.498(-11)	17
OrionBar H2S1	05 35 20.31	-05 25 19.99	ISO-SWS 01(2)	69501806	4	3.469(-13)	1.886(-13)	3.038(-13)	6.936(-13)	-	
OrionBar D2	05 35 21.40	-05 25 40.12	ISO-SWS 01(2)	69502005	-	1.197(-13)	9.229(-14)	1.196(-13)	4.671(-13)	-	
Orion	centered on Trapezium		MSX	-	5	1.768(-5) ^o	6.504(-06) ^o	1.507(-5) ^o	5.515(-05) ^o	3.084(-3) ^{o,△}	18
IRAS 10589-6034	11 00 59.78	-60 50 27.10	ISO-SWS 01(2)	26800760	1	1.279(-13)	1.047(-13)	1.380(-13)	4.462(-13)	1.472(-10)	1
IRAS 12063-6259	12 09 01.15	-63 15 54.68	ISO-SWS 01(2)	25901414	1	1.177(-13)	1.565(-13)	1.960(-13)	5.786(-13)	1.598(-10)	1
IRAS 12073-6233 [#]	12 10 00.32	-62 49 56.50	ISO-SWS 01(2)	25901572	1	7.761(-14)	5.137(-13)	6.115(-13)	7.748(-12)	1.098(-09)	1
IRAS 12331-6134 [#]	12 36 01.9	-61 51 03.9	ISO-SWS 01(2)	29900470	1	3.565(-14)	4.316(-14)	5.469(-14)	1.524(-13)	1.336(-10)	1
IRAS 15384-5348 [#]	15 42 17.16	-53 58 31.51	ISO-SWS 01(2)	29900661	1	3.261(-13)	1.530(-13)	2.553(-13)	6.500(-13)	4.433(-10)	1
IRAS 15502-5302	15 54 05.99	-53 11 36.38	ISO-SWS 01(2)	27301117	1	9.903(-14)	2.318(-13)	2.880(-13)	9.730(-13)	8.532(-10)	1
IRAS 16128-5109 [#]	16 16 39.3	-51 16 58.3	ISO-SWS 01(2)	29402233	1	8.479(-14)	7.197(-14)	8.134(-14)	2.227(-13)	5.330(-10)	1
IRAS 17160-3707 [#]	17 19 26.1	-37 10 53.8	ISO-SWS 01(2)	32400821	1	4.369(-14)	5.544(-14)	6.819(-14)	1.453(-13)	3.508(-10)	1
IRAS 17221-3619 [#]	17 25 31.7	-36 21 53.5	ISO-SWS 01(2)	33100380	1	7.459(-14)	5.355(-14)	7.238(-14)	2.380(-13)	2.082(-10)	1
IRAS 17279-3350 [#]	17 31 18.0	-33 52 49.4	ISO-SWS 01(2)	32200877	1	9.738(-14)	5.880(-14)	8.287(-14)	2.307(-13)	1.284(-10)	1
Sgr C [#]	17 44 35.6	-29 27 29.3	ISO-SWS 01(2)	84100301	1	6.791(-14)	3.820(-14)	2.718(-14)	2.193(-13)	-	
IRAS 17455-2800	17 48 41.5	-28 01 38.3	ISO-SWS 01(2)	28701327	1	1.147(-13)	1.238(-13)	1.809(-13)	1.033(-12)	2.286(-10)	1
IRAS 17591-2228	18 02 13.2	-22 27 58.9	ISO-SWS 01(2)	51500580	1	2.702(-14)	4.886(-14)	4.191(-14)	9.103(-14)	7.255(-11)	1
IRAS 18032-2032	18 06 13.93	-20 31 43.28	ISO-SWS 01(2)	51500478	1	1.090(-13)	7.877(-14)	1.032(-13)	3.532(-13)	3.186(-10)	1
IRAS 18116-1646	18 14 35.29	-16 45 20.99	ISO-SWS 01(2)	70300302	1	1.622(-13)	4.581(-14)	1.005(-13)	4.227(-13)	2.941(-10)	1
GGD-27 ILL*	18 19 12.00	-20 47 31.10	ISO-SWS 01(2)	14802136	1,6	1.373(-13)	2.812(-13)	2.883(-13)	5.206(-13)	2.157(-10)	1
M17 iram pos. 1	18 20 28.98	-16 11 50.78	ISO-SWS 01(2)	10201811	7	7.541(-14)	9.737(-14)	1.574(-13)	1.987(-12)	4.818(-11)	19
M17 iram pos. 2	18 20 27.59	-16 12 0.90	ISO-SWS 01(2)	09900212	7	4.477(-14)	1.443(-13)	3.046(-13)	4.069(-12)	-	
M17 iram pos. 3	18 20 26.19	-16 12 11.02	ISO-SWS 01(2)	09901413	7	1.203(-13)	1.589(-13)	2.176(-13)	3.212(-12)	-	
M17 iram pos. 4	18 20 24.79	-16 12 21.10	ISO-SWS 01(2)	09900214	7	3.345(-13)	1.588(-13)	2.494(-13)	1.279(-12)	-	
M17 iram pos. 5	18 20 23.40	-16 12 31.21	ISO-SWS 01(2)	09901415	7	2.675(-13)	1.463(-13)	2.024(-13)	4.536(-13)	-	
M17 iram pos. 6	18 20 22.09	-16 12 41.29	ISO-SWS 01(2)	09900216	7	2.033(-13)	8.342(-14)	1.505(-13)	2.258(-13)	-	
				32900866	7	2.045(-13)	1.030(-13)	1.516(-13)	1.811(-13)	-	
M17 iram pos. 7	18 20 20.70	-16 12 51.41	ISO-SWS 01(2)	09901417	7	5.807(-14)	2.105(-14)	2.979(-14)	8.304(-14)	-	
M17 iram pos. 8	18 20 19.31	-16 13 01.49	ISO-SWS 01(2)	09900218	7	5.425(-14)	5.278(-14)	6.690(-14)	1.023(-13)	1.222(-11)	19
M17 North	18 20 32.77	-16 01 42.49	ISO-SWS 01(2)	09901105	8	7.008(-14)	1.032(-13)	1.378(-13)	1.035(-13)	3.333(-11) [▷]	

TABLE 7.1 — Continued.

Source	α (J2000) ^a	δ (J2000) ^a	Instrument ^b	TDT ^c	Ref.	6.2 PAH ^d W/m ²	cont. [5.3,5.8] ^d W/m ²	cont. [6.0,..6.5] ^d W/m ²	cont. [14-15] ^d W/m ²	FIR ^d W/m ²	Ref. FIR
IRAS 18317–0757	18 34 24.94	−07 54 47.92	ISO-SWS 01(2)	47801040	1	2.931(-13)	1.508(-13)	2.552(-13)	7.280(-13)	1.965(-10)	1
IRAS 18434–0242	18 46 04.09	−02 39 20.02	ISO-SWS 01(2)	15201383	1,6	1.881(-13)	3.583(-13)	5.111(-13)	4.410(-12)	6.982(-10)	1
IRAS 18469–0132	18 49 33.0	−01 29 03.70	ISO-SWS 01(2)	71100888	1	7.630(-14)	6.592(-14)	6.779(-14)	2.113(-13)	1.264(-10)	1
IRAS 18479–0005	18 50 30.8	−00 01 59.40	ISO-SWS 01(2)	15201791	1	3.047(-14)	9.965(-14)	9.470(-14)	5.812(-13)	2.789(-10)	1
IRAS 18502+0051	18 52 50.21	+00 55 27.59	ISO-SWS 01(2)	15201645	1	1.079(-13)	9.129(-14)	8.660(-14)	5.912(-13)	1.246(-10)	1
IRAS 19207+1410 [#]	19 23 02.4	+14 16 40.60	ISO-SWS 01(2)	150001041	1	6.054(-14)	6.216(-14)	5.119(-14)	2.946(-13)	3.787(-10)	1
IRAS 19442+2427 ^{*?}	19 46 20.09	+24 35 29.40	ISO-SWS 01(2)	150000444	1,6	2.541(-13)	2.455(-13)	2.978(-13)	6.236(-13)	2.714(-10)	1
IRAS 19598+3324 [*]	20 01 45.6	+33 32 43.70	ISO-SWS 01(4)	38402466	1	1.409(-13)	2.217(-12)	2.319(-12)	7.533(-12)	8.889(-10)	1
IRAS 21190+5140	21 20 44.89	+51 53 26.99	ISO-SWS 01(2)	15901853	1	9.377(-14)	9.056(-14)	1.104(-13)	8.919(-13)	8.656(-11)	1
IRAS 22308+5812	22 32 45.95	+58 28 21.00	ISO-SWS 01(2)	17701258	1,6	1.141(-13)	8.177(-14)	1.119(-13)	1.632(-13)	7.392(-11)	1
				56101082	1	1.305(-13)	8.033(-14)	1.174(-13)	1.222(-13)	7.392(-11)	1
IRAS 23030+5958	23 05 10.60	+60 14 40.99	ISO-SWS 01(2)	22000961	1	7.792(-14)	7.590(-14)	8.539(-14)	2.090(-13)	1.248(-10)	1
IRAS 23133+6050	23 15 31.39	+61 07 08.00	ISO-SWS 01(2)	22001506	1	2.454(-13)	1.369(-13)	2.129(-13)	4.924(-13)	1.959(-10)	1
NGC 7023 I [#]	21 01 31.90	+68 10 22.12	ISO-SWS 01(4)	20700801	9	1.577(-13)	9.610(-14)	8.508(-14)	3.721(-14)	2.54(-12)	20
NGC 2023 [#]	05 41 38.29	−02 16 32.59	ISO-SWS 01(2)	65602309	10	8.275(-14)	5.643(-14)	4.665(-14)	2.431(-14)	3.04(-12)	21
NGC7538 IRS1	23 13 45.27	+61 28 09.98	ISO-SWS 01(3)	38501842	11	2.168(-13)	4.005(-12)	4.062(-12)	5.978(-12)	8.60(-10)	22
MONR2 IRS2	06 07 45.79	−06 22 50.02	ISO-SWS 01(1)	71102004	-	4.818(-13)	2.772(-12)	2.598(-12)	1.967(-12)	-	-
						W/m ² /sr	W/m ² /sr	W/m ² /sr	W/m ² /sr	W/m ² /sr	
Rho-Oph	16 25 41.09	−24 06 46.90	ISO-CAM 04	09202119	12	3.738(-07)	1.150(-07)	3.975(-07)	1.659(-07)	8.931(-06)	12
SMC B1 # 1 cloud	00 45 32.50	−73 18 16.30	ISO-CAM 04	23200127	13	2.294(-08)	7.543(-09)	6.504(-09)	1.183(-09)	<0.460(-06)	13
68602088											
Milky Way - ISM (average)			ISO-PHOT-S	-	14	3.722(-07)	2.166(-12)	2.613(-07)	-	32.30(-06)	13
NGC891 (average within 144'' from center)			ISO-PHOT-S	-	14	3.722(-07)	2.166(-12)	2.613(-07)	-	13.00(-06)	14
DISM 1	$44^{\circ} \leq l \leq 44^{\circ} 40'$, $-0^{\circ} 40' \leq b \leq 0^{\circ}$		IRTS	-	15	1.307(-07)	1.514(-07)	2.437(-07)	-	23.00(-06)	15
DISM 2	$50^{\circ} \leq l \leq 53^{\circ}$, $1^{\circ} \leq b < 2^{\circ}$		IRTS	-	15	5.139(-08)	8.234(-08)	1.350(-07)	-	10.00(-06)	15
DISM 3	$51^{\circ} \leq l \leq 54^{\circ}$, $2^{\circ} \leq b \leq 3^{\circ}$		IRTS	-	15	1.998(-08)	1.901(-08)	4.813(-08)	-	6.500(-06)	15

^a : Units of α are hours, minutes, and seconds, and units of δ are degrees, arc minutes, and arc seconds. ^b : SWS observing mode used (see de Graauw et al. 1996). Numbers in brackets correspond to the scanning speed. ^c : each ISO observation is given a unique TDT (Target Dedicated Time) number. ^d See text for details * : water ice absorption ($6 \mu\text{m}$) present (Peeters et al. 2002a).

[#] : MIR/FIR ratio influenced by beam effects, confusion with other sources or mispointings (Peeters et al. 2002a; Martín-Hernández et al. 2003). [◊] : in units of W/m²/sr. [▫] The contribution of IRC2 and BN is estimated on $3(4)L_{\odot}$ and subtracted from the observed FIR luminosity. [▷] : obtained by integrating the LWS spectrum after scaling the LWS 45 μm flux to the SWS 45 μm flux.

References : 1 : Peeters et al. (2002b); 2 : Sturm et al. (2000) 3 : Cesarsky et al. (2000); 4 : Verstraete et al. (2001); 5 : Simpson et al. (1998); 6 : Roelfsema et al. (1996); 7 : Verstraete et al. (1996);

8 : Henning et al. (1998); 9 : Moutou et al. (1999a); 10 : Moutou et al. (1999b); 11 : Gerakines et al. (1999); 12 : Boulanger et al. (1996) 13 : Kahanpää et al. (2003); 14 : Reach et al. (2000);

15 : Onaka et al. (1996); 16 : Vermeij et al. (2002); 17 : Werner et al. (1976); 18 : Thronson et al. (1984); 19 : Meixner et al. (1992); 20 : Casey (1991); 21 : Steiman-Cameron et al. (1997);

22 : Thronson & Harper (1979)

7.2.2 ISO galaxy sample

The MIR galaxy spectra presented in this Chapter have been drawn from our database of some 250 ISO galaxy spectra, described in Chapter 2. The sample comprises normal galaxies, starburst galaxies, Seyfert galaxies, QSOs, LIRGs, ULIRGs and HyLIRGs. Depending on the size of the aperture used and the distance to the source, the spectra probe physical sizes ranging between 73 pc (4.5'') for the nearest source (Cen A; D=3.5 Mpc) and the entire disk (assuming $R_{\text{disk}}=10$ kpc) for galaxies beyond 170 Mpc. The MIR spectra are supplemented with infrared photometry from the IRAS Faint Source Catalog (FSC). Given a beam size of $\sim 60''$, the physical sizes probed by IRAS range between 1 kpc for the nearest source and the entire disk for galaxies beyond Arp 220 (73 Mpc). For details on the data reduction of the sample, see Chapter 2.

7.3 The spectral characteristics

7.3.1 H II regions and ISM

Fig. 7.1 (middle panels) shows the MIR spectra of a few H II regions, carefully selected to span the range from highly embedded H II regions (e.g. W3) to optically visible H II regions (e.g. Orion). These IR spectra of H II regions are characterized by a strong rising dust continuum due to thermal dust emission, corresponding to dust temperatures of ~ 60 –70 K. Many H II regions also show strong continuum emission at $\lambda < 12 \mu\text{m}$, whose origin is unclear. Possibly, this continuum is due to a small fraction of dust inside the H II region, heated to high temperatures by resonantly scattered Lyman- α radiation. Alternatively, these are larger (~ 500 C-atoms) PAH-like structures stochastically heated by a single or multi-photon event. On top of the dust continuum, there is a series of fine-structure lines and hydrogen recombination lines. In addition, these spectra exhibit prominent PAH emission features, often silicate absorption and in some cases absorption bands due to molecular ice species (CO_2 , H_2O).

In contrast, reflection nebulae exhibit a much weaker dust continuum indicating lower dust temperatures, strong PAH emission and no fine-structure lines or recombination lines (bottom panel, Fig. 7.1). A peculiar spectrum is that of the heavily obscured H II region K3–50A, showing all characteristics of H II regions except for the dust continuum which is more similar to that of massive protostars (top panel, Fig. 7.1). This source also exhibits a multitude of ice absorption features (Peeters et al. 2002b).

Each of these emission/absorption components, characteristic for H II regions, is influenced by the local physical conditions and hence, although their global characteristics are very similar, the individual spectra display great diversity in their spectral properties (for this sample, see Roelfsema et al. 1996; Verstraete et al. 1996, 2001; Hony et al. 2001; Peeters et al. 2002a,b; Martín-Hernández et al. 2002; Vermeij et al. 2002; van Diedenhoven et al. 2003). Indeed, large variations are present in the relative strength of the PAH emission bands and the dust continuum at various wavelengths (see Fig. 7.1). While the PAH features are relatively weak in the spectra presented in the top panels (dominated by very strong dust continua), the opposite is true for the spectra in the lower panels. More specific, there seems to be a smooth trend among the H II regions in the ratio of PAH over dust continuum, ultimately evolving towards the ratio found for reflection nebulae. However, the strength of the thermal emission of dust below 20 μm is highly influenced by the dust temperature. Indeed, when normalized on the far-infrared (FIR) flux (Fig. 7.1 : right y-axis), the sequence of sources going from low to high relative strength of PAH over dust continuum is different, but, here as

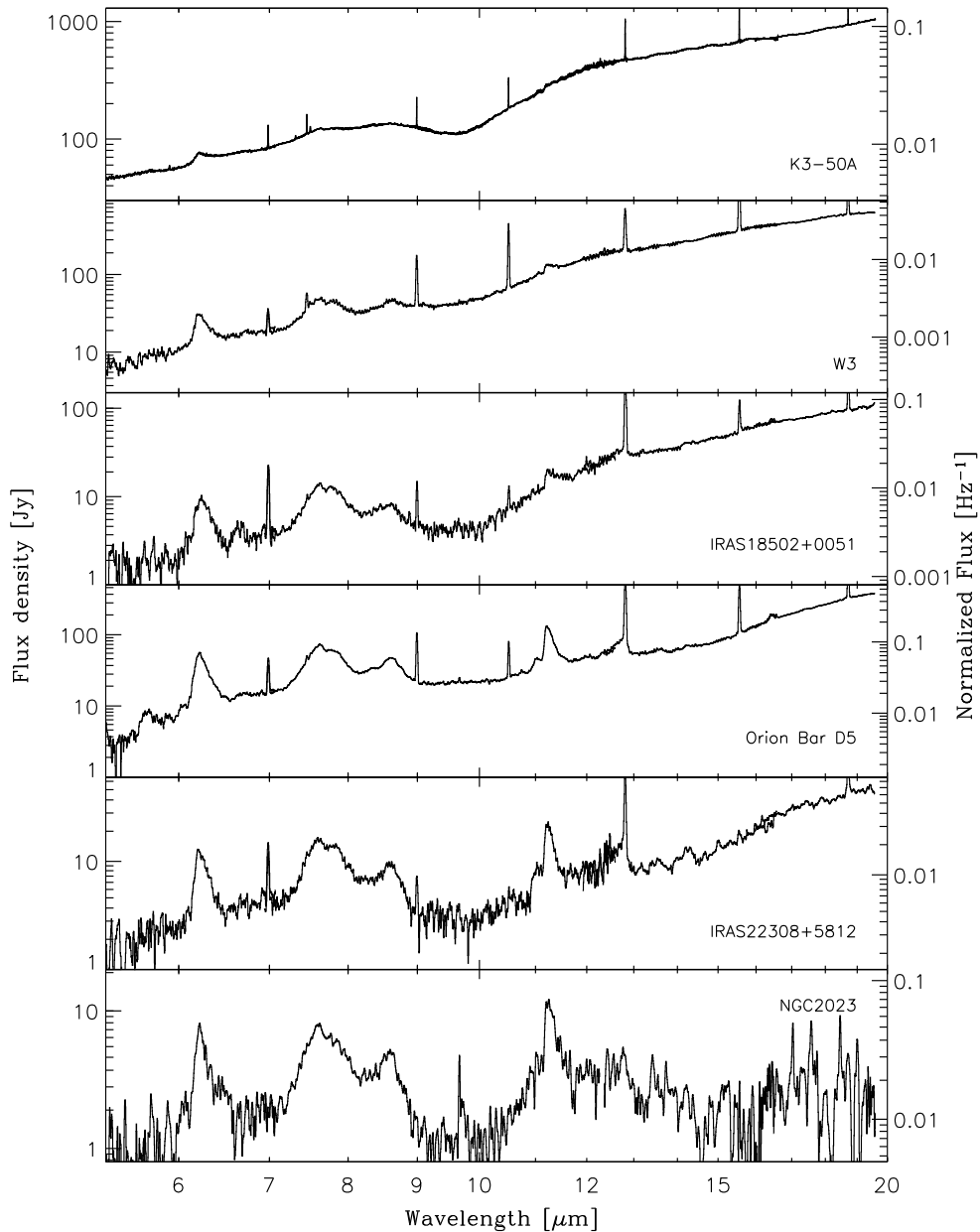


FIGURE 7.1 — Spectral variation in the mid-IR characteristics of H II regions. As a reference, the reflection nebula NGC 2023 is shown in the **bottom panel**. Note that the units on the left vertical axis represent the FIR normalized flux. Full 2–200 μm spectra for the compact H II regions can be found in Peeters et al. (2002b).

well, evolving toward reflection nebulae. This sequence indicates the evolution from highly embedded ultra-compact H II regions (e.g. W3) toward extended optically visible H II regions (e.g. Orion) and ultimately toward reflection nebulae (e.g. NGC 7023).

Similarly, the ratio of PAH over hot continuum (e.g. around $\sim 6 \mu\text{m}$) changes, albeit over a much smaller range. The latter ratio can be influenced by the possible presence of a broad emission plateau underneath the 6.2, 7.7 and 8.6 μm PAH bands of variable strength, sometimes rivalling the strength of the dust continuum at this wavelength. The beginning of this emission plateau seems to be variable, starting longwards of $\sim 6 \mu\text{m}$ and extending up to $\sim 9 \mu\text{m}$.

The profile and position of the PAH emission bands in H II regions, reflection nebulae and the ISM show very little variation from source to source (Peeters et al. 2002a; van Diedenhoven et al. 2003), although spatially within a source differences have been observed (Joblin et al., in prep., Bregman & Temi, in prep.). However, the relative strength of the different PAH emission bands and hence the fraction of the total PAH flux emitted in each individual band, varies significantly from source to source and spatially within a source. This is, for example, very clear when comparing the 6.2/11.2 PAH ratio for IRAS 18502 and the Orion Bar. For a detailed discussion concerning these intensity variations, we refer to e.g. Verstraete et al. (1996), Joblin et al. (2000), Hony et al. (2001) and Peeters et al. (2002a).

Clearly, the detailed spectral characteristics of H II regions varies and hence no “typical” spectrum for H II regions exists when considering relative strengths of different emission/absorption components. Since this is partly due to the inclusion of emission of the surrounding Photo Dissociation Region (PDR) and molecular cloud in the aperture, many authors (e.g. Laurent et al. 2000; Sturm et al. 2000) have considered the spectrum of starforming regions where continuum emission at 15 μm is dominant (e.g. M 17), as the typical MIR spectrum for the H II region itself, and a reflection nebula (e.g. NGC 7023) as the typical MIR spectrum of a PDR. Indeed, the PDRs associated with compact H II regions, such as Orion, dominate the PAH emission from the region as a whole (Chrysostomou et al. 1992; Giard et al. 1992, 1994; Graham et al. 1993; Sellgren et al. 1990; Tielens et al. 1993). The spectra of H II regions (PAHs plus continuum) measured within a large beam (like that of ISO-SWS and ISO-PHT-S) are then considered to be a combination of these two typical spectra. However, as discussed above, some highly embedded H II regions have a distinct dust continuum and therefore are not taken into account in this decomposition. Sect. 7.4 discusses in detail to which extent this decomposition is valid.

7.3.2 Galaxy sample

The MIR spectra of normal and starburst galaxies reveal the same spectral features that constitute the spectra of Galactic star forming regions. Invariably, the 6–12 μm range is dominated by the family of PAH emission features at 6.2, 7.7, 8.6 and 11.2 μm (see Figure 7.2). Beyond 9 μm , starburst galaxy spectra show the additional presence of a warm dust continuum, which is weak or absent in the spectra of normal galaxies. As for Galactic H II regions, high resolution spectra also reveal many strong emission lines.

The detailed characteristics of the IR spectra depend on the properties of the galaxy in a way which is not completely understood. In particular, some starburst galaxies also show evidence for the presence of dust in the nuclear region. The nuclear spectrum of NGC 4945 (top-right panel of Figure 7.2) is a clear example of such an environment, as can be deduced

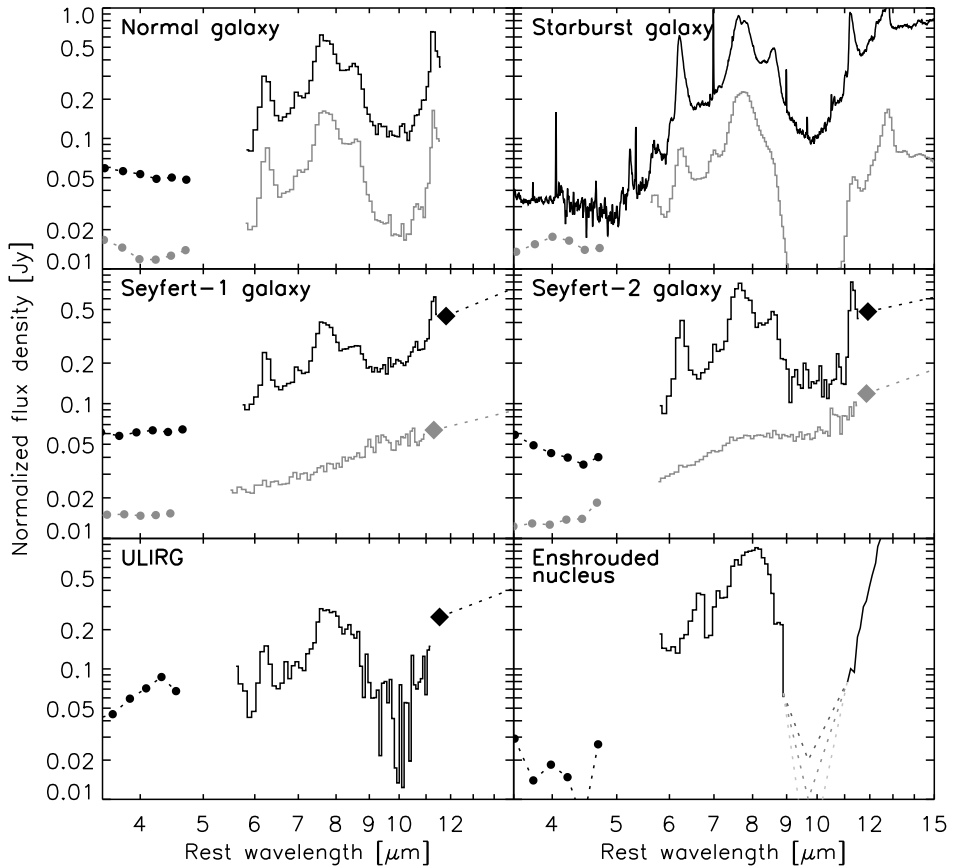


FIGURE 7.2— MIR galaxy spectra. Dots represent ISO-PHT-SS spectroscopy rebinned to a lower resolution. IRAS 12 μm points are denoted by diamonds. **Top-left panel:** Spectra of the 'normal' galaxies NGC 4102 (black) and NGC 3620 (grey). **Top-right panel:** Spectrum of the nuclei of the starburst galaxies M 82 (black) and NGC 4945 (grey). **Mid-left panel:** Spectra of the Seyfert-1 galaxies NGC 7469 (black) and I Zw 1 (grey). **Mid-right panel:** Spectra of the Seyfert-2 galaxies NGC 5953 (black) and PKS 2048-57 (grey). **Bottom-left panel:** Spectrum of the ultra-luminous infrared galaxy UGC 5101. **Bottom-right panel:** Spectrum of the heavily obscured nucleus of NGC 4418. The spectra have been scaled by an arbitrary factor for ease of presentation.

from the weakness of the continuum and PAH features closest to the center of the 9.7 μm silicate absorption feature. The presence of a 6.0 μm water ice absorption feature further reveals that the dust is cold and stored in dense molecular clouds.

Galaxies optically classified as Seyfert galaxies contain an Active Galactic Nucleus (AGN) — a massive central black hole, surrounded by a fiercely X-ray emitting accretion disk. The disk is believed to be surrounded by a thick molecular torus, the orientation of which determines the Seyfert subtype. Galaxies optically classified as Seyfert-1 offer a direct line of sight to the accretion disk and the hot dust at the inner face of the molecular torus. For

type-2 Seyferts this direct view is blocked by the torus. In these galaxies, gas above the plane of the torus, ionized by the X-rays from the accretion disk, serves to betray the presence of the central engine. As a result of irradiation by the central X-ray source the spectra of Seyfert galaxies are characterized by emission lines from highly ionized species like Si IX, Ne V, and Ne VI, which at MIR wavelengths have lines at $3.93\text{ }\mu\text{m}$, 14.3 & $24.3\text{ }\mu\text{m}$ and $7.65\text{ }\mu\text{m}$, respectively (Genzel et al. 1998; Lutz et al. 2002; Sturm et al. 2002). Other than that, the MIR spectral appearance of Seyfert galaxies is quite diverse, with some spectra bearing close resemblance to those of starburst galaxies, while other spectra are dominated by a hot dust power law spectrum (see middle panels of Figure 7.2). Although the average Seyfert-1 galaxy spectrum is continuum-dominated and the average Seyfert-2 galaxy spectrum is not (Clavel et al. 2000), our ISO spectral library contains many examples of Seyfert galaxy spectra showing the properties of the converse subtype (see middle panels of Figure 7.2). Evidently, the overall MIR spectral appearance cannot be just the result of the orientation of the AGN torus, but likely also depends on the properties of the host galaxy (i.e. inclination, degree of starburst activity) as well as the power of the central engine. The spatial scale of the observations is another factor determining the MIR spectral appearance of AGNs. Observations of nearby PAH dominated Seyfert-2 galaxies, like Circinus and Cen A, have shown the spectrum of the inner 70 – 150 pc to be dramatically different from the spectrum of the entire galaxy, revealing an underlying, silicate-absorbed, hot dust continuum, likely associated with the central engine (Laurent et al. 2000).

A very different type of MIR spectrum is detected towards the nucleus of the luminous infrared galaxy NGC 4418 (lower-right panel of Figure 7.2). The spectrum is characterized by a prominent broad peak, centered at $8\text{ }\mu\text{m}$, too wide and too far displaced to be attributed to $7.7\text{ }\mu\text{m}$ PAH emission. Instead, the spectrum appears to be the result of the absorption of a featureless continuum by ices and silicates, both shortward and longward of $8\text{ }\mu\text{m}$, reminiscent of the spectrum of a deeply embedded protostar (Chapter 5). MIR imaging has further revealed the source of the absorbed MIR continuum to be extremely compact ($<80\text{ pc}$; Evans et al. 2003) and to be responsible for most of the infrared luminosity of this galaxy. In the absence of any spectral line information, the nature of the nuclear energy source is unclear and may either be extremely dense star formation or AGN activity or a combination of both (e.g. Chapter 5, Evans et al. 2003). The spectrum of NGC 4418 is not unique. Several other galaxies have been found with spectra similar to NGC 4418, most of them are ULIRGs (see Chapter 2).

The MIR spectra of ULIRGs are more complicated than the spectra of other galaxy types due to the presence of copious amounts of dust in their nuclear regions, leading to spectral distortions and strong radiative transfer effects. Figure 7.3 shows a representative compilation of available ULIRG and HyLIRG spectra, sorted by infrared luminosity. While most low-luminosity ULIRG spectra are dominated by PAH emission features, the spectra at the high-luminosity end bear close resemblance to AGN hot dust continua, showing little or no sign of PAH emission features. At intermediate luminosities some ULIRG spectra are PAH dominated, while others show signs of the presence of an NGC 4418-like broad $8\text{ }\mu\text{m}$ peak, indicating the presence of deeply enshrouded power sources. Some of these ULIRGs also show absorptions of water ice in addition (Chapter 2). A fairly typical, PAH dominated, ULIRG spectrum is further displayed in the lower-left panel of Figure 7.2.

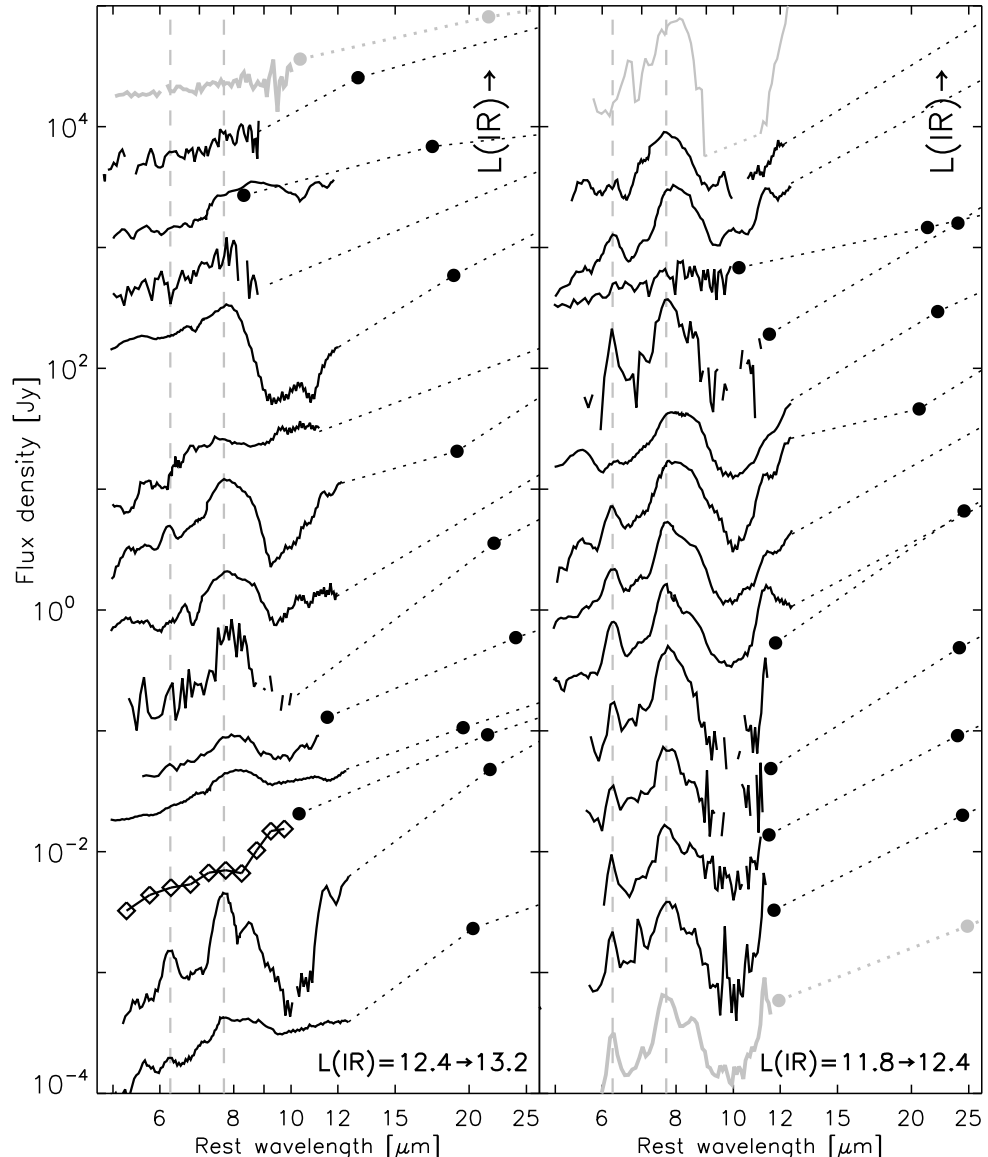


FIGURE 7.3 — ULIRG and HyLIRG spectra sorted by increasing infrared luminosity. Vertical lines indicate the central wavelengths of the $6.2\text{ }\mu\text{m}$ and $7.7\text{ }\mu\text{m}$ PAH features. The spectra shown in grey serve as template spectra for AGNs (**top-left**), starbursts (**bottom-right**) and deeply enshrouded nuclei (**top-left**). The spectra in the **left panel** are, from top to bottom: 3C 273, 15307+3252, 09104+4109, 00397–1312, 00183–7111, 23529–2119, 03538–6432, 23515–2917, 03158+4227, Mrk 231, 00275–2859, Mrk 1014, 03521+0028 and 22192–3211. In the **right panel**: NGC 4418, 17463+5806, 03000–2719, 23060+0505, 17208–0014, 00188–0856, 04384–4848, 02113–2937, 18030+0705, Arp 220, Mrk 273, 23128–5919, NGC 6240 and NGC 7552.

7.4 Diagnostic tools to distinguish AGNs and starbursts

As AGNs and star forming regions have distinct spectral characteristics, their relative contribution to observed IR spectra can be determined in various ways. In this section, we focus on three different diagnostic tools, all based on the strength of PAH emission bands.

7.4.1 A MIR/FIR diagnostic

Indicative of regions predominantly powered by star formation are the strong PAH emission bands. As a measure of the strength of these PAH emission bands, we prefer the $6.2\text{ }\mu\text{m}$ band over other PAH bands, because of several reasons: 1) unlike the 3.3 , 11.2 and $12.7\text{ }\mu\text{m}$ bands this band could be observed by all three MIR spectrometers onboard ISO; 2) the band is situated well outside the silicate absorption band; 3) of all major PAH emission bands, this band is the least influenced by extinction and 4) unlike the $7.7\text{ }\mu\text{m}$ feature, the band cannot be confused with a NGC 4418-like absorbed-continuum peak (see Chapters 2 and 5).

A clear line of sight towards AGN-heated hot dust may be recognized spectroscopically by the presence of a strong $6.2\text{ }\mu\text{m}$ continuum associated with a hot dust power law spectrum. Since hot dust predominantly radiates at MIR wavelengths, the ratio of $6.2\text{ }\mu\text{m}$ continuum over FIR flux will be high; far higher than for both star forming regions and AGNs without a clear line of sight to the AGN-heated hot dust. We therefore normalize our star formation indicator and our AGN hot dust indicator on the FIR flux of the source and plot these two quantities (referred to as 6.2PAH/FIR and 6.2cont/FIR) in a diagnostic diagram. A clear disadvantage of this diagnostic is the often different apertures of the MIR and FIR instruments.

For Galactic sources the strength of the hot continuum is estimated by drawing a polynomial of order 2 through points at ~ 5.9 and $\sim 6.6\text{ }\mu\text{m}$ and integrating the flux underneath it in the range from 6.0 to $6.5\text{ }\mu\text{m}$. Integrating the flux above this polynomial over the same range gives the strength of the $6.2\text{ }\mu\text{m}$ PAH feature. For galaxies, the continuum is determined from a linear interpolation between the fluxes at 5.9 and $6.55\text{ }\mu\text{m}$. Other than that, the method to measure the strength of the hot continuum and the $6.2\text{ }\mu\text{m}$ PAH flux is identical to the method for the Galactic spectra. If a source exhibits water ice absorption (indicated in Table 7.1 for Galactic sources and in Chapter 2 for the galaxies), for Galactic sources a local spline continuum is determined along the wing of the water ice band to estimate the $6.2\text{ }\mu\text{m}$ PAH flux. For these sources, the $6\text{ }\mu\text{m}$ continuum strength is estimated by integrating a spline fixed right outside the ice absorption features so that the continuum strength is corrected for the ice extinction. For extragalactic sources, the $6.2\text{ }\mu\text{m}$ PAH flux is recovered by defining a continuum at the base of the $6.2\text{ }\mu\text{m}$ PAH feature and integrating the flux above it in the range of 6.0 – $6.5\text{ }\mu\text{m}$. The spectra of some galaxies show no evidence for $6.2\text{ }\mu\text{m}$ PAH emission. For these galaxies upper limits for the $6.2\text{ }\mu\text{m}$ PAH flux are obtained by integrating a Gaussian with a peak flux of three times the rms noise and a FWHM of $0.185\text{ }\mu\text{m}$. Their FIR fluxes are computed from the $60\text{ }\mu\text{m}$ and $100\text{ }\mu\text{m}$ IRAS Faint Source Catalog (FSC) fluxes, using the formula derived by Sanders & Mirabel (1996). For the compact H II regions, the FIR flux is derived by fitting a modified blackbody to the IRAS PSC fluxes (Peeters et al. 2002b). The IRAS PSC fluxes nicely correspond to the flux seen by ISO in the IRAS bands at 60 and $100\text{ }\mu\text{m}$ (Peeters et al. 2002b). However, the SWS and IRAS instruments have very different beams ($20''$ versus $90''$). This may seriously affect the derived ratio of the MIR/FIR ratios if the source shows structure on a scale larger than the SWS beam. It probably affects about half our H II region observations. It is possible to scale the observed LWS flux to the SWS

flux at 45 μm . We opt to not apply this scaling and use the FIR as derived from the IRAS PSC fluxes, since scaling is no guarantee that the flux ratio is correct. Indeed, the dust temperature may typically vary by some 25% and the total IR flux scales with $\sim T^5$. The only exception to this is the extended molecular cloud M17–North where we did scale the LWS to the SWS observations at 45 μm . For a few sources — Orion, NGC 2023, NGC 7023, M17–SW and the ISM lines-of-sight —, higher spatial resolution data (e.g. KAO with a beam of 35–60'') exist and we have used those in our analysis (Table 7.1). Those sources, for which the MIR/FIR ratio may have been affected by spatial resolution issues are identified in Fig. 7.4 (by grey dots) and in Table 7.1. We note that these sources tend to be systematically displaced towards lower MIR/FIR ratios than the rest of the H II region sample by about a factor ≤ 3 . The derived fluxes for the Galactic sample and the extragalactic sample are given in, respectively, Table 7.1 and Spoon et al. (in prep.).

H II regions and ISM

As discussed in Sect. 7.3.1, both indicators vary clearly within our sample of H II regions and this range extends up to the reflection nebulae and the diffuse ISM lines of sight. This is also seen in Fig. 7.4; most sources are well localized in this diagram and are positioned along a strip going from the lower left towards the upper right, further referred to as the ‘main sequence’. A clear segregation is present with embedded compact H II regions situated on the lower left side of the main sequence, while the reflection nebulae and the (diffuse) ISM are on the top right side of the main sequence. In addition, situated in the middle-right are the exposed PDRs, such as M 17 (represented by the H II region M 17–1 and the molecular clouds M17–8 and M17–North) and Orion (the Orion nebula including the Orion Bar). This segregation with object type suggests that the underlying cause might be a variation in the physical/chemical properties of the PAHs going from compact H II regions to exposed PDRs and the diffuse ISM, e.g. with G_0/n_e (Bakes et al. 2001a,b). Whether the segregation within our sample of H II regions is dominated by an evolutionary sequence — from ultra-compact to compact and then classical H II regions — is less clear. The 6.2PAH/FIR ratio correlates weakly with both the electron density and the size of the H II region (taken from Martín-Hernández et al. 2002; Martín-Hernández et al. 2003). In contrast, the 6.2cont/FIR does not show a clear dependence on either the electron density nor the size of the H II region. The latter also show large scatter in Fig. 7.4, where many H II regions lie above the main sequence. Likely, this reflects the contribution of hot dust inside the H II region. We note that metallicity does not seem to influence the location of these sources in this diagram. In particular, the SMC and 30 Dor — with metallicities 0.3 and 0.1 of solar — lie on opposite ends of this diagram.

To guide the eye, we have drawn lines of constant 6.2PAH/6.2cont in Fig. 7.4. This ratio is relatively constant within the our sample of H II regions, RNe and diffuse ISM lines of sight, ranging from 0.12 to 2.50 (excluding K3–50A). There seems to be, however, a systematic trend: H II regions tend to lie above the middle line while RNe and the diffuse ISM tend to lie between middle and lower lines. Four notable outliers are the Orion Bar, IRAS 18116, IRAS 12073 and K3–50A. As noted above, the Orion Bar is located with the RNe suggesting a PDR dominated spectrum (cf. Tielens et al. 1993). IRAS 18116, on the other hand, has a 6.2PAH/6.2cont ratio similar to that of the RNe although it shows no other distinction in its properties with the H II regions in our sample. IRAS 12073 has the lowest 6.2PAH/6.2cont ratio of the H II regions due to its very strong hot dust continuum. Indeed, IRAS 12073 is also

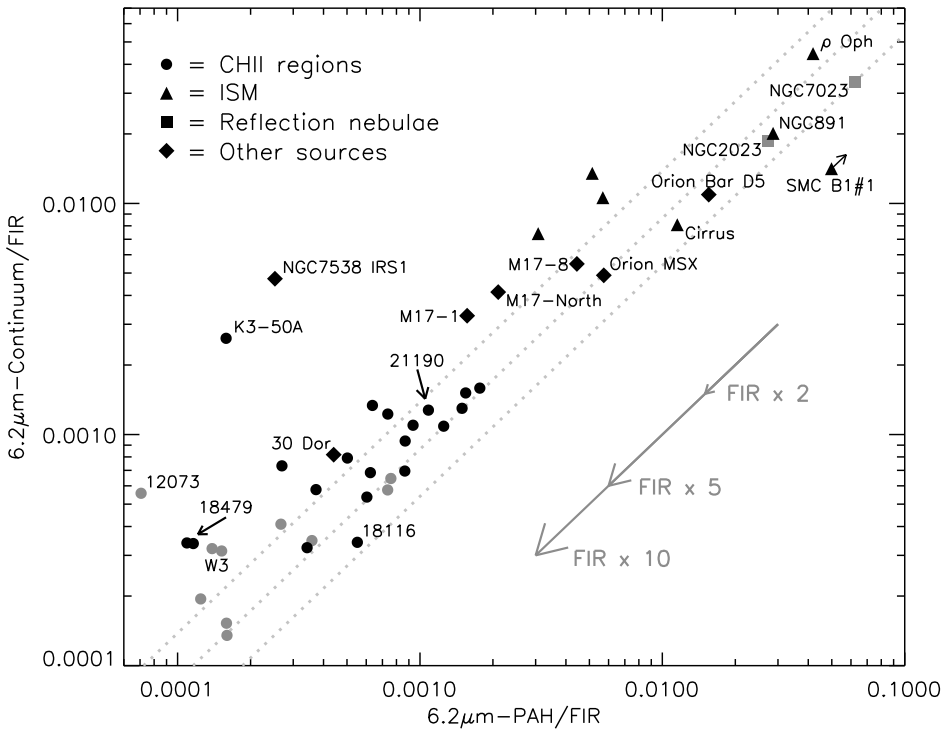


FIGURE 7.4 — A MIR/FIR diagnostic diagram. The vertical axis measures the ratio of integrated 6.0–6.5 μm continuum to FIR flux and the horizontal axis the ratio of integrated 6.2 μm -PAH to FIR flux. The three dotted lines are parallel to the arrows and hence correspond to a 6.2PAH/6.2cont ratio of 1.85, 1.16 and 0.72 for the lower, middle and top line, respectively. The sources possibly suffering from aperture effects are plotted in grey. The influence of an uncertain FIR flux is indicated by the arrows for respectively a factor of 2, 5 and 10.

the source with the largest Lyman continuum luminosity amongst the H II regions. As already pointed out, K3–50A has all the characteristics of H II regions except for its continuum which is more like that of massive protostars (see Sect. 7.3.1). The compact bipolar H II region NGC 7538 IRS1 is located close to K3–50A in this diagram.

For extended sources, the difference in aperture may influence the derived MIR to FIR ratios. In addition, the FIR beam is much larger than the MIR beam and hence confusion by nearby sources at FIR wavelengths is possible. We have indicated in Table 7.1 and Fig. 7.4 the sources suffering from these effects.

Based upon a comparison of H I recombination line fluxes and radio free-free fluxes, extinction in the MIR should be negligible for our sample of H II regions with $\tau_{\text{dust}}(6.2) \leq 1$ (Martín-Hernández et al. 2002; Martín-Hernández et al. 2003). Hence, we conclude that the presence of a range in the 6.2PAH/FIR and 6.2cont/FIR ratios is real and that the sequence span by our sample likely reflects an “evolution” with object type : from embedded compact H II regions towards exposed PDRs and (diffuse) ISM.

The galaxies

As already pointed out in Sect. 7.3.2, ISO MIR spectra probe smaller physical scales than the IRAS photometers. This mismatch becomes an issue when relating MIR to FIR fluxes for nearby galaxies for which the infrared luminous regions do not completely fit within the smaller of the two apertures. We therefore have screened our sample against spectra showing clear mismatches between the IRAS 12 μm flux and the ISO 11–12 μm continuum flux. The remaining sample should therefore only consist of galaxies whose MIR emitting region fits entirely within the ISO aperture. For the IRAS-derived FIR flux we will assume that it is dominated by the same (circum)nuclear star forming regions which give rise to the MIR continuum. The final sample was subsequently created by screening the sample further against any spectrum for which the 6.0–6.5 μm continuum is so noisy that the integrated 6.2 μm flux would have to be replaced by an upper limit.

Our final galaxy sample consists of 69 AGNs (7 of which are QSO, 31 are Seyfert-1 and 31 are Seyfert-2 galaxies), 22 starburst and H II-type galaxies, 8 normal galaxies, 49 ULIRGs, 2 HyLIRGs and 3 infrared galaxies with deeply obscured nuclei (I02530+0211, I03344–2103 and NGC 4418). The galaxy sample is presented in Figs. 7.5, 7.6, 7.8 and 7.9.

As can be seen in the top panel of Fig. 7.5, the normal galaxies occupy a remarkably narrow strip close to the position of the exposed PDR Orion MSX. Note the extreme position of IC 860, close to 30 Dor. ISO-LWS observations have revealed this source to be very unusual in not showing any of the typical FIR fine structure lines (Malhotra et al. 2001). Also the ISO-PHT-S spectrum is not typical for normal galaxies, as it does not show 6.2 μm PAH emission. The quality of the spectrum is, however, not good enough to speculate on the nature of the MIR spectrum.

A large fraction of the starburst galaxies can be found close to the position of the normal galaxies (top panel of Fig. 7.5), with the exception of two sources, IRAS 08007–6600 and CGCG 049–057. The ISO-PHT-S spectrum of IRAS 08007–6600 (classified by Veilleux & Osterbrock (1987) as H II-type) looks very similar to AGN hot dust dominated spectra and was therefore classified by Laureijs et al. (2000) as AGN-dominated. The spectrum of CGCG 049–057, on the other hand, is PAH-dominated, but has a very strong and cold FIR continuum. Note that the starburst galaxies (excluding the two just mentioned) occupy a larger range along the ISM main sequence than the normal galaxies do, but look, on average, like exposed PDRs.

The distribution of AGNs (QSOs and Seyfert galaxies) is shown in the middle panel of Fig. 7.5. The sample seems to segregate into two groups. One group is made up mostly of Seyfert-2 galaxies with IRAS S 25/S 60 ratios all below 0.25, while the other group consists mostly of Seyfert-1 galaxies and QSOs with IRAS S 25/S 60 ratios all larger than 0.25. The galaxies in the first group all show 6.2PAH/FIR ratios in the same range as normal and starburst galaxies. In contrast, most of the galaxies in the second group only have formal 6.2PAH/FIR upper limits, some of which are found at 6.2PAH/FIR ratios 2–3 times larger than the highest value found for normal and starburst galaxies. These upper limits shift left and fit in with the rest of their group if the scaling by FIR flux is replaced by a scaling by the total infrared flux (8–1000 μm ; Sanders & Mirabel 1996). Diagrams based on the IR flux are shown in Fig. 7.6. In line with the orientation dependent unification scheme (Antonucci 1993), the segregation in 6.2cont/FIR between the two groups likely reflects the orientation of the toroid structure around the nucleus which for the first (lower) group may block our line of sight to the warm inner toroid, responsible for the 6 μm continuum. Assuming this to

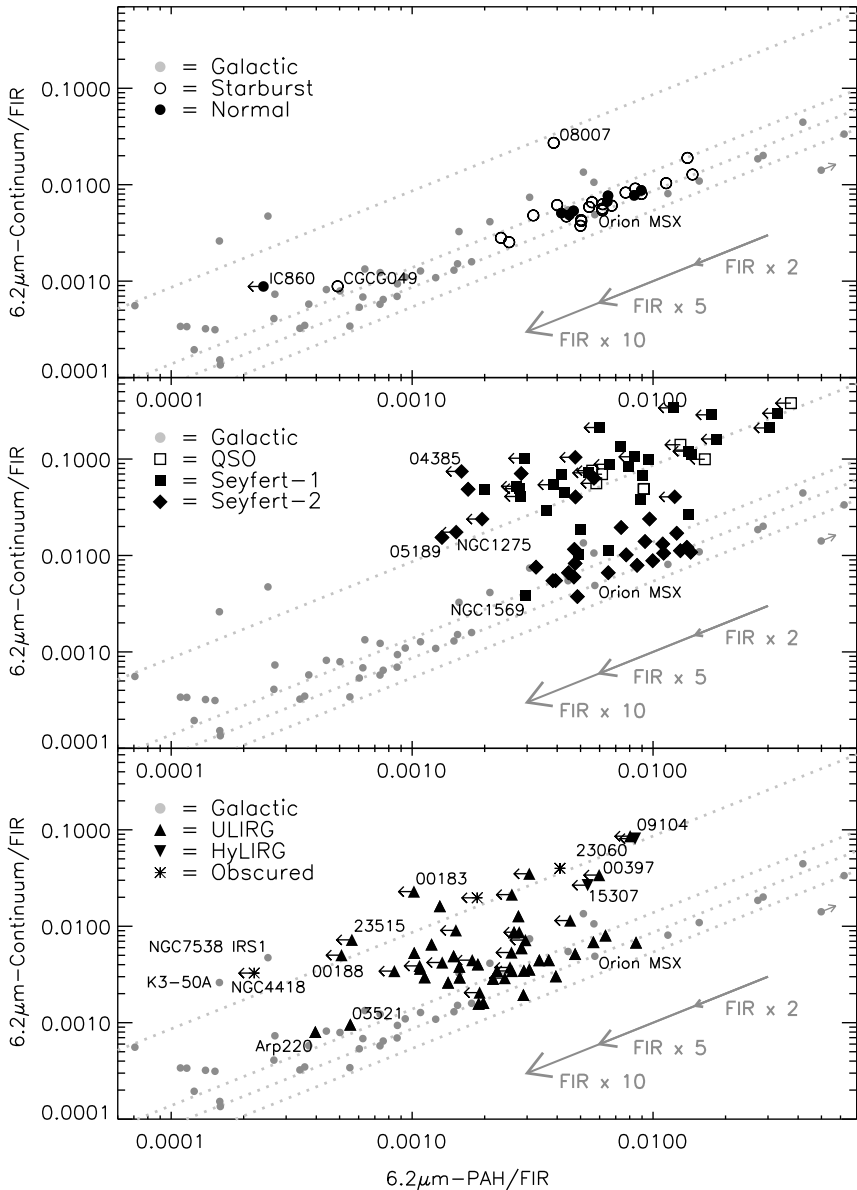


FIGURE 7.5 — MIR/FIR diagnostic diagram for different type of galaxies. The vertical axis measures the ratio of integrated 6.0–6.5 μm continuum to FIR flux and the horizontal axis the ratio of integrated 6.2 μm -PAH to FIR flux. Grey circles correspond to H II regions and the ISM sources. The three parallel dotted lines and the arrows are as in Fig. 7.4. The top dotted line corresponds to a 6.2PAH/6.2cont ratio of 0.12.

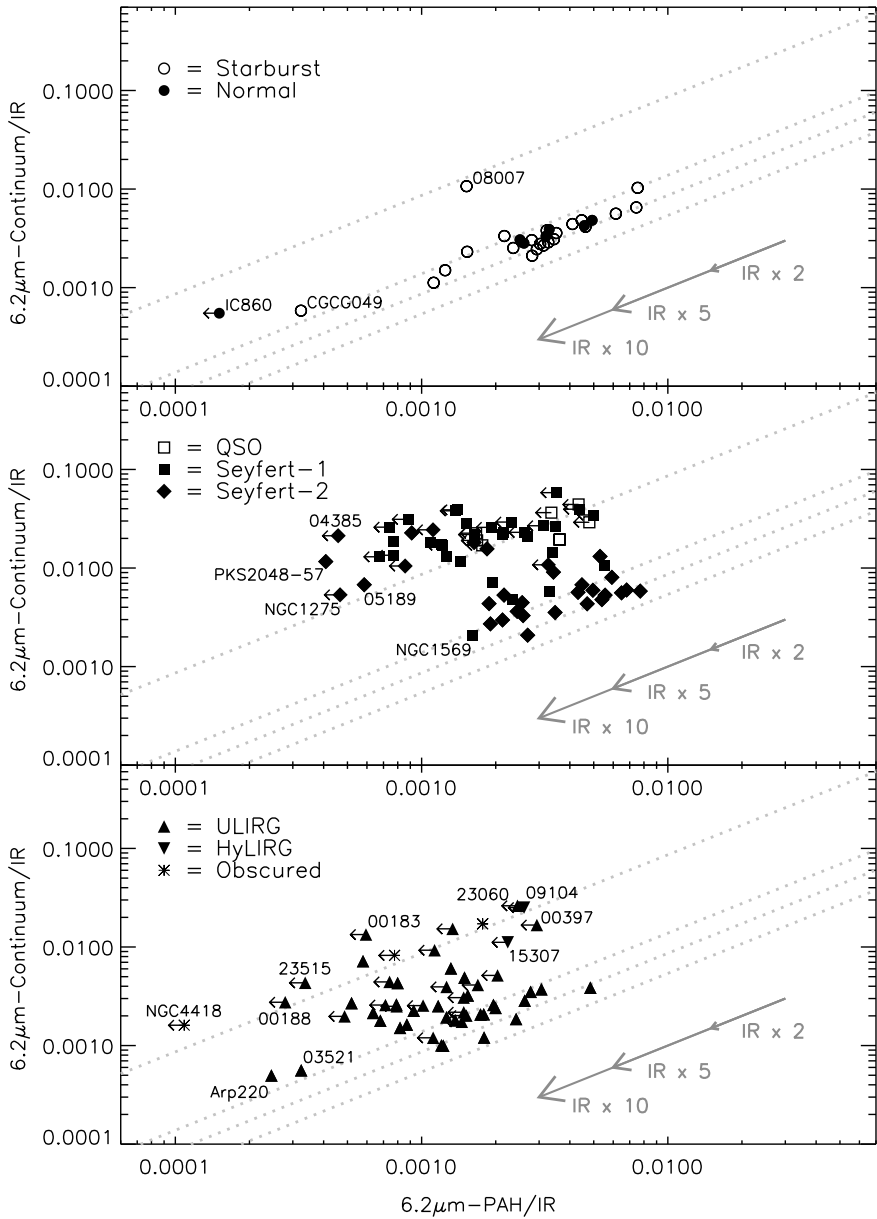


FIGURE 7.6— MIR/IR diagnostic diagram for different type of galaxies. The vertical axis measures the ratio of integrated $6.0\text{--}6.5\mu\text{m}$ continuum to IR flux and the horizontal axis the ratio of integrated $6.2\mu\text{m}$ -PAH to IR flux. The three parallel dotted lines and the arrows are as in Fig. 7.4. The top dotted line corresponds to a $6.2\text{PAH}/6.2\text{cont}$ ratio of 0.12.

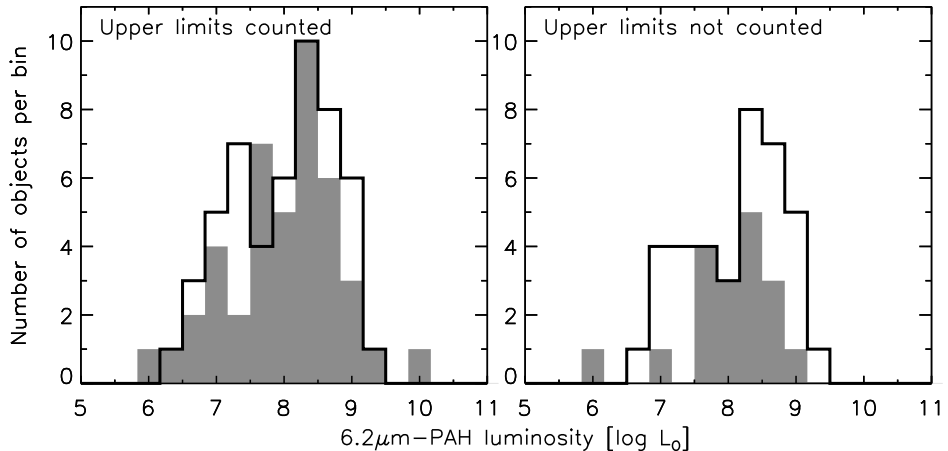


FIGURE 7.7— Luminosity distribution of the $6.2\mu\text{m}$ PAH feature for Seyfert-1 galaxies (grey) and Seyfert-2 galaxies (black). The bin sizes are 0.33 dex. **Left panels:** Upper limits on the PAH flux are counted as detections. **Right panels:** Upper limits on the PAH flux are excluded.

be the case, a separation of a factor 10 in 6.2cont/FIR may be interpreted as an $A(V)=50\text{--}150$ (depending on the choice of extinction law), which (assuming a normal gas to dust ratio $N_{\text{H}}=1.9\times 10^{21}\text{ cm}^{-2}$) is equivalent to a column density of $10^{23.0}\text{--}10^{23.5}\text{ cm}^{-2}$. This range is in good agreement with the mean Seyfert-2 absorbing column, as measured directly from X-ray data (Risaliti et al. 2002), and with the results of Clavel et al. (2000). The presence of some type-1 Seyferts in the lower cloud (NGC 1569, Mrk 789 and NGC 7469) would then imply that the intrinsic power of the AGN in these galaxies must be small for the AGN hot continuum not to dominate the MIR spectral appearance. Alternatively, the AGN hot continuum and the optical AGN diagnostic lines emanating from these three galaxies are obscured by patchy foreground dust clouds along the line of sight in the host galaxy, but still allowing an optical classification. Conversely, the presence of some type-2 Seyferts in the upper cloud (NGC 1068, NGC 1275, Mrk 463, IRAS 04385–0828, NGC 5506 and PKS 2048–57), would then be explained by a direct line of sight, at grazing angle, to the inner edge of the torus, or by the presence of dust clouds above the plane of the torus, which are irradiated and heated by the central source.

One of the key predictions of the orientation dependent unification scheme is that the properties of the Seyfert host galaxies are independent of the orientation of the torus and, hence, independent of the Seyfert type. Clavel et al. (2000) have tested this by measuring the $7.7\mu\text{m}$ PAH luminosity distributions for type-1 and type-2 Seyferts and found that they were the same. We have repeated this test for our entire sample of Seyfert galaxies (43 Seyfert-1's; 51 Seyfert-2's). The resulting luminosity distributions are shown in Figure 7.7. If upper limits are counted as detections, both Seyfert types have the same median $6.2\mu\text{m}$ PAH luminosity of $10^{8.1}\text{ L}_\odot$. If upper limits are excluded, the median values are still very similar, $10^{8.2}\text{ L}_\odot$ for type-1 and $10^{8.3}\text{ L}_\odot$ for type-2 Seyferts. Our results are therefore consistent with those of Clavel et al. (2000).

Given a similar range of $6.2\text{ }\mu\text{m}$ PAH luminosities for all Seyferts, it is interesting to note that the range of 6.2cont/FIR and 6.2PAH/FIR ratios found for continuum-dominated Seyferts extends to lower values than for PAH-dominated Seyferts. These sources are therefore likely enriched in FIR flux, as opposed to deficient in $6.2\text{ }\mu\text{m}$ PAH flux. The outlier I05189–2524, for example, has a $6.2\text{ }\mu\text{m}$ PAH luminosity four times above average ($\langle L(6.2\text{PAH}) \rangle = 10^{8.25} L_\odot$) and I04385–0828, at roughly the same 6.2PAH/FIR , has an average PAH luminosity. Both sources hence exhibit a FIR excess, as is likely also the case for most other Seyferts at this end of the distribution. The MIR spectrum of both sources is unusual. I05189–2524 is the only Seyfert galaxy in our sample displaying a $6.0\text{ }\mu\text{m}$ water ice absorption, while I04385–0828 shows a deep $9.7\text{ }\mu\text{m}$ silicate feature, which is also unusual. Further inspection of the samples of continuum-dominated and PAH-dominated AGNs reveals that the galaxies at the lower end of both distributions are not scattered along a line of constant line-to-continuum ratio, but rather along a line of constant 6.2cont/IR (Fig. 7.6), indicating a decreasing $6.2\text{ }\mu\text{m}$ PAH line-to-continuum ratio. Possibly, this indicates that the nuclei of Seyferts at the lower 6.2PAH/FIR end of the two distributions are more dusty than Seyferts at the other end of the two parallel distributions.

Even more dusty are the nuclei of most ultra-luminous infrared galaxies. The distribution of ULIRGs, HyLIRGs and galaxies with deeply obscured nuclei, is shown in the lower panel of Fig. 7.5. These objects cover a large portion of this diagram, reflecting their wide-ranging properties. Galaxies in the upper right section of the plot (e.g. I00397–1312, I00275–2859, I09104+4109, I 15307+3252 and I23060+0505), all have IRAS S 25/S 60 ratios and MIR spectra similar to AGNs in that same section. These ULIRGs and HyLIRGs are likely AGN-dominated. In contrast, some ULIRGs show spectra similar to Orion MSX and other bona fide star formation regions and are likely dominated by star formation. Many other ULIRGs occupy a space not covered by any other (extra)galactic source, roughly limited by the lower end of both Seyfert distributions, and the far-off position of the deeply enshrouded nucleus of NGC 4418. These ULIRGs are therefore likely very dusty or composite objects, made up of an NGC 4418-like embedded nucleus and circumnuclear star formation. Two notable outliers are Arp 220 and I03521+0028, which are found among the CH II regions, close to the position of another outlier, IC 860. Since the spectrum of Arp 220 is deficient in emission lines (Chapter 6) — characteristic of CH II regions — this source is likely shifted down from the ULIRG domain, due to the presence of an additional strong FIR component, which is not commonly present in other ULIRGs (Chapter 6). Given their close proximity to Arp 220, I03521+0028 and IC 860 may also harbor similar FIR bright components.

Fig. 7.8 shows the distribution of a subset of galaxies in which the $6.0\text{ }\mu\text{m}$ water ice feature has been identified (Chapter 2), the so-called ‘ice galaxies’. The sample has been appended with two galaxies (I03344–2103 and I02530+0211), which show similarly deep silicate absorption features as the class 1 and class 2 ice galaxies. However, shortward of the silicate feature both spectra show features which are likely artefacts. For I02530+0211 it is nevertheless clear that the 5.8 – $6.5\text{ }\mu\text{m}$ spectrum is feature-free. Likewise, for I03344–2103 the presence of weak $6.2\text{ }\mu\text{m}$ PAH emission can be confirmed, the presence of a $6.0\text{ }\mu\text{m}$ water ice absorption feature, however, not.

The presence of $6.0\text{ }\mu\text{m}$ water ice absorption causes the continuum in the 6.0 – $6.5\text{ }\mu\text{m}$ range to be depressed with respect to its intrinsic value. The distorting effect is minor for weakly ice-absorbed sources like Mrk 231, I05189–2524 and I00183–7111, but substantial for sources with both a strong continuum and an appreciable ice optical depth, like I00188–

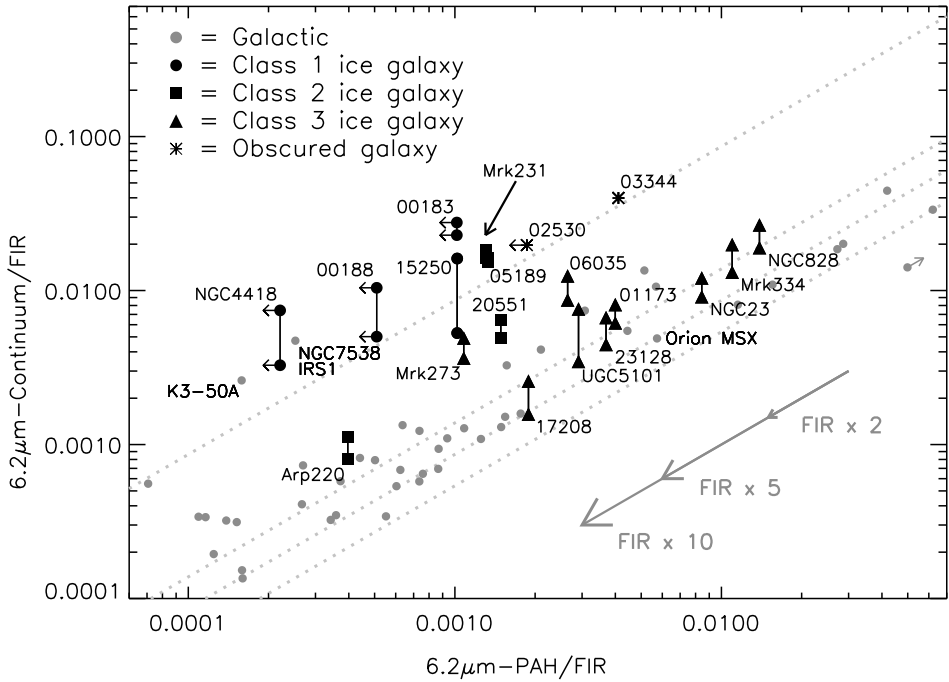


FIGURE 7.8— MIR/FIR diagnostic diagram for deeply obscured galaxies and ice galaxies. The vertical axis measures the ratio of integrated $6.0\text{--}6.5\,\mu\text{m}$ continuum to FIR flux and the horizontal axis the ratio of integrated $6.2\,\mu\text{m}$ -PAH to FIR flux. The four parallel dotted lines and the arrows are as in Fig. 7.5. A vertical black line indicates the upward shift of an ice galaxy if the measured $6.2\,\mu\text{m}$ continuum is corrected for the presence of $6.0\,\mu\text{m}$ water ice absorption.

0856, NGC 4418, I15250+3609 and UGC 5101. As can be seen in Fig. 7.8, these latter sources shift up by a factor 2–3 if the model continua derived in Chapter 2 are used as intrinsic continuum for the $6.0\text{--}6.5\,\mu\text{m}$ range.

Class 3 ice galaxies, showing weak $6.0\,\mu\text{m}$ ice band absorptions, coincide with the location of the normal and starburst galaxies in this diagram. Compared to class 3, class 1 ice galaxies, with no obvious PAH features and strong $6.0\,\mu\text{m}$ ice and silicate bands are shifted upwards and to the left in Fig. 7.8, betraying the addition of extra MIR continuum as well as FIR continuum. The few class 2 ice galaxies, with weak PAHs and moderate ice absorptions, are more scattered throughout this plot. Some (I20551–4250) fall in between the two other classes. Others coincide with class 1 (Mrk 231 and I05189–2524). Arp 220, which has weak ice absorption, has shifted downwards along the Galactic trend and is an outlier in this diagram (see above). It is clear that the absorption associated with molecular clouds can influence the location of a region in this diagram. In particular, we note that the extreme example of this class, NGC 4418, has shifted all the way to in between the two extreme embedded Galactic sources associated with molecular cloud material, K3–50A and NGC 7538 IRS1.

The infrared characteristics of our sample can also be described in a mid-infrared/total-infrared (MIR/IR) diagram. Close inspection of the distribution of the various galaxy types over this diagram (Fig. 7.10) reveals that in this diagram the AGNs also segregate into an upper and a lower group; the ULIRGs seem to be a continuation of these two AGN groups towards lower MIR/IR. The slope of the two parallel distributions seems to be far shallower than the slope of the main sequence. As discussed before for the Seyfert sample in the context of the MIR/FIR diagram, we suggest that galaxies at the lower end of the two distributions may be more dusty. Indeed, the galaxies at $6.2\text{PAH/IR} < 6 \times 10^{-4}$ are predominantly ice galaxies.

In Chapter 2 we proposed that the classification of ice galaxy spectra may reflect an evolutionary sequence from strongly obscured beginnings of star formation (and AGN activity) to a less enshrouded stage of advanced star formation (and AGN activity). Assuming NGC 4418 to represent the earliest, most obscured stage after a galaxy collision or a galaxy merger, evolution would then proceed towards the lower distribution for galaxies which in the MIR are dominated by star formation (and may contain a Seyfert-2 nucleus), or towards the upper distribution for galaxies which in the MIR are AGN-dominated.

Application of diagnostic

MIR galaxy spectra can show the spectral characteristics of star forming regions, AGN-heated dust and/or obscuration (see Sect. 7.3.2). As pointed out above, spectra of clear lines of sight to AGN-heated dust are located in other parts of the MIR/FIR diagnostic diagram than spectra for which this line of sight is blocked by the AGN torus and which therefore are PAH-dominated. In order to better understand the connection between these two groups we have calculated the diagnostic ratios that result from adding AGN hot dust to several choices of PAH-dominated spectra. As pure AGN-heated dust template, we used the nuclear spectrum of the prototypical Seyfert-1, NGC 4151, and set its 6.2PAH/FIR ratio equal to 0. As the FIR flux associated with AGN hot dust has not been directly measured for NGC 4151 (nor for any other galaxy), we determine two values for its 6.2cont/FIR ratio, assuming 25% and 50% of the IRAS FSC flux to be associated with the AGN hot dust. As starburst template, we choose the central region of the starburst galaxy M 83. Other PAH dominated galaxy spectra along the main sequence are subsequently mimicked by scaling the FIR flux up and down by a factor 3. Dashed and dash-dotted lines in Fig. 7.9 represent the calculated mixing lines, further referred to as ‘AGN-starburst’ tracks. These tracks strikingly illustrate the direction in which a Seyfert galaxy spectrum would move if the obscuring dust in the line of sight to the hot inner wall of the torus would be removed. The absence of Seyfert galaxies along the horizontal (upper) part of the mixing lines may be taken as a further confirmation that AGNs in the upper group only differ from those in the lower group by an obscuration equivalent to a factor of 10–50 in $6\mu\text{m}$ brightness.

Similarly, starburst galaxies and heavily obscured galaxies are found in far-apart regions in the MIR/FIR diagnostic diagram. We illustrate the connection between these two groups by calculating the diagnostic ratios that result from adding PAH dominated spectra to an heavily obscured spectrum. In this way, we mimick the degree of obscuration. As a template for a heavily obscured galaxy, we used the Galactic massive protostar NGC 7538 IRS1, located close to NGC 4418. We further used the same starburst templates as for the AGN-starburst tracks, but added another main sequence ‘starting’ point in the lower left quadrant, by scaling the FIR flux of M 83 up by a factor 30. These mixing lines — further referred to as ‘obscured-

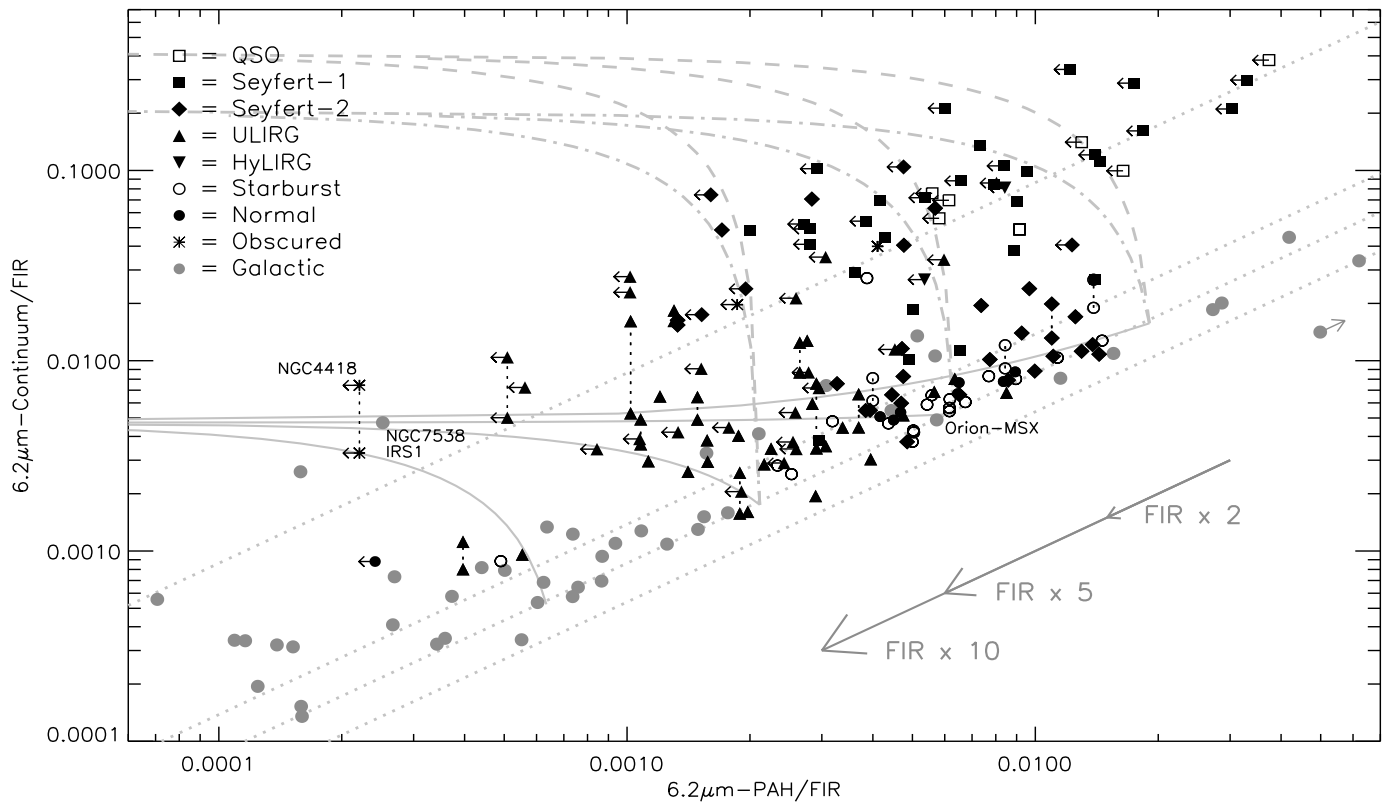


FIGURE 7.9 — The MIR/FIR diagnostic diagram for all sources. The vertical axis measures the ratio of integrated $6.0\text{--}6.5\mu\text{m}$ continuum to FIR flux and the horizontal axis the ratio of integrated $6.2\mu\text{m}$ -PAH to FIR flux. The *dotted lines* and the *arrows* are as in Fig. 7.5. The *continuous lines* are mixing lines between heavily obscured and exposed star formation. The mixing lines from starburst- to AGN-dominated MIR spectra are represented by the *dashed* and *dot-dashed* lines, assuming respectively 25% and 50% of the IRAS FSC flux to be associated with AGN hot dust. See text for details.

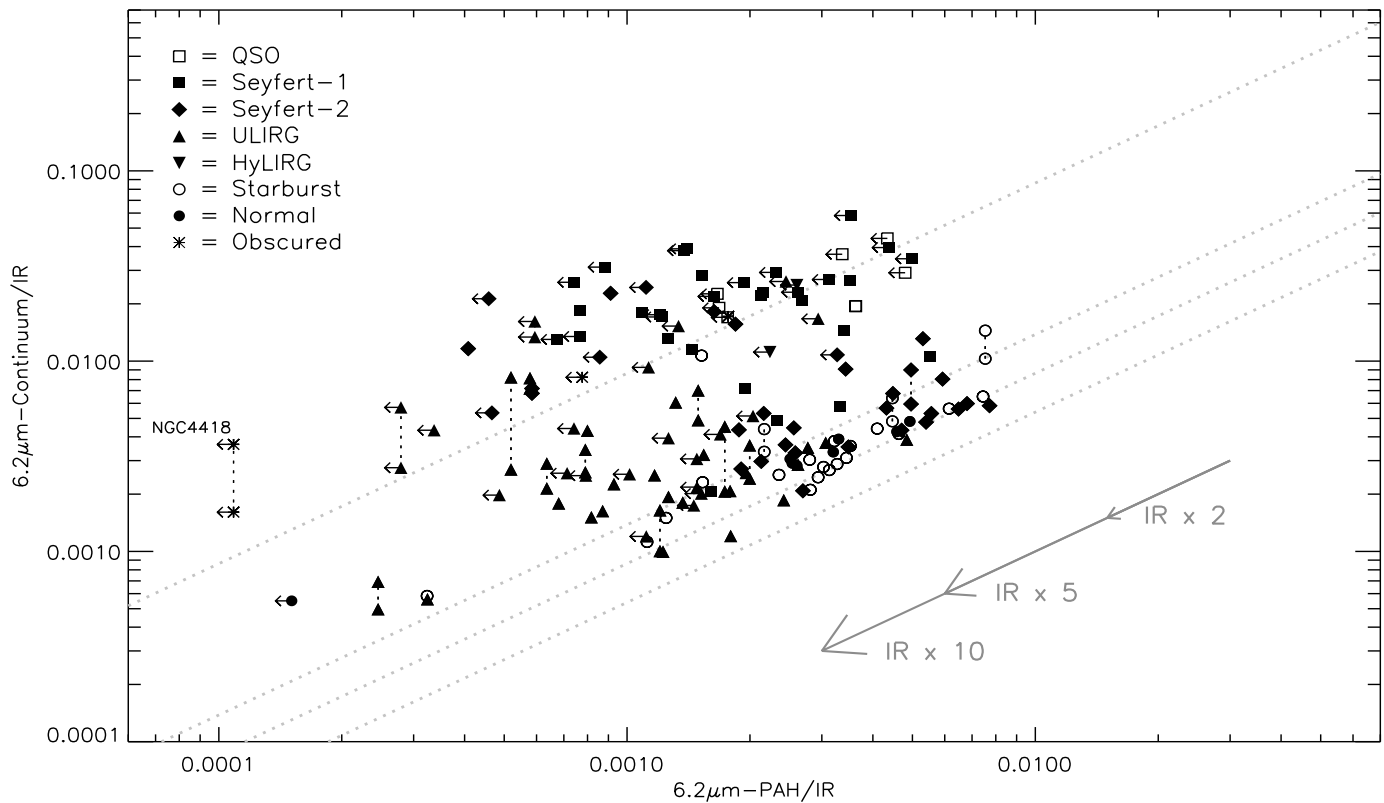


FIGURE 7.10 — MIR/IR diagnostic diagram for extragalactic sources. The vertical axis measures the ratio of integrated 6.0–6.5 μm continuum to IR flux and the horizontal axis the ratio of integrated 6.2 μm -PAH to IR flux. The dotted lines and the arrows are as in Fig. 7.5.

'starburst' tracks — are shown by solid lines in Fig. 7.9. Note that H II regions located above the main sequence do not necessarily suffer from obscuration.

As can be seen in Fig. 7.9, on the main sequence no galaxies are found with 6.2PAH/FIR ratios below 0.002–0.003. Assuming this to be the lowest attainable 6.2PAH/FIR value for pure starburst galaxies, our tracks suggest that galaxies found at $6.2\text{PAH}/\text{FIR} < 0.002$ must contain an obscured nuclear component. Interestingly, this would then indicate that a large fraction of the ULIRG nuclei is obscured. Note that our simple mixing model does not offer an explanation for the extreme positions of Arp 220, IC 860, CGCG 049–057 and I03521+0028, found in the lower left quadrant of the diagram.

7.4.2 Laurent diagnostic diagram

Another diagnostic solely based on the MIR spectrum has been proposed by Laurent et al. (2000). These authors assume that the MIR emission of galaxies is a composition of emission from 1) AGN-heated dust, characterised by a strong dust continuum shortwards of $10\ \mu\text{m}$, 2) PDRs, characterized by a PAH emission spectrum, and 3) H II regions, characterized by strong dust continuum longwards of $10\ \mu\text{m}$. To quantify their relative contributions, two diagnostic indicators are used, the ratio of warm ($14\text{--}15\ \mu\text{m}$) to hot ($5.1\text{--}6.8\ \mu\text{m}$) dust continuum and the ratio of $6.2\ \mu\text{m}$ PAH emission to hot dust continuum. Note that the latter indicator is similar to the offset ($6.2\text{PAH}/6.2\text{cont}$) of a source from the main sequence in the MIR/FIR diagnostic.

We have chosen to sample the hot continuum at a somewhat shorter wavelength than done by Laurent et al. (2000), in order to be a) more sensitive to the slope between hot and warm continuum and b) to avoid sampling within the $6.0\ \mu\text{m}$ water ice absorption band. Our preferred integration range for the hot continuum therefore runs from 5.3 to $5.8\ \mu\text{m}$. For the warm continuum we adopt the same integration range as Laurent et al. (2000): $14.0\text{--}15.0\ \mu\text{m}$. The $6.2\ \mu\text{m}$ PAH flux is determined in the same way as discussed in the previous section. The derived fluxes for the Galactic sample and the extragalactic sample are given in, respectively, Table 7.1 and Spoon et al. (in prep.).

H II regions and ISM

The H II regions do not form a narrow sequence in this diagram but rather show a wide spread scattering over about 1/3 of the plot. However, they do avoid the low PAH to warm continuum properties of the AGNs. The Orion Bar is now positioned with the H II regions — with strong PAHs and moderately warm continuum — instead of with the reflection nebulae. Obviously, Galactic sources which are not on the main sequence in the MIR/FIR diagram (i.e. with unusual $6.2\text{PAH}/6.2\text{cont}$ ratios) are also outliers in the Laurent diagram (i.e. at correspondingly unusual $6.2\text{PAH}/5.5\text{cont}$ ratios). In the Laurent diagram outliers are, however, more apparent. For the rest, similar conclusion can be drawn as for the MIR/FIR diagnostics. First, metallicity seems not to influence the location of the sources in the diagram, as exemplified by the distinct locations of 30 Dor and the SMC in the diagram. Second, massive protostars (NGC7538 IRS1 and Mon R2 IRS2, but also K3–50A) are found at low $6.2\text{PAH}/5.5\text{cont}$ and low $15\text{cont}/5.5\text{cont}$, clearly away from most other H II regions and much closer to the AGN template. Likewise, IRAS 18479, an H II region suffering from heavy extinction, is situated near the center of the diagram. Note that correcting for extinction (for sources with known A_K) does not reduce the observed spread. However, it clearly has some influence on the

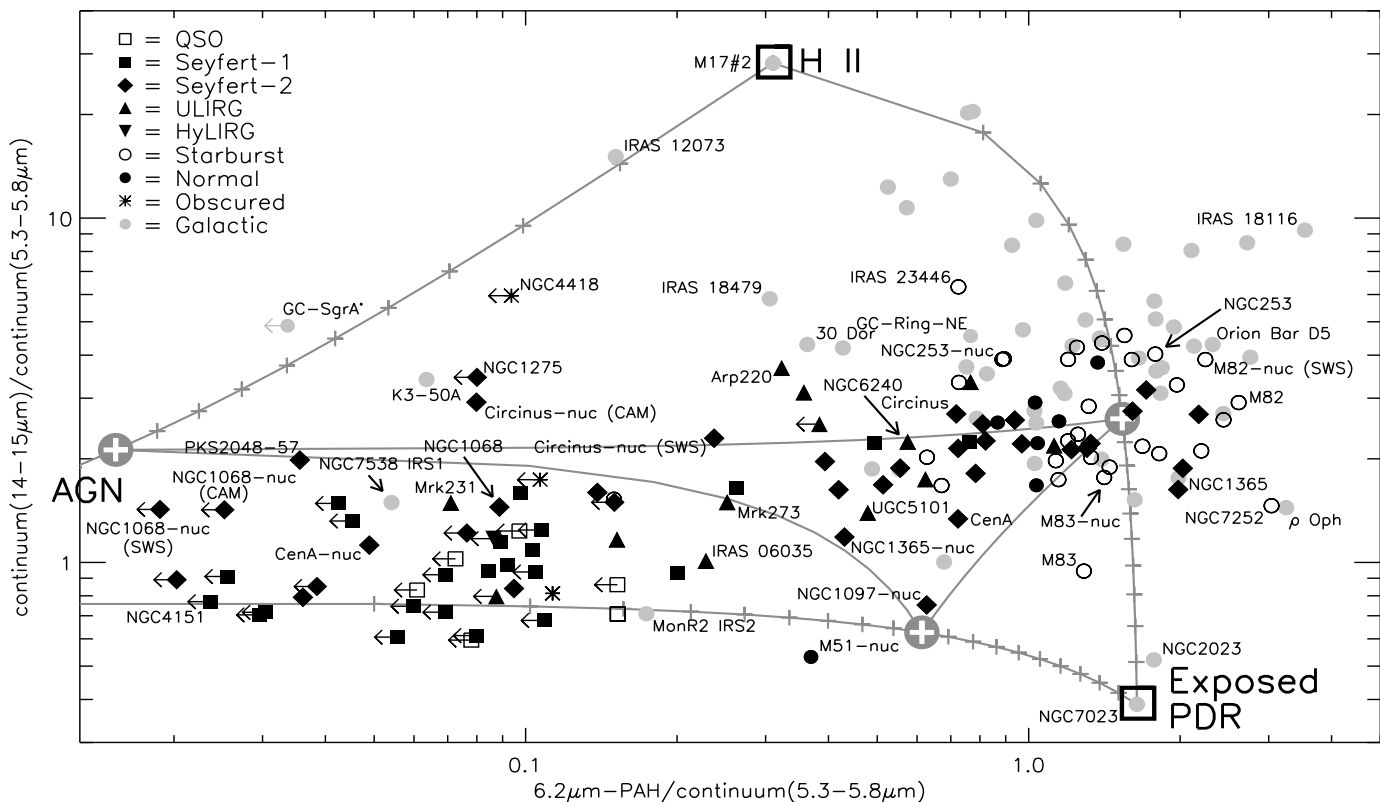


FIGURE 7.11 — MIR diagnostic diagram adapted from Laurent et al. (2000). The *grey lines* connecting the three template positions are mixing lines between the templates. Each *grey cross* indicates a 5% change in relative contribution. *Thick crosses* mark equal contribution of two templates. The *grey lines* connecting the three *thick crosses* indicate a constant 50% fraction of one component along each line. The SMC source B1#1 is located off the diagram at position (3.0,0.16).

precise position of the sources; an A_K of 2, which is typical for these H II regions (Martín-Hernández et al. 2002; Martín-Hernández et al. 2003), gives rise to an increase of 7% and 15% in 6.2PAH/5.5cont and 15cont/5.5cont, respectively.

Galaxies

The selection criteria for this diagram are somewhat different than for the 6.2PAH/FIR vs. 6.2cont/FIR diagram, as not all galaxy spectra are available over the full 5.3–15.0 μm range. ISO–PHT–S spectra, for instance, only cover the ranges 2.47–4.77 μm and 5.84–11.62 μm . For targets at low redshift this means that the 5.3–5.8 μm hot continuum spectrum cannot be measured directly. We therefore performed a linear interpolation over the 4.77–5.84 μm gap for those spectra which have sufficient S/N on either side of the gap. Targets which did not meet this criterium, mostly ULIRGs, were eliminated from the sample. Note that for sources with redshifts $z > 0.1$ the gap in the ISO–PHT–S spectral coverage is not an issue. As mentioned above, ISO–PHT–S spectra also present a problem at the long wavelength end, as their wavelength coverage stops at 11.62 μm . In order to derive a 14–15 μm continuum for these cases, we logarithmically interpolated the IRAS 12 μm and 25 μm fluxes to the 14–15 μm range. However, sources were removed from the sample if their IRAS 12 μm fluxes are upper limits, or if there is a clear mismatch between the ISO–PHT–S spectrum and the IRAS 12 μm flux. While the former criterium results in the exclusion of many fainter ULIRG spectra (including the ULIRGs from the ZZULIRG proposal (Tran et al. 2001), whose ISO–CAM–CVF spectra do not extend beyond 13 μm), the latter criterium results in the deselection of many nearby galaxies. The final sample was created after screening against sources with 5.3–5.8 μm spectra which are either too noisy or which show artefacts, as is the case for several ISO–CAM–CVF spectra.

Our final galaxy sample consists of 66 AGN spectra (6 QSO, 23 Seyfert-1 and 37 Seyfert-2 spectra), 30 starburst and H II-type galaxy spectra, 7 normal galaxy spectra, 13 ULIRG spectra, one HyLIRG spectrum (I09104+4109) and 3 spectra of infrared galaxies with deeply obscured nuclei (I02530+0211, I03344–2103 and NGC 4418). Note that some galaxies are close enough for ISO to obtain spectra of both the central region and the entire ISO–CAM–CVF field of view. These galaxies are NGC 253, NGC 1068, NGC 1365, NGC 1808, Cen A, Circinus and M 83. In Fig. 7.11 these galaxies are included with both their integrated and their nuclear spectra.

Fig. 7.11 clearly shows that the large majority of galaxy spectra is found in a wide strip, running almost horizontally across the diagram, with a few clear outliers. This sequence runs from normal and starburst galaxies on the right (coinciding with the H II regions), through the ULIRGs in the middle (overlapping to some extent with the Galactic embedded star forming regions) to the Seyfert 1's on the left. Seyfert 2's are predominantly located on the right, but are found along the full range, depending on the degree of dilution of the AGN hot dust continuum by a PAH dominated spectrum, which depends on both the physical size covered by the aperture and the fraction of the bolometric luminosity contributed by star formation. We note especially the close similarity between the MIR characteristics of the Orion Bar and the nucleus of starburst galaxy M 82. This similarity does, however, end here, as the spectrum of the entire M 82 field-of-view tends more towards that of a reflection nebula. The same trend is observed for M 83. Apparently, galaxy disks are dominated by stellar types which give rise to reflection nebulae. At the other end of the galaxy sequence, the AGN MIR spectra show little to no discernable 6.2 μm PAH emission on top of a pure hot

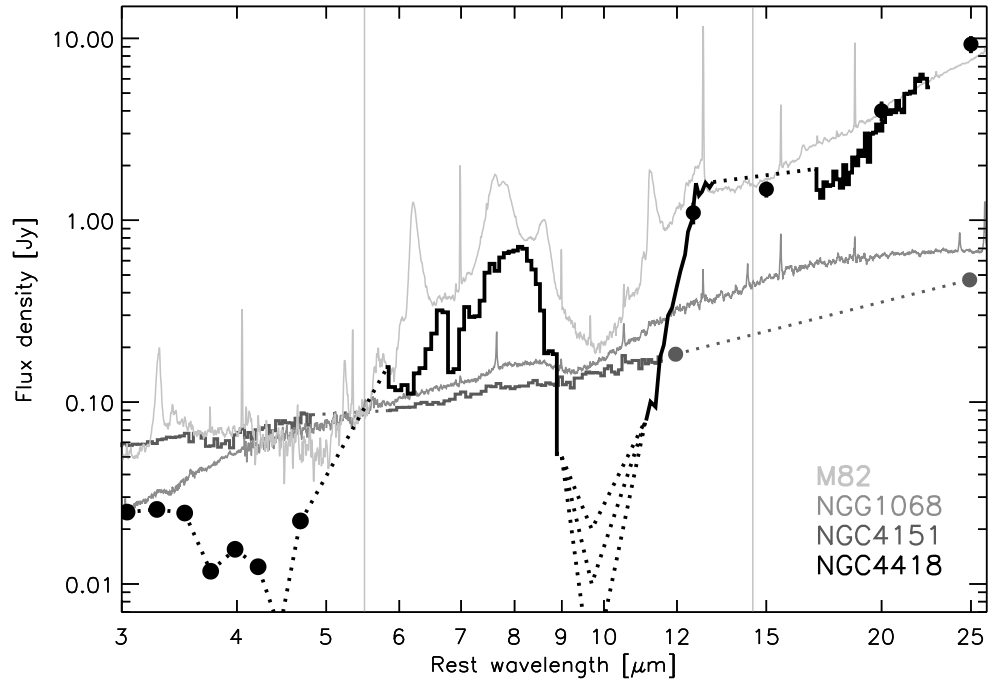


FIGURE 7.12— Comparison of the MIR spectra of the nucleus of M82 (*light grey*), the nucleus of NGC 1068 (*middle grey*), the nucleus of NGC 4151 (*dark grey*) and the deeply obscured nucleus of NGC 4418 (*black*). Vertical lines denote the central wavelengths of the hot ($5.5\,\mu\text{m}$) and warm ($14.5\,\mu\text{m}$) continuum integration ranges.

dust continuum. Fig. 7.12 reveals small differences in continuum slope among AGN nuclei, for example in the nuclear spectra of NGC 1068 (Seyfert-2) and NGC 4151 (Seyfert-1). As already pointed out by Laurent et al. (2000) on the basis of their sample of ISO–CAM–CVF spectra, the spectra of the AGN host galaxies are dramatically different from those of the AGN itself and resemble those of normal and starburst galaxies instead. A good example is the nearby Seyfert-2 galaxy Cen A (Laurent et al. 2000). While its integrated galaxy spectrum is PAH dominated and can be found among the starburst galaxies, the nuclear spectrum shows hardly any PAH emission and is situated with the AGNs.

Unlike the MIR/FIR diagram, where ULIRGs occupy their own niche, ULIRGs in the Laurent diagram are not separated out as much. Some ULIRGs (Mrk 231 and I23060+0505) and the HyLIRG I09104+4109 are found among the pure AGNs, while other ULIRGs, like I 17208–0014, are found among the starburst galaxies. The remaining ULIRGs are found more towards the center of the plot.

A highly obscured source, like NGC 4418, has a ratio of warm-to-hot continuum which is very similar to that of the prototypical starburst galaxy M 82. However, it lacks the strong

$6.2 \mu\text{m}$ PAH feature of M 82. Conversely, its $6.2\text{PAH}/5.5\text{cont}$ ratio is typical of pure AGN spectra, but the slope of its continuum is much steeper. Other sources with moderate to strong obscuration include the galaxies I02530+0211 and I03344–2103 (indicated by asterisks in Fig. 7.11). The range over which these sources are scattered includes the domain of the pure AGNs and most of the AGN-dominated portion of the strip leading towards the position of the Orion Bar and M 82.

Note that the ULIRG Arp 220 is located in between NGC 4418 and the average position of starburst galaxies. This is in good agreement with the results of MIR spectral composition presented in Chapter 6.

Application of diagnostic

Similar to Laurent et al. (2000), we calculated mixing lines where the contribution of each template to the MIR flux (measured from 5.3 to $16 \mu\text{m}$) varies between 0 and 100% (see Fig. 7.11). The three templates used, are the spectra of NGC 7023 (exposed PDR template), M 17 at position 2 (H II template) and NGC 4151 (AGN-heated dust template, see Fig. 7.12). The templates are represented in Fig. 7.11 by large open squares. We assumed a PAH flux of zero for the AGN template instead of the formally derived upper limit. It is important to realize that the mixing percentages can only be interpreted as percentages of *mid*-infrared and not *total* infrared luminosity. This is especially true for the AGN contribution, as the same AGN may have a factor 10 higher or lower continuum flux, solely depending on the degree of obscuration towards the central source.

It is clear that our sample of H II regions is not solely dominated by emission of hot dust from the H II region but also shows a significant contribution of the surrounding PDR. However, the sequence from PDRs to H II regions is much less well determined observationally. Using other H II and PDR templates would change the position of the mixing line. Indeed, this is forcefully brought home by the many objects which lie outside the mixing lines which span the diagram. In any case, changing the templates will not remove the spread of the observed H II regions along a mixing line. Hence, H II regions can only be described in first order by a combination of an H II and PDR template.

Embedded protostars can be easily distinguished from H II regions and PDRs in this diagram by their lower $6.2\text{PAH}/5.5\text{cont}$ ratio. Unfortunately, however, their location coincides with that of AGN-dominated spectra. Therefore, this diagnostic diagram cannot distinguish well between MIR spectra which are AGN-dominated or dominated by a deeply embedded source. This is of particular interest to ULIRGs whose MIR spectra can have the signature of star formation, AGN-heated dust or dust extinction (Sect. 7.3.2). With this diagram, only the first can be discerned.

The PAH contribution to the MIR spectrum of Seyferts is best traced by the $6.2\text{PAH}/5.5\text{cont}$ ratio, which is highly sensitive to small fractions of PDR (Orion Bar) contribution included within the beam. These contributions usually arise from circumnuclear star formation rings or from the galaxy disk. Note that for starburst galaxies, which lack an active nucleus, the inclusion of a larger part of the galaxy disk does not result in a similar strong shift in either diagnostic ratio.

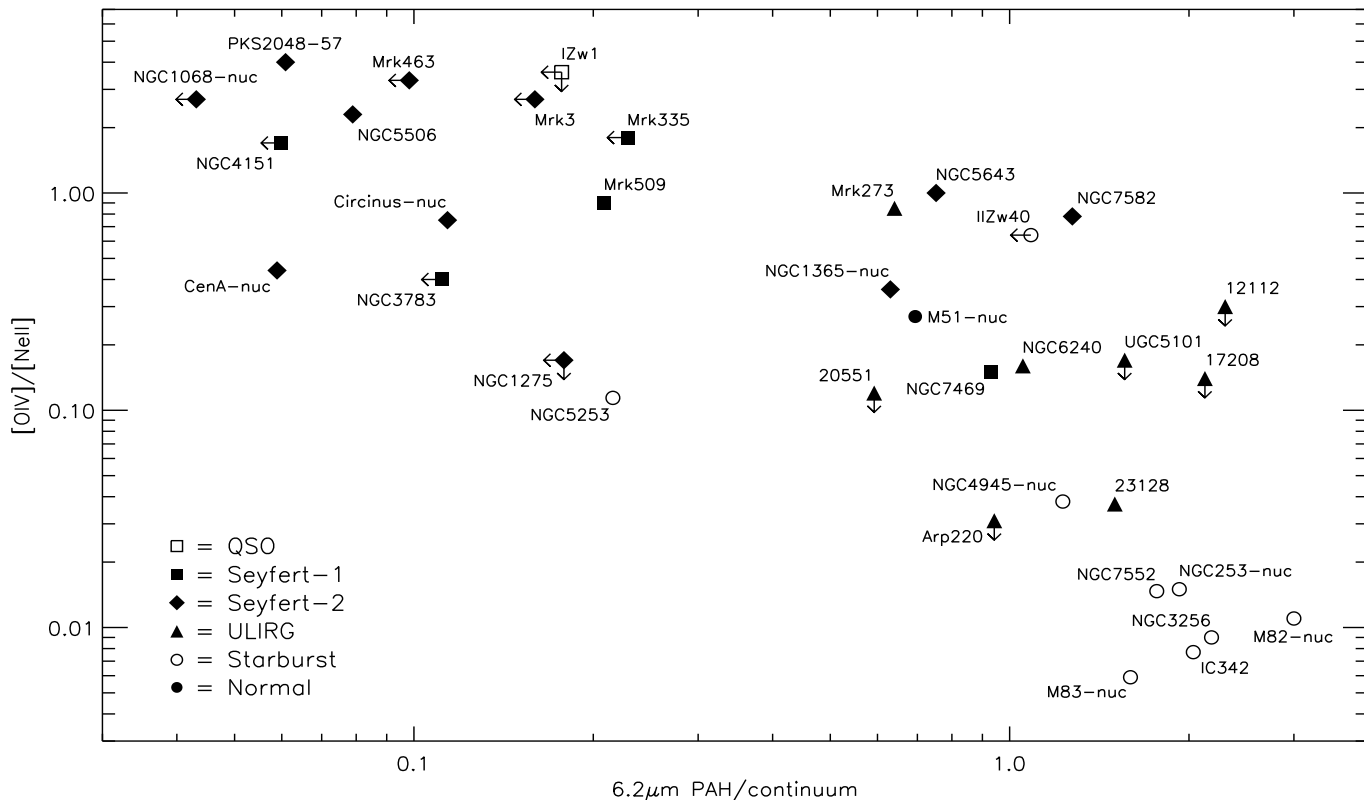


FIGURE 7.13 — MIR diagnostic diagram for different type of galaxies, adapted from Genzel et al. (1998). The vertical axis measures the ratio of $25.9\mu\text{m} [\text{O IV}]$ (high excitation) to $12.8\mu\text{m} [\text{Ne II}]$ (low excitation) and the horizontal axis measures the $6.2\mu\text{m PAH}/6.2\mu\text{m cont}$ ratio. AGN-dominated MIR spectra are found in the upper left quadrant, while starburst-dominated MIR spectra are found in the lower right quadrant.

7.4.3 The Genzel diagnostic diagram

A MIR diagnostic diagram which successfully separates Seyfert galaxies from starburst galaxies is the diagram originally proposed by Genzel et al. (1998). Following the discussion in the previous sections, the use of the $6.2 \mu\text{m}$ PAH line-to-continuum (or equivalently the use of the $7.7 \mu\text{m}$ PAH line-to-continuum) is an excellent choice for determining the importance of star formation for the MIR flux. Indeed, while the flux varies by orders of magnitude relative to the FIR flux, their ratio is very constant in Galactic star forming regions. Conversely, the observed variation in the $6.2\text{PAH}/\text{FIR}$ ratios in the Galactic sample invalidates this ratio as a tracer of the contribution of star formation to the total infrared luminosity.

Here we show a modified version of this diagram, in which we replaced the $7.7 \mu\text{m}$ PAH line-to-continuum ratio by the ratio based on the $6.2 \mu\text{m}$ PAH feature (Fig. 7.13). The diagram classifies the sources as AGN- or starburst-dominated according to their position along the arc extending from fully AGN-dominated (upper left) to fully starburst-dominated (lower right).

The number of galaxies in our Genzel diagram is limited by the availability of line fluxes of $12.81 \mu\text{m}$ [Ne II] and $25.9 \mu\text{m}$ [O IV] from the literature. For AGNs the line fluxes were taken from Sturm et al. (2002), for starburst galaxies from Verma et al. (2003) and for ULIRGs from Genzel et al. (1998). Our final sample consists of 17 AGNs (1 QSO, 5 Seyfert-1, 11 Seyfert-2), 8 ULIRGs, 9 starburst galaxies and 1 normal galaxy.

Fig. 7.13 clearly illustrates that the $[\text{O IV}]/[\text{Ne II}]$ ratio is effective in separating Seyfert from starburst galaxies, as Seyferts have ratios higher than 0.1 and starburst galaxies have ratios lower than ~ 0.02 . Note especially the Seyferts NGC 7469 and NGC 7552, which appear starburst-like in their $6.2 \mu\text{m}$ PAH line-to-continuum ratio, but which are AGN-like in their $[\text{O IV}]/[\text{Ne II}]$ ratios.

Several of the Seyferts in the upper left quadrant of the diagram are represented by the properties of their nuclei (high excitation gas and low $6.2 \mu\text{m}$ PAH line-to-continuum ratio). Were these galaxies to be represented by their integrated-galaxy properties instead (higher $6.2 \mu\text{m}$ PAH line-to-continuum ratio and lower excitation, contributed by the starburst), these sources would move considerably to the right and also down. Circinus and Cen A, for example, would shift by more than an order of magnitude to the right, towards NGC 7469 and NGC 7582, and also down (by an unknown amount), towards the ULIRGs NGC 6240 and UGC 5101. At this position, only their high $[\text{O IV}]/[\text{Ne II}]$ ratios would identify them as Seyferts. Applying the $[\text{O IV}]/[\text{Ne II}]$ ratio to find AGNs in ULIRGs, only 2 out of 8 ULIRGs seem to harbour an AGN. These ULIRGs are NGC 6240 and Mrk 273. The other 6 ULIRGs either have upper limits or have a ratio intermediate to those typical for Seyferts and starbursts (e.g. I23128–5919).

The nucleus of the nearby starburst galaxy NGC 4945 is found at an intermediate $[\text{O IV}]/[\text{Ne II}]$ ratio. Hard X-ray observations have shown this galaxy to contain a buried AGN (Iwasawa et al. 1993; Guainazzi et al. 2000), which so far has escaped detection at NIR and MIR wavelengths. The elevated $[\text{O IV}]/[\text{Ne II}]$ ratio for this source is likely due to strong differential extinction between $12.81 \mu\text{m}$ and $25.9 \mu\text{m}$ in this notoriously dusty nucleus (Chapter 3). However, the example of NGC 4945 may be taken as a warning that some AGNs may escape detection also from MIR excitation indicators like $[\text{O IV}]/[\text{Ne II}]$. Other highly obscured Galactic nuclei, like NGC 4418 and Mrk 231, have not even been detected in $12.81 \mu\text{m}$ [Ne II] (Genzel et al. 1998, Chapter 5). For these galaxies, and likely also for many ULIRGs, the Genzel diagnostic diagram is not well suited.

7.4.4 Comparison of the three diagnostic diagrams

Each of the three diagnostic diagrams is constructed with the immediate goal to reveal the identity of a galaxy.

Heavily obscured galaxies are best recognized in the MIR/FIR diagram. Since they show no fine-structure lines, they are absent in the Genzel diagram while in the Laurent diagram — which was also not constructed for these type of galaxies — they can be mistaken for AGN-dominated sources. Only the MIR/FIR diagram seems to be able to separate out ULIRGs showing signatures of obscured star formation.

The ability to identify type-1 Seyferts is possible with all three diagnostics. However, only the Genzel diagram is able to break the degeneracy between starburst and Seyfert-2's. Indeed, by using the $[\text{O IV}]/[\text{Ne II}]$ ratio, the Seyferts are clearly separated from the starburst galaxies. In contrast, starburst galaxies and Seyfert-2's occupy the same region in the MIR/FIR and Laurent diagnostic diagram. This illustrates that the identification of the dominant power source — AGN or starburst — highly depends on the wavelength region considered. Conversely, such an identification does not imply a similar degree of dominance in the *total* infrared luminosity. Obviously, no AGN signature can be observed in the IR for a heavily obscured nucleus and hence none of the three diagrams will work.

7.5 Discussion

7.5.1 PAH abundance

The ratio of the total emission in the PAH emission bands to the FIR emission measures the competition of the PAHs and the dust for the illuminating FUV photons and is, thus, an indicator for the PAH/dust abundance. To first order, this can be measured by the 6.2PAH/FIR ratio due to the fact that the fraction of total PAH flux emitted in the $6.2 \mu\text{m}$ PAH band varies only slightly from about 14 to 38 % with an average of $28 \pm 4\%$ (Vermeij et al. 2002; Peeters et al. 2002a). The observations presented here (Figs. 7.4 through 7.9) show variations in 6.2PAH/FIR of almost 3 orders of magnitude. Thus, the observations seem to imply that the PAH abundance in the ISM varies over three orders of magnitude. Moreover, this ratio nicely breaks up the Galactic sources according to object type (see Sect. 7.4.1). Thus, PAHs seem to be much more abundant in the diffuse ISM than in embedded or compact H II regions.

Studies of PAH/FIR ratios in Galactic sources have revealed that this ratio is independent of the local radiation field, G_0 , for low radiation fields and decreases with G_0 at higher radiation fields (Boulanger et al. 1998a,b; Onaka 2000). These authors suggested that this linearity of PAH strength with G_0 for low G_0 is consistent with emission coming from species small enough to be stochastically heated. The decrease for high G_0 is then taken to indicate a decreasing abundance of these species relative to that of the grains with increasing strength of the illuminating radiation field.

The observed segregation in our sample with object type seems to support this at first sight. The sources with the lowest G_0 also have the highest 6.2PAH/FIR ratios, while the compact H II regions characterized by high G_0 's have much lower 6.2PAH/FIR ratios. However, closer inspection reveals that there is no clear relationship between 6.2PAH/FIR and G_0 . Fig. 7.14 shows the variation between 6.2PAH/FIR and G_0 for the sample of H II regions with G_0 varying over almost 4 orders of magnitude. Extended or complex H II regions are excluded due to possible aperture effects. Possibly, there is a very weak relationship between 6.2PAH/FIR and G_0 . However, we emphasize that sources with similar 6.2PAH/FIR show a

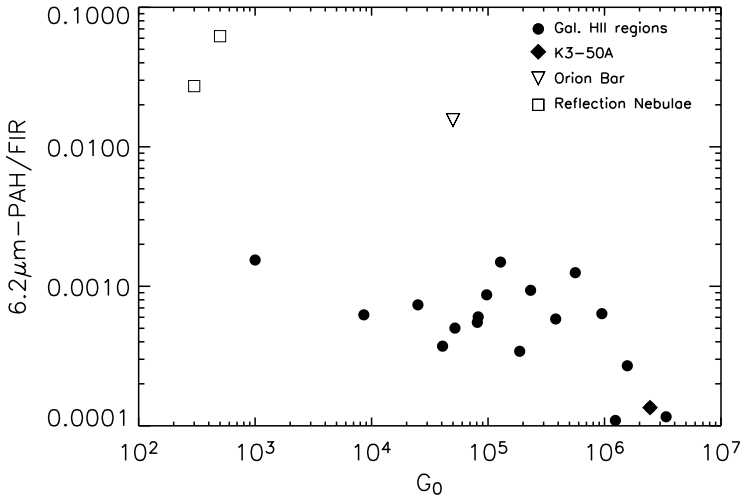


FIGURE 7.14 — The relation of 6.2PAH/FIR with the radiation field for H II regions. As a reference, two RNe are also shown in this plot.

large spread in G_0 ; up to a factor 130. Boulanger et al. (1998a,b) considered only 2 sources in this G_0 range; the reflection nebula NGC 7023, located in the top-left corner of Fig. 7.14, and the PDR associated with the H II region M17 with a 6.2PAH/FIR ratio similar to the ratio found in the H II regions. In our study, these two sources also show a decrease of 6.2PAH/FIR with G_0 . But this trend is not confirmed in our larger sample. In contrast, Onaka (2000) found a loose correlation between 7.7PAH/FIR versus G_0 for different positions within the Carina Nebula (with only a factor up to 7 difference in G_0 for positions with similar 6.2PAH/FIR). The presence of such a relationship within a single object seems to be a more general characteristic of the PAH emission behavior. Apparently, within a single object, variations in G_0 are important in driving the emission spectrum. However, the source to source variation in the PAH/FIR ratio does not seem to follow G_0 , but is rather dominated by other factors. The observed variation in the 6.2PAH/FIR demonstrates that PAHs compete much better for FUV photons in the diffuse ISM than in compact H II regions. This may reflect the destruction of PAHs inside the ionized gas volume. In particular, dust can be present inside H II regions and thereby absorb much of the FUV flux before it even reaches the surrounding PAH-rich PDRs. The importance of PAH destruction in the ionized gas will increase with decreasing size of the H II region because this corresponds to a larger dust optical depth in the ionized gas for a given dust abundance. Possibly, the observed large spread in the 6.2PAH/FIR ratio with G_0 reflects the variation in the internal dust content of H II regions. It is fair to say, however, that at this point the origin of the large variation in the 6.2PAH/FIR ratio is unclear.

7.5.2 PAHs as a tracer of star formation

Star formation properties of galaxies are essential in assessing their evolutionary histories. Different tracers for star formation are used based upon integrated colors, the UV continuum, recombination and forbidden lines and FIR emission (e.g. Kennicutt 1998, and references

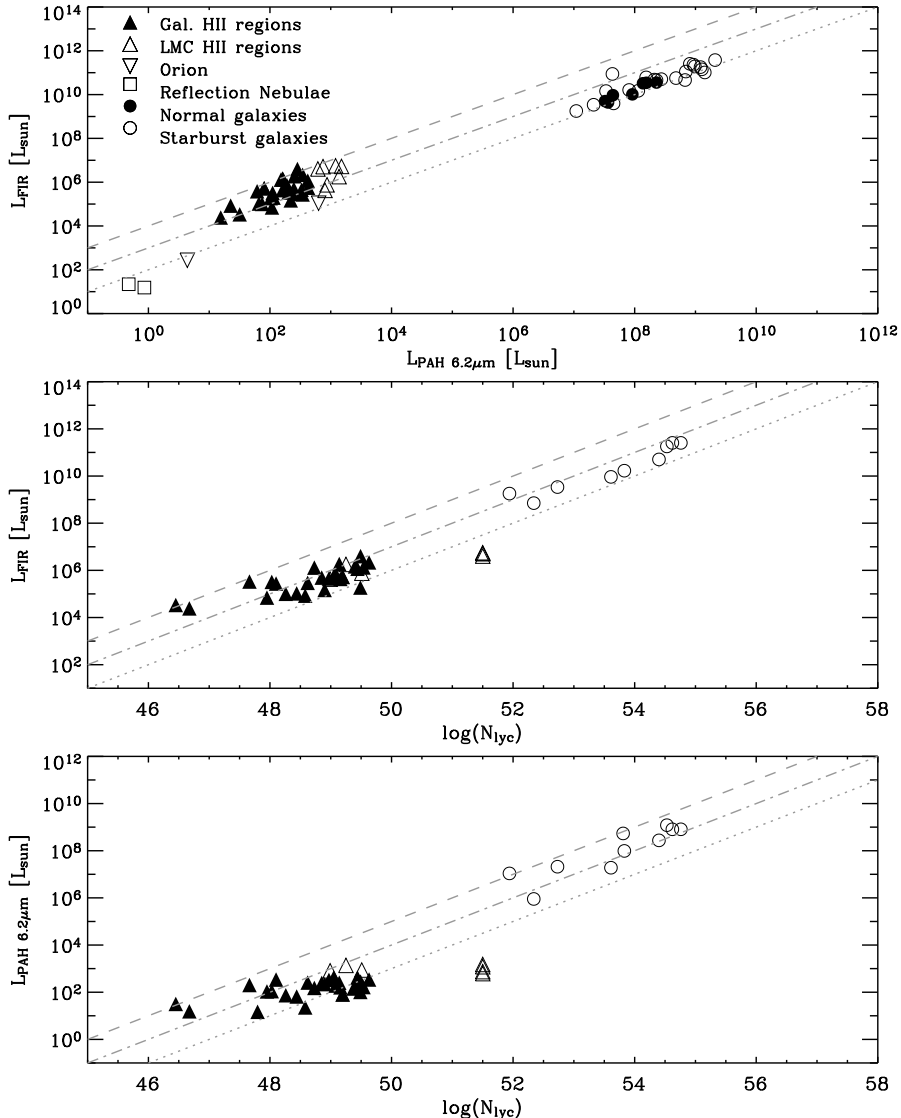


FIGURE 7.15 — Three tracers of star formation, 6.2 PAH luminosity, $\log(N_{\text{LyC}})$ and FIR luminosity plotted against each other for a wide variety of sources; i.e. Galactic HII regions, LMC HII regions (taken from Vermeij et al. 2002) and normal and starburst galaxies. In case of a distance ambiguity for the Galactic HII regions, only the far distance is shown. The isolated group of triangles refer to 4 positions within 30 Dor. The other LMC HII regions are situated outside 30 Dor. The grey lines (dotted, dash-dotted, dashed) indicate a 6.2 PAH luminosity equal to respectively 1, 0.1 and 0.01 % of the FIR luminosity (**top panel**), a $N_{\text{LyC}}/L_{\text{FIR}}$ ratio of respectively 10^{44} , 10^{43} and 10^{42} (**middle panel**) and a $N_{\text{LyC}}/L_{6.2\text{PAH}}$ ratio of respectively 10^{47} , 10^{46} and 10^{45} (**bottom panel**).

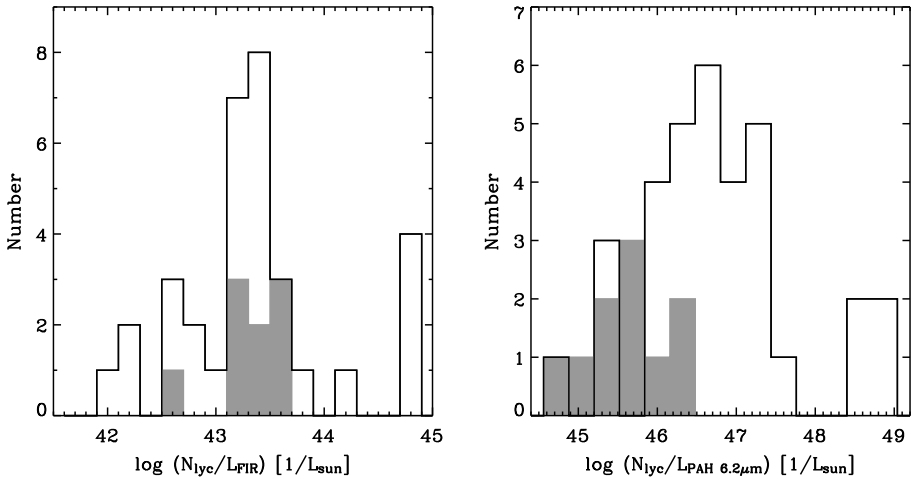


FIGURE 7.16 — The different distributions in $N_{\text{lyc}}/L_{\text{FIR}}$ (**left panel**) and $N_{\text{lyc}}/L_{\text{PAH } 6.2\mu\text{m}}$ (**right panel**) for the Galactic and LMC H II regions (*solid line*) and the starburst galaxies (*grey scale*). The highest value for both ratios corresponds to the 4 positions within 30 Dor.

therein). PAHs may also provide a convenient tracer of star formation activity as the discussion on the starburst and ULIRGs in this paper exemplifies. PAHs are stochastically heated by UV photons produced by massive stars. Assuming fixed emission and absorption properties and fixed PAH abundance, the PAH emission is a measure of the amount of photons available between 6 and 13.6 eV (the former corresponding with the averaged ionisation potential of PAHs) and hence of star formation. To assess the robustness of this new tracer, we compared it to two tracers, N_{lyc} and L_{FIR} , for both Galactic star forming regions and galaxies (normal and starbursts).

L_{FIR} is a tracer for star formation since a significant fraction of the stellar radiation is emitted by (young) stars with spectral types mid-B or earlier. Much of this radiation is absorbed by dust and re-emitted thermally in the FIR. The number of ionizing photons, N_{lyc} , is commonly used as a measure of massive star formation. It is mainly derived in three ways, 1) from the H α recombination line; 2) from radio recombination lines and 3) from the hydrogen free-free continuum emission at radio wavelengths. For the Galactic and LMC H II regions, N_{lyc} is obtained from radio continuum emission (Martín-Hernández et al. 2002; Martín-Hernández et al. 2003; Vermeij et al. 2002). For galaxies, on the other hand, free-free radio emission may be confused by non-thermal synchrotron emission from young SNR or AGNs. Their N_{lyc} is therefore obtained from near- and mid-infrared hydrogen recombination lines (Genzel et al. 1998; Verma et al. 2003; Förster Schreiber et al. 2001).

The three tracers are compared with each other in Fig. 7.15. L_{FIR} is in first order clearly proportional to $L_{6.2\text{PAH}}$. However, their ratio is significantly different between the Galactic H II regions ($5.5 \pm 4.6 \cdot 10^{-4}$) and the galaxies ($6.3 \pm 3.2 \cdot 10^{-3}$), with Orion and the reflection nebulae having a similar and lower ratio as the galaxies, respectively (also seen in Figs. 7.4 through 7.9). In contrast, this discrepancy between the Galactic and extragalactic sample is not present in the $L_{\text{FIR}}/N_{\text{lyc}}$ ratio, though a slightly larger scatter is observed in each of these

groups. In addition, $L_{6.2\text{PAH}}$ is roughly proportional to N_{LyC} for the galaxies while for the Galactic H II regions, it is much less dependent on N_{LyC} . In fact, the $L_{6.2\text{PAH}}$ observed in H II regions, seems to be almost independent of the hardness of the radiation field.

As discussed by e.g. Kennicutt (1998), and references therein, the efficiency of L_{FIR} as a tracer for star formation depends on the type of galaxies considered, being highest for dusty circumnuclear starbursts. Indeed, the FIR spectra of galaxies are composed of emission of dust around young star-forming regions and emission of more extended dust heated by the interstellar radiation field. The same holds for PAHs as a tracer of star formation. Likewise, the observed PAH flux is integrated over the whole galaxy and therefore includes PAH emission originating in the ISM, reflection nebulae, exposed PDRs and embedded compact H II regions. This ISM contribution can be estimated by comparing $L_{6.2\text{PAH}}$ with N_{LyC} (since it does not suffer from this contamination) for both the H II regions — as a template for massive star formation — and the galaxies. Concerning L_{FIR} , the galaxies show a similar distribution of $N_{\text{LyC}}/L_{\text{FIR}}$ as the H II regions (Fig. 7.16) and so L_{FIR} is likely not influenced by an ISM contribution in these galaxies. In contrast, the galaxies have a clearly different distribution in $N_{\text{LyC}}/L_{6.2\text{PAH}}$, with — on average — a lower ratio, indicating that the PAH emission in galaxies partly originates in the ISM. Therefore, PAHs may be better suited as a tracer of B stars, which dominate the Galactic stellar energy budget, than as a tracer of massive star formation.

7.5.3 Conversion from PAH luminosity to IR luminosity

Recently, Soifer et al. (2002) and Lutz et al. (2003) have used PAH emission features as a quantitative measure for the contribution of exposed star formation to the bolometric luminosity of two ULIRGs (Arp 220 and NGC 6240). While Soifer et al. (2002) assumed the ratio of $L(11.2\text{PAH})$ and $L(\text{IR})$ for the starburst core in M 82 to be a measure for exposed star formation, Lutz et al. (2003) instead used the mean $L(7.7\text{PAH})/L(\text{IR})$ ratio derived from a sample of 10 starburst nuclei. A third method to derive the bolometric correction was proposed in Chapter 6 and is based on the mean $L(6.2\text{PAH})/L(\text{IR})$ ratio for our sample of normal and starburst nuclei. This ratio is 0.0034 ± 0.0017 .

For sources where the environment of massive star formation resembles exposed PDRs (such as M 82 and NGC 253; Carral et al. 1994; Lord et al. 1996), the three methods discussed above will give reasonable results. On the other hand, for sources which resemble embedded star formation (e.g. Arp 220 and NGC 4418), a ten times lower ratio, appropriate for compact H II regions like W3, might be a better choice. This issue cannot be decided based upon the mid-IR spectra alone. Observations of PDR lines such as the $[\text{O I}] 63 \mu\text{m}$ and $[\text{C II}] 158 \mu\text{m}$ lines can be very instrumental in resolving this issue. In that respect, we note that the PDR fine structure lines are very weak in Arp 220 (Luhman et al. 2003), suggesting also that the PDR component is underdeveloped, perhaps due to absorption of a major fraction of the FUV flux by dust inside the H II region (Luhman et al. 2003).

7.6 Conclusions

In this Chapter, the MIR spectral characteristics of Galactic and extragalactic soures are investigated. Our sample includes Galactic (C)H II regions, ISM lines of sight and embedded massive protostars as well as normal galaxies, starburst galaxies, Seyferts, QSOs and (ultra-luminous) infrared galaxies.

First, the MIR spectrum of each object type is described and compared, revealing distinct spectral characteristics for each object type. In order to distinguish the different natures of the galaxies, i.e. AGN-dominated, starburst-dominated or heavily obscured, we then present a new MIR/FIR diagnostic based on the ratio of the 6.2 PAH emission band to FIR flux and the ratio of the $6.2\text{ }\mu\text{m}$ continuum to FIR flux. This study has demonstrated that the 6.2PAH/6.2cont ratio is remarkably constant over a wide range of Galactic H II regions, as well as more general ISM material. As such, it provides a very clear handle on any AGN contribution to the MIR. Indeed, AGNs are found to segregate in two groups; most type-2 Seyferts are located with the normal and starburst galaxies, while most type-1 Seyferts show strong 6.2cont/FIR ratios. The $6.2\text{ }\mu\text{m}$ PAH luminosity distributions are found to be independent of the Seyfert type, in accordance with the orientation dependent AGN unification scheme, and hence confirm the results of Clavel et al. (2000). This diagram further reveals the spectral resemblance of starburst and normal galaxies to exposed PDRs rather than embedded compact H II regions. ULIRGs show a diverse spectral appearance. Some show a typical AGN hot dust continuum. More, however, are either starburst-like or show signs of strong dust obscuration in the nucleus. One characteristic of the ULIRGs seems also to be the presence of more prominent FIR emission than either starburst galaxies or AGNs. Comparison with the diagnostic diagrams proposed by Genzel et al. (1998) and Laurent et al. (2000) for our sample indicates that the ability to identify obscured objects is best achieved with our MIR/FIR diagnostic, while the ability to identify the presence of an optically-recognized AGN is best achieved with the Genzel diagram.

We found that the observed variation of the MIR/FIR diagnostic ratios in the Galactic sample is linked with their evolutionary state and the PAH/dust abundance. Finally, we have examined the use of PAHs as quantitative tracers of star formation activity and find that PAHs may be better suited as a tracer of B stars, which dominate the Galactic stellar energy budget, than as a tracer of massive star formation. Hence, the PAH emission of normal and starburst galaxies is best represented by that of exposed PDRs such as the Orion Nebula. However, the infrared spectra of some sources — notably the archetypal ULIRG Arp 220 — may be dominated by embedded massive star formation rather than exposed PDRs. NGC 4418 may be an even more extreme example of such buried star formation, where even the faintest traces of PAH are lacking.

Acknowledgements

The authors are grateful to W. Reach for providing the ISO-CAM-CVF data of the SMC molecular cloud, S. Madden for providing ISO-CAM-CVF galaxy spectra prior to publication and J.P. Simpson for providing the MSX Orion spectrum. This research has made use of the NASA/IPAC Extragalactic Database (NED) which is operated by the Jet Propulsion Laboratory, California Institute of Technology, under contract with the National Aeronautics and Space Administration.

8

Conclusions and outlook

A key question in astronomy is the interrelationship of mergers, starburst and AGN activity. In this thesis, I have focussed on infrared observational diagnostics of the energetic phenomena in the nuclei of ULIRGs and the insight they provide into the ultimate energy source of such objects. The main conclusions are summarized here and an outlook for future research is presented.

The mid-IR characteristics of energetic phenomena in (U)LIRG nuclei

In order to address the issues mentioned above, good infrared tracers of the different energetic processes in the nuclei have to be identified. The bulk of this research is based upon mid-infrared spectroscopy of a sample of ~ 250 normal galaxies, starburst galaxies, Seyferts, QSOs and ULIRGs. The spectra were obtained using the spectrometers SWS, PHT-S and CAM-CVF onboard ISO, at spectral resolutions of $R=1500$, 90 and 35, respectively (Chapter 2). The sample has been appended with groundbased L- and M-band spectroscopy for the nucleus of one of the nearest starburst galaxies, NGC 4945 (Chapter 4).

Ice absorption features are a common characteristic of low temperature molecular gas seen against a bright background source. The composition of the ice is strongly related to thermal and energetic processing by the background source. This is reflected in observed ice absorption spectrum. The profile of the solid CO band reveals the importance of thermal processing of the ice, while the prominence of the XCN band attests to the importance of energetic processing of the ices by energetic photons and/or particles.

Based on my sample, we found that water ice is present in most of the ULIRGs, whereas it is weak or absent in the large majority of Seyferts and starburst galaxies. The ice galaxy spectra seem to form a sequence from strongly ice and silicate absorption dominated spectra to strongly PAH emission dominated spectra. The spectral variation shows strong similarities with Galactic star forming clouds. This leads us to believe that this sequence might reflect an evolutionary sequence from strongly obscured beginnings of star formation (and AGN activity) to a less enshrouded stage of advanced star formation (and AGN activity).

The $6\text{--}12 \mu\text{m}$ spectrum of NGC 4418 is dominated by deep absorption features of water ice and methane ice, Hydrogenated Amorphous Carbon (HAC) and silicates against a fea-

tureless mid-infrared continuum. The spectrum closely resembles that of embedded massive protostars in our Galaxy. From the depth of the absorption features it is inferred that the powerful central source responsible for the mid-infrared emission must be deeply enshrouded. Since this emission is warm and originates in a compact region, an AGN must be hiding in the nucleus of NGC 4418. The overall shape of the NGC 4418 6–11 μm spectrum shows a ‘false’ emission peak at 7.7 μm , which mimicks at first glance a PAH spectrum. The need for high S/N spectra is obvious to clearly distinguish between bona fide PAH spectra and absorption dominated spectra.

The 3–6 μm nuclear spectrum of starburst/Seyfert-2 galaxy NGC 4945 shows, in addition to PAH emission, deep absorption features of water ice, CO₂ ice, OCN[−] ice and CO ice. Tracers of AGN activity are not detected. Analogous to the processing of ices by embedded protostars in our Galaxy and assuming the AGN to be deeply buried, the processing of the ices in the center of NGC 4945 is attributed to ongoing massive star formation.

PAH emission features are generally assumed to be tracers of exposed star formation. We have investigated this assumption for a sample of Galactic regions of massive star formation on the basis of a MIR/FIR diagnostic diagram of far-infrared normalized 6.2 μm PAH flux versus far-infrared normalized 6.2 μm continuum flux. Within this diagram the Galactic H II regions span a sequence from embedded compact H II regions to exposed PDRs. The 6.2 μm PAH band-to-continuum ratio is remarkably constant over this range. We have compared our extragalactic sample to these Galactic sources. This revealed that normal and starburst galaxies have a uncanny resemblance to reflection nebulae. While Seyfert-2’s coincide with the starburst trend, Seyfert-1’s are displaced by a factor 10 in 6.2 μm -continuum flux. This is in accordance with AGN unification schemes. ULIRGs show a diverse spectral appearance. Some are found with the Seyfert-1’s. More, however, are either starburst-like or show signs of strong dust obscuration in the nucleus. The latter group is displaced with respect to all other galaxy types towards the position of embedded massive protostars and the deeply enshrouded nucleus of NGC 4418. One characteristic of the ULIRGs seems also to be the presence of more prominent far-infrared emission than either starburst galaxies or AGNs. We have examined the use of PAHs as quantitative tracers of star formation activity. Based on these investigations, we find that the PAH emission of normal and starburst galaxies is best represented by that of exposed PDRs associated with reflection nebulae such as the Orion Bar and NGC 2023. However, the infrared spectra of some sources — notably the archetypal ULIRG Arp 220 — may be dominated by embedded massive star formation rather than exposed PDRs. NGC 4418 may be an even more extreme example of such buried star formation, where even the faintest traces of PAH are lacking.

Embedded AGN and starburst activity

The near- and mid-infrared spectrum of NGC 4945 does not provide any evidence for the existence of the powerful AGN, inferred from hard X-ray observations. The upper limits on our AGN tracers 3.94 μm [Si IX], 7.65 μm [Ne VI] and 14.3 & 24.3 μm [Ne V] imply an A(V)>160 towards the NLR, assuming the NLR to be of equal strength as in the Circinus galaxy.

NGC 4418 has a very compact ($r<15\text{--}40\text{ pc}$) luminous ($L_{\text{IR}} \sim 10^{11} L_{\odot}$) nucleus, which reveals no sign of AGN or starburst activity at mid-infrared wavelengths. The compactness of the nucleus suggests that an embedded AGN is responsible for the very high luminosity.

Arp 220 does not reveal any sign of an AGN either, not even in hard X-rays or in radio continuum emission. The radio emission instead reveals several emission ‘knots’ across the two nuclei, which are interpreted as luminous radio supernovae. PAHs as tracers of exposed star formation are strongly underluminous with respect to the far-infrared luminosity. Spectral decomposition of the 6–12 μm ISO spectrum suggests that 40% of the 6–12 μm flux is associated with an NGC 4418-like absorbed continuum component and 60% with a weakly absorbed starburst component. The PAH emitting and heavily dust/ice absorbed components are tentatively associated with the diffuse emission region and the two compact nuclei respectively identified by Soifer et al. (2002) in their higher spatial resolution 10 μm study. Both the similarity of the absorbed continuum with that of embedded Galactic protostars and results of dust modeling imply that the embedded source(s) in Arp 220 could be powered by, albeit extremely dense, starburst activity. Due to the high extinction, it is not possible with the available data to exclude that AGN(s) also contribute some or all of the observed luminosity. In this case, however, the upper limit measured for its hard X-ray emission would require Arp 220 to be the most highly obscured AGN known.

Outlook

The research presented in this thesis has opened a number of research lines that should be explored in the future. For instance, the role of embedded star formation has to be further explored. The high interstellar pressure in the central region of ULIRGs may limit the expansion of UCH II regions and the development of the normal bright signposts of star formation. Further diagnostic tools have to be developed for the study of such regions. In Chapter 4, we have demonstrated by the example of NGC 4945 that medium resolution ($R=3000$) M-band spectroscopy is a viable option to study the molecular environment in nearby galactic nuclei. Similar studies of other starburst nuclei are needed to determine whether the conditions probed in NGC 4945 are extreme or typical for starburst nuclei. With respect to AGNs, the energetic processing of (ices in) the molecular torus needs to be investigated.

The recent launch of the *Satellite InfraRed Telescope Facility* (SIRTF) marks the start of a decade in which infrared and submillimeter astronomy will undergo an authentic revolution. Space-based missions such as the *Herschel Space Observatory* (HSO), the *James Webb Space Telescope* (JWST), new groundbased facilities as the *Atacama Large Millimeter Array* (ALMA) and new VLT instruments like the *VLT Imager and Spectrometer for the mid-InfraRed* (VISIR) will, together with SIRTF, be the cornerstones of the future investigation of starburst and AGN activity in the Early Universe.

Particularly, the IRS spectrograph on SIRTF will provide medium-resolution ($R=600$) spectroscopy in the 10–37 μm range and low-resolution ($R=50$) spectroscopy in the 5–40 μm range. IRS is therefore ideally suited to measure the emission line spectra of AGN and starburst phenomena, while PAH emission bands and ice absorption features can be observed at lower resolution. As a bonus, beyond $z=0.6$, all important near-infrared ice absorption bands are redshifted into the IRS low-resolution range, while the main PAH emission bands can be measured in medium-resolution spectroscopy. The PACS instrument on Herschel will provide high-resolution ($R=1700$) spectroscopy in the 60–210 μm range. This will give access to the main cooling lines of star forming regions and, for targets at $z>1.5$, also to rest-frame mid-infrared AGN tracers. The NIRSpec and MIRI spectrographs on the JWST will offer medium resolution spectroscopy in the ranges 0.6–5 μm and 5–28 μm , respectively.

This will allow the detection of mid-infrared star formation and AGN tracers out to redshifts of 2–3. ALMA will bring HST resolution to the field of submillimeter astronomy. This will allow the detection of galaxies out to extreme redshifts by sampling them close to the peak of their flux distributions.

These instruments offer enough sensitivity to study the energetic processes in ULIRGs and HyLIRGs in sufficient spectral detail that the contributions of (embedded) AGN and starburst activity may be traced back all the way to the youthful days of our Universe. This will allow us to determine whether all mergers go through a ULIRG/HyLIRG phase and how the role of (embedded) starburst and AGN activity changes as a function of merger phase. The observations will also allow us to study the composition of the ISM in the Early Universe and to assess the influence of extreme nuclear activity on chemical enrichment.

High spatial resolution in combination with sufficient spectral resolution will permit analysis of individual nuclear and circumnuclear components in (ultra)luminous galaxies in a large portion of the Local Universe. For instance, the nature of merger nuclei may be inferred; properties of individual (super)star clusters may be inferred; and the influence of the central X-ray sources on the chemical composition of AGN tori may be finally studied.

For ULIRG astronomy the best is still to come!



FIGURE 8.1 — The launch of SIRTF on August 25, 2003 marks the start of a decade in which infrared and submillimeter astronomy will undergo an authentic revolution. Photo: NASA.

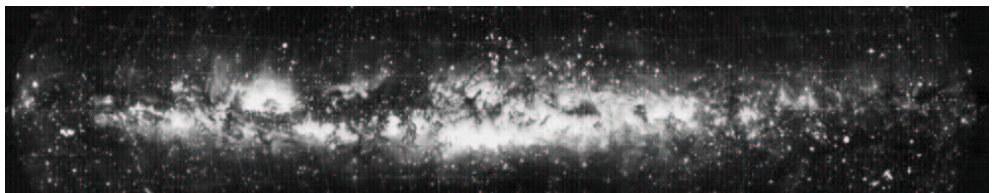
Nederlandse samenvatting

De ruggegraat van de nacht

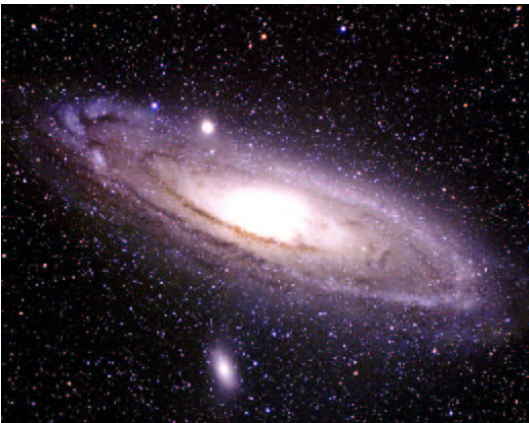
STERRENKUNDE wordt door Nederlanders meestal geassocieerd met de enkele honderden lichtpuntjes die onze onbewolkte nachthemel rijk is: behalve de Maan zijn dat een paar planeten en enkele honderden kris-kras over de hemel verdeelde sterren. Maar iedereen, die in de zomer wel eens op vakantie is geweest in dunbevolkte zuidelijke streken en daar de tijd heeft genomen om de nachthemel wat beter te bestuderen, weet dat wij in Nederland maar een fractie van de naar schatting 8000 sterren kunnen zien die voor het blote oog zichtbaar zijn. De overdaad aan sterren kan er soms zelfs zo groot zijn dat het moeilijk wordt de afzonderlijke sterrenbeelden terug te vinden. In plaats daarvan openbaart zich een andere, niet door mensen verzonnen structuur: een vage lichtende band, door de oude Grieken ‘Melkweg’ genaamd¹. Deze band omspant de hele hemel, maar is op het noordelijk halfrond het duidelijkst te zien tussen de sterrenbeelden Zwaan, Arend, Boogschutter en Schorpioen. Tussen deze laatste twee sterrenbeelden is hij ook het breedst en helderst, maar dat is zelfs vanuit Zuid-Europa maar moeilijk vast te stellen. Een beter zicht daarop hebben volkeren dichter bij de evenaar, waar dit deel van de Melkweg vaak hoog aan de hemel staat. De !Koeng-stam uit Botswana bijvoorbeeld. In hun legenden heet de Melkweg ‘de ruggegraat van de nacht’, naar het grillige, gewervelde verloop van lichte en donkere plekken over vrijwel de gehele lengte van de band² (Figuur 1). Daarmee zitten de !Koeng verbazingwekkend dicht bij de waarheid.

¹ Volgens de Griekse mythologie dankt de Melkweg zijn naam aan de melk die uit de borsten van Hera, de echtgenote van Zeus, langs de hemel is gespoten bij het zogen van Hercules.

² Op onze breedten is deze afwisseling van lichte en donkere plekken het best te zien in een stuk Melkweg ter hoogte van het sterrenbeeld Zwaan, waar een donkere band de Melkweg in de lengterichting in tweeën slijpt.



FIGUUR 1 — 360° panorama-foto van de hele Melkwegband. Duidelijk zichtbaar is het grillige patroon van lichte en donkere plekken, voor de !Koeng-stam uit Botswana aanleiding de Melkweg de ‘ruggegraat van de nacht’ te noemen. Foto: Lund Observatory.



FIGUUR 2 — De Andromedanevel is het meest nabije grote melkwegstelsel erkend vanuit het onze en wordt beschouwd als het evenbeeld van de Melkweg. De losse sterren op de foto zijn voorgrond-sterren uit ons eigen melkwegstelsel, die als druppels op een ruit zijn meegefotografeerd met de er op grote afstand achter gelegen Andromedanevel. Het aantal sterren in de Andromedanevel wordt geschat op een paar honderd miljard. Hun gezamenlijk licht is verantwoordelijk voor de diffuse nevelachtige verschijning. Foto: Jason Ware.

Want wat de ruggegraat is voor een gewerveld dier, is de Melkweg voor de sterrenhemel. Alle sterren aan de hemel, inclusief de Zon, worden door deze structuur bijeen gehouden en maken er deel van uit. Het lichtende karakter van de Melkweg is dan ook niets anders dan het gecombineerde licht van de vele miljarden sterren die de Melkweg rijk is en die te ver weg staan om afzonderlijk met het blote oog gezien te worden.

Het universum na de uitvinding van de telescoop

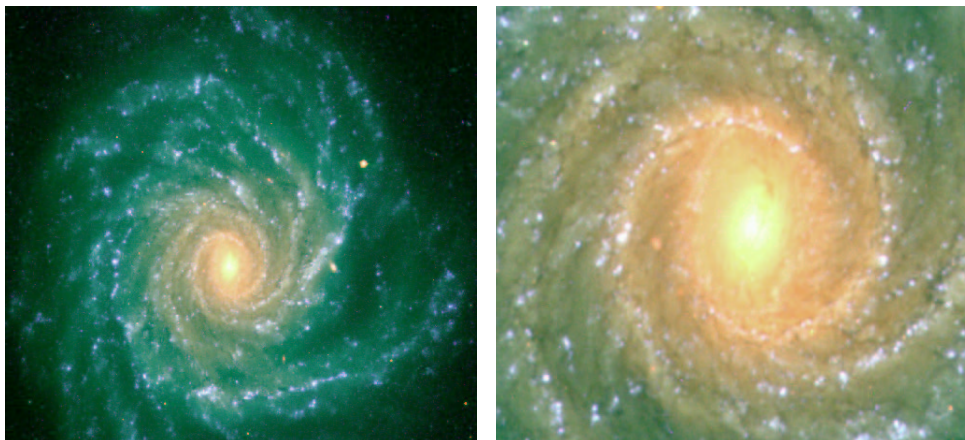
Inzicht in de feitelijke structuur van de Melkweg heeft lang op zich laten wachten. Onderzoek kwam pas goed op gang met de uitvinding van de telescoop door de Duitse Nederlander Hans Lippershey, in 1608. Met een veelvoud van de lichtgevoeligheid van het menselijk oog en de mogelijkheid objecten uit te vergroten stelde de telescoop natuurwetenschappers zoals Galileo Galilei en Christiaan Huygens in staat meer te zien dan alle generaties mensen vóór hen. Nieuwe werelden openden zich voor hun ogen: de Maan bleek bezaaid te zijn met kraters en gebogenen; Venus gehuld te zijn in wolken; Jupiter omgeven te zijn door manen; Saturnus getooid te zijn met een ring; en de wazige Melkwegband te bestaan uit ontelbare sterren en nevels. Een blik door een hedendaagse verrekijker geeft misschien een goed idee van wat deze pioniers gezien moeten hebben en — voor wie dit voor het eerst doet — van het gevoel dat deze aanblik bij hen moet hebben opgeroepen.

In de eeuwen die volgden op de uitvinding van de telescoop werd de beeldscherpte steeds beter en de lichtgevoeligheid steeds groter. Dit stelde de astronomen in staat de vele nevels die inmiddels ontdekt waren³ in detail te bestuderen. Hierbij kwamen grote verschillen aan het licht. Zo bleken sommige nevels bij nader inzien uit een compacte groep sterren te bestaan, anderen uit één of meerdere sterren gehuld in lichtende nevelflarden, terwijl anderen nog het meest weg hadden van lichtende draakkolken.

Hoe groot de teleskopen ook werden, één parameter bleef maar zeer moeilijk te achterhalen: de afstand⁴ tot de verschillende hemelobjecten en daarmee de driedimensionale structuur

³een aantal heldere nevels is al sinds mensenheugenis bekend, omdat zij met het blote oog zichtbaar zijn: voorbeelden zijn de Orionnevel, de Andromedanevel, de η -Carina nevel en de Magelhaense Wolken. Laatstgenoemden werden voor het eerst door een westerling aanschouwd in 1520, door ontdekkingsreiziger Fernão de Magelhães.

⁴Tot op de dag van vandaag zijn er een aantal typen sterren en nevels in de Melkweg waarvan de afstand niet goed bekend is.



FIGUUR 3 — NGC 1232 (**links**: het gehele stelsel; **rechts**: alleen de kern) is een prachtig voorbeeld van een melkwegstelsel waar we recht van boven op neerkijken. Duidelijk zichtbaar zijn de spiraalarmen, die het stelsel een draaikolk-achtige vorm geven. Onze Melkweg heeft ook een dergelijke structuur, maar die kunnen wij niet als zodanig herkennen, omdat wij er zelf tussen zitten. Ook de Andromedanevel zou er zo uitzien, ware het niet dat we het stelsel onder een grote hoek zien, waardoor de afzonderlijke spiraalarmen elkaar deels afdekken. Foto: ESO

van de sterrenhemel en die van de Melkweg in het bijzonder. Een belangrijke rol in het achterhalen van de structuur van de Melkweg speelde Jacobus Kapteyn⁵, die ongeveer een eeuw geleden op basis van een groots opgezet project van stertellingen en meting van sterbewegingen concludeerde dat de Melkweg de vorm van een platte schijf moet hebben, met de Zon nabij het centrum van deze verdeling. De diameter van de schijf schatte hij op 30 duizend lichtjaar⁶ en de dikte op 6 duizend lichtjaar. Hoewel de Melkweg inderdaad het beste met een schijf kan worden vergeleken, zat hij er voor de rest flink naast. Het duurde echter tot de jaren twintig van de vorige eeuw totdat de juiste afmetingen van de schijf (diameter 150 duizend lichtjaar; dikte 1500 lichtjaar) en de correcte positie van de Zon in deze schijf (28 duizend lichtjaar van het centrum vandaan) werden bepaald. In die tijd werd ook duidelijk dat draaikolk-achtige nevels, zoals de Andromedanevel (Figuur 2) en NGC 1232 (Figuur 3), vele honderden tot duizenden malen verder weg staan dan andere nevels aan de hemel. Dit soort nevels maken dan ook geen deel uit van de Melkweg, maar zijn melkwegstelsels op zich.

De structuur van de Melkweg en andere spiraalstelsels

Melkwegstelsel NGC 1232 (Figuur 3) is een erg mooi voorbeeld van hoe de Melkweg er van bovenaf bekeken uit zou zien. Zeer karakteristiek is de spiraalstructuur die de aanblik van dit soort melkwegstelsels domineert. De vorm vertoont veel gelijkenis met de patronen die een draaikolk teweeg brengt rond een afvoerput. En inderdaad, net als het water in een draaikolk, draaien ook de sterren in een melkwegstelsel rondjes rond de kern. Maar waar

⁵Astronoom te Groningen; grondlegger van het huidige naar hem vernoemde sterrenkundig instituut.

⁶Eén lichtjaar is de afstand die het licht in één jaar aflegt. Ter vergelijking: de Maan staat op een afstand van 1,3 lichtseconde (384 duizend kilometer) en de Zon op een afstand van 8 lichtminuten van de Aarde.



FIGUUR 4 — De Orionnevel in het wintersterrenbeeld Orion wordt tot lichten gebracht door de ioniserende straling van één van de sterren in het centrum van de nevel. Vergelijkbare nevels zijn ook in NGC 1232 (Figuur 3) te zien als heldere stippen langs de spiraalarmen. Die nevels staan 66 duizend maal verder weg dan de Orionnevel. Foto: Robert Gendler.

de drijvende kracht in een draaikolk de zuigkracht van het putje is, is de drijvende kracht voor de rotatie van sterren rond een melkwegkern de zwaartekracht van de materie in het melkwegstelsel. Dezelfde kracht zorgt er in ons zonnestelsel voor dat de Maan rond de Aarde draait, de planeten rond de Zon draaien maar ook dat een glas rode wijn op een nieuw wit tapijt kapot kan vallen.

In onze Melkweg bevindt de Zon zich op ongeveer 28 duizend lichtjaar van de kern. Op die afstand en met een omloopsnelheid van zo'n 800 duizend kilometer per uur (!) doet de Zon er 246 miljoen jaar over om één rondje rond de kern te voltooiien. Dit betekent dat gedurende de paar miljoen jaar dat er mensen op Aarde rondlopen de Zon dus maar een klein stukje van haar baan rond de Melkweg heeft afgelegd! Melkwegstelsels mogen dan dus wel roteren, maar binnen een mensenleven zien we daar heel erg van⁷.

Opnames van melkwegstelsels zoals NGC 1232 (Figuur 3) tonen behalve het diffuse samengetrokken sterlicht van de vele honderden miljarden sterren die het bevolken ook een groot aantal heldere vlekjes die de spiraalarmen accentueren. Dit zijn gebieden waar compacte groepjes jonge, zeer heldere sterren staan, temidden van de resten van de geboortewolk van waaruit zij zijn ontstaan. Ook in ons eigen Melkwegstelsel komen dit soort gebieden voor. De Orionnevel (Figuur 4) in het wintersterrenbeeld Orion bijvoorbeeld. De pas gevormde sterren in deze nevel zijn zo heet dat zij in staat zijn de randen van hun geboortewolk met hun sterlicht te *ioniseren*, dat wil zeggen, te onttrekken aan losse protonen en elektronen, de twee bouwstenen van het waterstof-atoom. Dergelijke zogenaamde H II-gebieden lichten op kleurenfoto's rood op, omdat bij het *recombineren*, zeg maar, het weer versmelten van een proton en een elektron tot een waterstof-atoom, één heel bepaalde kleur rood licht vrijkomt. Met het blote oog, door een verrekijker en zelfs door een vrij forse amateurtelescoop is deze kleur niet als kleur te herkennen. Daarvoor zouden de kleurgevoelige kegeltjes in ons oog zeker een miljoen maal gevoeliger⁸ moeten zijn. In plaats daarvan zien we de nevelflarden grijs

⁷Voor onze eigen Melkweg is dit niet helemaal waar. Het is mogelijk kleine verschillen in sterposities te meten op opnames die met tussenpozen van een paar jaar zijn gemaakt. Voor sterren in andere, nabije melkwegstelsel is deze techniek niet haalbaar, omdat die sterren duizenden tot miljoenen malen verder weg staan en, gemeten langs de hemel, even zo vele malen minder snel bewegen.

⁸de zwart-wit gevoelige staafjes in ons oog zijn veel gevoeliger dan de kleurgevoelige kegeltjes. Daarom kunnen

FIGUUR 5 — NGC 891 is een melkwegstelsel waar we van opzij tegenaan kijken, waardoor de spiraalstructuur niet zichtbaar is. In plaats daarvan wordt duidelijk hoe dun de schijf eigenlijk is. De opname wordt gedomineerd door een donkere band van verduisterend materiaal dat het licht van achtergelegen sterren tegenhoudt. Foto: WIYN Consortium, Inc.



oplichten, hetgeen een stuk minder spectaculair is. Ons melkwegstelsel telt vele van dit soort H II-gebieden. De meeste van hen zijn te vinden in de Melkwegband en daarvan vooral het deel tussen de sterrenbeelden Schild, Boogschutter en Schorpioen. In deze richting ligt dan ook het grootste deel van ons eigen melkwegstelsel.

Melkwegstelsels worden onder alle mogelijke hoeken aan de hemel aangetroffen. Sommige zien we recht van boven, zoals NGC 1232; anderen van schuin opzij, zoals de Andromedanevel; en een aantal precies in het verlengde van hun platte schijf. NGC 891 (Figuur 5) is een voorbeeld van de laatste categorie. Te oordelen aan de breedte-dikte verhouding van de lichtende schijf zijn melkwegstelsels inderdaad afgeplatte structuren. Opvallend is de donkere band die het stelsel over de gehele breedte van de schijf in tweeën lijkt te delen. Deze aanblik vertoont veel gelijkenis met die van de Melkwegband (Figuur 1), die ook smal is en onder de donkere vlekken zit. Deze overeenkomst is niet toevallig. Want als wij aan de hemel in de richting van de Melkwegband kijken, dan gaat onze blik, net als in het geval van NGC 891, langs het vlak van ons melkwegstelsel. Aangezien de meeste sterren van ons melkwegstelsel in dit vlak zitten, vormt hun versmolten licht samen een lichtende band: de Melkwegband. De donkere vlekken in deze band zijn plekken waar verduisterende wolken, die ook deel uitmaken van de melkwegschijf, het achtergelegen sterlicht tegenhouden. Een paar van die wolken staan precies in de richting van de kern van ons melkwegstelsel. Waren die verduisterende wolken er niet, dan zou de Melkwegband ter hoogte van het sterrenbeelden Boogschutter en Schorpioen vele malen helderder zijn!

Verduisterende materie is niet alleen in de Melkwegband en in NGC 891 vorhanden. Ook op de foto's van de Andromedanevel (Figuur 2) en NGC 1232 (Figuur 3) zijn dergelijke structuren duidelijk zichtbaar. Net als sterren en H II-gebieden horen zij in de spiraalarmen van melkwegstelsels thuis. Een erg fraaie aanblik biedt de Sombreronevel (Figuur 6), een melkwegstelsel waar we vrijwel van opzij tegenaan kijken en dat door een aantal sierlijke

we 's nachts of in de schemering wel grijsinten zien, maar er geen kleur aan verbinden.



FIGUUR 6 — De Sombrero-nevel. **Links:** detailopname van een deel van de verduisterende stofring. **Rechts:** het gehele melkwegstelsel. De Sombrero-nevel dankt zijn bijnaam aan een buitenproportionele grootte van de kern in combinatie met de aanwezigheid van duistere wolken in het melkwegvlak. Op de detailfoto is goed te zien dat de donkere wolken veel, tot de verbeelding sprekende, structuur vertonen.
Foto: ESO

banden van verduisterende materie toont. Ook op kleinere schaal, in onze eigen Melkweg, levert verduisterende materie mooie plaatjes op. Wat te denken van bijvoorbeeld de Paardekopnevel of de Slangenevel (Figuur 7)?

Het bestaan van verduisterende materie wordt door veel astronomen echter eerder ervaren als een plaag, omdat het de waarneming van achtergelegen objecten bemoeilijkt of zelfs onmogelijk maakt. De kern van ons melkwegstelsel is al genoemd. Maar ook de sterrenlijnen van Jacobus Kapteyn werden er sterk door beïnvloed. Hij corrigeerde zijn sterrenlijnen namelijk niet voor het percentage sterren dat achter de verduisterende wolken schuil gaat, omdat hij de berichten die destijd de ronde deden over het bestaan van verduisterende materie niet geloofwaardig achtte. Dit leidde er echter wel toe dat hij de grootte van ons Melkwegstelsel zwaar onderschat heeft. Het huidige heelalmodel is daarom dan ook niet met zijn naam verbonden.

Interstellaire materie

Inmiddels is er veel onderzoek gedaan naar de ware aard van de verduisterende materie, of *interstellaire materie*, zoals astronomen het noemen. Interstellaire materie komt voor het grootste deel voor in de vorm van grillig gevormde gaswolken, die bijeengehouden worden door de onderlinge aantrekkracht⁹ van de deeltjes. Deze zogenoeten *moleculaire wolken* komen vooral voor in de spiraalarmen van melkwegstelsels. De grootste moleculaire wolken kunnen tot een miljoen maal de massa van de Zon hebben. Diep in het binneste heersen er temperaturen van zo'n -260°C en bedraagt de dichtheid 100 tot 300 deeltjes per kubieke centimeter. Ter vergelijking, op zeeniveau is de dichtheid van de lucht 10 miljoen miljard (10^{16}) maal zo hoog. Buiten de moleculaire wolken is de dichtheid van de interstellaire materie veel en veel lager. De interstellaire ruimte is dan ook in het algemeen ontzettend ijlig, ijler nog dan het beste vacuüm dat wij op Aarde kunnen maken. Dit is dan ook de reden dat wij zo ver de ruimte in kunnen kijken: 384 duizend kilometer tot aan de kraters op de Maan, 1440 miljoen kilometer tot aan de ringen van Saturnus en nog eens 13 miljard maal zo ver

⁹Alle materie oefent een aantrekende kracht uit op andere materie.



FIGUUR 7 — **Links:** de Paardekopnevel in het sterrenbeeld Orion ontleent z'n naam aan het paardekopachtige vorm waarmee een wolk verduisterende materie in ons melkwegstelsel een achtergelegen H II-gebied gedeeltelijk afdekt. Foto: ESO. **Rechts:** De Slangenevel in het sterrenbeeld Ophiuchus. Op het eerste gezicht lijken de donkere slangvormige structuren gebieden te zijn waar geen sterren voorkomen. In werkelijkheid wordt het licht van de achtergelegen sterren er tegengehouden door een complex van sliertvormige verduisterende materie, op slechts 650 lichtjaar van de Zon. Foto: CFHT

tot aan de Andromedanevel. En het kan nog veel verder. Staat er echter toevallig net een moleculaire wolk, zoals de Slangenevel of de Paardekopnevel (Figuur 7) in de weg, dan stopt het zicht al ergens in een spiraalarm van ons eigen melkwegstelsel.

Moleculaire wolken: kraamkamers van sterren

Moleculaire wolken spelen een belangrijke rol in de evolutie van melkwegstelsels. Zij bestaan namelijk voor het grootste deel uit waterstofgas en helium, de elementen waaruit sterren kunnen worden gevormd. Moleculaire wolken zijn dan ook de plekken waar nieuwe sterren ontstaan. De manier waarop dit begint, is echter nog niet helemaal begrepen, omdat dit proces zich diep in het inwendige van de wolk afspeelt en daarom moeilijk waarneembaar is. Duidelijk is wel dat lokale verstoringen van de dichtheid de aanleiding kunnen zijn dat een deel van de wolk onder invloed van de eigen zwaartekracht begint samen te trekken en op te warmen. Aan dit proces, dat miljoenen jaren kan duren, komt pas definitief een eind wanneer de temperatuur en druk in de kern van de *proto-ster* zo hoog is opgelopen dat er spontaan *kernfusie* gaat optreden: het versmelten van een aantal lichte atoomkernen tot een zwaardere kern — in dit geval waterstof tot helium. Omdat bij dit proces veel energie in de vorm van straling vrijkomt, ontstaat er een uitwaarts gerichte stralingsdruk, die verdere samentrekking van de gasbol tot staan brengt. De jonge ster is geboren!

Sterren worden geboren met massa's variërend tussen 1/10 en 100 maal de massa van de Zon. Aangezien deze massa tevens ook hun brandstofvoorraad is, zou je verwachten dat zware sterren langer leven dan lichte sterren. Zware sterren gaan echter veel kwistiger met hun brandstof om dan lichte sterren door sterker te stralen. Een ster van 100 zonsmassa's bijvoorbeeld straalt een miljoen maal helderder dan de Zon. Maar met een brandstofvoorraad van slechts het honderdvoudige van die van de Zon heeft een zware ster een stuk minder lang

te leven: een paar miljoen jaar, tegen 15 miljard jaar voor de Zon.

Helder als ze zijn, zetten zware sterren hun omgeving gemakkelijk naar hun hand. Met hun enorme stralingsdruk blazen zij al snel na hun geboorte grote gaten in hun geboorte-wolk en ioniseren zij hun omgeving. De eerder besproken Orionnevel (Figuur 4), met in het centrum een aantal jonge hete sterren, is het resultaat van dit proces.

Kosmische recycling

Eenmaal op leeftijd gekomen hebben sterren in hun inwendige heel wat kernfusie-afval verzameld. In lichte sterren, zoals de Zon, komen deze produkten kort voor de terminale fase aan het steroppevlak terecht en worden zij door een dan inmiddels ontstane *sterwind*¹⁰ van de ster weggeblazen. Tot de afvalprodukten die op deze manier in het interstellaire medium terecht komen behoren helium, koolstof en zuurstof. Zware sterren ‘verrijken’ hun omgeving op een minder subtiele manier. Zij doen dit door, middels een geweldige *supernova-explosie*, hun buitenste lagen van zich af te slingeren. Op deze manier worden grote hoeveelheden in deze sterren gevormde metalen aan het interstellaire medium prijsgegeven.

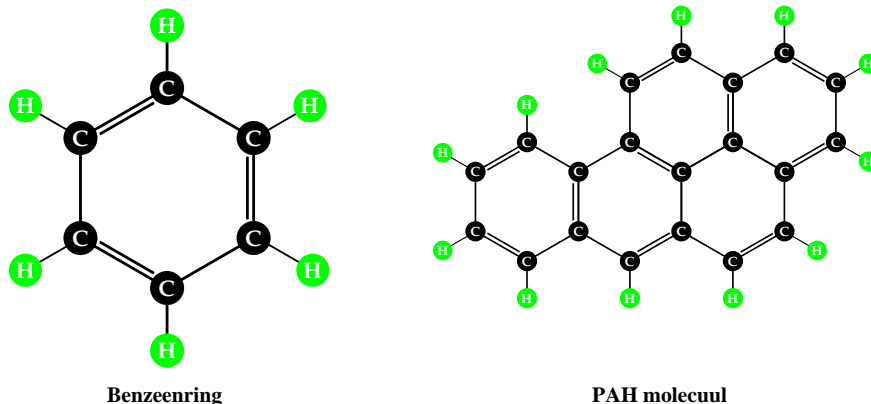
Uiteindelijk komt al dit sterafval weer terecht in moleculaire wolken. Hetzij in oude bestaande wolken in de buurt van waar de ster ter ziele is gegaan, hetzij in nieuwe wolken die onder invloed van de zwaartekracht over een tijdspanne van vele miljoenen jaren uit het sterafval samentrekken. Een volgende generatie sterren die uit deze ‘as’ herrijst, zal met deze metalen vervuild zijn. Ook onze Zon draagt de sporen met zich mee van een eerder leven. Net als ieder van ons overigens: alle zuurstof, koolstof en andere elementen waaruit ons lichaam is opgebouwd, zijn ooit gevormd in het inwendige van vorige generaties sterren en worden door ons gerecycled.

Het interstellaire medium: een groot chemisch laboratorium

De verrijking van het interstellaire medium met de in sterren gevormde elementen zoals koolstof (C), zuurstof (O), stikstof (N) en silicium (Si) openst de deur voor een breed scala aan chemische reakties in het interstellaire medium. Sommige reakties beginnen nog voor de fusieprodukten goed en wel de ster hebben verlaten. Zo gaan koolstofatomen al in de sterwind van een lichte ster eenvoudige verbindingen aan met andere atomen, waarbij o.a. water en koolmonoxide ontstaan. Andere koolstofatomen klitten hier al samen tot roet en ontstaat uit o.a. zuurstof en silicium zand. Meedeinend op de sterwind kunnen de roet- en zanddeeltjes uitgroeien tot grotere clusters, die door astronomen heel huiselijk *stofdeeltjes* genoemd worden.

Eenmaal aangekomen in het *diffuse interstellaire medium* wacht de net gevormde moleculen en stofdeeltjes een hard klimaat. De bindingen tussen de atomen in een molecuul worden gemakkelijk verbroken onder invloed van energierijk sterlicht, door de inslag van energierijke deeltjes of door schokken afkomstig van supernova-explosies. Veel net gevormde moleculen vallen dan ook al weer snel uit elkaar of gaan in zwaar gehavende staat verbindingen aan met andere atomen. Stofdeeltjes zijn beter bestand tegen het zware interstellaire klimaat. Aan hun oppervlak bieden zij atomen en moleculen de gelegenheid om aan te hechten en met hun naaste buren nieuwe chemische verbindingen uit te proberen. Sommige van deze

¹⁰Door de druk van uitstredend sterlicht worden gasdeeltjes behorend tot de buitenste gasschillen van een ster weggeblazen. Sterren die hun leven als hete ster beginnen kunnen op deze manier de helft van hun massa al tijdens hun leven kwijtraken.



FIGUUR 8 — Benzeenringen en PAH moleculen zijn complexe moleculen die in de buurt van oude sterren ontstaan uit de door de sterwind van dit soort sterren aangedragen bouwstenen. Tekening: Els Peeters.

reakties gaan razendsnel, andere vergen vele eeuwen voordat het passende deeltje aandokt. Is zo'n nieuwe verbinding stabiel, dan zal het bestand zijn tegen bestraling met energierijk licht, bombardementen van energierijke deeltjes en schokgolven afkomstig van supernova-explosies'. Eén van de meest complexe, maar ook stabielste moleculen die zich uiteindelijk kunnen vormen, zijn de uit benzeenringen opgebouwde Polycyclische Aromatische Koolwaterstoffen (PAKs), of 'PAHs' in het Engels (zie Figuur 8). Op Aarde ontstaan deze zeer giftige moleculen o.a. bij de verbranding van benzine, tabak en hamburgers. PAHs worden inmiddels overal aangetroffen, tot in de ijsberen op de Noordpool aan toe. Ook in mijn onderzoek spelen deze deeltjes een belangrijke rol.

Een veel vriendelijker klimaat ontstaat wanneer het diffuus verdeelde gas en stof door toedoen van de aantrekkende werking van de zwaartekracht de kans krijgt samen te trekken tot dichtere wolken. De grootsten hiervan worden *moleculaire wolken* genoemd en hebben massa's tot wel een miljoen maal die van de Zon. De buitenste lagen van deze wolken beschermen de verder naar binnen gelegen delen tegen de inwerking van sterstraling en snelle deeltjes. Dit betekent echter ook dat de binnendelen minder goed verwarmd worden dan de buitenlagen. De temperatuur is hier dan ook lager dan buiten de wolk: -200° C of lager. In de allerdichtste delen kan de temperatuur zelfs zakken tot onder de -250° C. Stofdeeltjes raken hier dan ook bedekt met dunne laagjes ijs, o.a. in de smaken: water-ijs, koolmonoxide-ijs, kooldioxide-ijs, zuurstof-ijs en stikstof-ijs. In deze ijzige omstandigheden, maar goed beschermd tegen agressie van buitenaf, kunnen zich broze moleculen vormen die het buiten de wolk niet lang zouden uithouden.

De ijsafzettingen verdwijnen weer één voor één als een stofkorrel de warmte te voelen krijgt van een zich in zijn omgeving uit de moleculaire wolk vormende ster. Met toenemende temperatuur en helderheid van deze *proto-ster* wordt het klimaat in de wolk steeds onvriendelijker voor moleculen en stofdeeltjes. Een deel vindt een veilig heenkomen in kleine compacte verdichtingen rond de proto-ster, die later tot planeten en kometen uitgroeien. Een ander deel valt ten prooi aan de intense straling van de jonge ster en wordt weer opgesplitst in de losse bouwstenen.

Infrarood-astronomie

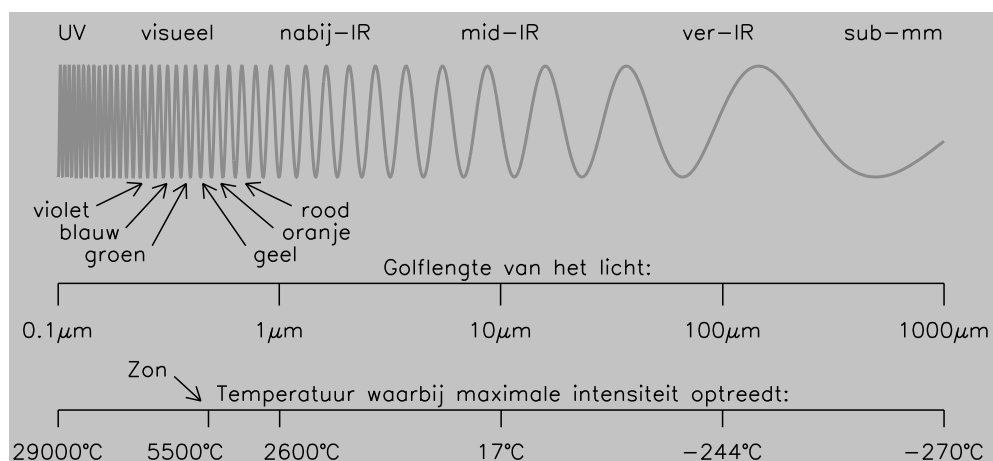
Veel van de kennis die is vergaard over de processen die zich in het heelal afspelen zouden we nooit hebben kunnen opdoen zonder het bestuderen van het licht dat onze studie-objecten uitzenden. Veldwerk verrichten behoort voor astronomen immers niet tot de mogelijkheden, aangezien de eerst volgende ster, na de Zon, zo'n 40 duizend miljard kilometer van ons vandaan staat.

Licht is net als geluid een golfverschijnsel. Zoals bij geluid lage tonen een lange golflengte hebben en hoge tonen een korte golflengte, zo heeft ook iedere kleur licht z'n eigen karakteristische golflengte. Rood licht, bijvoorbeeld, heeft een golflengte van $0.70\text{ }\mu\text{m}$ ¹¹, oranje licht een golflengte van $0.60\text{ }\mu\text{m}$, geel licht een golflengte van $0.55\text{ }\mu\text{m}$, groen licht een golflengte van $0.53\text{ }\mu\text{m}$, blauw licht een golflengte van $0.49\text{ }\mu\text{m}$ en violet licht een golflengte van $0.44\text{ }\mu\text{m}$. Deze volgorde is precies dezelfde als die in een regenboog. Maar net zoals er geluiden zijn die ons oor niet kan horen — maar een hond bijvoorbeeld wel — zijn er ook kleuren licht die onze ogen niet kunnen zien. Zo wordt licht met een golflengte korter dan violet ‘ultra-violet’ genoemd (afgekort: UV) en licht met een golflengte langer dan rood licht ‘infra-rood’ (afgekort: IR). De hele kleurenwaaijer, inclusief de voor ons onzichtbare kleuren, wordt het *electro-magnetisch spektrum* genoemd. Een groot deel hiervan staat in het bovenste deel van Figuur 9 afgebeeld.

Alles dat een temperatuur heeft hoger dan -273° C (de laagst mogelijke temperatuur) produceert¹² zelf licht. Dat geldt net zo zeer voor een blokje ijs van -5° C , als voor het men-

¹¹ $1\text{ }\mu\text{m} = 1$ micro-meter = het 1 miljoenste deel van een meter.

¹² Licht produceren is iets anders dan licht weerkaatsen. De hete gloeidraad in een lamp produceert zichtbaar licht; de muur weerkaatst het alleen maar. Hetzelfde geldt voor zonlicht: de Zon produceert het, het strand weerkaatst het.



FIGUUR 9 — Het elektromagnetisch spektrum. Iedere kleur licht heeft zijn eigen karakteristieke golflengte. Behalve voor ons zichtbare kleuren (visueel) bestaan er ook kleuren met kortere golflengten (ultra-violet) en langere golflengten (infrarood). Infrarood licht is opgedeeld in de kleuren nabij-infrarood, mid-infrarood en ver-infrarood. Onderaan de figuur staat afgebeeld welke temperatuur de lichtbron moet hebben om op de bijbehorende kleur het helderst te zijn. Zo straalt een glas Madeira wijnt met een temperatuur van 17° C het helderst op een golflengte van $10\text{ }\mu\text{m}$.

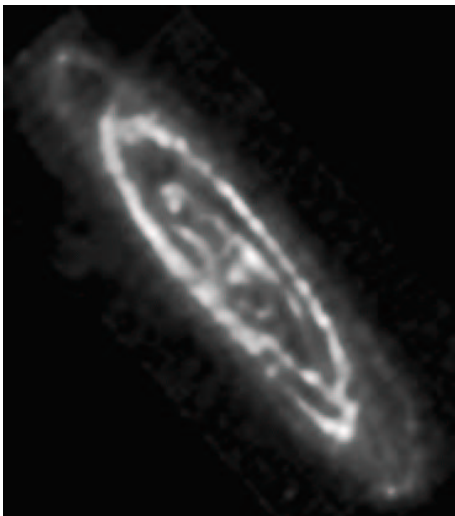


FIGUUR 10 — **Links:** Een werkende haardroger, gefotografeerd in zichtbaar licht. De hete lucht is niet heet genoeg om zichtbaar licht uit te stralen. **Rechts:** Dezelfde werkende haardroger, nu gefotografeerd in infrarood licht. De hete lucht straalt helder op infrarode golflengten. Foto: NASA/IPAC.

selijk lichaam (37°C), een roodgloeiende ijzeren staaf (500°C) en het oppervlak van de Zon (5500°C). Toch kunnen we een blokje ijs in het donker niet zien. Dit komt doordat, afhankelijk van de temperatuur, alleen maar een deel van alle kleuren wordt opgewekt. Een ijsblokje is dan ook alleen te zien in infrarode kleuren (die ons oog niet kan waarnemen), terwijl de Zon ook, en vooral, zichtbaar licht uitstraalt. De kleur waarop een lichtgevend object het helderst is, wordt bepaald door zijn temperatuur. Zo straalt een ijsblokje het helderst in mid-infrarode kleuren, terwijl de Zon het helderst straalt in geel licht. Dit wordt nog duidelijker door een blik op de onderste helft van Figuur 9. Hier kan worden afgelezen welke kleur het helderst oplicht voor verschillende temperaturen van een lichtbron. Zo kunnen wij ook afleiden dat een rode ster koeler is dan een gele ster en een gele ster koeler is dan een blauwe ster.

Tot een jaar of 50–60 geleden konden sterrenkundigen alleen waarnemingen doen in zichtbaar licht. Dit is een prima kleurbereik als het er om gaat warme (5000°C) en hete ($20,000^{\circ}\text{C}$) sterren waar te nemen, maar niet als het er om gaat het licht van koude (2000°C) sterren en van koude (-260°C) moleculaire wolken te detecteren. Deze laatsten stralen namelijk alleen infrarood licht uit. De ontwikkeling van infrarood-gevoelige detectoren kwam in de jaren 60 op gang, toen duidelijk werd dat naderende kernraketten goed kunnen worden opgespoord aan de hand van de hete uitlaatgassen van hun motoren. Dat dit principe inderdaad werkt, wordt treffend geïllustreerd door het rechter paneel van Figuur 10, dat het infrarode licht van de hete ‘uitlaatgassen’ van een modale haardroger toont. De eerste sterrenkundige infrarood-waarnemingen volgden uiteindelijk eind jaren zestig.

Waarnem-technisch komt er bij een infrarood-waarneming veel meer kijken dan bij een waarneming in zichtbaar licht. De aardatmosfeer is namelijk tamelijk ondoorlatend voor infrarood licht afkomstig van buiten de dampkring (op een paar ver van elkaar gelegen infraroodkleuren na) en produceert bij een luchtemperatuur van tussen de -50 en $+20^{\circ}\text{C}$ zelf ook veel infraroodstraling! De uitdagingen zijn misschien het best te vergelijken met die voor een waarnemer, die in zichtbaar licht overdag zijn waarnemingen moet doen en zich daarbij moet beperken tot slechts één bepaalde kleur, bijvoorbeeld geel. Een verder belangrijk verschil met optische waarnemingen is de noodzaak om de infrarood-camera in een vacuüm-koelkast (cryogeen vat) te plaatsen, omdat de camera inclusief detector anders zelf teveel infraroodstraling produceert. De eisen, die hierbij aan het koele vermogen gesteld worden, nemen



FIGUUR 11 — De Andromedanevel gezien op een golflengte van $175\text{ }\mu\text{m}$, in de kleur ver-infrarood. Op deze golflengte stralen vooral koude moleculaire wolken met temperaturen van typisch -257° C . Opmerkelijk is dat de moleculaire wolken in de Andromedanevel in een ringvormige in plaats van een spiraalvormige structuur zijn ondergebracht. Foto: ESA/ISO/ISOPHOT & Martin Haas.

toe naarmate de golflengte waarop waargenomen wordt langer is. Voor moleculaire wolken met een temperatuur van -250° C , die vooral op $100\text{ }\mu\text{m}$ in het ver-infrarood stralen, moet daarom zeer veel meer worden gekoeld dan voor ‘warm’ gas van -10° C , dat vooral rond $11\text{ }\mu\text{m}$ in het mid-infrarood straalt. Alle met de aardatmosfeer gerelateerde problemen verdwijnen wanneer de infrarood-telescoop in de ruimte wordt gebracht. De belangrijkste winst van een observatorium in de ruimte is de vrijheid om alle, in plaats van slechts een paar, infraroodkleuren te kunnen waarnemen. Nadelen zijn echter de hoge kosten om de telescoop ‘space-qualified’ te bouwen, hem te lanceren en de hoge afschrijvingskosten vanwege de beperkte levensduur, bepaald door de beperkte hoeveelheid koelmiddel dat mee omhoog kan. De eerste infrarood-telescoop die desondanks boven de dampkring werd getild was de Amerikaans/Brits/Nederlandse satelliet IRAS (1983). Deze werd 12 jaar later gevolgd door de Europese satelliet ISO (1995–1998). De waarnemingen van deze satelliet vormen de aanleiding voor dit proefschrift.

Een treffende illustratie van waartoe een infrarood-telescoop in de ruimte in staat is, toont de opname van de Andromedanevel, gemaakt op een golflengte van $175\text{ }\mu\text{m}$ in het ver-infrarood (Figuur 11). Op deze golflengte stralen vooral koude wolken met temperaturen van om en de nabij -257° C . Dergelijke wolken zijn veel te koud om zichtbaar licht uit te stralen. Op foto’s genomen in zichtbaar licht vallen die koude wolken niettemin op, omdat zij het licht van er achter gelegen sterren tegenhouden (zie Figuur 2).

Botsende melkwegstelsels

In 1983 bracht de IRAS satelliet-telescoop de hele hemel in kaart in vier kleuren infraroodlicht. De metingen zouden astronomen in staat stellen om voor hun favoriete objecten de temperatuursverdeling van de daar aanwezige interstellaire materie te bepalen uit de infrarode helderheid op golflengten van 12, 25, 60 en $100\text{ }\mu\text{m}$, corresponderend met temperaturen van -32° C , -157° C , -225° C en -244° C . Aangezien dit tot die tijd nooit eerder was gedaan, was het aan het begin van de missie wel duidelijk dat er een aantal verrassingen zouden volgen. Eén van die verrassingen was de vondst van een aantal infraroodbronnen die op

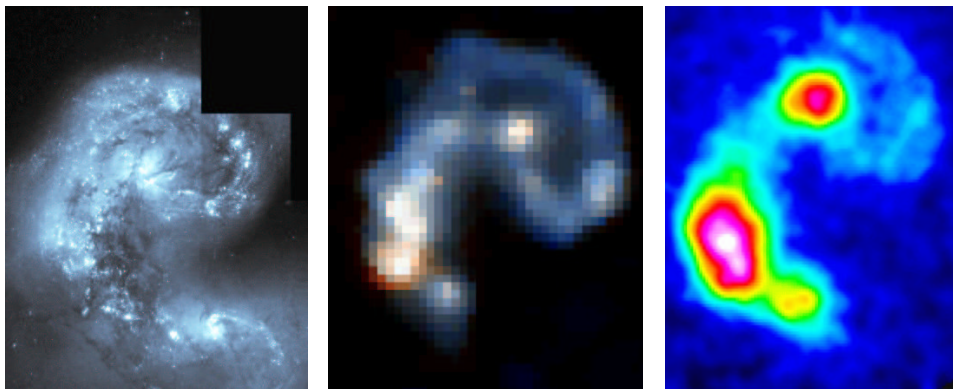


FIGUUR 12 — “De Antennes” (NGC 4038/39). **Links:** Groothoek-opname van de botsende stelsels. Duidelijk zichtbaar zijn twee sierlijke lierten bestaande uit sterren die bij de botsing weggeslingerd zijn. Foto: CTIO. **Rechts:** Detail-opname van de twee in elkaar verwrochte melkwegstelsels. De kern van het ene stelsel is rechtsonder zichtbaar, de kern van het andere stelsel staat net iets boven het midden. De interactie-zone bevindt zich ietwat links van de verbindinglijn tussen de beide kernen en is te herkennen aan de vele donkere wolken. Foto: Brad Whitmore (STScI) & NASA.

foto’s in zichtbaar licht niet voorkwamen. Na het meten van de afstand tot deze nieuwe bronnen bleek dat zij heel ver weg staan, op afstanden van 240 miljoen lichtjaar (120 maal de afstand tot de Andromedanevel) en verder. Om op die afstand nog voor IRAS zichtbaar te zijn moesten zij dus een *lichtkracht*¹³ hebben die minstens 100 maal zo hoog is als die van onze Melkweg! Dit bezorgde deze melkwegstelsels de naam *Ultra-Luminous Infrared Galaxies* (afgekort: ULIRG). Gerichte zoekacties met optische teleskopen resulterde uiteindelijk in de detectie van deze merkwaardige stelsels. Hierbij bleken zij in zichtbaar licht vele malen zwakker te zijn dan op grond van hun infrarood helderheid had mogen worden verwacht. Dit, gecombineerd met de extreme lichtkracht, vroeg om een extreme verklaring.

Inmiddels is duidelijk geworden dat ULIRGs het resultaat zijn van de botsing van twee melkwegstelsels. Scherpe opnames onthullen dat vrijwel alle ULIRGs er ‘verstoord’ uitzien. In plaats van een mooie spiraalstructuur, zoals NGC 1232 (Figuur 3), tonen zij een chaotisch patroon van heldere en donkere gebieden. Een prachtig voorbeeld van een botsing, die nog aan de gang is, wordt geboden door een tweetal melkwegstelsels die vooral bekend staan onder hun bijnaam “de Antennes”. In het linker paneel van Figuur 12 is goed te zien waaraan zij hun naam ontleen. De twee diffuse lierten die aan de beide stelsels ‘kleven’ bestaan uit sterren die ten gevolge van de zwaartekrachtsaantrekking van het andere melkwegstelsel uit hun omloopsbanen zijn geraakt en vervolgens zijn weggekatapulteerd. Uiteindelijk zullen deze sterren allemaal weer terugkeren naar het centrum van de botsing, waar dan inmiddels de beide stelsels tot één groter stelsel zullen zijn versmolten. Tijdens de botsing, die nog vele miljoenen jaren zal voortduren, komen sterren niet daadwerkelijk met elkaar in aanvaring. De afstand tussen sterren in een melkwegstelsel is namelijk zo groot dat andere sterren er ge-

¹³Lichtkracht is een andere naam voor uitgestraald vermogen en wordt uitgedrukt in de eenheid Watt. De lichtkracht van de Zon bedraagt 3.9×10^{26} Watt. De lichtkracht van een 60-Watt-lamp bedraagt . . . 60 Watt.



FIGUUR 13 — “De Antennes” (NGC 4038/39) gefotografeerd in drie verschillende kleuren. **Links:** De opname in zichtbaar licht toont de verdeling van sterren. Foto: Brad Whitmore (STScI) & NASA. **Midden:** De opname in mid-infrarood licht bewijst dat warm stof vooral in de interactie-zone voorkomt. Foto: ESA/ISO/ISOCAM & Laurent Vigroux. **Rechts:** De opname in sub-mm licht ($850 \mu\text{m}$) laat zien dat er zich ook veel koud stof in de interactie-zone bevindt. Foto: Paul van der Werf.

makkelijk tussendoor¹⁴ kunnen. Voor de moleculaire wolken en het diffuus verdeelde gas ligt dit anders. Zij komen daadwerkelijk met elkaar in aanvaring en worden opgehoopt en samengeperst op de plek waar de twee stelsels elkaar ‘geraakt’ hebben. Foto’s gemaakt in zichtbaar licht tonen op deze plek vooral donkere wolken (linker paneel van Figuur 13). Infraroodfoto’s daarentegen laten zien dat er in de *interactie-zone* veel warm gas en stof voorkomt (middelpaneel van Figuur 13), terwijl de foto genomen in ‘sub-millimeter’ licht (op $850 \mu\text{m}$) er ook de aanwezigheid van grote hoeveelheden zeer koud gas in aantoon (rechter paneel van Figuur 13). Het is daarmee duidelijk dat er in de moleculaire wolken die in de *interactie-zone* zijn opgehoopt een geweldige golf van stervorming heeft plaatsgevonden, ingezet door de compressie van het gas. Anno 2003 verhitten de pas gevormde sterren hun geboortewolk en doen hem in infrarood licht helder stralen. Later, als deze ‘babyboomers’ hun geboortewolk hebben stukgeblazen, zullen op deze plek grote hoeveelheden heldere sterren blijken te staan, die dan vooral in zichtbaar licht goed te zien zullen zijn.

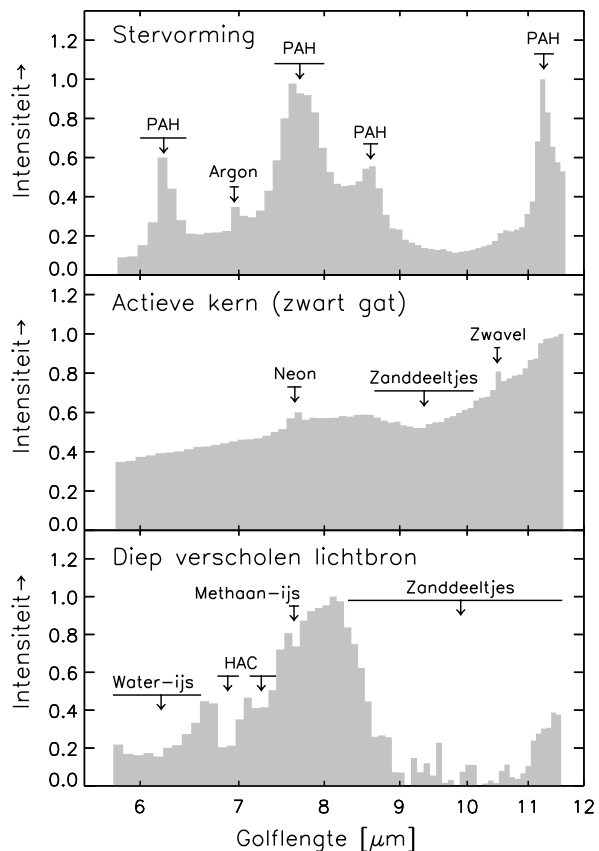
Ook onze Melkweg en de Andromedanevel liggen op ramkoers. Op dit moment vliegen zij met een snelheid van 1 miljoen kilometer per uur op elkaar af. Met een huidige onderlinge afstand van 2 miljoen lichtjaar duurt het echter nog wel even voordat wij dekking moeten gaan zoeken.

Met een lichtkracht van 10 tot 100 maal de lichtkracht van de Antennes moeten de botsingen in ULIRGs zo mogelijk nog dramatischer van aard zijn dan die in het Antenne-stelsel. Astronomen vragen zich dan ook serieus af of de enorme lichtkracht van ULIRGs wel enkel en alleen veroorzaakt kan worden door een golf van stervorming (in het Engels: *starburst*). Een alternatief is namelijk *accretion* (massa-aanvoer) op een groot zwart gat¹⁵, waarbij ook erg veel energie vrijkomt. Veel bekende melkwegstelsels hebben zo’n *actieve kern* en ontlenen er een (groot) deel van hun lichtkracht aan. Helaas gaan de kernen van ULIRGs schuil achter

¹⁴Stel: we verkleinen de diameter van de Zon van 1.4 miljoen km tot die van een tennisbal. De eerstvolgende ster staat op deze schaal dan op een afstand van 3000 km. Dit laat zien dat de ruimte tussen de sterren heel erg leeg is!

¹⁵Een zwart gat is een object dat zo zwaar is dat zelfs licht niet kan ontsnappen. Het object is dan ook onzichtbaar.

FIGUUR 14 — Boven: Het spektrum van een stervormingsgebied wordt gedomineerd door intensiteitspieken die toe te schrijven zijn aan tot stralen gebrachte PAH-molekülen en Argon-atomen. **Midden:** De aanwezigheid van een actieve kern kan in het infrarood worden afgeleid uit de aanwezigheid van infraroodstraling van heet (500°C) stof, dat deel uitmaakt van een torus rond het centrale zwarte gat. Heet stof straalt heel gelijkmatig over een breed golflengtebereik. Ook karakteristiek zijn intensiteitspieken van neon en zwavel. **Onder:** Het spektrum van een hete infraroodbron, verschenen achter een dikke laag moleculaire wolken, wordt gekenmerkt door de afwezigheid van intensiteit op bepaalde golflengten. De missende intensiteit wordt tegengehouden door zand en door verschillende soorten ijs. Zowel zand als ijs komen voor in stofdeeltjes die deel uitmaken van zeer koude moleculaire wolken.



dikke ‘dekens’ van moleculaire wolken, die ten gevolge van de botsing op de nieuwe kern terecht zijn gekomen. Hierdoor is het moeilijk om na te gaan of de lichtkracht van de kern wordt gedomineerd door een golf van stervorming of door accretie op een groot zwart gat. Eén ding staat in elk geval vast: de ‘dekens’ bevatten voldoende gas en stof om zowel een grote starburst als een groot zwart gat te kunnen ‘voeden’.

Eén van de eigenschappen van interstellaire materie is dat het minder sterk verduistert naarmate de golflengte waarop wordt waargenomen langer is. Een waarnemer in infrarood licht heeft het dus minder moeilijk door de verduisterende ‘deken’ heen de componenten van de kern te ontwaren dan een waarnemer in zichtbaar licht. Met de lancering van het *Infrared Space Observatory* (ISO) in 1995 werd het voor het eerst mogelijk om ULIRGs over een breed infrarood golflengtebereik te bestuderen en een poging te wagen de belangrijke vraag te beantwoorden: wat veroorzaakt de enorme lichtkracht van ULIRGs? Stervorming of accretie op een groot zwart gat.

De beste manier om in het infrarood de aanwezigheid van een actieve kern (zwart gat) of van jonge sterren (stervorming) vast te stellen in de kern van een ULIRG is door de intensiteit (helderheid) van de ontvangen infraroodstraling te meten als functie van de golflengte. De bovenste twee panelen van Figuur 14 laten zien dat de intensiteitsverdeling — of *spektrum* in vaktaal — er voor een stervormingsgebied duidelijk anders uitziet dan voor een actieve

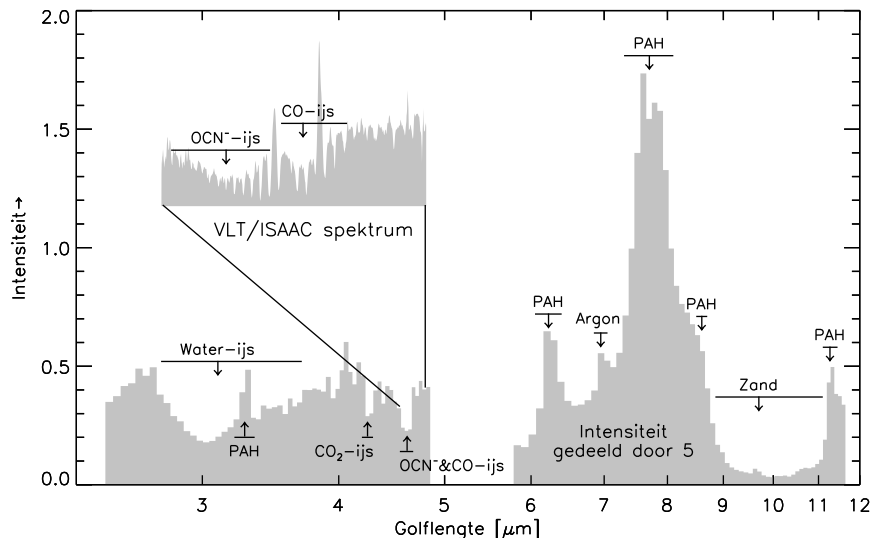


FIGUUR 15 — Een extreem lang belichte opname van een klein stukje ‘lege’ nachthemel in het sterrenbeeld Grote Beer (het zogeheten “Hubble Deep Field”). Op één ster uit ons eigen melkwegstelsel na (onder in beeld) toont de foto uitsluitend andere melkwegstelsels. De afstanden tot deze stelsels bedragen vele miljarden lichtjaren, hetgeen betekent dat wij hen zien zoals zij er uitzagen toen het heelal zo’n 5 tot 10 miljard jaar jonger was. Bron: R. Williams & het HDF Team (STScI) en NASA.

kern. Zo wordt het infraroodspektrum van een stervormingsgebied gedomineerd door intensiteitspieken op 6.2, 7.7, 8.6 en 11.2 μm . Deze pieken zijn de spektrale ‘vingerafdrukken’ van PAH-molekülen (Figuur 8), die door het licht van jonge sterren tot stralen gebracht worden. Het infraroodspektrum van een zwart gat daarentegen, wordt vooral gedomineerd door de warmtestraling afkomstig van een *torus* (een dikke ring; nog het best te vergelijken met een zwemband) van heet (500°C) stof, dat rond het zwarte gat draait. De mate waarin het spektrum van een ULIRG meer lijkt op het spektrum van een stervormingsgebied (bovenste paneel van Figuur 14) dan op dat van een actieve kern (middelste paneel van Figuur 14), wordt sinds de ISO-missie door velen gebruikt om te bepalen of de lichtkracht van ULIRGs gedomineerd wordt door stervorming of door accretie op een zwart. De meeste astronomen zijn er inmiddels van overtuigd dat de enorme lichtkracht toch vooral door een botsings-geïnduceerde golf van stervorming veroorzaakt wordt en niet door een actieve kern.

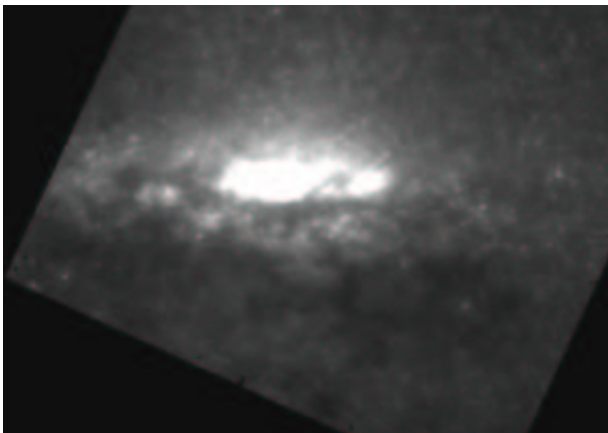
ULIRGs: de laatsten der Mohicanen

Het onderzoek aan ULIRGs neemt een bijzondere plaats in in het onderzoek naar de evolutie van het heelal. ULIRGs zijn mogelijk de meest recente exponenten van een tijdvak in de geschiedenis van heelal waarin melkwegstelsels er nog niet zo uitzagen zoals wij hen nu zien en waarin het veel vaker voorkwam dat melkwegstelsels met elkaar in botsing kwamen. Aanwijzingen voor het bestaan van een dergelijke roerige periode komen van waarnemingen aan zeer ver weg gelegen melkwegstelsels. Het licht dat wij van deze stelsels ontvangen is vele vele miljarden jaren onderweg geweest, waardoor wij deze stelsels zien zoals zij er in hun



FIGUUR 16— Het door ISO gemeten spektrum van de kern van NGC 4945 toont de spekrale vingerafdrukken van vele soorten ijs. Dit duidt op de aanwezigheid van koude moleculaire wolken nabij de kern van het stelsel. De aanwezigheid van sterke vingerafdrukken van PAH-molekülen wijst op sterke stervorming in de kern. **Inzet:** De ISAAC-spectrograaf van de VLT was in staat de spekrale vingerafdrukken van OCN[−]-ijs en CO-ijs van elkaar te scheiden.

jeugd hebben uitgezien. Een prachtig voorbeeld van een dergelijke reis terug in de tijd biedt de opname van het zogeheten ‘Hubble Deep Field’, gemaakt in een combinatie van zichtbaar en infrarood licht (Figuur 15). Alle lichtbronnen op deze foto, op één ster na, zijn melkwegstelsels. Een aantal van hen ziet er heel normaal uit, terwijl anderen de lidtekens tonen van aanvaringen met andere melkwegstelsels. De meest ver weg gelegen stelsels zijn helaas te klein om goed geanalyseerd te kunnen worden. Andere opnames, gemaakt in sub-millimeter licht bevatten aanwijzingen dat er in het jonge heelal een periode van sterke stervorming moet zijn geweest, waarschijnlijk het gevolg van botsingen tussen deze jonge melkwegstelsels. Tot dezelfde conclusie komen waarnemers die de mate van stervormingsactiviteit afleiden uit de sterke van de *recombinatie-straling*¹⁶ afkomstig van melkwegstelsels. Helaas zijn waarnemingen aan ver weg gelegen stelsels zeer tijdsintensief en moeilijk uitvoerbaar, omdat de stelsels vanwege hun afstanden extreem zwak zijn. De opname van het Hubble Deep Field alleen al koste 10 volle dagen (240 uur) waarnemingstijd! Willen we dus meer te weten komen over de processen die zich afspeelden in de roerigste periode in de geschiedenis van het heelal, dan zijn de relatief dichtbij gelegen ULIRGs, als laatsten der Mohicanen, uitstekende vervangende studie-objecten.



FIGUUR 17— De kern van het melkwegstelsel NGC 4945 in nabij-infrarood licht. Goed zichtbaar zijn de vele moleculaire wolken (*donker*) die het licht van de sterren (*wit*) in de kern deels verduisteren. Een dergelijke aanzicht doet denken aan de effecten van verduisterende wolken in de Melkwegband. Foto: Allesandro Marconi.

Mijn proefschrift

Als medewerker van het ISO Spectrometer Data Center (ISO-SDC) van het Max-Planck-Institut für Extraterrestrische Physik (MPE) in Garching (Duitsland) had ik het voorrecht gedurende de operationele fase van de ISO-missie (1995–1998) nauw betrokken te zijn bij de analyse van de mid-infrarood spektra van diverse soorten infrarood-heldere melkwegstelsels. Hieronder waren ook een groot aantal ULIRGs. Aangezien de meeste van deze stelsels nooit eerder in dit golflengte-gebied waren bestudeerd, was vrijwel alles dat ons onderzoek opleverde nieuw. Hierdoor was ik bij het begin van mijn promotie-onderzoek in 1999 helemaal klaargestoomd om het pionierswerk van onze groep voort te zetten. Mijn speciale interesse ging hierbij uit naar een nauwkeurige vergelijking van de mid-infrarood spektra van de kerne van starburst-stelsels, actieve stelsels en ULIRGs om te kijken in hoeverre de methode, die wij hadden bedacht om de bijdrage van stervorming tot de helderheid van ULIRGs te meten, robuust is. Alle hoofdstukken in mijn proefschrift hebben hier in meerdere of mindere mate mee te maken.

Een zeer bijzonder spektrum is in dit verband het spektrum van de kern van het starburststelsel NGC 4945. Dit spektrum is zo anders dan dat van andere vergelijkbare melkwegkeren dat wij eerst de waarneming hebben laten herhalen voordat wij waarneemfouten durfden uit te sluiten en ons aan een analyse hebben durven te wagen. Deze analyse vormt nu het hart van het eerste gepubliceerde onderzoek voor mijn proefschrift, het huidige hoofdstuk 3. Het bijzondere van het spektrum van de kern van NGC 4945 (Figuur 16) is dat het in tegenstelling tot de spektra van de kerne van vele andere *starburst-stelsels*¹⁷ sterke spektrale vingerafdrukken toont van verschillende soorten ijs. Aangezien ijs alleen kan voorkomen in zeer koude moleculaire wolken betekent dit dat er zelfs in deze, door sterke sterstralingsge-domineerde, kern plekken zijn waar nog zeer koud materiaal vorhanden is. Deze zijn goed zichtbaar als donkere vlekken op de infrarood-foto van de kern (Figuur 17). Onze ontdekking vormde voor ons de aanleiding om de *Very Large Telescope* (VLT) van de *European Southern Observatory* te gebruiken om de sterrenvorming in de kern van NGC 4945 te observeren.

¹⁶De rode kleur van bijvoorbeeld de Orionnevel is het resultaat van recombinatie-straling. Rond deze nevel worden vele nieuwe sterren gevormd.

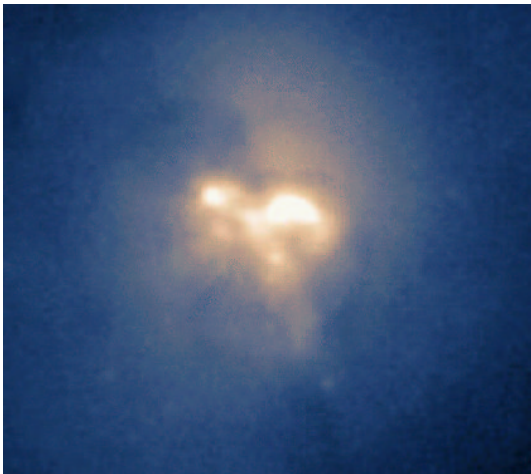
¹⁷Starburst-stelsels zijn melkwegstelsels die een periode van sterke stervorming doormaken. De lichtkracht van dit soort melkwegstelsels is dientengevolge groter dan de lichtkracht van normale melkwegstelsels, maar altijd nog een factor 10 tot 100 lager dan die van ULIRGs.

Observatory (ESO) in te zetten om de vingerafdrukken van drie soorten ijs nog eens in detail waar te nemen. Deze waarnemingen staan beschreven in hoofdstuk 4 en staan mee afgebeeld in Figuur 16. De gedetailleerde spekrale vingerafdrukken verraden ons dat de moleculaire wolken rond de kern van NGC 4945 inderdaad koud zijn, maar dat de langdurige blootstelling aan sterstraling toch al voor enige opwarming en voor chemische reacties diep binnenin heeft gezorgd. Zo is er al een flinke vingerafdruk te zien van een speciaal soort ijs (OCN^- -ijs; Figuur 16), dat in ‘maagdelijke’ moleculaire wolken niet voorkomt. Ook zijn bepaalde vluchtbare soorten CO-ijs al verdampd ten gevolge van de stijging van de temperatuur in de wolk. Onze waarnemingen van de stoffige en ijzige kern van NGC 4945 geven voor het eerst inzicht in de toestand van stofdeeltjes in moleculaire wolken van een ander melkwegstelsel dan het onze. Ook bieden zij inzicht in de samenstelling van de moleculaire wolken in de nog veel ‘stoffigere’ kernen van ULIRGs.

Het in mijn ogen belangrijkste resultaat van mijn proefschrift (hoofdstuk 5) kwam geheel bij toeval tot stand toen ik het mid-infrarood spektrum van het melkwegstelsel NGC 4418 aan mijn verzameling melkwegstelsel-spektra toevoegde. Het spektrum (onderste paneel van Figuur 14) wijkt sterk af van dat van andere nabije melkwegstelsels (overige panelen van Figuur 14) en toont spekrale vingerafdrukken van onder andere water-ijs, methaan-ijs en zanddeeltjes. De kern van dit stelsel is dus kennelijk helemaal omgeven door een dikke laag gas en stof, in de vorm van koude moleculaire wolken. vergeleken met deze kern is de kern van NGC 4945 zo stofvrij als een operatie-kamer! De aanwezigheid van de dikke stoflaag in NGC 4418 laat niet toe te bepalen wat er onder de deken gebeurt; of de lichtkracht van de kern veroorzaakt wordt door een grote golf van stervorming of door de aanwezigheid van een groot centraal zwart gat, of door een combinatie van beiden. Wat is nu het belang van ‘de ontdekking’ van het spektrum van NGC 4418? De realisatie dat de kernen van melkwegstelsels compleet verscholen kunnen gaan achter een dikke laag zeer koud gas en stof en dat dergelijke kernen te herkennen zijn aan een mid-infrarood spektrum als dat van NGC 4418.

Van de kernen van ULIRGs is bekend dat zij zeer veel gas en stof bevatten. Zouden hun spektra misschien op die van NGC 4418 lijken? Dit blijkt inderdaad zo te zijn voor een aantal van hen, zoals ik in de hoofdstukken 2 en 6 aantoon. Het mooiste voorbeeld is Arp 220 (Figuur 18; melkwegstelsel nummer 220 uit de catalogus van Hilton Arp), de meest nabije en bekendste ULIRG. Het spektrum van Arp 220 (Figuur 19) blijkt het midden te houden tussen dat van een stervormingsgebied en dat van een diep verscholen lichtbron. Dit betekent dat het spektrum van Arp 220 uit twee componenten bestaat, die even sterk bijdragen: een stervormings-component en een diep-verscholen-lichtbron-component. Dit betekent dat er in de kern zowel stervorming optreedt als dat er een diep verscholen, niet nader te identificeren, lichtbron huist. Het laatste kan dus een groot zwart gat of een stervormingsgebied blijken te zijn. Eerdere interpretaties van hetzelfde mid-infrarood spektrum hebben het *gehele* mid-infrarood spektrum aan stervorming toegeschreven en daarmee, zoals nu blijkt, de verscholen lichtbron over het hoofd gezien.

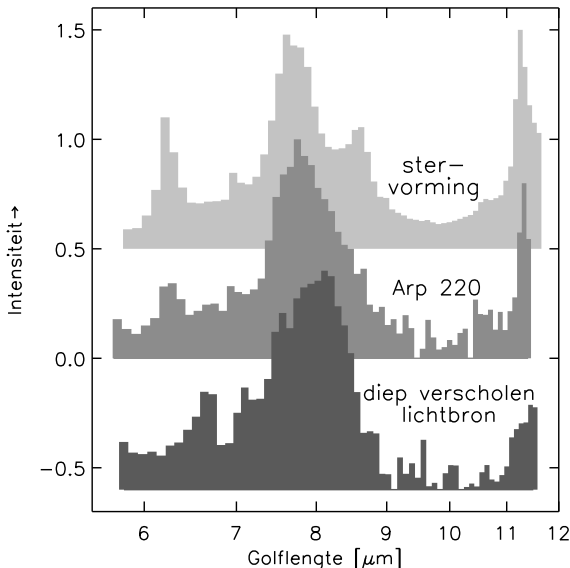
De ontdekking van ijs in de kernen van NGC 4945 en NGC 4418 vormde de aanleiding om alle door mij verzamelde ISO mid-infrarood spektra te onderzoeken op het voorkomen van de vingerafdrukken van water-ijs. Deze studie (hoofdstuk 2 van mijn proefschrift) levert 16 nieuwe gevallen op. Vooral onder ULIRGs blijkt het vaak voor te komen dat er water-ijs in de gezichtslijn naar de kern zit: 60% van de onderzochte ULIRG-spektra toont de bijbehorende spekrale vingerafdruk. Aangezien water-ijs alleen in koude moleculaire wolken voorkomt, betekent dit dat er in de kernen van ULIRGs nog veel moleculair materi-



FIGUUR 18 — Het kerngebied van de bekendste ULIRG, Arp 220, gezien in nabij-infrarood licht. De grote hoeveelheden verduisterend stof in het kerngebied maakt het moeilijk de twee afzonderlijke kernen van het stelsel te ontwaren. Elk van beide kernen is apart nog eens omgeven door een dikke laag stof. Hierdoor vertoont het spektrum van Arp220 grote gelijkenis met dat van NGC 4418. Bron: R. Thompson, N. Scoville en NASA.

aal voorhanden moet zijn om sterren uit te vormen. Een aantal ULIRGs heeft zelfs zo veel moleculair materiaal voor de kern zitten dat het mid-infrarood spektrum zeer veel lijkt op dat van NGC 4418 (onderste paneel van Figuur 14).

Voor veel ULIRGs is het dus niet mogelijk om middels infrarood-spektroscopie er achter te komen of hun enorme lichtkracht (grotendeels) baseert op accretie op een centraal zwart gat of op stervorming. De grote hoeveelheden gas en stof in hun kernen versluieren het antwoord. De kortgeleden gelanceerde opvolger van ISO, genaamd SIRTF, zal het onderzoek aan ULIRGs een nieuwe impuls geven. De detektoren van de satelliet zijn gevoeliger en de telescoop is groter. Er staan ons zeker nog veel verrassingen te wachten!



FIGUUR 19 — Het infraroodspektrum van Arp 220 (**midden**) houdt het midden tussen het spektrum van een stervormingsgebied (**boven**) en dat van een diep verscholen lichtbron (**onder**). In het centrum van Arp 220 vindt er dus stervorming plaats en is er ook een diep verscholen lichtbron aanwezig. Deze laatste kan een actieve kern (zwart gat) zijn of nog meer, zij het verscholen, stervorming.

Bibliography

- Ables J.G., Forster J.R., Manchester R.N., et al., 1987, *MNRAS* 226, 157
- Acosta-Pulido J.A., 1999, In: *ISO Explanatory Library*, http://www.iso.vilspa.esa.es/users/expl_lib/PHT/chop_report02.ps.gz, p. 1
- Acosta-Pulido J.A., Klaas U., Laureijs R.J., et al., 1996, *A&A* 315, L121
- Allamandola L.J., Bregman J.D., Sandford S.A., et al., 1989a, *ApJ Lett.* 345, L59
- Allamandola L.J., Tielens A.G.G.M., Barker J.R., 1985, *ApJ Lett.* 290, L25
- Allamandola L.J., Tielens A.G.G.M., Barker J.R., 1989b, *ApJS* 71, 733
- Anantharamaiah K.R., Viallefond F., Mohan N.R., Goss W.M., Zhao J.H., 2000, *ApJ* 537, 613
- Antonucci R., 1993, *ARA&A* 31, 473
- Armstrong J.T., Barrett A.H., 1985, *ApJS* 57, 535
- Armus L., Shupe D.L., Matthews K., Soifer B.T., Neugebauer G., 1995, *ApJ* 440, 200
- Arp H., 1966, *ApJS* 14, 1
- Baan W.A., Haschick A.D., 1995, *ApJ* 454, 745
- Bakes E.L.O., Tielens A.G.G.M., Bauschlicher C.W., 2001a, *ApJ* 556, 501
- Bakes E.L.O., Tielens A.G.G.M., Bauschlicher C.W., Hudgins D.M., Allamandola L.J., 2001b, *ApJ* 560, 261
- Beckwith S., Evans N.J., Becklin E.E., Neugebauer G., 1976, *ApJ* 208, 390
- Bergman P., Aalto S., Black J.H., Rydbeck G., 1992, *A&A* 265, 403
- Bertoldi F., Timmermann R., Rosenthal D., Drapatz S., Wright C.M., 1999, *A&A* 346, 267
- Blain A.W., Smail I., Ivison R.J., Kneib J.P., Frayer D.T., 2002, *Phys. Rep.* 369, 111
- Bohlin R.C., Savage B.D., Drake J.F., 1978, *ApJ* 224, 132
- Boogert A.C.A., Blake G.A., Tielens A.G.G.M., 2002a, *ApJ* 577, 271
- Boogert A.C.A., Hogerheijde M.R., Blake G.A., 2002b, *ApJ* 568, 761
- Boogert A.C.A., Schutte W.A., Helmich F.P., Tielens A.G.G.M., Wooden D.H., 1997, *A&A* 317, 929
- Boogert A.C.A., Schutte W.A., Tielens A.G.G.M., et al., 1996, *A&A* 315, L377
- Boulanger F., Abergel A., Bernard J.P., et al., 1998a, In: *ASP Conf. Ser. 132: Star Formation with the Infrared Space Observatory*, p. 15

- Boulanger F., Cox P., Jones A., 1998b, In: *a NATO Advanced Study Institute Les Houches, session LXX, Infrared Space Astronomy, today and tomorrow*, p. 251
- Boulanger F., Reach W.T., Abergel A., et al., 1996, *A&A* 315, L325
- Braito V., Della Ceca R., Piconcelli E., et al., 2003, *A&A* accepted, ([astro-ph/0307551](#))
- Bridger A., Wright G.S., Geballe T.R., 1994, In: *ASSL Vol. 190: Astronomy with Arrays, The Next Generation*, p. 537
- Brock D., Joy M., Lester D.F., Harvey P.M., Ellis H.B.J., 1988, *ApJ* 329, 208
- Cami J., 2002, In: *PhD thesis, Groningen Univ.*, p. 169
- Carral P., Hollenbach D.J., Lord S.D., et al., 1994, *ApJ* 423, 223
- Casey S.C., 1991, *ApJ* 371, 183
- Cesarsky C.J., Abergel A., Agnese P., et al., 1996, *A&A* 315, L32
- Cesarsky D., Jones A.P., Lequeux J., Verstraete L., 2000, *A&A* 358, 708
- Charmandaris V., Laurent O., Mirabel I.F., et al., 1999, *Ap&SS* 266, 99
- Chiar J.E., Adamson A.J., Kerr T.H., Whittet D.C.B., 1995, *ApJ* 455, 234
- Chiar J.E., Adamson A.J., Pendleton Y.J., et al., 2002, *ApJ* 570, 198
- Chiar J.E., Gerakines P.A., Whittet D.C.B., et al., 1998, *ApJ* 498, 716
- Chiar J.E., Tielens A.G.G.M., Whittet D.C.B., et al., 2000, *ApJ* 537, 749
- Chrysostomou A., Brand P.W.J.L., Burton M.G., Moorhouse A., 1992, *MNRAS* 256, 528
- Clavel J., Schulz B., Altieri B., et al., 2000, *A&A* 357, 839
- Clements D.L., McDowell J.C., Shaked S., et al., 2002, *ApJ* 581, 974
- Cohen M., Allamandola L., Tielens A.G.G.M., et al., 1986, *ApJ* 302, 737
- Condon J.J., 1992, *ARA&A* 30, 575
- Condon J.J., Helou G., Sanders D.B., Soifer B.T., 1990, *ApJS* 73, 359
- Dahlem M., Golla G., Whiteoak J.B., et al., 1993, *A&A* 270, 29
- Dale D.A., Helou G., Contursi A., Silbermann N.A., Kolhatkar S., 2001, *ApJ* 549, 215
- Dartois E., d'Hendecourt L., 2001, *A&A* 365, 144
- de Graauw T., Haser L.N., Beintema D.A., et al., 1996, *A&A* 315, L49
- de Grijjs R., O'Connell R.W., Gallagher J.S., 2000, In: *ESA SP-445: Star Formation from the Small to the Large Scale*, p. 43
- Demyk K., Dartois E., D'Hendecourt L., et al., 1998, *A&A* 339, 553
- Demyk K., Jones A.P., Dartois E., Cox P., D'Hendecourt L., 1999, *A&A* 349, 267
- Done C., Madejski G.M., Smith D.A., 1996, *ApJ Lett.* 463, L63
- Downes D., Solomon P.M., 1998, *ApJ* 507, 615
- Downes D., Winnberg A., Goss W.M., Johansson L.E.B., 1975, *A&A* 44, 243
- Draine B.T., 1989, In: *Infrared Spectroscopy in Astronomy*, pp. 93–98
- Draine B.T., Bertoldi F., 1999, In: *ESA SP-427: The Universe as Seen by ISO*, p. 553
- Dudley C.C., 1997, In: *PhD thesis, Univ. of Hawaii*
- Dudley C.C., Wynn-Williams C.G., 1997, *ApJ* 488, 720
- Dunne L., Eales S., Edmunds M., et al., 2000, *MNRAS* 315, 115
- Dunne L., Eales S.A., 2001, *MNRAS* 327, 697

- Eales S.A., Becklin E.E., Hodapp K.W., Simons D.A., Wynn-Williams C.G., 1990, *ApJ* 365, 478
- Eales S.A., Wynn-Williams C.G., Duncan W.D., 1989, *ApJ* 339, 859
- Elvis M., Wilkes B.J., McDowell J.C., et al., 1994, *ApJS* 95, 1
- Evans A.S., Becklin E.E., Scoville N.Z., et al., 2003, *AJ* 125, 2341
- Förster Schreiber N.M., Genzel R., Lutz D., Kunze D., Sternberg A., 2001, *ApJ* 552, 544
- Förster Schreiber N.M., Sauvage M., Charmandaris V., et al., 2003, *A&A* 399, 833
- Figer D.F., McLean I.S., Morris M., 1999, *ApJ* 514, 202
- Fischer J., 2001, In: *The Promise of the Herschel Space Observatory*. Eds. G.L. Pilbratt, J. Cernicharo, A.M. Heras, T. Prusti, & R. Harris. ESA-SP 460, p. 131, p. 131
- Fischer J., Satyapal S., Luhman M.L., et al., 1997, In: *ESA SP-419: The first ISO workshop on Analytical Spectroscopy*, p. 149
- Forbes D.A., Norris R.P., 1998, *MNRAS* 300, 757
- Franceschini A., Braito V., Persic M., et al., 2003, *MNRAS* 343, 1181
- Furton D.G., Laiho J.W., Witt A.N., 1999, *ApJ* 526, 752
- Gabriel C., Acosta-Pulido J., Heinrichsen I., Morris H., Tai W.M., 1997, In: *ASP Conf. Ser. 125: Astronomical Data Analysis Software and Systems VI*, p. 108
- Gallagher S.C., Brandt W.N., Chartas G., Garmire G.P., Sambruna R.M., 2002, *ApJ* 569, 655
- Geballe T.R., Lacy J.H., Persson S.E., McGregor P.J., Soifer B.T., 1985, *ApJ* 292, 500
- Genzel R., Cesarsky C.J., 2000, *ARA&A* 38, 761
- Genzel R., Lutz D., Sturm E., et al., 1998, *ApJ* 498, 579
- Gerakines P.A., Schutte W.A., Greenberg J.M., van Dishoeck E.F., 1995, *A&A* 296, 810
- Gerakines P.A., Whittet D.C.B., Ehrenfreund P., et al., 1999, *ApJ* 522, 357
- Giard M., Bernard J.P., Dennefeld M., 1992, *A&A* 264, 610
- Giard M., Bernard J.P., Lacombe F., Normand P., Rouan D., 1994, *A&A* 291, 239
- Gibb E.L., Whittet D.C.B., Schutte W.A., et al., 2000, *ApJ* 536, 347
- Gillett F.C., Forrest W.J., Merrill K.M., 1973, *ApJ* 183, 87
- Gorjian V., Turner J.L., Beck S.C., 2001, *ApJ Lett.* 554, L29
- Graham J.R., Serabyn E., Herbst T.M., et al., 1993, *AJ* 105, 250
- Greenhill L.J., Moran J.M., Herrnstein J.R., 1997, *ApJ Lett.* 481, L23
- Grim R.J.A., Greenberg J.M., 1987, *ApJ Lett.* 321, L91
- Grim R.J.A., Greenberg J.M., de Groot M.S., et al., 1989, *A&AS* 78, 161
- Guainazzi M., Matt G., Brandt W.N., et al., 2000, *A&A* 356, 463
- Haas M., Klaas U., Müller S.A.H., Chini R., Coulson I., 2001, *A&A* 367, L9
- Hagen W., Greenberg J.M., Tielens A.G.G.M., 1983, *A&AS* 51, 389
- Hagen W., Tielens A.G.G.M., 1981, *J. Chem. Phys.* 75, 4198
- Heckman T.M., Armus L., Miley G.K., 1990, *ApJS* 74, 833
- Helou G., Lu N.Y., Werner M.W., Malhotra S., Silbermann N., 2000, *ApJ Lett.* 532, L21
- Henning T., Klein R., Launhardt R., Lemke D., Pfau W., 1998, *A&A* 332, 1035
- Hesser J.E., Harris H.C., van den Bergh S., Harris G.L.H., 1984, *ApJ* 276, 491

- Hibbard J.E., van der Hulst J.M., Barnes J.E., Rich R.M., 2001, *AJ* 122, 2969
- Hollenbach D.J., Tielens A.G.G.M., 1999, *Rev. Mod. Phys.* 71, 173
- Hony S., Van Kerckhoven C., Peeters E., et al., 2001, *A&A* 370, 1030
- Houck J.R., Soifer B.T., Neugebauer G., et al., 1984, *ApJ Lett.* 278, L63
- Howard E.M., Pipher J.L., Forrest W.J., 1994, *ApJ* 425, 707
- Hudgins D.M., Sandford S.A., Allamandola L.J., Tielens A.G.G.M., 1993, *ApJS* 86, 713
- Imanishi M., 2000, *MNRAS* 319, 331
- Imanishi M., Dudley C.C., 2000, *ApJ* 545, 701
- Imanishi M., Dudley C.C., Maloney P.R., 2001, *ApJ Lett.* 558, L93
- Iwasawa K., Koyama K., Awaki H., et al., 1993, *ApJ* 409, 155
- Iwasawa K., Matt G., Guainazzi M., Fabian A.C., 2001, *MNRAS* 326, 894
- Jarrett T.H., Chester T., Cutri R., Schneider S.E., Huchra J.P., 2003, *AJ* 125, 525
- Joblin C., Abergel A., Bregman J., et al., 2000, *ISO beyond the peaks: The 2nd ISO workshop on analytical spectroscopy. Eds. A. Salama, M.F.Kessler, K. Leech & B. Schulz. ESA-SP* 456, 49
- Jones A.P., Tielens A.G.G.M., Hollenbach D.J., McKee C.F., 1994, *ApJ* 433, 797
- Kahanpää J., Mattila K., Lehtinen K., Leinert C., Lemke D., 2003, *A&A* 405, 999
- Kawara K., Nishida M., Phillips M.M., 1989, *ApJ* 337, 230
- Kawara K., Taniguchi Y., Nakai N., Sofue Y., 1990, *ApJ Lett.* 365, L1
- Keane J.V., Tielens A.G.G.M., Boogert A.C.A., Schutte W.A., Whittet D.C.B., 2001, *A&A* 376, 254
- Kennicutt R.C., 1998, *ARA&A* 36, 189
- Kessler M.F., Steinz J.A., Anderegg M.E., et al., 1996, *A&A* 315, L27
- Kewley L.J., Heisler C.A., Dopita M.A., et al., 2000, *ApJ* 530, 704
- Kim D.C., Veilleux S., Sanders D.B., 2002, *ApJS* 143, 277
- Klaas U., Haas M., Heinrichsen I., Schulz B., 1997, *A&A* 325, L21
- Komossa S., Burwitz V., Hasinger G., et al., 2003, *ApJ Lett.* 582, L15
- Koornneef J., 1993, *ApJ* 403, 581
- Koornneef J., Israel F.P., 1996, *New Astronomy* 1, 271
- Kormendy J., Sanders D.B., 1992, *ApJ Lett.* 390, L53
- Kruegel E., Siebenmorgen R., 1994, *A&A* 288, 929
- Kunze D., Rigopoulou D., Lutz D., et al., 1996, *A&A* 315, L101
- Lacy J.H., Baas F., Allamandola L.J., et al., 1984, *ApJ* 276, 533
- Lahuis F., Wieprecht E., Bauer O.H., et al., 1998, In: *ASP Conf. Ser. 145: Astronomical Data Analysis Software and Systems VII*, p. 224
- Larkin J.E., Armus L., Knop R.A., Matthews K., Soifer B.T., 1995, *ApJ* 452, 599
- Laureijs R.J., Watson D., Metcalfe L., et al., 2000, *A&A* 359, 900
- Laurent O., Mirabel I.F., Charmandaris V., et al., 2000, *A&A* 359, 887
- Léger A., Puget J.L., 1984, *A&A* 137, L5
- Lehnert M.D., Heckman T.M., 1995, *ApJS* 97, 89

- Lehnert M.D., Heckman T.M., Weaver K.A., 1999, *ApJ* 523, 575
- Leitherer C., Heckman T.M., 1995, *ApJS* 96, 9
- Lemke D., Klaas U., Abolins J., et al., 1996, *A&A* 315, L64
- Lilly S.J., Le Fevre O., Hammer F., Crampton D., 1996, *ApJ Lett.* 460, L1
- Lira P., Ward M.J., Zezas A., Murray S.S., 2002, *MNRAS* 333, 709
- Lisenfeld U., Isaak K.G., Hills R., 2000, *MNRAS* 312, 433
- Lord S.D., Hollenbach D.J., Haas M.R., et al., 1996, *ApJ* 465, 703
- Luhman M.L., Satyapal S., Fischer J., et al., 2003, *ApJ* 594, 758
- Lutz D., 1999, In: *ESA SP-427: The Universe as Seen by ISO*, p. 623
- Lutz D., Feuchtgruber H., Genzel R., et al., 1996, *A&A* 315, L269
- Lutz D., Maiolino R., Moorwood A.F.M., et al., 2002, *A&A* 396, 439
- Lutz D., Spoon H.W.W., Rigopoulou D., Moorwood A.F.M., Genzel R., 1998, *ApJ Lett.* 505, L103
- Lutz D., Sturm E., Genzel R., et al., 2003, *A&A* in press, ([astro-ph/0307522](#))
- Maldoni M.M., Smith R.G., Robinson G., Rookyard V.L., 1998, *MNRAS* 298, 251
- Malhotra S., Hollenbach D., Helou G., et al., 1999, In: *ESA SP-427: The Universe as Seen by ISO*, p. 813
- Malhotra S., Kaufman M.J., Hollenbach D., et al., 2001, *ApJ* 561, 766
- Marconi A., Oliva E., van der Werf P.P., et al., 2000, *A&A* 357, 24
- Martin P.G., Whittet D.C.B., 1990, *ApJ* 357, 113
- Martín-Hernández N.L., van der Hulst J.M., Tielens A.G.G.M., 2003, *A&A* 407, 957
- Martín-Hernández N.L., Peeters E., Morisset C., et al., 2002, *A&A* 381, 606
- Massi M., Felli M., Simon M., 1985, *A&A* 152, 387
- Matt G., Guainazzi M., Maiolino R., et al., 1999, *A&A* 341, L39
- Mattila K., Lehtinen K., Lemke D., 1999, *A&A* 342, 643
- Mauersberger R., Henkel C., Whiteoak J.B., Chin Y.N., Tieftrunk A.R., 1996, *A&A* 309, 705
- Meixner M., Haas M.R., Tielens A.G.G.M., Erickson E.F., Werner M., 1992, *ApJ* 390, 499
- Mirabel I.F., Vigroux L., Charmandaris V., et al., 1998, *A&A* 333, L1
- Mitchell G.F., Allen M., Maillard J., 1988, *ApJ Lett.* 333, L55
- Moneti A., Cernicharo J., Pardo J.R., 2001, *ApJ Lett.* 549, L203
- Moorwood A.F.M., Glass I.S., 1984, *A&A* 135, 281
- Moorwood A.F.M., Lutz D., Oliva E., et al., 1996a, *A&A* 315, L109
- Moorwood A.F.M., Oliva E., 1988, *A&A* 203, 278
- Moorwood A.F.M., Oliva E., 1994, *ApJ* 429, 602
- Moorwood A.F.M., van der Werf P.P., Kotilainen J.K., Marconi A., Oliva E., 1996b, *A&A* 308, L1
- Moutou C., Sellgren K., Léger A., Verstraete L., Le Coupanec P., 1999a, In: d'Hendecourt L., Joblin C., Jones A. (eds.), *Solid Interstellar Matter : The ISO Revolution*, EDP Sciences, p. 90
- Moutou C., Sellgren K., Leger A., et al., 1998, In: *ASP Conf. Ser. 132: Star Formation with*

- the Infrared Space Observatory*, p. 47
- Moutou C., Verstraete L., Sellgren K., Léger A., 1999b, In: *ESA SP-427: The Universe as Seen by ISO*, vol. 427, p. 727
- Mundell C.G., Ferruit P., Pedlar A., 2001, *ApJ* 560, 168
- Oliva E., Moorwood A.F.M., Drapatz S., Lutz D., Sturm E., 1999, *A&A* 343, 943
- Oliva E., Salvati M., Moorwood A.F.M., Marconi A., 1994, *A&A* 288, 457
- Onaka T., 2000, *Advances in Space Research* 25, 2167
- Onaka T., Yamamura I., Tanabe T., Roellig T.L., Yuen L., 1996, *PASJ* 48, L59
- Ott M., 1995, *Ph.D. Thesis*
- Ott M., Whiteoak J.B., Henkel C., Wielebinski R., 2001, *A&A* 372, 463
- Palumbo M.E., Pendleton Y.J., Strazzulla G., 2000, *ApJ* 542, 890
- Peeters E., Hony S., Van Kerckhoven C., et al., 2002a, *A&A* 390, 1089
- Peeters E., Martín-Hernández N.L., Damour F., et al., 2002b, *A&A* 381, 571
- Pendleton Y.J., Chiar J.E., 1997, In: *ASP Conf. Ser. 122: From Stardust to Planetesimals*, p. 179
- Pendleton Y.J., Sandford S.A., Allamandola L.J., Tielens A.G.G.M., Sellgren K., 1994, *ApJ* 437, 683
- Pendleton Y.J., Tielens A.G.G.M., Tokunaga A.T., Bernstein M.P., 1999, *ApJ* 513, 294
- Pontoppidan K.M., Fraser H.J., Dartois E., et al., 2003, *A&A* accepted, ([astro-ph/0307097](#))
- Ptak A., Heckman T., Levenson N.A., Weaver K., Strickland D., 2003, *ApJ* 592, 782
- Puget J.L., Léger A., 1989, *ARA&A* 27, 161
- Quillen A.C., Alonso-Herrero A., Rieke M.J., et al., 1999, *ApJ* 527, 696
- Reach W.T., Boulanger F., Contursi A., Lequeux J., 2000, *A&A* 361, 895
- Rice W., Lonsdale C.J., Soifer B.T., et al., 1988, *ApJS* 68, 91
- Ridgway S.E., Wynn-Williams C.G., Becklin E.E., 1994, *ApJ* 428, 609
- Rigopoulou D., Lutz D., Genzel R., et al., 1996, *A&A* 315, L125
- Rigopoulou D., Spoon H.W.W., Genzel R., et al., 1999, *AJ* 118, 2625
- Risaliti G., Elvis M., Nicastro F., 2002, *ApJ* 571, 234
- Risaliti G., Maiolino R., Salvati M., 1999, *ApJ* 522, 157
- Roche P.F., Aitken D.K., 1984, *MNRAS* 208, 481
- Roche P.F., Aitken D.K., 1985, *MNRAS* 215, 425
- Roche P.F., Aitken D.K., Smith C.H., 1989, *MNRAS* 236, 485
- Roche P.F., Aitken D.K., Smith C.H., James S.D., 1986, *MNRAS* 218, 19P
- Roche P.F., Chandler C.J., 1993, *MNRAS* 265, 486
- Roelfsema P.R., Cox P., Tielens A.G.G.M., et al., 1996, *A&A* 315, L289
- Sadler E.M., Slee O.B., Reynolds J.E., Roy A.L., 1995, *MNRAS* 276, 1373
- Sakamoto K., Scoville N.Z., Yun M.S., et al., 1999, *ApJ* 514, 68
- Sanders D.B., Mirabel I.F., 1996, *ARA&A* 34, 749
- Sanders D.B., Soifer B.T., Elias J.H., et al., 1988a, *ApJ* 325, 74

- Sanders D.B., Soifer B.T., Elias J.H., Neugebauer G., Matthews K., 1988b, *ApJ Lett.* 328, L35
- Sandford S.A., Allamandola L.J., Tielens A.G.G.M., et al., 1991, *ApJ* 371, 607
- Schaeidt S.G., Morris P.W., Salama A., et al., 1996, *A&A* 315, L55
- Schurch N.J., Roberts T.P., Warwick R.S., 2002, *MNRAS* 335, 241
- Schutte W.A., Greenberg J.M., 1997, *A&A* 317, L43
- Scoville N.Z., Evans A.S., Thompson R., et al., 2000, *AJ* 119, 991
- Scoville N.Z., Yun M.S., Bryant P.M., 1997, *ApJ* 484, 702
- Sellgren K., Tokunaga A.T., Nakada Y., 1990, *ApJ* 349, 120
- Seyfert C.K., 1943, *ApJ* 97, 28
- Siebenmorgen R., Krügel E., Laureijs R.J., 2001, *A&A* 377, 735
- Siebenmorgen R., Krügel E., Zota V., 1999, *A&A* 351, 140
- Siebenmorgen R., Moorwood A., Freudling W., Kaeufl H.U., 1997, *A&A* 325, 450
- Simpson J.P., Witteborn F.C., Price S.D., Cohen M., 1998, *ApJ* 508, 268
- Smith C.H., Aitken D.K., Roche P.F., 1989a, *MNRAS* 241, 425
- Smith H.E., Lonsdale C.J., Lonsdale C.J., Diamond P.J., 1998, *ApJ Lett.* 493, L17
- Smith H.E., Lonsdale C.J., Lonsdale C.J., Diamond P.J., 1999, *Ap&SS* 266, 125
- Smith R.G., Sellgren K., Tokunaga A.T., 1989b, *ApJ* 344, 413
- Soifer B.T., Boehmer L., Neugebauer G., Sanders D.B., 1989, *AJ* 98, 766
- Soifer B.T., Neugebauer G., Helou G., et al., 1984a, *ApJ Lett.* 283, L1
- Soifer B.T., Neugebauer G., Matthews K., et al., 1999, *ApJ* 513, 207
- Soifer B.T., Neugebauer G., Matthews K., Egami E., Weinberger A.J., 2002, *AJ* 124, 2980
- Soifer B.T., Rowan-Robinson M., Houck J.R., et al., 1984b, *ApJ Lett.* 278, L71
- Solomon P.M., Downes D., Radford S.J.E., Barrett J.W., 1997, *ApJ* 478, 144
- Spoon H.W.W., Genzel R., Lutz D., 1998, In: *ASP Conf. Ser. 132: Star Formation with the Infrared Space Observatory*, p. 414
- Spoon H.W.W., Koornneef J., Moorwood A.F.M., Lutz D., Tielens A.G.G.M., 2000, *A&A* 357, 898
- Steidel C.C., Adelberger K.L., Giavalisco M., Dickinson M., Pettini M., 1999, *ApJ* 519, 1
- Steidel C.C., Giavalisco M., Pettini M., Dickinson M., Adelberger K.L., 1996, *ApJ Lett.* 462, L17
- Steiman-Cameron T.Y., Haas M.R., Tielens A.G.G.M., Burton M.G., 1997, *ApJ* 478, 261
- Sturm E., Lutz D., Genzel R., et al., 1996, *A&A* 315, L133
- Sturm E., Lutz D., Tran D., et al., 2000, *A&A* 358, 481
- Sturm E., Lutz D., Verma A., et al., 2002, *A&A* 393, 821
- Tacconi L.J., Genzel R., Tecza M., et al., 1999, *ApJ* 524, 732
- Taniguchi Y., Sato Y., Kawara K., Murayama T., Mouri H., 1997, *A&A* 318, L1
- Tayal S.S., Gupta G.P., 1999, *ApJ* 526, 544
- Thornley M.D., Schreiber N.M.F., Lutz D., et al., 2000, *ApJ* 539, 641
- Thronson H.A., Harper D.A., 1979, *ApJ* 230, 133

- Thronson H.A., Harper D.A., Smith H.A., et al., 1984, In: *Airborne Astronomy Symposium*, p. 127
- Tielens A.G.G.M., Hollenbach D., 1985, *ApJ* 291, 722
- Tielens A.G.G.M., Meixner M.M., van der Werf P.P., et al., 1993, *Science* 262, 86
- Tielens A.G.G.M., Tokunaga A.T., Geballe T.R., Baas F., 1991, *ApJ* 381, 181
- Tielens A.G.G.M., van Kerckhoven C., Peeters E., Hony S., 2000, In: *Astrochemistry: From Molecular Clouds to Planetary*, vol. 197, p. 349
- Tielens A.G.G.M., Whittet D.C.B., 1997, In: *Molecules in Astrophysics: Probes and Processes*, p. 45
- Toomre A., Toomre J., 1972, *ApJ* 178, 623
- Tran Q.D., Lutz D., Genzel R., et al., 2001, *ApJ* 552, 527
- Tremaine S., Gebhardt K., Bender R., et al., 2002, *ApJ* 574, 740
- Vacca W.D., Johnson K.E., Conti P.S., 2002, *AJ* 123, 772
- Valentijn E.A., Feuchtgruber H., Kester D.J.M., et al., 1996a, *A&A* 315, L60
- Valentijn E.A., van der Werf P.P., de Graauw T., de Jong T., 1996b, *A&A* 315, L145
- van den Ancker M.E., Tielens A.G.G.M., Wesselius P.R., 2000, *A&A* 358, 1035
- van Diedenhoven B., Peeters E., Van Kerckhoven C., et al., 2003, *ApJ*, submitted
- van Dishoeck E.F., Helmich F.P., de Graauw T., et al., 1996, *A&A* 315, L349
- Veilleux S., Kim D.C., Sanders D.B., 2002, *ApJS* 143, 315
- Veilleux S., Osterbrock D.E., 1987, *ApJS* 63, 295
- Verma A., Lutz D., Sturm E., et al., 2003, *A&A* 403, 829
- Vermeij R., Peeters E., Tielens A.G.G.M., van der Hulst J.M., 2002, *A&A* 382, 1042
- Verstraete L., Pech C., Moutou C., et al., 2001, *A&A* 372, 981
- Verstraete L., Puget J.L., Falgarone E., et al., 1996, *A&A* 315, L337
- Voit G.M., 1992, *MNRAS* 258, 841
- Weingartner J.C., Draine B.T., 2001, *ApJ* 548, 296
- Werner M.W., Gatley I., Becklin E.E., et al., 1976, *ApJ* 204, 420
- Wexler A.S., 1967, *Applied Spec. Rev.* 1, 29
- Whiteoak J.B., Dahlem M., Wielebinski R., Harnett J.I., 1990, *A&A* 231, 25
- Whitmore B.C., Schweizer F., 1995, *AJ* 109, 960
- Whittet D.C.B., Adamson A.J., Duley W.W., Geballe T.R., McFadzean A.D., 1989, *MNRAS* 241, 707
- Whittet D.C.B., Bode M.F., Baines D.W.T., et al., 1983, *Nature* 303, 218
- Whittet D.C.B., Bode M.F., Longmore A.J., et al., 1988, *MNRAS* 233, 321
- Whittet D.C.B., Pendleton Y.J., Gibb E.L., et al., 2001, *ApJ* 550, 793
- Whittet D.C.B., Schutte W.A., Tielens A.G.G.M., et al., 1996, *A&A* 315, L357
- Wiprecht E., Lahuis F., Bauer O.H., et al., 1998, In: *ASP Conf. Ser. 145: Astronomical Data Analysis Software and Systems VII*, p. 279
- Wright C.M., Drapatz S., Timmermann R., et al., 1996a, *A&A* 315, L301
- Wright G.S., Bridger A., Geballe T.R., Pendleton Y., 1996b, In: *ASSL Vol. 209: New Extra-*

- galactic Perspectives in the New South Africa*, p. 143
Wynn-Williams C.G., Becklin E.E., 1993, *ApJ* 412, 535
Xia X.Y., Xue S.J., Mao S., et al., 2002, *ApJ* 564, 196
Young J.S., Scoville N.Z., 1991, *ARA&A* 29, 581

Acknowledgements

From experience I can tell you that these last pages of a PhD thesis are the most widely read pages of the entire publication. It is here where you think that you will find out whether you have meant something in the life of the PhD candidate. While this may be true to some level, you have to weigh my verdict with the disturbingly low level of sanity left in this PhD candidate after several years of studying toxic molecules in distant galaxies while poking around the Galactic dust bin to discover how they relate to matter closer to home. I reckon it is about time to put the extragalactic silicate and ice absorption features aside and take a look again at some real rocks and glaciers for a while.

First of all, I would like to thank my friends from my undergraduate years in Utrecht. Gert-Jan, Jeroen, Marc, Michiel, René² and Wouter (note the alphabetical order!): you have been in my life ever since we started in Transitorium-I and had to endure the ‘quantum-gelat’ echoing around us. I cherish our many holidays together and hope that we will be able to stay in touch despite the large distances between us.

Several people have played a decisive role in saving me from leaving astronomy. These persons are: Karel van der Hucht, Otto Bauer, Dieter Lutz, Lex Kaper, Alan Moorwood and Peter Barthel. Without your willingness, suggestions and job offers, this PhD thesis would not have been written.

Although I officially started my PhD project in January 1999, I consider my nearly three years at MPE to be a crucial learning period. Most of the data on which this thesis is based have been obtained in MPE guaranteed time programmes and most of my scientific contacts date back to this period. Especially important in this respect were the Ringberg workshops, which I was fortunate enough to attend. Chris, Dan, Dieter, Dietmar, Dimitra, Eckhard, Eiichi, Eva, Helmut, Linda, Lowell, Matt, Michele, Natascha (‘Natastars’), Nirajan, Olivier, Otto, Reinhard and ‘Die Mannschaft’ (Lothar, Ecki and Gerd) were my respected colleagues at this time. Also thanks to Susanne, our secretary.

The first two and a half years of my thesis project, I spent at ESO, the center of European astronomy. To me ESO is also synonymous with ‘social@eso.org’, the group of students and fellows with whom I had the pleasure to explore Munich and the Alps. Particularly fun were the games nights, during which I had the pleasure to butcher — among others — Elise, Greg, Ilse, Jacco, Joël, Mark, Martin, Patrick and ‘Sanders’. Some of these events were preceded by the haute cuisine of Joël and Elise: I still can’t stand the smell of Reblouchon cheese, but the Tartiflette, which results from it, is delicious! Jacco, thank you for introducing me to mountain biking and for infecting me with your passion for arid landscapes. I further would like to mention my office mates, Gerti and Ralph. Did you know that one of our always clinically-dead plants has survived us? Finally, I would like to thank Ed Janssen and Hänen Heyer for their help with creating conference posters and my thesis cover and Ralf Siebenmorgen for our La Silla expeditions.

I cannot leave Munich without mentioning Andrea, Carolina, Gerti, Guido, Hannes, Jan, Liam, Patrick, Richard², Stefan, Wolfgang and ‘Utita’, who accompanied me on the bumpy road of coming out. Without your support and friendship, I would not have been able to simultaneously explore galaxies and myself.

In Groningen, I was welcomed by Ilse and Mark who helped me to turn my house into my home. Ilse, I still like your choice of colours. You would make a great interior decorator. Speaking of which, I’ll soon be moving to a place near you.... Like ESO, I was happy to find an equally healthy and international mix of PhD students and postdocs at Kapteyn Institute. Mercedes Wax, I’m sure you will soon have your own show on Italian TV. Hans, I love your Kölsch! Nieves Leticia, you represent for me the beauty and charm of La Palma. Jacquie, I still remember showing you the spectrum of NGC 4418 at a workshop in Leiden, which marked the start of our successful collaboration. You have considerably redshifted since then! Jero and Stéphanie, we shared some frustrations regarding our frequently absent Leader. Thanks also to Jan who delivered the toxic substances for the theses of Els and me. Els, thanks for coaching me during my last year. This saved me a lot of frustrations and it created time to co-write my last chapter. I’d recommend you as a co-author to anyone! Thanks also to Neil, who succeeded Els as my office mate. We hardly had time to discuss anything but my thesis work; I’m afraid you got to know me when the party was over. Marco, I greatly value our discussions ranging from AEX to RUG. Michiel, thanks for introducing me to the rotation curve business. Ronald, what would this institute be like without your ironical remarks? Kor, thanks for installing my laptop ‘Maus’ for me. Thanks also to Eite and Wim for keeping Alcuin up and running. Thanks also to the ladies of the Secretariaat.

Klaus Pontoppidan in Leiden, thank you for spending so much time on the reduction of the ISAAC dataset and sharing your insights on XCN and CO ice absorption features.

My colloquium tour last November would not have been possible without the financial support from the Leids Kerkhoven Bosscha Fonds (LKBF), the Kapteyn Institute and the host institutions. In particular, I would like to thank Bernhard Brandl, Guido deMarchi, Nick Scoville, Bob Joseph and Lou Allamandola for their hospitality. Vassilis, Jim, Bernhard, Don, Sarah & Jim, Daniel and the rest of the IRS team at Cornell: thanks for your warm welcome on my three visits and for making me look forward to becoming your colleague.

Henny: in the end it was not such a big step from LBVs to ULIRGs. LBVs are the most luminous stars and ULIRGs the most luminous galaxies. Flör: bedankt voor de Smarties. ‘Gedeelde smart is halve smart!’ I’m also grateful to my ’ole friend Jack for designing my thesis cover. It was about time we worked together again, 5 years after the ISO T-shirt project!

I am deeply indebted to Alan Moorwood, Dieter Lutz and my promotor Xander Tielens for embarking with me on this thesis journey. I could not have wished for better collaborators and coaches. Your contributions, detailed comments and insight have been of great value to me. Xander, I hope you will redshift even further with me.

Jamie, you have been a great ‘rots in de branding’ over the last two years and especially over this last summer which you spent here with me. I miss you and I am looking forward to living much closer to you.

Henk, Hella en Birgit: hadden jullie ooit gedacht dat wat begon met het uitschakelen van lantaarnpalen tijdens nationale sterrenkijkdagen later zulke ernstige vormen zou aannemen? Bedankt voor jullie onvoorwaardelijke steun. Ik had me geen beter nestje kunnen wensen.

Henrik Spoon, Groningen, September 2003